FEDERAL UNIVERSITY OF JUIZ DE FORA
GRADUATE PROGRAM OF CHEMISTRY
DOCTORAL PROGRAM IN CHEMISTRY

Eduardo Ribeiro Almeida

Molecular modeling of drug delivery systems based on carbon nanostructures:
Structure, function, and potential applications for anticancer complexes of Pt(II)

Juiz de Fora
2023

Eduardo Ribeiro Almeida

Molecular modeling of drug delivery systems based on carbon nanostructures:

Structure, function, and potential applications for anticancer complexes of Pt(II)

Thesis presented to the Graduate Program of Chemistry at Federal University of Juiz de Fora as partial requirement to obtain the title of Ph.D. in Chemistry.

Advisor: Prof. Dr. Hélio Ferreira dos Santos

Co-advisor: Prof. Dr. Priscila Vanessa Zabala Capriles Goliatt

Juiz de Fora

2023

Ficha catalográfica elaborada através do programa de geração
automática da Biblioteca Universitária da UFJF,
com os dados fornecidos pelo(a) autor(a)

Almeida, Eduardo Ribeiro.
Molecular modeling of drug delivery systems based on carbon nanostructures : Structure, function, and potential applications for anticancer complexes of Pt(II) / Eduardo Ribeiro Almeida. -- 2023.
308 p. : il.

Orientador: Hélio Ferreira Dos Santos
Coorientadora: Priscila Vanessa Zabala Capriles Goliatt
Tese (doutorado) - Universidade Federal de Juiz de Fora, Instituto de Ciências Exatas. Programa de Pós-Graduação em Química, 2023.

1. carbon nanohorn. 2. chemical functionalization. 3. Pt(II) complexes. 4. cell membrane. 5. molecular dynamics. I. Dos Santos, Hélio Ferreira, orient. II. Goliatt, Priscila Vanessa Zabala Capriles, coorient. III. Título.

Eduardo Ribeiro Almeida

Molecular modeling of drug delivery systems based on carbon nanostructures: Structure, function, and potential applications for anticancer complexes of Pt(II)

Tese apresentada ao Programa de Pós-Graduação em Química da Universidade Federal de Juiz de Fora como requisito parcial à obtenção do título de Doutor em Química. Área de concentração: Química.

Aprovada em 15 de setembro de 2023.

BANCA EXAMINADORA

Prof. Dr. Hélio Ferreira dos Santos - Orientador
Universidade Federal de Juiz de Fora

Profa. Dra. Priscila Vanessa Zabala Capriles Goliatt - Coorientadora
Universidade Federal de Juiz de Fora

Profa. Dra. Thereza Amélia Soares da Silva
Universidade de São Paulo

Dr. Laurent Emmanuel Dardenne
Laboratório Nacional de Computação Científica

Prof. Dr. Luiz Antônio Sodré Costa
Universidade Federal de Juiz de Fora

Prof. Dr. Fernando Sato

Universidade Federal de Juiz de Fora

Juiz de Fora, 31/08/2023.

Documento assinado eletronicamente por **Helio Ferreira dos Santos**, **Professor(a)**, em 15/09/2023, às 17:24, conforme horário oficial de Brasília, com fundamento no § 3º do art. 4º do Decreto nº 10.543, de 13 de novembro de 2020.

Documento assinado eletronicamente por **Priscila Vanessa Zabala Capriles Goliatt**, **Professor(a)**, em 15/09/2023, às 17:25, conforme horário oficial de Brasília, com fundamento no § 3º do art. 4º do Decreto nº 10.543, de 13 de novembro de 2020.

Documento assinado eletronicamente por **Luiz Antonio Sodre Costa**, **Professor(a)**, em 15/09/2023, às 17:25, conforme horário oficial de Brasília, com fundamento no § 3º do art. 4º do Decreto nº 10.543, de 13 de novembro de 2020.

Documento assinado eletronicamente por **Fernando Sato**, **Professor(a)**, em 15/09/2023, às 17:25, conforme horário oficial de Brasília, com fundamento no § 3º do art. 4º do Decreto nº 10.543, de 13 de novembro de 2020.

Documento assinado eletronicamente por **Thereza Amelia Soares da Silva**, **Usuário Externo**, em 15/09/2023, às 17:25, conforme horário oficial de Brasília, com fundamento no § 3º do art. 4º do Decreto nº 10.543, de 13 de novembro de 2020.

Documento assinado eletronicamente por **Laurent Emmanuel Dardenne**, **Usuário Externo**, em 15/09/2023, às 17:26, conforme horário oficial de Brasília, com fundamento no § 3º do art. 4º do Decreto nº 10.543, de 13 de novembro de 2020.

A autenticidade deste documento pode ser conferida no Portal do SEI-Ufjf (www2.ufjf.br/SEI) através do ícone Conferência de Documentos, informando o código verificador **1446042** e o código CRC **EE6EA4E8**.

I dedicate this work to my parents and my sister for all support and encouragement over these years.

ACKNOWLEDGMENTS

First, I would like to thank my parents, Ana Cláudia e Cleumar, and my sister Natália, for all motivation, support, celebrations, and kindness throughout the years of this academic journey.

I would also like to thank my advisors, Prof. Hélio F. Dos Santos and Prof. Priscila V. S. Z. C. Goliatt, for the guidance, teachings, and patience throughout these four years of work. Thank you for all the discussions during the meetings, talks, and seminars, which were essential for building my researcher profile.

I would like to express my deeper gratitude to my supervisor in France, Prof. Fabien Picaud, at the *Université de Franche-Comté*, for the kind hospitality, support, patience, and guidance during my doctoral stay in the *Laboratoire de Nanomédicine, Imagerie, Thérapeutique*.

My special thanks to my colleagues from the research group *Núcleo de Estudos em Química Computacional* (NEQC): Yuliana Delgado, Nathália Rosa, Rodrigo Fraga, Júlio Arvelhos, and Luã Oliveira. A special thanks to Bjørn for being a great friend always in a good mood even during the tough times as graduate students. I would also like to thank the recent colleagues that form the new generation of the NEQC: Rivael, Daniel, Frederico, Larissa, Luíz Felipe, and Eloah. There is also need to thank my colleagues from other laboratories, such as Bruna Neves, Maria Eduarda Vieira, and Marcelo Carvalho.

A special thanks to Neilton dos Reis for the kindness, celebrations, and encouragement during the happy and tough moments. I would also like to express my deeper gratitude to my psychoanalyst Mariluci Vieira for all these years of listening and analysis.

Finally, I would like to thank the Federal University of Juiz de Fora and the Brazilian research funding agencies FAPEMIG (*Fundação de Amparo à Pesquisa do Estado de Minas Gerais*), CAPES (*Coordenação de Aperfeiçoamento de Pessoal de Nível Superior*), and CNPq (*Conselho Nacional de Desenvolvimento Científico e Tecnológico*). A special thanks to FAPEMIG for providing me the Ph.D. scholarship and CAPES for providing me the scholarship for the sandwich Ph.D. program. These resources were fundamental for conducting this research.

“We are a way for the cosmos to know itself.” (Carl Sagan, 1980, Cosmos).

ABSTRACT

The medication with Pt(II) drugs (cisplatin, carboplatin, and oxaliplatin) has been an effective alternative for treating cancers due to their notable inhibition of cancer cells growth and the prevention of metastasis. Nevertheless, the low selectivity of these metallodrugs for malignant cells produces severe side effects, which limit this chemotherapy. In this context, carbon nanohorns (CNHs) have been considered potential nanovectors for drugs, since they present low toxicity, drug-loading capacity, biodegradation routes, and biocompatibility when oxidized. However, there is still a lack of studies regarding the molecular behavior of these nanocarriers on cell membranes. The present work aims to characterize the interactions between inclusion complexes drug@CNH, which are formed by platinum drugs encapsulated in CNHs, and plasma membranes by using molecular dynamics simulations. The results demonstrated that the van der Waals contribution played a primary role (~74%) for the complex stability, which explain the confined dynamics of drugs inside the CNHs. The free energy profiles revealed an endergonic character of the drug release processes from CNHs, in which the energy barrier for oxaliplatin release (~24 kcal mol^{-1}) was ~30% larger than those for carboplatin and cisplatin (~18 kcal mol^{-1}). The simulations also showed four stages of the interaction mechanism CNH--membrane: approach, insertion, permeation, and internalization. Despite the low structural disturbance of the membranes, the free energy barrier of ~55 kcal mol^{-1} for the CNHs translocation indicated that this transport is kinetically unfavorable by passive process. The *in silico* experiments evidenced that the most likely mechanism of cisplatin delivery from CNHs involve the approach and insertion stages, where the nanovector adheres on the surface of cancer cells, as reported in *in vitro* studies. After this retention, the drug load may be slowly released in the tumor site. Finally, simulations of the cellular uptake of Pt(II) drugs also pointed out significant energy barriers (~30 kcal mol^{-1}) for this process, which reflects their low permeability in membranes as discussed in experimental studies. In addition to reinforcing the potential of CNH as nanovector of Pt(II) drugs, the results presented in this thesis may assist and drive new experimental studies with CNHs, focusing on the development of less aggressive formulations for cancer treatments.

Keywords: Carbon nanohorn. Chemical functionalization. Pt(II) complexes. Cell membrane. Molecular dynamics. Umbrella sampling. Potential of mean force.

RESUMO

A medicação com fármacos a base de Pt(II) (cisplatina, carboplatina e oxaliplatina) tem sido uma alternativa efetiva para tratar cânceres devido à sua notável inibição do crescimento de células cancerosas e a prevenção de metástases. No entanto, a baixa seletividade dessas metalodrogas por células cancerosas gera severos efeitos colaterais. Nesse contexto, nanohorns de carbono (CNHs) têm sido considerados potenciais nanovetores de fármacos, devido a baixa toxicidade, capacidade de carreamento de fármacos, rotas de biodegradação, e biocompatibilidade quando oxidados. Porém, existe uma carência de estudos tratando o comportamento desses nanocarreadores em biomembranas. Esse trabalho tem como objetivo caracterizar as interações entre complexos de inclusão fármaco@CNH, formados por fármacos de Pt(II) encapsulados em CNHs, e membranas usando simulações por dinâmica molecular. Os resultados demonstraram que a contribuição de van der Waals teve um papel primário (~74%) na estabilidade dos complexos, o que explica a dinâmica confinada dos fármacos dentro dos CNHs. Os perfis de energia livre revelaram o caráter endergônico da liberação dos fármacos a partir de CNHs, nos quais a barreira de energia para a liberação da oxaliplatina (~24 kcal mol^{-1}) é ~30% maior do que aquelas para carboplatina e cisplatina. As simulações mostraram quatro estágios do mecanismo de interação CNH-membrana: aproximação, inserção, permeação e internalização. Apesar do baixo distúrbio estrutural das membranas, a barreira de energia livre de ~55 kcal mol^{-1} para a translocação de CNHs indicou que esse transporte é desfavorável cineticamente via o processo passivo. Os experimentos *in silico* evidenciam que o mecanismo mais provável de entrega de cisplatina a partir de CNHs envolve a aproximação e inserção, onde o nanovetor adere na superfície de células cancerosas, como reportado em estudos *in vitro*. Após essa retenção, a carga de fármaco deve ser ligeiramente liberada no tumor. As simulações de captação celular de fármacos de Pt(II) também apontaram barreiras de energia significativas (~30 kcal mol^{-1}) para esse processo, o que reflete a baixa permeabilidade deles em membranas como discutido em estudos experimentais. Além de reforçar o potencial de CNHs como nanovetores de fármacos de Pt(II), os resultados apresentados nessa tese podem auxiliar e impulsionar novos estudos com CNHs, focando no desenvolvimento de formulações menos agressivas para tratamentos de câncer.

Palavras-chave: Nanohorn de carbono. Funcionalização química. Complexos de Pt(II). Membrana celular. Dinâmica molecular. Umbrella Sampling. Potencial de força média.

LIST OF FIGURES

LIST OF TABLES

LIST OF ABBREVIATIONS

ABF	adaptive biasing method
ATP	adenosine triphosphate
BC	breast cancer
cdcla	monoaqua derivative of cisplatin
cdclo	monohydroxo derivative of cisplatin
cddp	cisplatin
CHelpG	charges from electrostatic potentials using a grid based method
C_memb	membrane of a breast cancer cell
CN	Coordination number
CNH	carbon nanohorn
CNHf	functionalized carbon nanohorn
CNHox	oxidized carbon nanohorn
CNT	carbon nanotube
cpx	carboplatin
DDS	drug delivery systems
EPR	enhanced permeability and retention
FDA	Food and Drug Administration
GAFF	general amber force field
HB	Hydrogen bond
HF	Hartree-Fock
IEFPCM	Integral equation formalism for polarized continuum method
INCA	Instituto Nacional do Câncer
LJ	Lennard-Jones
MD	molecular dynamics
MM/GBSA	molecular mechanics generalized Born surface area method
MP2	Møller-Plesset Second-Order Pertubation Theory
N_memb	Membrane of normal breast cell
NMR	Nuclear magnetic resonance
oxa	oxaliplatin
PCM	Polarizable continuum method
PES	Potential energy surface

RDF	radial distribution function
RMSD	Root mean square deviation
QM	Quantum mechanics
SMD	steered molecular dynamics
std	standard deviation
TS	Transition state
US	umbrella sampling
vdW	van der Waals

SUMMARY

1 CHAPTER 1

Introduction

Since the context of this thesis involves the treatment of cancer using a strategy of the nanomedicine, this chapter is dedicated to the presentation of the scenario referring to this disease, its mains aspects, the classical chemotherapies with the well-known side effects, and finally the potential therapeutic strategy to treat it, which is the central idea of this work. This chapter ends with the scientific motivation and the objectives of this research.

1.1 CANCER

Cancer has been one of the main problems of public health worldwide with notable rates of incidence and mortality. According to Sung *et al.* (SUNG, *et al.*, 2021), the global estimates for the year 2020 indicated 19.1 millions of new cancer cases and 9.9 millions of deaths. The recent literature points out a worsening of this scenario in both United States (SIEGEL, *et al.,* 2023) and European Union (JOINT RESEARCH CENTRE, 2023) due to the frequent interruption or slowdown of the treatment of this disease during the COVID-19 pandemic. The projections for 2040 are even more critical, since it is expected an increase of 47% in the incidence rate of this malignant neoplastic disease (SUNG, *et al.*, 2021).

Regarding the Brazilian context, the estimates reported by the *Instituto Nacional do Câncer* (INCA) highlighted the occurrence of 704,000 new cancer cases for the period from 2023 to 2025, where the most common types are the nonmelanoma skin cancer (31.3%), breast cancer (10.5%), and prostate (10.3%) (INSTITUTO NACIONAL DO CÂNCER, 2019). The pandemic period of the COVID-19 also impacted the treatment of cancer in Brazil, since it was observed a significant reduction of the diagnosis (-24.3% in the North region and -42.7% in the Northeast region), which was caused by the restrictions and failures in the public healthcare system during this period (MARQUES, *et al.*, 2023).

When it comes to the types of cancer, breast cancer is currently the most commonly diagnosed modality and the second leading cause of women deaths worldwide. The global estimates of 2020 indicated 2.3 million of new cases and 685,000 deaths related to this disease (ARNOLD, *et al.*, 2022; GIAQUINTO, *et al.*, 2022). According to the estimates (2023-2025) reported by the INCA, breast cancer will be the most incident after the nonmelanoma skin cancer in all regions of Brazil. The increasing mortality of this cancer reached more than 16,000

deaths in 2017, and when it comes to the period 2016-2020, the mortality of breast cancer represented 16.3 % of all cancer-related deaths in Brazil (INSTITUTO NACIONAL DO CÂNCER, 2019; BUZAID, *et al.*, 2020).

In the face of this grave scenario, the research involving the development of efficient treatments to this disease is highly important, in addition to public policies that guarantee the global access to such therapies. This combination contributes not only to the reduction of the mortality rate, but also to a better quality of life for cancer patients.

Before proceeding any further, it is important to define the term cancer and its main aspects. This term actually refers to a large group of diseases that are characterized by an unregulated cell growth leading to the process of invasion of surrounding tissues and, in the most critical level, the spread of these cancer cells to other parts of the body, which is known as the metastasis stage (KING & ROBINS, 2006). This disease is also accompanied by a resistance to the programmed cell death mechanisms and the recruitment of blood and nutrients supply to the cancerous regions (NENCLARES & HARRINGTON, 2020). Above all, the cancer is classified as a genetic disease, since the aforementioned anomalous cell behavior is induced by abnormal genes, which are generated from the corruption, mainly the mutation, of the information in the cellular DNA (NENCLARES & HARRINGTON, 2020).

The disordered cell growth is contrary to the cycle of a normal cell, which involves stages such as the formation, growth, cell division to form new cells as the body demands, aging, and cell death (NATIONAL CANCER INSTITUTE, 2023). Specifically, in addition to the ability to circumvent the immune system, cancer cells can also become immortal with a permanent replicative kinetics due to the lengthening mechanism of their telomeres (NENCLARES & HARRINGTON, 2020). Moreover, by comparing to normal cells, cancer cells are less specialized and they can promote the cellular replacement, leading to the loss of functions referring to the invaded tissues.

Unlike normal cells, the morphology of cancer cells is also distinct by presenting a high variability in size, abnormal shapes, modifications in the cell membranes, irregularities in the cytoplasm, and dark and enlarged nuclei as evidenced by microscopy images (MANUAL DE BASES TÉCNICAS BÁSICAS DA ONCOLOGIA, 2013). The darkness of these irregular nuclei (Figure 1.1) with a coarse chromatin distribution is the result of the DNA overexpression and the disorganization of chromosomes in these malignant cells (FISCHER, 2020).

The cancer tissues are formed from grouping of cancer cells by means of the changes in the multiplication profile of these cells. In Figure 1.1, while the hyperplasia is the first stage of anomalous replication of cells displaying an apparent normal profile, the dysplasia refers to an

advanced stage of cellular multiplication, where it is possible to identify abnormal morphologies with a potential to develop a cancer (NATIONAL CANCER INSTITUTE, 2023).

Figure 1.1 Cell profile changes of tissues that may develop into the advanced condition characterizing what is known as cancer.

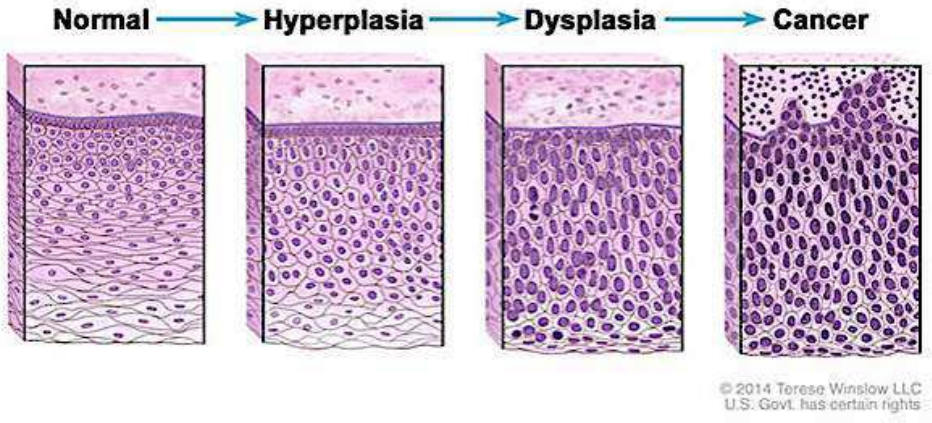

Reference: NATIONAL CANCER INSTITUTE (2023).

If the development of cancer cells is slow forming a localized cell mass with a fibrous pseudocapsule, the tumor, which defines both benign and malignant cell growth (KING & ROBINS, 2006), is classified as a benign neoplasm that is not, in general, life-threatening. On the other hand, a malignant neoplasm or malignant tumor presents an accelerated cell multiplication that may reach the severe and lethal stage of metastasis where new tumors are formed in other parts of the body from the primary metastatic tumor (SUDHAKAR, 2009).

The carcinogenesis, which is defined as the formation of a cancer, is directly related to mutations in the DNA of a normal cell caused by external factors, such as the exposure and interaction with the environment, and internal factors as the heredity (SUDHAKAR, 2009). However, the literature reveals that the incidence of cancer due to hereditary factors represents only 5-10% of the cases in contrast to the range of 90-95% due to lifestyle and environment, which includes the tobacco use, excessive alcohol consumption, unhealthy diets, obesity, sun overexposure, and other risk factors (KING & ROBINS, 2006; ANAND, *et al.*, 2008; WORLD HEALTH ORGANIZATION, 2022).

With regard to breast cancer, this term refers to a series of neoplastic diseases that proliferate in the mammary gland. The most common histologic profile of this cancer is the carcinoma, *i.e.* a cancer that is formed in epithelial cells. These lesions can be either *in situ* or invasive (INSTITUTO NACIONAL DO CÂNCER, 2019). The details from Figure 1.2 show

the development scheme of breast cancers, and the structures of the breast where this disease may progress. Specifically, the breast epithelium is formed by luminal and myoepithelial cells, which are structured in lobules and ducts. It is worth mentioning that 85% of the diagnosis of breast cancers correspond to ductal carcinomas (WELSH, 2013).

Figure 1.2 - Carcinogenesis in a human breast.

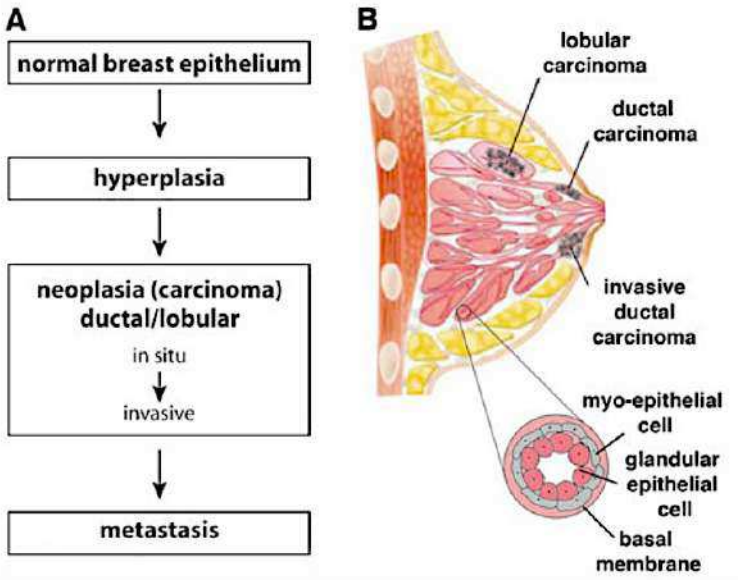

Reference: DE KONING (2009).

According to the studies reported by INCA, the incidence of breast cancer is associated to risk factors such as age over 50 years, mutations in the BRCA1 and BRCA2 genes, family history of breast and ovarian cancers, late menopause, obesity, sedentary lifestyle, and exposure to ionizing radiation (INSTITUTO NACIONAL DO CÂNCER, 2019). The high genetic heterogeneity of breast cancer is responsible by its diversity in terms of subtypes and aggressive behavior, which demands the application and development of more specialized treatments (GODONE, *et al*., 2018).

In general, the treatment of cancer encompasses a combination of conventional procedures, including surgery, chemotherapy, and radiotherapy. Modern modalities such as immunotherapy, hyperthermia, photodynamic therapy, hormone-based therapy, and stem cell therapy, can be also employed (ABBAS & REHMAN, 2018; NATIONAL CANCER INSTITUTE, 2023). The definition of the treatment scheme depends on the cancer type, locality, and stage of development referring to this disease. The next section will focus on the chemotherapy of cancer, since it is connected to the subject of this thesis.

1.2 Pt(II)-BASED DRUGS

Chemotherapy remains as one of the main strategies to treat a series of cancers, including the localized and metastatic ones. This treatment is based on the application of antineoplastic drugs aiming to fight cancer cells, and the administration of this medication can be oral, intravenous, intramuscular, intra-abdominal, subcutaneous, intrathecal, and topical (ANAND, U., *et al.*, 2022; INSTITUTO NACIONAL DO CÂNCER, 2023).

Based on the structure, function, and mode of action, the chemotherapeutics are classified in different groups, such as alkylating agents, antimetabolites, vinca alkaloids, antitumor antibiotic, hormonal agents, and other classes (ANAND, U., *et al.*, 2022). In this context, the Pt(II)-based drugs (see Figure 1.3) are categorized as alkylating agents, since they form derivatives with the DNA by means of covalent interactions, leading to alterations in the cell cycle, including the suppression of the replication and transcription stages (ANAND, U., *et al.*, 2022).

Figure 1.3 - Structures of the Pt(II)-based drugs: cisplatin (A), carboplatin (B), oxaliplatin (C), nedaplatin (D), lobaplatin (E), and heptaplatin (F).

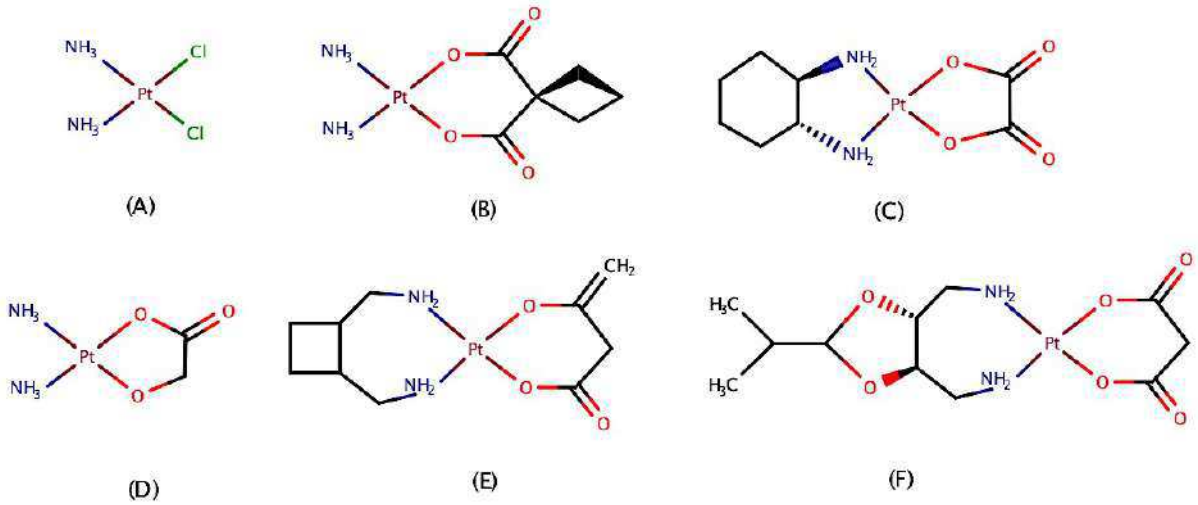

Reference: Own author (2023).

The use of platinum drugs in cancer chemotherapy started in 1978 with the approval of the *cis*-diaminedichloroplatinum(II), also known as cisplatin (cddp) (Figure 1.3A), by the Food and Drug Administration (FDA). This metallodrug had already been synthesized in 1844 by Michele Peyrone (PEYRONE, 1844), and its antitumor activity was accidently identified in 1965 by Rosenberg and coworkers (ROSENBERG, *et al.*, 1965). This pioneer platinum drug is

widely applied in the cancer treatments of a diversity of solid tumors in the lung, liver, bladder, breast, cervical, head, neck, ovaries, and testicles (TCHOUNWOU, *et al.*, 2021). In addition to the well-known cddp, there are other generations of platinum drugs approved worldwide as the *cis*-diammine(1,1-cyclobutane dicarboxylato)platinum(II), also known as carboplatin (cpx) with the approval by the FDA in 1980 (Figure 1.3B), and the *cis*-oxalato-trans-l-1,2-diaminocyclohexaneplatinum(II), also known as oxaliplatin (oxa) with the approval by the FDA in 2004 (Figure 1.3C). While cpx is applied in the treatment of cancers in the ovarian, head, neck, lung, and breast, oxa is used to treat non-small cell lung cancer, cancers in the head and neck, ovarian cancer, and breast cancer (OBRESHKOVA, *et al.*, 2022; QIN, *et al.*, 2020).

On the other hand, there are other platinum drugs with clinical approvals in specific countries, such as the *cis*-diaminoglicolatoplatinum(II), also known as nedaplatin (Figure 1.3D) with approval in Japan in 1995; the lactatediaminomethylcyclobutaneplatinum(II), also known as lobaplatin (Figure 1.3E) with approval in China in 2003; and the *cis*-malonate[(4R,5R)-4,5-bis(aminomethyl)-2-isopropyl-1,3-dioxolane]platinum(II), also known as heptaplatin (Figure 1.3F) with approval in Republic of Korea in 1999. Regarding the applications, nedaplatin has been administered to treat cancers in the head, neck, esophagus, small cell lung and non-small cell lung, whereas loboplatin is used in the treatment of chronic myelogenous leukemia, small cell lung and metastatic breast cancer, and heptaplatin is applied in the chemotherapies of gastric cancer (OBRESHKOVA, *et al.*, 2022; JOHNSTONE, *et al.*, 2016).

The high antitumor potential of cddp is connected to the fact that this drug is capable of inducing damages to the DNA of cancer cells, inhibiting vital steps of the cell cycle, which activates the mechanisms o programmed cell death as the apoptosis. Specifically, the mechanism of action of cddp involves the cellular uptake, activation by aquation (hydrolysis reaction), DNA binding, and the processing of DNA physical lesions leading to cancer cell death (GANDIN, *et al.*, 2023). Before describing more details of the mechanism of action referring to this pioneer platinum drug, it is important to understand the behavior of this molecule in aqueous solution. Figure 1.4 illustrates the equilibrium of cddp and its derivatives in water. Since the blood has a chloride (Cl^-) concentration of about 105 mM, cddp remains mainly in the neutral form (Figure 1.4A) with a slight progression to the right side of the hydrolysis reaction shown in Figure 1.4.

Figure 1.4 - Hydrolysis reaction of cisplatin in aqueous: cisplatin, *cis*-$[Pt(NH_3)_2(Cl)_2]$ (A), mono-aqua derivative, *cis*-$[Pt(NH_3)_2(H_2O)Cl]^+$ (B), di-aqua derivative, *cis*-$[Pt(NH_3)_2(H_2O)_2]^{2+}$ (C), mono-hydroxo derivative, *cis*-$[Pt(NH_3)_2(Cl)(OH)]$ (D), mono-aqua-hydroxo derivative, cis-$[Pt(NH_3)_2(H_2O)(OH)]^+$ (E), and di-hydroxo derivative, *cis*-$[Pt(NH_3)_2(OH)_2]$ (F).

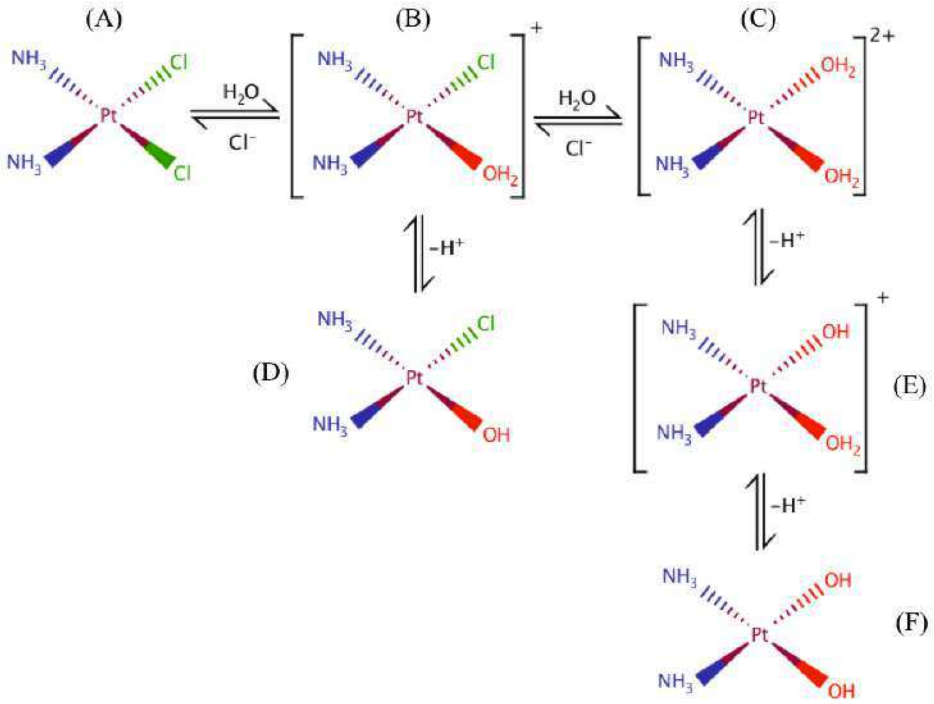

Reference: Own author (2023).

The loss of one Cl^- from cddp and the binding of a water molecule leads to the formation of the very acid mono-aqua derivative (*cis*-$[Pt(NH_3)_2(H_2O)Cl]^+$, Figure 1.4B), which can be dissociated in the mono-hydroxo derivative (*cis*-$[Pt(NH_3)_2(Cl)(OH)]$, Figure 1.4D). Therefore, in the extracellular medium, which is characterized by a high Cl^- concentration, the equilibrium of cisplatin is mainly composed by cisplatin, *cis*-$[Pt(NH_3)_2(H_2O)Cl]^+$, and *cis*-$[Pt(NH_3)_2(Cl)(OH)]$ (Figure 1.4A,B,D). When it comes to the cytoplasm, where there is a low Cl^- concentration (about 4 mM), the hydrolysis reaction showed in Figure 1.4 is shifted to the right side, favoring the formation of the di-aqua derivative, *cis*-$[Pt(NH_3)_2(H_2O)_2]^{2+}$ (Figure 1.4C) and its deprotonated species (*cis*-$[Pt(NH_3)_2(H_2O)(OH)]^+$ and *cis*-$[Pt(NH_3)_2(OH)_2]$, Figure 1.4E-F) (MAKOVEC, 2019). The two hydrolyzed species (Figure 1.4B-C) of cddp are relevant to the anticancer activity of this metallodrug, since they are the active species that will indeed bind and damage the DNA of a cancer cell. However, it is estimated that only 1% of the intracellular cddp interacts and form adducts with the DNA (ANTHONY, *et al.*, 2020). It is worth mentioning that the hydrolysis of cddp is not thermodynamically and kinetically

favorable, with an energy barrier for the first hydrolysis in the range of 22.55–23.32 $kcal^{-1}$ (experimental values) (BANCROFT, *et al.*, 1990; HINDMARSCH, *et al.*, 1997).

By comparing with cddp, cpx (Figure 1.3B) is less reactive and toxic due to the presence of the chelating ligand cyclobutane-1,1-dicarboxylate, which enables, consequently, the administration of higher doses in the chemotherapy (BERGAMO, *et al.*, 2018). Moreover, the presence of the ligand carboxylate also influences the hydrolysis reaction of cpx (Figure 1.5), which is more unfavorable and slower than the one of cddp (Figure 1.4), due to the stabilizing effect induced by the chelating ligand that makes difficult the ring opening (Figure 1.4B) for the subsequent formation of the hydrolyzed and deprotonated species (Figure 1.5C,E-F) (AHMAD, 2017). For instance, in Cl^--free phosphate buffer at pH 7 and 37°C, the half-life of cpx is about 268 h, whereas the half-life of cddp under the same conditions is 24 h (AHMAD, 2017; PAVELKA, *et al.*, 2007). The low tendency to the hydrolysis of cpx (Figure 1.5) has indicated the existence of other routes for its mechanism of action, such as an enzymatic activation, reaction based on the in interaction with sulfur nucleophiles, or the interaction between the neutral form of cpx and the DNA referring to a cancer cell (AHMAD, 2017).

Figure 1.5 - Hydrolysis mechanism of carboplatin (cpx).

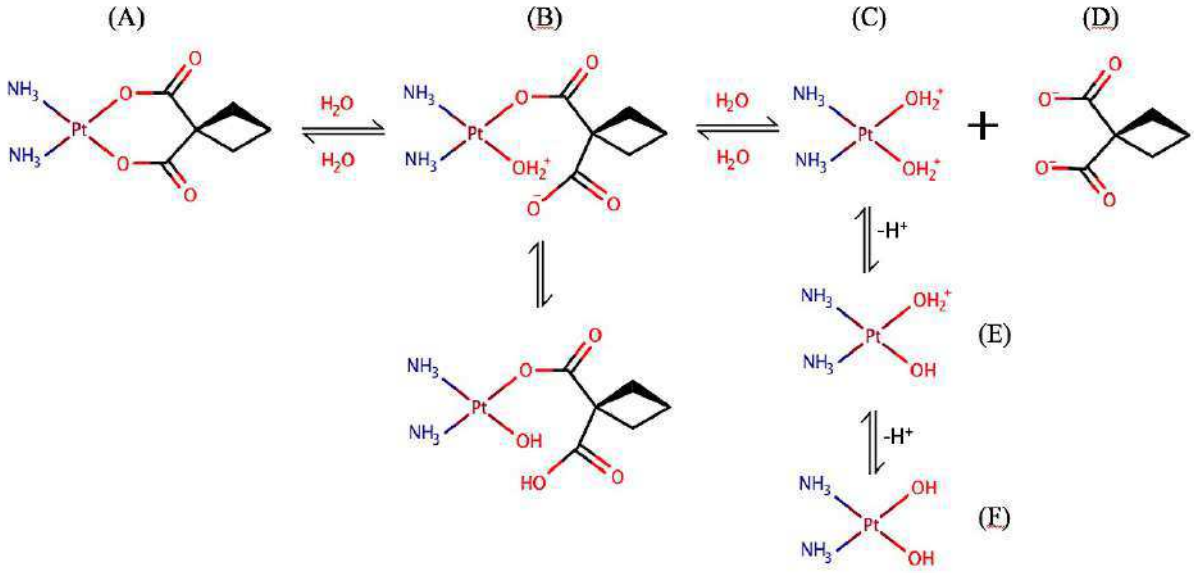

Reference: Own author (2023).

The activation barrier for the hydrolysis of cpx in neutral conditions, which is defined by the ring opening step, is 30 $kcal\ mol^{-1}$ (experimental value) and 30.1 $kcal\ mol^{-1}$ (theoretical value). Under acid conditions, there is a slight decrease on this energy barrier (26 $kcal\ mol^{-1}$ for the theoretical value and 23 $kcal\ mol^{-1}$ for the experimental value) (AHMAD, 2017).

With regard to the hydrolysis of oxa (see Figure 1.6), the reaction is similar to the acidic hydrolysis of cpx (Figure 1.5), since there is also the stabilizing effect of the chelating ligand oxalate. The first step is the ring opening characterized by a half-life of 16 min, forming the oxalate monodentate derivative (Figure 1.6B). In the next step, the oxalate ligand is lost (Figure 1.6D) with a half-life of 92 min forming the dihydrated oxa (Figure 1.6C). Data from literature indicate that the ring opening step is about six times faster than the stage referring to the loss of the oxalate ligand, and it involves an energy barrier of 28 kcal mol^{-1} in neutral condition and 22 kcal mol^{-1} in acidic condition (AHMAD, 2017). Therefore, the main stage of the mechanism of action of oxa, which is the formation of DNA-adducts involving oxa, is slow as well as the one involving cpx (OBRESHKOVA, *et al.,* 2022).

Figure 1.6 - Hydrolysis mechanism of oxaliplatin (oxa).

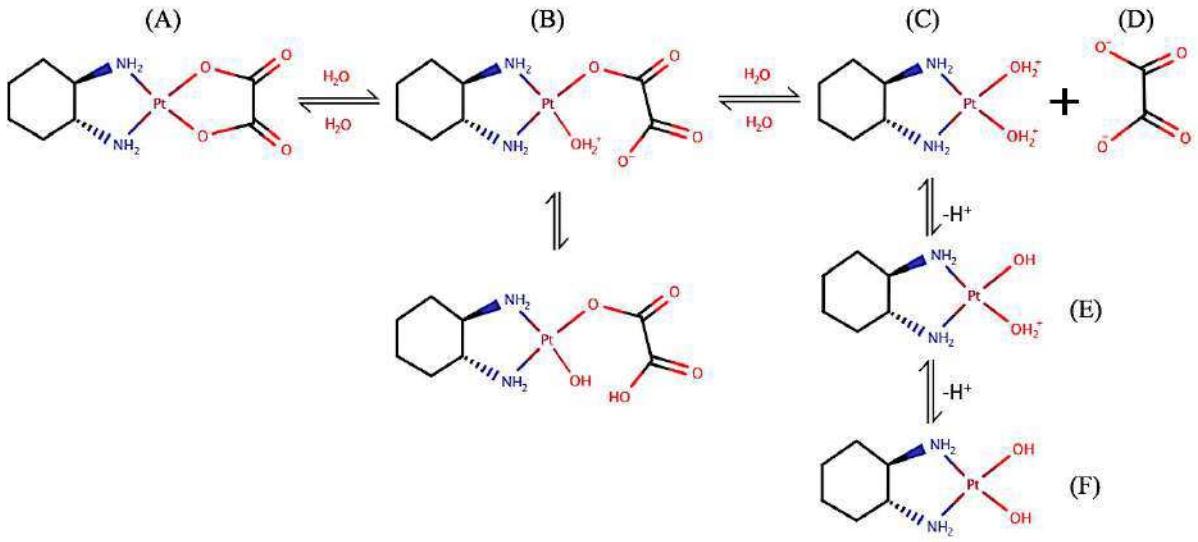

Reference: Own author (2023).

In view of the hydrolysis reactions of the platinum drugs (Figure 1.4-1.6), it is possible to conclude that these transformations are slightly more relevant under acidic conditions, such as in the extracellular medium of cancer cells, which presents a smaller extracellular potential of hydrogen (pH_e = ~6.8–7.0) than the one in normal cells (pH_e = ~7.2) (WHITE, *et al.*, 2017). Additionally, the formation of hydrolyzed species of cddp (Figure 1.4) is more likely than the one referring to both cpx and oxa, due to the presence of a good leaving group (Cl^- ion) in the cddp drug in contrast to the other two platinum drugs approved worldwide.

In spite of the anticancer potential of the Pt(II)-based drugs, their chemotherapies result in severe side effects to the patients, especially when it comes to cddp, which may lead to the

limitation of the prescribed doses. According to the literature, cancer patient under this therapy may experience a combination of 40 types of adverse effects, which demands the co-prescription of other drug modalities in addition to the chemotherapeutics to treat these effects, such as antiemetics, antibiotics, magnesium supplements, antioxidants, propafenone, and many others (OUN, *et al*., 2018).

In addition to the side effects of cddp (Figure 1.3A) such as nausea, vomiting, ototoxicity, neurotoxicity, and fatigue, this metallodrug induces nephrotoxicity as dose-limiting effect (OUN, *et al*., 2018). This variety of adverse events of cddp boosted the research and development of new generations of less toxic analogues referring to this drug, resulting in the global approval of both cpx and oxa.

The cpx drug (Figure 1.3B) is less toxic and potent than cddp, since it presents a lower reactivity due to the presence of the chelating ligand carboxylate, which consequently reduces the formation of the active products of the hydrolysis reaction in the blood. The reduction of these products is important in the extracellular medium, because these species can promptly interact with other biomolecules in this medium rather than the DNA of the target cell (SOUZA, *et al*., 2014). Despite these positive aspects, the cpx doses are also limited due to the problem of myelosuppression, and the chemotherapy is accompanied by side effects, including nausea, vomiting, auditory toxicity, and nephrotoxicity (YAMAMOTO, *et al.*, 2022; OUN, *et al*., 2018).

Regarding to oxa (Figure 1.3C), the presence of the oxalate as the leaving group reduces the reactivity of this third-generation platinum drug and, consequently, its toxicity in comparison to cddp (DILRUBA & KALAYDA, 2016). However, the oxa-based chemotherapy is also restricted in terms of the administered dose due to neurotoxicity that may lead to either acute or chronic forms of neuropathy (OBRESHKOVA, *et al*., 2022). This treatment can also result in hepatotoxicity, hematological toxicity, gastrointestinal toxicity, and others (ALCINDOR, *et al.*, 2011; OUN, *et al*., 2018).

When it comes to the platinum drugs with regional approvals (nedaplatin, lobaplatin, and heptaplatin, see Figure 1.3D-F), the Japan Society of Clinical Oncology reported that nedaplatin (Figure 1.3D) presents a moderate emetic risk and a decrease in the kidney and gastrointestinal toxicities in comparison to the one of cddp. Notwithstanding these aspects, the doses employed in the chemotherapy are also restricted due to the effects of myelosuppression that can induce leucopenia, anemia, and primarily thrombocytopenia (SHIMADA, *et al*., 2013). The platinum drug approved in China (lobaplatin, Figure 1.3E) has the thrombocytopenia as its dose-limiting toxicity. Besides, a study conducted by Wu and coworkers (WU, *et al*., 2019)

pointed out that the use of lobaplatin for treating metastatic breast cancer induced side effects, including myelosuppression, thrombocytopenia, neutropenia, fatigue, rash, nausea and vomiting, stomatitis, peripheral neuropathy, and hepatoxicity (WU, *et al*., 2019). Finally, the heptaplatin-based chemotherapy does not induce a high toxicity and its combination with 5-fluorouracil results in less prominent hematological side effects (DILRUBA & KALAYDA, 2016). However, it is worth emphasizing that conclusive results regarding the anticancer activity, mechanism of action, and toxicity data referring to these three platinum drugs (nedaplatin, lobaplatin, and heptaplatin) are still lacking, as well as their global approval.

All these side effects of the platinum drugs are mainly connected to their inability to differentiate between cancer and normal cells, low permeability in membranes, and fast release in the physiological medium, which promotes, in large part, undesirable interactions (DUAN, *et al*., 2016). This low selectivity for cancer cells is intensified in the case of drugs that have a greater tendency to undergo the hydrolysis reaction, forming the reactive species (charged species in Figure 1.4-1.6) in the extracellular medium. Since cddp presents the most labile leaving group (Cl^- ions) among the three main drugs, this pioneer platinum drug has a notable selectivity on the target sites and a high toxicity.

Another problem in the context of the platinum drugs-based chemotherapies is the drug resistance in the tumors that can be either of intrinsic nature or acquired nature along the treatment (DUAN, *et al*., 2016). This resistance is also a consequence of low selectivity of the Pt(II) drugs for cancer cells, since it is related the reduced drug accumulation in the tumor sites, the intensified DNA repairs mechanisms, the decreased apoptosis, and autophagy (ZHOU, *et al*., 2020).

In this sense, despite the current application of the Pt(II)-based drugs in 50% of the cancer chemotherapies (ANTHONY, *et al*., 2020), the research and development of new formulations for these metallodrugs aiming to reduce the severe side effects and the loss of efficacy due to the drug resistance is highly relevant in order to significantly improve the quality of treatment to the cancer patients.

1.3 CARBON NANOHORNS AS DRUG DELIVERY SYSTEMS

In the context of the research for new therapies and technologies to treat cancer, nanomedicine has been a promising field with a multidisciplinary character, including chemistry, physics, biology, materials science, and medicine, which represents the convergence for futures drugs and therapies (TOMAR, *et al*., 2020). In summary, nanomedicine is defined as the medical

application of the nanotechnology in the development of more efficient diagnoses, monitoring, control, prevention, drug design, and treatments (SOARES, *et al.*, 2018; DAS, *et al*., 2023). Nanotechnology refers, in turn, to the application of science and technology to design and synthesize materials at the nanoscale with dimensions in the range of 1 to 100 nm (SHAH, *et al.*, 2021). The development of nanotechnology-based approaches has been an increasing topic with intense studies and preclinical evaluations aiming to improve the effectiveness of diagnosis/treatment (KIRTANE, *et al*., 2021).

One of the potential and widely studied strategies of nanomedicine for treatments of cancer is the encapsulation of antineoplastic drugs, such as the platinum drugs (Figure 1.3), in drug delivery systems (DDS). This is a promising strategy, since these nanovectors can provide the protection of the drug load from undesirable side reactions and degradation in the physiological medium, slow and target release to the tumor sites, and a better drug absorption by specific mucosa or cells (ATTIA, *et al*., 2019). Therefore, the use of drug formulations containing nanocarriers represents a potential strategy to reduce the toxicity and increase the efficacy of the chemotherapeutics (JIN, *et al.*, 2020). In this research field, there is a series of DDS that have been proposed and studied, including liposomes, micelles, dendrimers, polymeric nanoparticles, niosomes, gold nanoparticles, carbon nanotubes (CNTs), and many others (SINGHVI, *et al*., 2020).

In this context, the carbon nanohorn (CNH) represents a potential class of carbon-based DDS (Figure 1.7) that was identified by Iijima and coworkers in 1999 (IIJIMA, *et al.*, 1999) as an allotropic form of carbon characterized by a tubular region with a typical diameter of 2-5 nm and length of 40-50 nm. This tubular region is coupled to a closed end with a conical shape defined by an average cone angle of 20°. Besides, images of transmission electron microscopic reveal that CNHs are experimentally obtained as clusters named as Dahlias (Figure 1.7A, Figure 1.8), which display a spherical geometry with an average diameter of 100 nm, containing thousands of individual structures of CNHs that are radially distributed from the center of these aggregates (KAROUSIS, *et al.*, 2016).

Figure 1.7 – Average dimensions of the CNH cluster named Dahlia (A) and a typical structure of a CNH (B). *The parameters D, L, and θ refer to the average diameter, length, and cone opening angle, respectively.

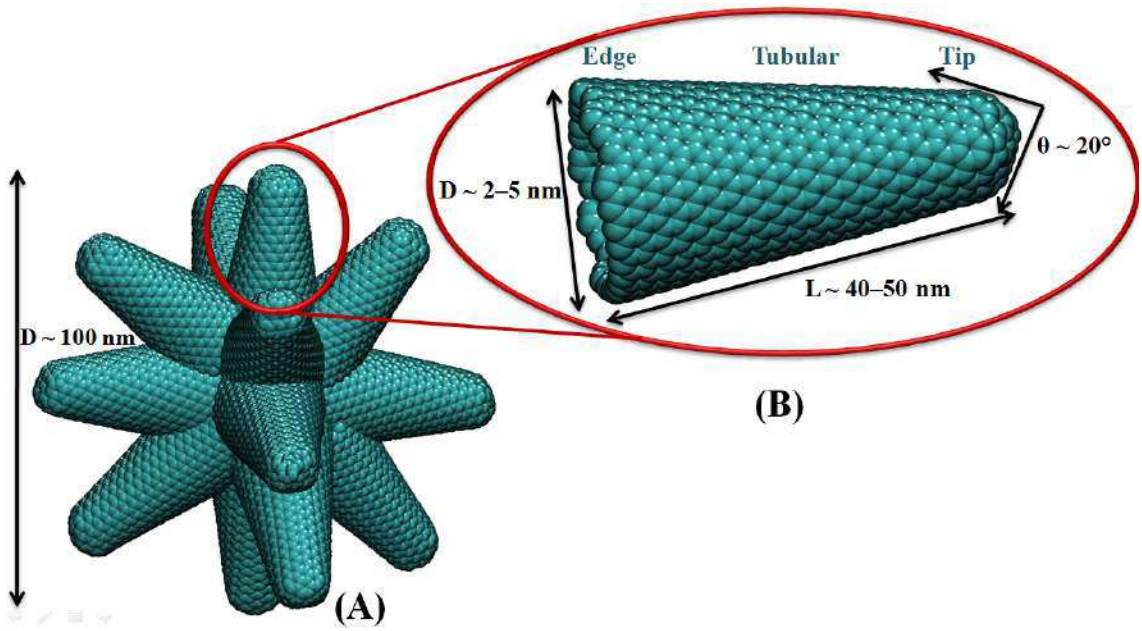

Reference: ALMEIDA, *et al.* (2019).

In addition to the presence of suitable cavities to accommodate clusters of small therapeutic molecules, the relevance of CNHs is related to its current mass production with high purity, since metallic catalysts are not included in the synthesis, resulting in the dispensability of purification steps (KAROUSIS, *et al.*, 2016). The low acute toxicity of CNHs was also confirmed by Miyawaki and coworkers in an extensive toxicological study *in vitro* and *in vivo*, indicating that they are not carcinogenic (MIYAWAKI, *et al.*, 2008).

Figure 1.8 – Images of transmission electron microscopic of carbon nanohorns (CNH): individual structure of a CNH (a), Dahlia-like clusters of CNHs (b,c).

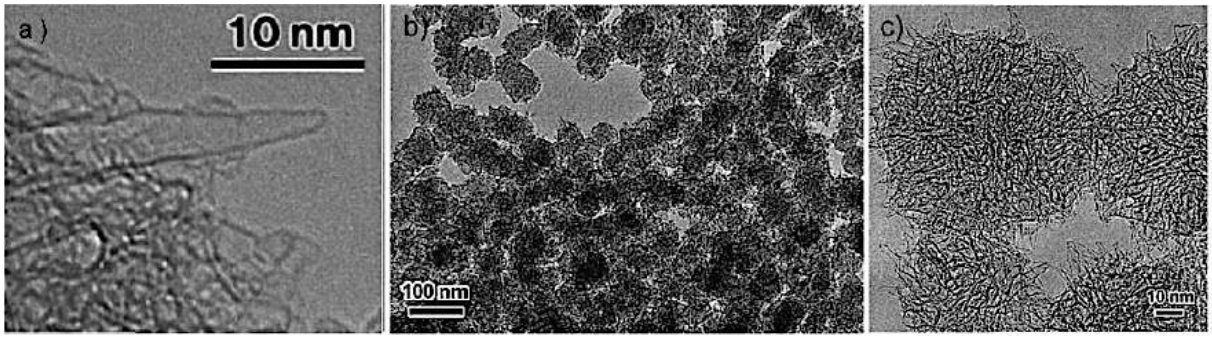

Reference: KAROUSIS, *et al.* (2016).

More recently, the literature has shown that CNHs are notably less toxic than CNTs (HE, *et al.*, 2018; GARRIGA, *et al.*, 2020). Moreover, Zhang and coworkers reported that CNHs can be biodegraded *in vitro* by the myeloperoxidase enzyme (60% within 24 h) and by macrophage cells within 9 days (ZHANG, *et al.*, 2015). Importantly, He and coworkers demonstrated that CNHs are more biocompatible than CNTs in a wide study that evaluated the dissimilarities between these carbon nanomaterials (HE, *et al.*, 2018). These authors discovered that the nanotoxicity of these nanovectors is triggered by the interaction with the glycoprotein nonmetastatic melanoma protein B. Since CNHs have a lower degree of interaction with this transmembrane protein, the cascade of toxicity reactions, including necrosis, pyroptosis, apoptosis, protein expression, hydrolases leakage, is less intense than the one activated by CNTs (HE, *et al.*, 2018).

Regarding the synthesis, pristine CNH can be produced via arc discharge, laser ablation, and Joule heating. Among these techniques, the laser ablation method has been the basis of the current mass production of CNHs, which involves an average rate of 1 kg/day, due to its high efficiency (KAROUSIS, *et al.*, 2016). In this process, the CNHs are synthesized via CO_2 laser ablation of a graphite target with a diameter of 100 mm and height of 500 mm. The scheme in Figure 1.9 illustrates the production process of CNHs.

Figure 1.9 - Scheme of the large-scale production process of pristine carbon nanohorns (CNH).

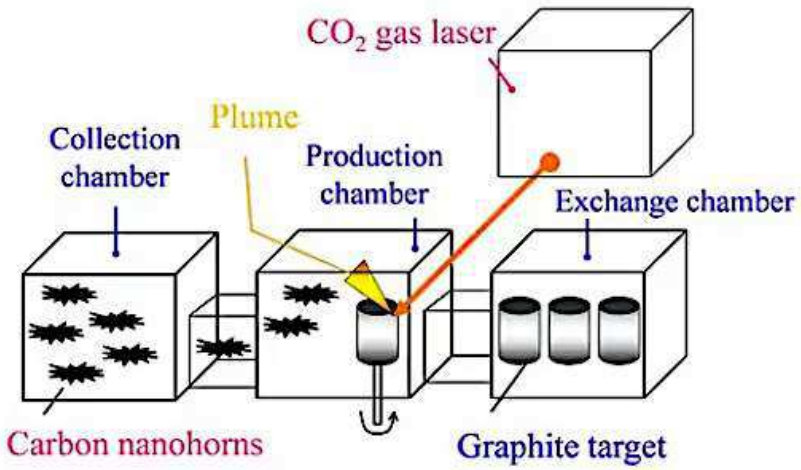

Reference: SIGMA-ALDRICH (2023).

Figure 1.9 shows that the synthesis of CNHs is conducted in a system composed by three closed chambers: the exchange chamber where the graphite targets are stored, production chamber, and collection chamber. In general, these chambers are subjected to an inert gas flow,

mainly the argon gas, with a pressure of 760 Torr (1 atm) and at room temperature. While the inert gas is injected from the bottom of the laser ablation chamber, the same gas is evacuated from the top of the collection chamber. The graphite targets are automatically replaced from the exchange chamber after each laser ablation stage. Besides, each graphite target, which is rotated at 2 rpm for 90 min, is irradiated by the CO_2 laser with o power of 3.5 kW. Finally, after the formation of the CNH mass at the bottom of the production chamber, the nanomaterial is transferred to the collection chamber, where there are storage bottles that are gradually filled by CNH until the final collection without interrupting the continuous production (SIGMA-ALDRICH, 2023).

Recently, Casteignau and coworkers proposed a new method called inductively coupled plasma method to produce CNHs (CASTEIGNAU, *et al.*, 2022). According to these authors, this method has a better scalability than the conventional ones, and the CNHs are formed by the introduction of a gas flow composed by 1:2 ratio of H_2 and CH_4 at 84.7 kPa (0.84 atm). Moreover, the authors propose that the production of CNH with this method can be expanded by increasing the size of the reactor and the power and flow rate of the plasma torch (CASTEIGNAU, *et al.*, 2022).

However, pristine CNH have undesirable characteristics for medical applications, such as low solubility and dispersibility in aqueous solution, due to the high hydrophobicity of these nanomaterials, which compromises their use in the physiological medium. In this sense, the use of post-synthesis chemical treatments, also known as chemical functionalization methods, can circumvent this hydrophobicity by decorating the surface of CNHs with polar functional groups, which improves, in turn, their solubility and dispersibility in aqueous solution (KAROUSIS, *et al.*, 2016). In this context, the oxidation process of CNHs is a strategy of chemical treatment that provides the inclusion of oxygenated functional groups, such as carbonyls, hydroxyls, carboxyls, and others on the surface of these carbon nanomaterials (KAROUSIS, *et al.*, 2016). In general, the oxidative processes of CNTs and CNHs involve chemical reactions with either O_2 or other oxidizing agents, including H_2O_2 and $KMnO_4$. Besides, acidic solutions of HCl, H_2SO_4, HNO_3, and mixtures of these acids, such as H_2SO_4/HNO_3 in different proportions are also used (PORTO, *et al.*, 2018).

In addition to the oxidation processes of CNHs that represent the first step of chemical activation of these nanomaterials, there are other subsequent functionalization strategies involving covalent and non-covalent decorations of their surface. For instance, these nanovectors can be functionalized with amino groups, polymers, doping with Fe and N atoms, and a plethora of groups that can attach on the surface of CNH via π-π interactions, including

pyrene derivatives, porphyrins, and many others (KAROUSIS, *et al.*, 2016). This versatility for chemical modifications, which is another promising aspect of CNHs, is also facilitated by the topological defects on the surface of these nanomaterials, including pentagonal and heptagonal rings in addition to the hexagonal ones, which form reactive regions due to the structural tensioning (NAKAJIMA, *et al.*, 2020).

The potentiality of oxidized CNHs (CNHox) as DDS was initially investigated by Murakami and coworkers in 2004 using the anti-inflammatory glucocorticoid dexamethasone. This study demonstrated an improvement of the therapeutic efficiency of this drug when encapsulated into CNHs, a biological integrity of the released drug load, and a more efficient drug absorption in CNHox that was six times greater than the one in pristine CNHs (MURAKAMI, *et al*., 2004). When it comes to the platinum drugs encapsulation, the inclusion of cddp in the cavities of CNHox was firstly evaluated by Ajima and coworkers (AJIMA, *et al.*, 2005). The authors showed that the formulation cddp@CNHox (cddp encapsulated into CNHox) provides not only a significant inhibition of human lung-cancer cells, but also a slow release of this platinum drug (AJIMA, *et al.*, 2005). In 2006, Ajima and coworkers also investigated the effect referring to the modification of the functional groups located at the nanowindows (MURATA, *et al.*, 2002) of the CNHs on the cddp release (AJIMA, *et al.*, 2006). This study pointed out that 70% of the cddp load was released from the nanowindows with hydrogen-terminated edges, whereas only 15% of the drug molecules was released from nanowindows functionalized with -COOH and –OH groups along the edges. This result is connected to the fact that the -COOH and –OH groups are converted into –COONa and –ONa groups in phosphate-buffered saline, thereby inducing a steric hindrance to the cddp release from the nanowindows (AJIMA, *et al.*, 2006). To avoid this blockage, the authors proposed a reduction reaction (H_2 flow at 1,200 ºC for 3h) after the oxidation process that converts the –COOH and –OH groups into $–CH_3$ and –H.

Moreover, the same authors studied the intratumoral injection of the cddp@CNHox formulation (Figure 1.10) to transplanted tumors in mice. This study highlighted a slow release of the cddp molecules from this nanovector, a substantial reduction of the tumor volume in comparison to the application of the formulation of free cddp, and a concentration of the nanoparticle formulation of cddp in the tumor site for 25 days, thereby confirming the potential application of CNHs in cancer chemotherapies (AJIMA, *et al.*, 2008). Figure 1.10 illustrates the images of transmission electron microscopy of the system cddp@CNHox, which involves clusters of cddp molecules (black dots) incorporated into the CNHox that are aggregated as Dahlia-like clusters.

Figure 1.10 - Images of transmission electron microscopy referring to clusters of oxidized carbon nanohorns (CNHox), also known as Dahlias, containing encapsulated clusters of cisplatin (cddp) molecules. The black dots refer to the cddp clusters.

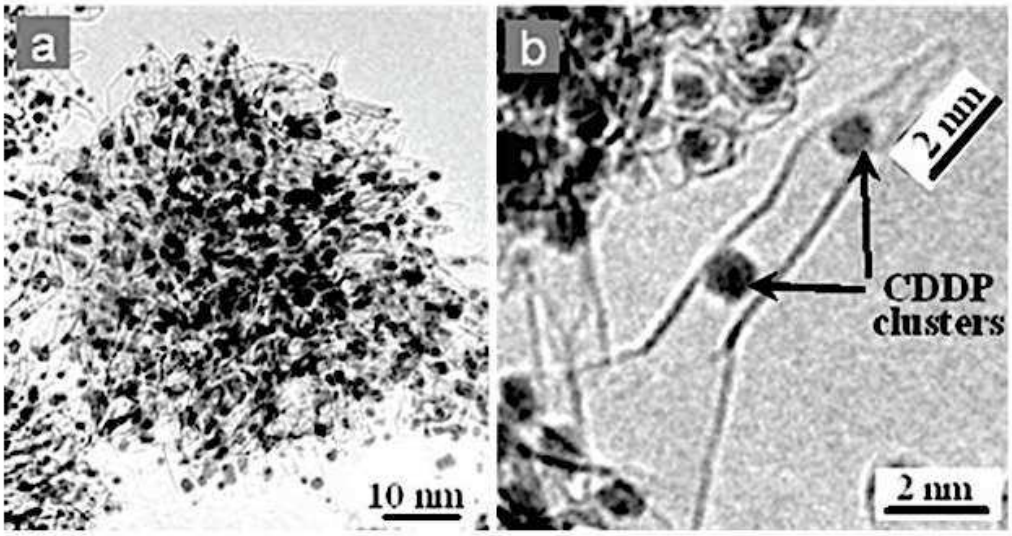

Reference: Adapted from AJIMA, *et al*. (2008).

More recently, Isaac and coworkers evaluated the use of functionalized CNH (CNHf) as theranostics vehicles of cddp molecules to treat bladder cancer lesions. The preparation of these modified CNHs involved their oxidation, decoration with amide-thiols groups and then, the conjugation of the cddp@CNHf complexes with quantum dots (CdSe/ZnS core/shell). In addition to provide the monitoring by fluorescence imaging of this hybrid DDS in AY-27 cell lines over 3 days, the application of this formulation provided a slow and gradual release of the drug load in the tumor site with 50% inhibitory concentration (IC50) (ISAAC, *et al*., 2018).

Another approach to analyze inclusion complexes formed by cddp molecules encapsulated inside CNHs involves the use of computational chemistry methods, which provide the description and interpretation of the structure of the matter at atomic/molecular levels that are not accessed by experiments. By using these methods, it is possible to predict, for instance, the electronic, spectroscopic, and thermodynamic properties, parameters and profiles of reaction mechanisms (MORGON, 2001; LEWARDS, 2003). In this context, Souza and coworkers conducted a quantum mechanical study of inclusion complexes cddp@CNH and cddp@CNT, which involved the inclusion of one cddp molecule inside a model of CNH and CNT aiming to characterize the stability and charge distribution in addition to calculate the NMR spectra (DE SOUZA, *et al.*, 2013). The calculations demonstrated that these carbon nanomaterials form stable complexes with cddp, which can be identified in the NMR spectra.

The same authors also investigated inclusion complexes formed by oxidized topologies of CNH and CNT containing cddp molecules in the light of quantum chemistry methods (DE SOUZA, *et al.*, 2018). In addition to indicate the stable formation of these inclusion complexes involving oxidized nanomaterials, the authors reported the molecular spectra of IR, Raman and ^{1}H NMR, which display notable changes due the formation of these DDS that can be taken, in turn, as reference, thereby assisting the experimentalists for the synthesis of these systems.

The dynamical behavior of both structures and properties referring to these inclusion complexes (cddp@CNH) can be accessed by using molecular dynamics (MD) simulations. This theoretical method provides the analysis of the temporal evolution of a system described by a sum of interatomic potentials by means of the integration of the equation of motion at femtosecond resolution (HOLLINGSWORTH & DROR, 2019). In this field, both dynamical behavior and stability of the inclusion complexes involving cddp clusters encapsulated in pristine topologies of CNHs were analyzed via MD simulations (ALMEIDA, *et al.*, 2019). In this study, the authors characterized the inner solvation shell of the CNHs, which was composed, on average, by ~11 water molecules inside the CNH cavity for the narrow nanostructures in addition to encapsulated cddp. The binding free energy ($\Delta_b G$) calculations indicated the favorable formation of these inclusion complexes, with most of the system stability coming from the van der Waals contribution. The same authors also evaluated the dynamics of inclusion complexes formed by a series of oxidized and reduced CNHs loaded with cddp clusters (ALMEIDA, *et al.*, 2020). The authors showed that the increase of the number of hydrogen bonds formed with the solvent may improve the biocompatibility of these chemically modified CNHs. Despite the stable formation of all inclusion complexes, the free energy calculations indicated that the system containing CNHox were less stable than the ones with reduced CNH (CNHh).

In view of all these promising aspects, CNHs has still garnered worldwide attention in the last years with recent papers and reviews dedicated to their application in cancer chemotherapies (LANCETA, *et al.*, 2020; CURCIO, *et al.*, 2021). In spite of these potential results, the research involving this carbon nanomaterial is still in the preclinical stage with questions to be clarified, especially when it comes to the toxicological aspects in short and long term. The biodistribution of CNHs is a relevant aspect that is related to the level of toxicity. A study conducted in 2011 demonstrated the reduction of the accumulation of CNHs in mice lungs by increasing the hydrophilicity of this nanomaterial (TAHARA, *et al*., 2011). After the lungs, CNHs were also accumulated in the liver and spleen. Besides, the agglomerates of CNHs, especially the ones with CNHox, decreased in size with time due to capture by macrophages.

Despite the accumulation, the authors did not detect inflammatory responses and histological abnormalities in the tissues in contact with CNHs. In 2014, Matsumura and coworkers evaluated the microscopic localization of pristine CNHs in tumor tissues (MATSUMURA, *et al.*, 2014). This study identified the presence of CNHs in macrophages and endothelial cells within the blood vessels, and in tumor cells. The authors explained that CNHs (size of 100 nm) are able to reach the tumors, since they satisfy the criterion of blood vessels that are highly permeable to materials with sizes of 50-200 nm. Besides, 21 h after intravenous injection of CNHs, the biodistribution studies indicated the presence of CNHs mainly in the liver, spleen and stomach/intestine, in addition to the concentration in tumors, blood and skin.

More recently, Shi and coworkers investigated the fate of CNHox in mice using multispectral optoacoustic tomography method (SHI, *et al*., 2019). The analyzes indicated the main concentration of this carbon nanomaterial after oral gavage in the gastrointestinal tract and the excretion by the gut. Importantly, the CNHox were not detectable in kidney, liver, blood, and spleen. When it comes to the intravenous injection, it was observed a persisted distribution of this oxidized nanomaterial in the spleen, liver, and very little in the kidney. Finally, by using hypodermic and intramuscular injections, all CNHox load remained around the injection sites due to the low absorption rate of this nanomaterial that prevents the penetration in the spleen, kidney or liver from this injection modality.

In spite of the existence of the aforementioned studies, the literature referring to the application of CNHs as nanocarriers of platinum drugs and their effects in living organisms is still scarce. Particularly, a central issue to be evaluated is the cellular uptake of these DDS through tumor tissues, which has a great relevance in the field of nanomedicine. In fact, CNHs as well as other nanoparticles benefit from the enhanced permeability and retention (EPR) effect in tumors due to not only the leaky vasculature, but also the defective lymphatic drainage system, discontinuous endothelial cells having large gaps, and defective basement membrane verified in malignant tissues (SHINDE, *et al*., 2022; CURCIO, *et al.*, 2021; LANCETA, *et al.*, 2020). In this sense, a deeper understanding at a molecular level of the interaction between CNHs as nanovectors of platinum drugs and tumor tissues requires, as a first investigative step, the study of the interaction of these inclusion complexes with cell membranes.

1.4 CELL MEMBRANES

Before presenting the objectives of this work, which involve the analysis of CNH-membrane interactions, it is important to revisit the topic of biomembranes. Cell membranes are essentials

components existing in the structure of all cells, since they delimit the cellular content defining the external limits of cells and compartments (see Figure 1.11). In particular, eukaryotic cells are characterized by not only plasma membranes, which delimit the intracellular medium composed by subcellular compartments immersed in the cytosol and the extracellular medium, but also by internal membranes that surround the nucleus and organelles, including mitochondria, Golgi apparatus, endoplasmic reticulum, and lysosomes (HARAYAMA & RIEZMAN, 2018; NELSON & COX, 2014). Since this work involves the analysis of the interaction between carbon nanovectors (CNHs) for Pt(II)-based drugs and membranes of human breast cancer cells, the present discussion will focus on mammalian plasma membranes.

Plasma membranes play an important role as semipermeable biological barriers that protect cells and define the molecular translocations processes, maintaining homeostasis in organisms. In addition to modulate permeation of compounds, these biomembranes are able to capture signals from the extracellular medium, and then trigger reactions cascades that modify the cellular medium. The synthesis of lipids and some proteins can be also activated by internal membranes (RUSESKA & ZIMMER, 2020; NELSON & COX, 2014).

Figure 1.11 - Electron microscopy image of a plasma membrane referring to an erythrocyte cell. This lipid bilayer has 5 to 8 nm in thickness.

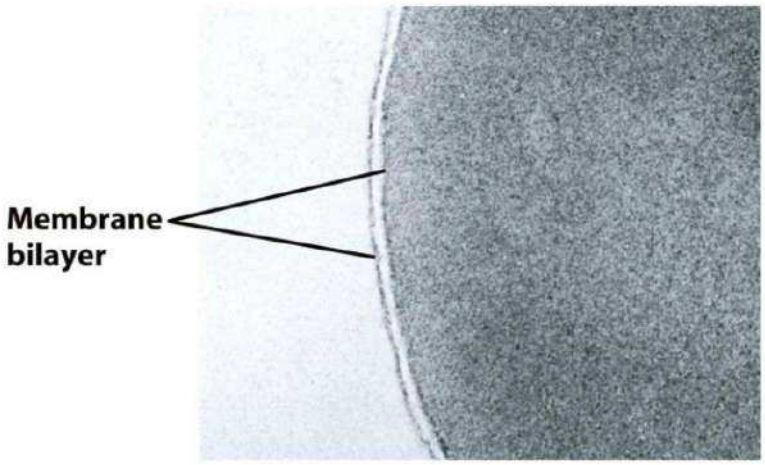

Reference: NELSON & COX (2004).

From the molecular point of view, plasma membranes consist of lipid bilayers formed by hundreds of lipid types asymmetrically distributed in the two fluids leaflets, containing membrane proteins. These biomolecules that compose this heterogeneous system are indeed responsible to regulate the transport of ions and molecules through the cells (MARRINK, *et al.*,

2019). Data from electron microscopy, lipid composition, and permeability/mobility studies of lipids, proteins and other molecules led to the development of the fluid mosaic model (Figure 1.12) by Singer and Nicolson in 1972 to explain the general structure of a cell membrane (SINGER & NICOLSON, 1972). According to this model, the membrane is formed by phospholipids that are organized in two monolayers, in which the nonpolar region of the lipid molecules (the lipid tails) in each leaflet faces the core of the bilayer whereas the polar region of the lipid molecules (the polar heads groups) faces the edges of the bilayer forming the inner and outer surfaces of this system. These surfaces are, in turn, in contact with the intracellular and extracellular media. In addition to the lipids, the fluid mosaic model indicates the presence of embedded proteins in the lipid bilayer held by interactions between lipids and amino acids of these proteins. There are different orientations for these membrane proteins, including peripheral proteins with non-covalent interactions, peripheral proteins with covalent interactions, proteins with single trans-membrane helix, and proteins with multiple trans-membrane helices. The fluidity of the membranes is characterized by the free lateral motion of lipids and proteins along the plane of the bilayer (NELSON & COX, 2014).

Figure 1.12 - Scheme of the fluid mosaic model for the cell membrane structure. The yellow, orange, blue, red, and light blue structures represent nonpolar tails of the lipids, cholesterol molecules, polar head groups of the lipids, the different membrane proteins, and oligosaccharide chains, respectively.

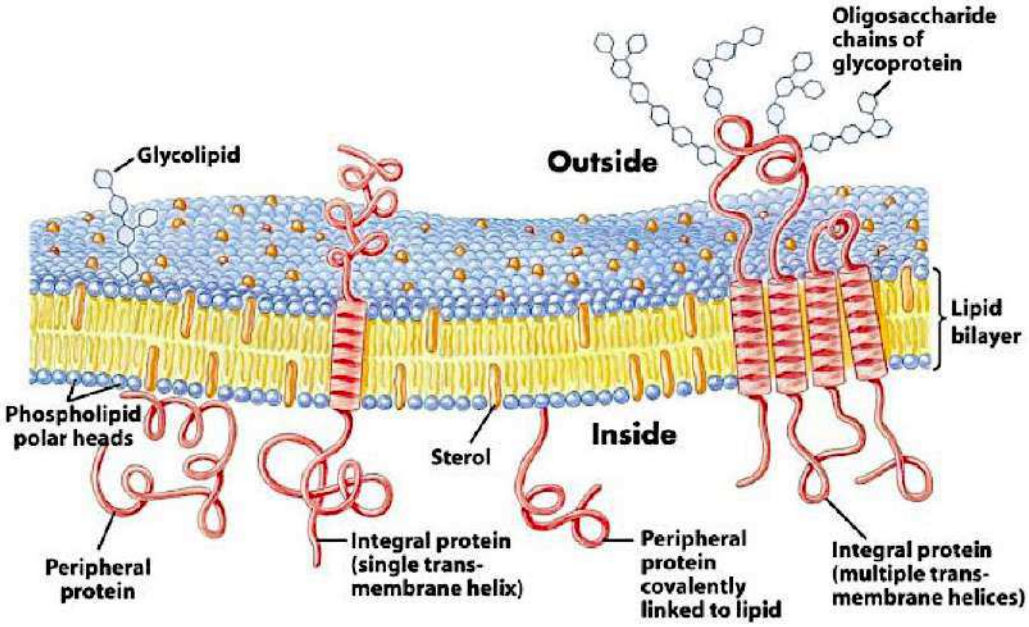

Reference: NELSON & COX (2004).

The geometry of polar heads groups and the amphipathic character of phospholipids, the main components of cell membranes, are important factors that define the configuration of the matrix of biomembranes maintained by the hydrophobic effect and van der Waals forces. These interactions enable the fluidity of these biostructures, thereby providing the processes of deformation, distortion, disturbance, compression and expansion due to different perturbations (NICOLSON & MATTOS, 2021). It is worth mentioning that the fluid mosaic model of membranes has proven to be consistent with the current interpretation and experimental evidences of the structure of these systems. In spite of that, there are some updates of this model that increase its complexity, such as the presence of protein domains that reduce the fluidity and mobility of lipids in some regions, and interactions with the cytoskeletal elements in the protein domains (NICOLSON & MATTOS, 2021). Both structure and dynamics of plasma membranes can be accessed by elastic and spectroscopic methods employing, for instance, neutrons and X-rays, which are also dependent on the time scale of the events to be investigated. Some examples of these techniques are the dynamic light scattering, fluorescence correlation spectroscopy, X-ray photon correlation spectroscopy, and solid-state ^{2}H NMR spectroscopy (GUPTA & ASHKAR, 2021).

To understand the interactions between CNHs and cell membranes, we first need to briefly discuss the nature of lipids that are the basic components of biomembranes. In general, lipids can be classified in membrane lipids and storage lipids. The membrane lipids are divided into phospholipids, glycolipids, and archaebacterial ether lipids (NELSON & COX, 2014). Specifically, this work will focus on phospholipids and sterols (cholesterol) since they are the major components of biomembranes that will be evaluated herein.

The phospholipids, such as glycerophospholipids, are the major components of biomembranes. In particular, the glycerophospholipids are composed by a glycerol backbone, to which are attached a polar head group and two nonpolar long-chains. The scheme in Figure1.13 shows that two fatty acids (lipid tails) are covalently connected to the glycerol by an ester linkage to the first and second carbon atoms of the glycerol. The third carbon atom of the glycerol is attached to a highly polar or charged substituent through a phosphodiester linkage. The polar heads of glycerophospholipids encompass glycerol, phosphate, and a head-group substituent (NELSON & COX, 2014).

Figure 1.13 - General structure of a glycerophospholipid.

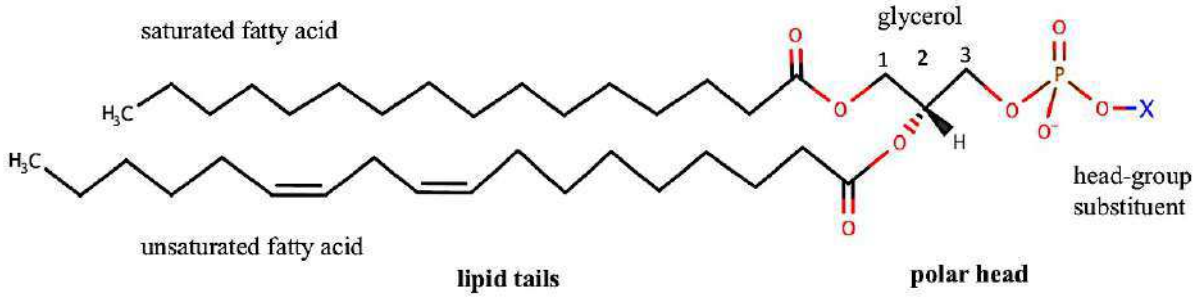

Reference: Adapted from NELSON & COX (2004).

Still regarding Figure 1.13, the fatty acids, which compose the lipid tails, are carboxylic acids with long hydrocarbon chains containing from 4 to 36 carbon atoms. These hydrophobic molecules can either present saturated and/or unsaturated chains, where the double bonds of the unsaturated fatty acids are mainly found with *cis* configuration. The nomenclature of fatty acids indicates the number of carbon atoms of the chain (chain length), a colon, and then the number of double bonds in the chain. Additionally, the position of a double bond is specified as a superscript number after the symbol Δ. For instance, the term 20:2($\Delta^{9,12}$) refers to a fatty acid with 20 carbon atoms and 2 double bonds with the first one located between C-9 and C-10 and the second one located between C-12 and C-13 (NELSON & COX, 2014). Table 1.1 presents the most common fatty acids, which displays, in turn, even number of carbon atoms (from 12 to 24 C atoms).

In addition to the variability of fatty acids, the phospholipids also display a diversity in terms of polar groups, also known as polar heads groups, with modifications represented by the symbol X in Figure 1.13. The most commonly occurring glycerophospholipids and polar heads are organized in Table 1.2. In this table, the simplest glycerophospholipid is the phosphatidic acid, a phosphomonoester, which is therefore the parent compound of this class of lipids. The derivatives of this phosphatidic acid are named by the head-group substituent X with the prefix "phosphatidyl-" (NELSON & COX, 2004).

Concerning the charges of the glycerophospholipids, it is worth emphasizing that the polar head is attached to the glycerol by a phosphodiester linkage, in which the phosphate group has a negative charge at neutral pH. Besides, the head-group substituent X (see Table 1.2) can be negatively charged (*e.g.*, phosphatidylinositol-4,5-bisphosphate), neutral (phosphatidylserine), or positively charged (phosphatidylcholine and

phosphatidylethanolamine). The net charge shown in Table 1.2 considers the charges of both phosphate and group X (NELSON & COX, 2014).

Table 1.1 - Structure, properties, and nomenclature of the main fatty acids that are naturally occurring in cell membranes.

Carbon skeleton	Structure	Systematic name	Common name
12:0	$CH_3(CH_2)_{10}COOH$	*n*-Dodecanoic acid	Lauric acid
14:0	$CH_3(CH_2)_{12}COOH$	*n*-Tetradecanoic acid	Myristic acid
16:0	$CH_3(CH_2)_{14}COOH$	*n*-Hexadecanoic acid	Palmitic acid
18:0	$CH_3(CH_2)_{16}COOH$	*n*-Octadecanoic acid	Stearic acid
20:0	$CH_3(CH_2)_{18}COOH$	*n*-Eicosanoic acid	Arachidic acid
24:0	$CH_3(CH_2)_{22}COOH$	*n*-Tetracosanoic acid	Lignoceric acid
16:1(Δ^9)	$CH_3(CH_2)_5CH=CH(CH_2)_7COOH$	*cis*-9-Hexadecenoic acid	Palmitoleic acid
18:1(Δ^9)	$CH_3(CH_2)_7CH=CH(CH_2)_7COOH$	*cis*-9-Octadecenoic acid	Oleic acid
18:2($\Delta^{9,12}$)	$CH_3(CH_2)_4CH=CHCH_2CH=CH(CH_2)_7COOH$	*cis-,cis*-9,12-Octadecadienoic acid	Linoleic acid
18:3($\Delta^{9,12,15}$)	$CH_3CH_2CH=CHCH_2CH=CHCH_2CH=CH(CH_2)_7COOH$	*cis-,cis-,cis*-9,12,15-Octadecatrienoic acid	α-Linoleic acid
20:4($\Delta^{5,8,11,14}$)	$CH_3(CH_2)_4CH=CHCH_2CH=CHCH_2CH=CHCH_2CH=CH(CH_2)_3COOH$	*cis-,cis-,cis-,cis*-5,8,11,14-Icosatetraenoic acid	Arachidonic acid

Reference: Adapted from NELSON & COX (2014).

The lipid diversity involving different fatty acids (Table 1.1) and polar heads (Table 1.2) is also verified in different cells, tissues, and organisms. In spite of that, the most common fatty acids involve chains with 16, 18, and 20 carbon atoms (NELSON & COX, 2014). The general nomenclature of lipids specifies the abbreviations of lipid tails and polar heads. For instance, a DOPC lipid refers to a lipid with two oleoyl (OL) tails, which are derived from the oleic acid (Table 1.1), therefore named as DO, and the polar head phosphatidylcholine (PC, Table 1.2). The name of the DOPC lipid is 1,2-dioleoyl-*sn*-glycero-3-phosphocholine. Another common example is the POPC lipid that is composed by a lipid tail palmitoyl (P), which is derived from the palmitoleic acid (Table 1.1), a lipid tail oleoyl (OL), and the polar head phosphatidylcholine (PC). The IUPAC name of this lipid is 1-palmitoyl-2-oleoyl-*sn*-glycero-3-phosphocholine.

Table 1.2 - The most common glycerophospholipids and their head-group substituents. The X group refers to the head-group substituent in the phosphate group of these lipids.

Name of glycerophospholipids (abbreviation)	Name of X	Structure of X	Net charge (at pH 7)
Phosphatidic acid (PA)	-	-H	-1
Phosphatidylethanolamine (PE)	Ethanolamine	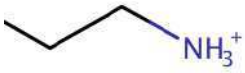	0
Phosphatidylcholine (PC)	Choline		0
Phosphatidylserine (PS)	Serine	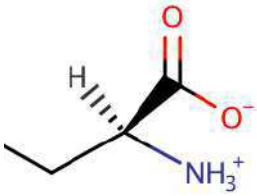	-1
Phosphatidilglycerol (PG)	Glycerol		-1
Phosphatidylinositol 4,5-biphosphate (PI)	*myo*-Inositol 4,5-bisphosphate	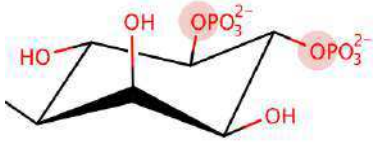	-4
Cardiolipin (CL)	Phosphatidyl-glycerol	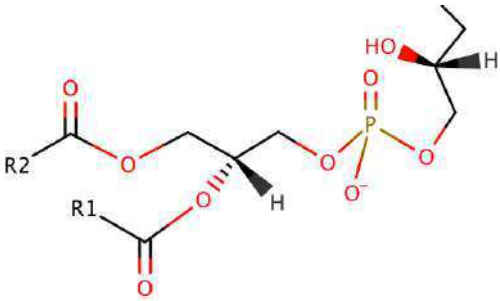	-2

Reference: Adapted from NELSON & COX (2014).

Most eukaryotic cells also have sterols in their membranes, which are not only structural lipids, but also precursors for the synthesis of compounds with biological activity, such as steroid hormones and bile acids. In this group, the cholesterol (CHL) is the major sterol in

animal tissues, which have relevant roles the membrane fluidity, passive permeation, protein and enzyme activity, cell signaling, and formation of lipid domains (CHAKRABORTY, *et al.*, 2020). The CHL is an amphipathic molecule that has a hydroxyl as the polar head group and a nonpolar hydrocarbon body formed by four fused rings, being three hexagonal rings of C and one pentagonal ring of C, and an alkyl side chain (see Figure 1.14).

Figure 1.14 - Molecular structure of the cholesterol.

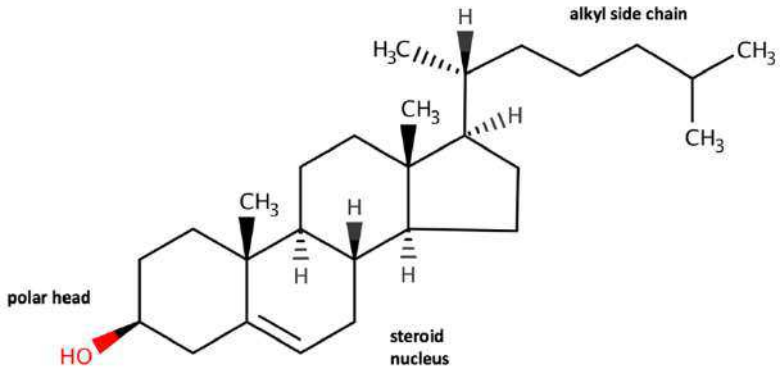

Reference: Own author (2023).

When it comes to a cancer cell, the development of this disease lead to a series of alterations in the lipid profile, metabolism, and in the biophysical properties of cells. These abnormalities are identified by biomarkers of cancer cells (BERNARDES & FIALHO, 2018). For instance, the loss of asymmetry in the lipid composition of membranes is a biomarker of cancer cells, since normal cells express a lipid asymmetry that is maintained by the enzymes flippases and floppases (RIVEL, *et al.*, 2019).

Overexpression of lipids with the polar head phosphatidylserine (PS in Table 1.2) on the outer leaflet of plasma membranes is another biomarker of cancer cells, since these lipids are mainly distributed on the inner leaflet of healthy cell membranes. The same lipid inversion in malignant cells is verified for the phospholipids containing the polar head phosphatidylethanolamine (PE in Table 1.2) (BERNARDES & FIALHO, 2018). Since the lipid PS has an anionic character, the surface of cancer cell membranes is negatively charged, which also has a relation with the acid pH observed in the tumor microenvironment. In this context, studies have indicated a modified pH in the intracellular and extracellular regions in cancer cells in addition to the morphological alterations observed in these cells discussed in the section 1.1. In cancer cells, it is observed an acidification of the extracellular medium with pH (pH_e) of ~6.7-7.1, while it is observed an alkalinization of the intracellular medium with pH (pH_i) greater

than 7.2 (ALVES, *et al.*, 2016; PERSIL; *et al*., 2019). Although this pH dysregulation compared to normal cells (pH_i ~ 7.2 and pH_e ~ 7.4) seems to be small, it is worth mentioning that it is sufficient not only to the activation of cellular processes in the context of cancers, such as proliferation and migration, but also to the modification of protonation states of drugs, thereby modifying the interactions profile with biomembranes.

Regarding the membrane dynamics, the existence of non-covalent interactions between phospholipids provides mobility and fluidity of this system, which also depend on both temperature and lipid composition. By variating these conditions, the lipids in membranes can form three types of phases: gel phase, liquid-disordered state, and liquid-ordered state. Below physiological temperatures, the ensemble of lipids in membranes form a semisolid gel phase, also known as paracrystalline state, which is characterized by a structural ordering of lipids, including both polar heads and acyl chains, with constraints in all motions. At high temperatures (above physiological temperatures), the membrane is found in the liquid-disorder state, also known as fluid state, which is notably disordered and fluid with free motion of the carbon chains referring to fatty acids, thereby providing the lateral diffusion of lipids in the plane of each monolayer. Finally, at intermediate temperatures, the biomembrane exist in a liquid-ordered state, which is characterized by a reduced thermal motion in the lipid tails, despite the lateral diffusion of lipids in the plane of the bilayer. When it comes to mammals, which have a physiological temperature in the range of 20 to 40°C, the long-chain saturated fatty acids, mainly the ones named 16:0 and 18:0, are well agglomerated in the liquid-ordered phase, but the presence of unsaturated fatty acids, such as 18:1 and 16:1, favor the liquid-disorder state due to the bending caused by the double bond that deforms the non-polar region of biomembranes (NELSON & COX, 2004). The presence of sterols (e.g., cholesterol) is also a factor that influences the membrane state. While 8-15% cholesterol contents in membranes favor the liquid-disorder state, 20-40% may favor the liquid-ordered state (BERNARDES & FIALHO, 2018). It worth emphasizing that different states can coexist over different regions of membranes due to the lipid diversity that can be packed in some sections of this soft matter (NELSON & COX, 2014).

The discussion of the interactions between inclusion complexes formed by platinum drugs encapsulated inside CNHs (drug@CNH) and biomembranes also requires the understanding of the membrane transport processes. The amphipathic nature of cell membranes is an important factor that defines its semipermeability, modulating what solutes can enter and leave a cell. For instance, a few nonpolar molecules can cross lipid bilayers by following an unassisted process, whereas ions and some polar or charged compounds requires the assistance

of external agents, such as proteins and carbohydrates, to carry out such transport (NELSON & COX, 2014). The diffusion of solutes assisted by proteins across membranes can occurs either in favor of the concentration gradient or against gradients of concentration and/or electrical charge. Processes that are developed against gradients require energy, which can be supplied by the adenosine triphosphate (ATP) hydrolysis. Besides, while ion channels provide the ion transport across membranes, structures such as transmembrane channels, carriers, and pumps provide the assisted translocation of small molecules through cell membranes (NELSON & COX, 2014).

In this context, the transport of solutes across membranes can be divided in two categories: passive transport and active transport (see Figure 1.15). The passive transport is a spontaneous process, in which the solute moves through the membrane from the region of high solute concentration to the region with low solute concentration, *i.e.* in favor of the concentration gradient, until this molecule reaches the equilibrium through the biomembrane. There are three common modalities of passive transport: simple diffusion, osmosis, and facilitated diffusion.

Figure 1.15 - Modalities of the membrane transport.

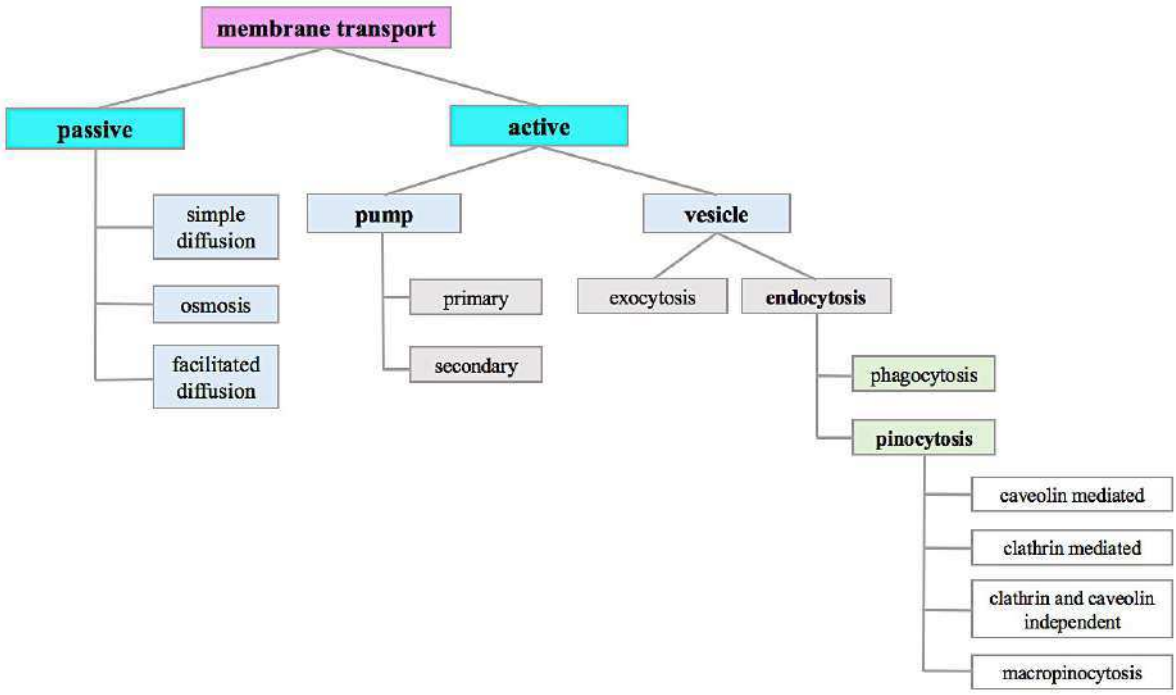

Reference: Own author (2023).

While the simple diffusion is a common transport to small or lipophilic molecules that can dissolve into and diffuse through biomembranes, the facilitated diffusion involves the

transport of large or charged molecules through membrane via solute-specific facilitators or carriers, such as membrane proteins as gated channels (STILLWELL, 2016). Examples of mediated diffusion include potassium channels, sodium channels, and aquaporins. The spontaneous diffusion of charged molecules across membranes depend on both concentration gradient, also known as chemical gradient, and electrical gradient. These two gradients, which are the driving forces of the passive transport, form the electrochemical gradient (NELSON & COX, 2014). Unlike solute transport during simple diffusion and facilitated diffusion, the osmosis refers to the specific diffusion of water molecules across the membrane down its gradient, *i.e.* from high to low water potential, until this potential reaches zero along the lipid bilayer (STILLWELL, 2016).

It is worth emphasizing that passive transport also requires energy in a small extent compared to the active transport, since the process involves the loss of the solvation shell of the permeants, the actual diffusion across the lipid bilayer, and the final organization of the hydration waters on the opposite side of the membrane. The activation barrier ($\Delta G^{\ddagger}$) for transmembrane diffusion has a relation with the waters of hydration, mainly over homologous series, so that the greater the number of water-solute interactions that composes this solvation shell, the greater the energy barrier for the permeation process. This energy barrier is also reduced in the facilitated diffusion due the presence of proteins that provide an alternative and less energetic route for the solute permeation (STILLWELL, 2016). In summary, only water molecules, small non-charged solutes, and gases are able to permeate cell membranes via passive transport.

Conversely, the active transport (see Figure 1.15) is a thermodynamically unfavorable process that requires energy to drive the translocation of solutes against the electrochemical gradient across the biomembrane. This endergonic process is possible due to the coupling with an exergonic process, such as ATP hydrolysis, absorption of sunlight, oxidation reaction, and the concomitant diffusion of other species down the electrochemical gradient. In Figure 1.15, it is possible to see that the active transports can occur via pumps and vesicles. The active transport via pump is divided in two modalities: primary active transport and secondary active transport (Figure 1.16). Specifically, the primary active transport is a mechanism that employs the released energy from the ATP hydrolysis to pump a species across a lipid bilayer against the its electrochemical gradient. This diffusion can also be accompanied at the same time by the inverse translocation of other species. This way, if a transporter carries a single type of species in one direction, the process is classified as uniport. If a transporter carries two types of species in the same direction, it is defined as symport.

Figure 1.16 - Mechanisms of active transport via pumps: classes of transport systems (A), and types of active transport (B).

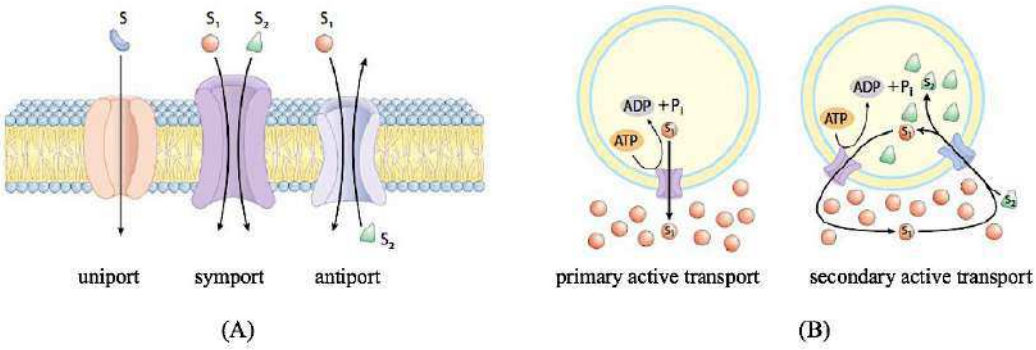

Reference: Adapted from NELSON & COX (2014).

Finally, if the transport of two types of species is carried out in two opposite directions, the process is antiport (see Figure 1.16A) (STILLWELL, 2016; NELSON & COX, 2014). The sodium-potassium pump is an example of primary active transport that pump sodium ions out of the cells and potassium ions into the cells. On the other hand, the secondary active transport (Figure 1.16B) is a type of co-transport where an endergonic process is coupled to an exergonic process. Figure 1.16B exemplify this transport by showing that after the establishment of a gradient of the species S_1 by primary active transport (endergonic process), the subsequent movement of S_1 down its electrochemical gradient (exergonic process) provide the energy for driving the pumping of a second solute S_2 against its electrochemical gradient. The ATP formation and the sodium-glucose transport protein-1 are examples of secondary active processes (STILLWELL, 2016).

Another relevant modality of active transport, which provides the translocation of large macromolecules, such as proteins and nanoparticles, across membranes is the transport mediated by vesicles. The vesicle transport is divided in two categories: exocytosis and endocytosis (see Figure 1.15). The endocytosis involves the formation of vesicles from the lipids of the biomembrane that engulf macromolecules and move such species into the cell. The endocytic pathways are classified according to the physical state of the captured species and the specificity of this cellular uptake in three categories: phagocytosis, pinocytosis, and receptor-mediated endocytosis (STILLWELL, 2016). In this classification, phagocytosis is a form of endocytosis that involves the engulfment of large solid particles (above 0.5 μm), such as aggregates of macromolecules, parts of cells, microorganisms, and other foreign substances by means of the formation vesicles named as phagosomes. This selective transport, which was discovered in 1882 by the biologist Elie Metchnikoff, is mediated by proteins that specifically

recognize and bind to solid particles. In multicellular organisms, this is the main transport mechanism employed by cells of the immune system, including macrophages, monocytes, and many others, in order to regulate homeostasis (STILLWELL, 2016; PATHAK, *et al*., 2023).

The pinocytosis, which was discovered in 1929 by Warren Lewis, involves the cellular uptake of fluids containing small molecules from the formation of vesicles named as endosomes that are smaller than the phagosomes. In addition to require a notable quantity of energy from the ATP hydrolysis, the pinocytosis can be divided in four main types depending of its specificity: clathrin-mediated pinocytosis, caveolin-mediated pinocytosis, clathrin and caveolin independent pinocytosis, and macropinocytosis (see Figure 1.15 and Figure 1.17) (STILLWELL, 2016).

Figure 1.17 - Classification of the pinocytosis mechanisms and details of the exocytosis.

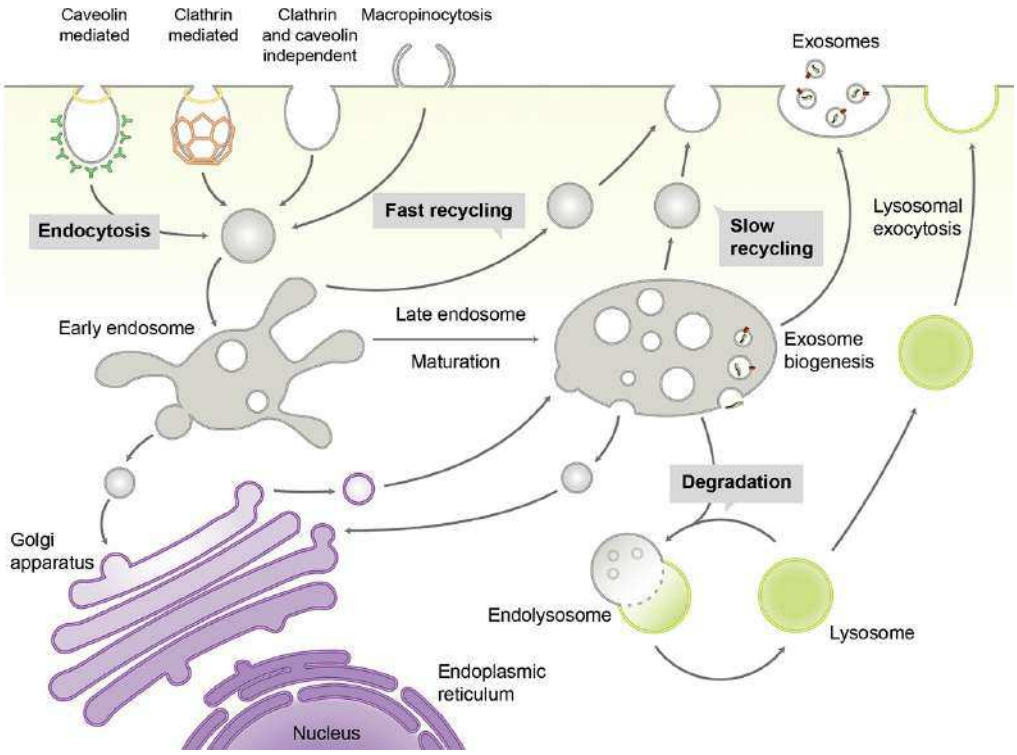

Reference: PATEL, *et al.* (2019).

The first three processes of this list of pinocytosis involves the internalization of macromolecules by means of the binding to specific receptors located at the plasma membrane, such as the clathrin and caveolin proteins. The caveolin-mediated pinocytosis involves structural and accessory proteins forming 50-60 nm cell membrane invaginations that are capable to engulf cargos, including folic acid, albumin, specific lipids, and virus. The vesicles

of this transport (caveosomes) can carry the sequestered particles to the endoplasmic reticulum or to the Golgi network (PATHAK, *et al*., 2023; MANZANARES & CEÑA, 2020).

The clathrin-mediated pinocytosis is the major endocytic mechanism that provides the engulfment of macromolecules, including viral proteins, toxins, metabolites, protein growth factors, and polypeptide hormones, by means of the formation of a ~100 nm clathrin-coated vesicles at the membrane. After the release of these vesicles, the clathrin gradually detach of these invaginations and eventually release the load near to early endosomes (JU, *et al.*, 2020). There is also a diversity of membrane receptors that mediate endocytotic pathways without involving clathrin and caveolin proteins, thereby being referred as clathrin and caveolin independent pinocytosis (JU, *et al.*, 2020). At last, the macropinocytosis involve the formation of vesicles named as macropinosomes, which allow the cellular uptake of fluids with particles in the range of 0.2-5 μm in diameter. This process occurs in many types of cells, including the ones in the intestine, where this cellular transport is employed during nutrient absorption. Cancer cells also use this transport not only to cellular proliferation, but also to a rapid nutrient acquisition (JU, *et al.*, 2020; PATHAK, *et al*., 2023).

Exocytosis is the other type of vesicle transport (see Figure 1.15) where fluids and particles are captured by secretory vesicles in the cytoplasm from the early endosome to the recycling endosome that is able, in turn, to fuse to the plasma membrane and finally eject the encapsulated species out of the cell (see Figure 1.17). This is classical process by which cells can excrete waste and other large molecules from the intracellular region to the extracellular medium. Besides, the release of neurotransmitters is also mediated by the process of exocytosis (STILLWELL, 2016; PATEL, *et al*., 2019).

The aforementioned active processes, such as endocytosis, present a substantial temperature dependence and high activation barriers. For instance, at low temperatures (5-10 °C), the receptor-mediated endocytosis is inhibited due to the rigidity of membranes at the semisolid gel phase, whereas at above these temperatures, this endocytosis can take place through two stages with distinct energies barriers: pore opening ($\Delta G^{\ddagger}$ ~10-20 kcal mol^{-1}) and pore closure ($\Delta G^{\ddagger}$ ~6-10 kcal mol^{-1}). In general, the energy barrier for the pinocytosis process, in the range of 25-37 °C, is 15-25 kcal mol^{-1}. Conversely, the exocytosis is less dependent on temperature over the initial steps, since the fusion of granules on membranes can take place even at 6 °C. However, after the fusion step, the full collapse of the exosomes becomes highly dependent on temperature. (CHANADAY & KAVALALI, 2018). In spite of these data, there is a lack of information about the magnitude of the different endocytotic pathways in different

cells and tissues, which also raise questions when it comes to the cellular uptake of nanoparticles, such as carbon nanomaterials (RENNICK, *et al.*, 2021).

1.5 INTERACTIONS BETWEEN CARBON NANOMATERIALS AND CELL MEMBRANES

Unlike CNHs, the interaction between other carbon nanomaterials, especially CNTs, and plasma membranes have been investigated at a molecular level in a series of theoretical studies using MD simulations (WALLACE & SANSOM, 2010; KRANSZEWSKI, *et al.*, 2013; LACERDA, *et al.*, 2013; MEJRI, *et al*., 2015; CHERNIAVSKYI, *et al.*, 2015; TABARI, *et al.*, 2015; RACZYŃSKI, *et al*., 2018; HERLEM; *et al.*, 2019; MEJRI, *et al*., 2021). In this context, a MD study conducted by Kranszewski and coworkers demonstrated the passive diffusion of functionalized CNT models with amino groups through a homogenous membrane model based on POPC lipids. This uptake process was described in three consecutives steps: landing, floating, and penetration in the hydrophobic core of the biomembrane (KRANSZEWSKI, *et al.*, 2013). By combining MD simulations and analyzes with transmission electron microscopy, Lacerda and coworkers concluded that the interaction between functionalized CNTs and polar heads groups of membranes (POPC for the theoretical study and lipid vesicles and A549 cells for the experimental study) were mainly electrostatic. Besides, the authors reported that penetration process started by the tip region of these nanostructures and provided the concomitant permeation of solvent (water molecules) in the hydrophobic region of the membrane, thereby increasing its polarity. The improvement of the interactions CNT-membrane was achieved due to the functionalization of this carbon nanomaterial, which is essential to increase its biocompatibility (LACERDA, *et al.*, 2013).

In 2015, MD simulations carried out by Mejri and coworkers indicated the spontaneous release of cddp molecules from the cavities of CNTs located near to a POPC membrane model (MEJRI, *et al*., 2015). The interactions between fullerenes and biomembranes were also a topic of study by Cherniavskyi and coworkers using simulations with coarse-grained models. By using asymmetric and curved DOPC/DOPS bicelles, the authors showed the preferential concentration of fullerenes in the regions with moderate curvature. The permeation of this spherical nanomaterial was also verified during the simulations in addition to an increasing on the ordering of the lipid tails (CHERNIAVSKYI, *et al.*, 2015).

The translocation process of CNTs through membranes was also studied by Raczyński and coworkers using steered molecular dynamics (SMD) simulations. The authors used pristine

CNT models with different diameters (7 Å, 10 Å, 12 Å, and 15 Å) and a membrane model containing 232 DMPC lipids and 48 CHL molecules. In this study, the authors showed that the permeation of CNT did not induce permanent damages on the lipid bilayer. Moreover, the translocations were highly unfavourable with the average work required to pull out these nanomaterials from the membrane in the range of ~200-750 kcal mol^{-1} (RACZYŃSKI, *et al*., 2018). In addition to emphasize the relevance to understand the cellular internalization of carbon nanomaterials, Herlem and coworkers proposed that phagocytosis and passive diffusion may be the likely cellular uptake mechanisms of CNTs, which are, in turn, dependent on size and molecular weight of these carbon nanostructures. In this sense, the chemical functionalization plays a relevant role in determining not only the biocompatibility, but also the internalization pathways of carbon nanomaterials (HERLEM; *et al.*, 2019).

More recently, endocytosis has been pointed out as one of the main transport routes of DDS across membranes. Particularly, the macropinocytosis (Figure 1.17) of CNTs is a common process for nanotubes with long (630 nm), medium (390 nm), and short (195 nm) lengths. Conversely, ultrashort CNTs with ~50 nm (or smaller) and C_{60} fullerenes can be internalized into membrane via passive diffusion. Besides, the uptake of multiwalled CNT in human cervical carcinoma cells can also occurs through a mechanism of clathrin-mediated endocytosis (MANZANARES & CEÑA, 2020). Notwithstanding these studies, the understanding of cellular uptake of CNTs is not yet well established, especially for CNHs, which points out the need for more analyzes and conclusive results (HERLEM; *et al.*, 2019).

1.6 MOTIVATION AND OBJECTIVES

In spite of the promising aspects of CNHs as DDS cited in section 1.3, the literature is still scarce when it comes to the encapsulation of worldwide approved platinum drugs (Figure 1.3) in this carbon nanomaterial. For instance, the nanovectorization of cpx and oxa in CNHs has not been previously investigated at a molecular resolution in the literature. Moreover, there are no previous reports in the literature on the interaction mechanism at a molecular level between inclusion complexes formed by platinum drugs incorporated into CNHs and plasma membranes.

With regard to the cell membranes that interact with carbon nanomaterials (e.g. CNTs), there is also a lack of study on realistic models of biomembranes that capture the main aspects of specific cells referring to a human tissue. In general, the theoretical studies consider either homogeneous membranes or membranes with a simple mixture of lipids (WALLACE &

SANSOM; KRANSZEWSKI, *et al.*, 2013; LACERDA, *et al.*, 2013; MEJRI, *et al*., 2015; CHERNIAVSKYI, *et al.*, 2015; TABARI, *et al.*, 2015; ZHU, *et al.*, 2016 RACZYŃSKI, *et al*., 2018; MEJRI, *et al*., 2021). In contrast, recent studies have taken into account the asymmetric lipid composition and the realistic cholesterol content found in mammalian cells (YESYLEVSKYY, *et al*., 2017; PERAMO, *et al.*, 2018; ENKAVI, *et al*., 2019; MARRINK, *et al.*, 2019; RIVEL, *et al.*, 2019). In this context, by conducting MD simulations of membranes referring to mouse hepatocytes and hepatomas, Andoh and coworkers identified not only a reduction in the fluidity, but also an increase of the lateral ordering of these lipid bilayers due to the development of hepatic tumors (ANDOH, *et al.*, 2016). Rivel and coworkers also evaluated the cddp permeation through membrane models referring to cancer and normal cells. In addition to report a decrease on the drug permeability due to the increase on the cholesterol content, the authors indicated that the cancer cell membrane offered greater resistance to the permeant than the normal cell membrane (RIVEL, *et al.*, 2019).

The asymmetric salt concentration between the extracellular and intracellular media is another relevant aspect to be considered in the modeling of biomembranes (KHALILI-ARAGHI, *et al.*, 2013). Ross and coworkers highlighted the sensibility of molecular behaviors, such as conformations, dynamics, function, and binding affinity of biomacromolecules, due to the existence of ionic gradients in the physiological medium (ROSS, *et al*., 2018). When it comes to the platinum drugs, there are no previous reports in the literature on the investigation at a molecular level of how asymmetric distribution of ions in cancer cells affects the translocation of these anticancer metallodrugs.

The development of realistic prototypes of biomembranes is a relevant research topic, since it can notably improve not only the connection between simulation data and experimental data by integrating characteristics of real cells, but also the prediction properties and behaviors of these complex systems. For instance, the building of membranes models of human breast cancer cells provides a clear description of both environment and surface of these malignant cells in simulations, which may assist the development and improvement of anticancer drugs and nanocarriers. Therefore, the understanding of the interactions between CNHs and realistic cell membranes is an unexplored and challenge field, which may reinforce the application of this nanomaterial as DDS and boost its translation to the preclinical analyzes. This is also a relevant strategy that can reduce the side effects that are commonly observed during platinum drugs-based chemotherapies.

In view of this context, the present thesis aims to characterize the dynamics of the interaction between inclusion complexes drug@CNH, which are formed by platinum drugs

encapsulated in chemically functionalized CNHs, and realistic models of cell membranes by using molecular dynamics simulations with different approaches. The specific objectives are:

a) built realistic models of plasma membranes referring to human cells, as well as parameterize and adjust the MD simulation protocols of these lipid bilayers;
b) create new models of chemically modified CNHs, which provide the transport of Pt(II)-based drugs, and study the dynamical and energetic behavior of these systems as nanovectors of these metallodrugs;
c) investigate the process of interaction and release of cddp molecules from CNH models near to biomembranes, and compare these results with the ones referring to MD simulations of these free inclusion complexes in aqueous solution without considering membranes;
d) characterize the energetic profile referring to the permeation of platinum drugs through plasma membrane models by means of MD simulations;
e) characterize the free energy profiles of the translocation of the inclusion complexes cddp@CNH, which may include different CNH models, through realistic prototypes of cell membranes using MD simulations.

1.7 ORGANIZATION

In summary, this thesis is organized as follows:

a) chapter 2 presents an overview of the main aspects of MD methods that were applied in this work;
b) chapter 3 treats the interaction of the cddp@CNHox nanovector with membrane models of cancer and normal cells referring to a typical human breast using unbiased MD simulations. The supplementary information (figures and tables) of this section is included in the Appendix A. These results were published in the Physical Chemistry Chemical Physics journal (ALMEIDA, *et al.*, 2021);
c) in chapter 4, the releasing of platinum drugs from the cavities of CNHs models in aqueous solution (150 mM NaCl) is characterized by means of biased MD simulations. The supplementary information (figures and tables) of this section is included in the Appendix B. These results were published in The Journal of Physical Chemistry B (ALMEIDA, *et al.*, 2022);

d) chapter 5 evaluates the translocation process of CNHf models as nanocarriers of cddp (cddp@CNHf) through breast cancer cell membrane using enhanced sampling methods in MD simulations. The supplementary information (figures and tables) of this section is included in the Appendix C. These results were carried out with the supervision of Prof. Fabien Picaud in the *Laboratoire de Nanomédecine, Imagerie, Thérapeutique* at the *Université de Franche-Comté* (France). The results were published in the Molecular Pharmaceutics journal (ALMEIDA, *et al.*, 2023);
e) in chapter 6, it is discussed the permeation process of platinum drugs (cddp, cpx, and oxa) through a realistic model of a human breast cancer cell membrane in the light of biased MD simulations. The supplementary information (figures and tables) of this section is included in the Appendix D. These results were also obtained during the doctoral stay in the *Université de Franche-Comté* (France) with the supervision of Prof. Fabien Picaud. The results were recently published in the Journal of Chemical Information and Modeling (ALMEIDA, *et al.*, 2023);
f) at last, the concluding remarks in chapter 7 summarize the main results of this thesis and point out the perspectives of studies.

REFERENCES

ABBAS, Z. & REYMAN, S. An Overview of Cancer Treatment Modalities. *In*: SHAHZAD, H. N. **Neoplasm**. IntechOpen, p. 139-157, 2018.

AHMAD, S. Kinetic aspects of platinum anticancer agents. **Polyhedron**, v. 138, p. 109-124, 2017.

AJIMA, K.; *et al*. Carbon nanohorns as anticancer drug carriers. **Molecular Pharmaceutics**, v. 2, n. 6, p. 475-480, 2005.

AJIMA, K.; *et al.* Effect of functional groups at hole edges on cisplatin release from inside single-wall carbon nanohorns. **Journal of the Physical Chemistry B**, v. 110, n. 11, p. 5773-5778, 2006.

AJIMA, K. *et al*. Enhancement of In Vivo Anticancer Effects of Cisplatin by Incorporation Inside Single-Wall Carbon Nanohorns. **ACS Nano**, v. 2, n. 10, p. 2057-2064, 2008.

ALCINDOR, T. & BEAUGER, N. Oxaliplatin: a review in the era of molecularly targeted therapy. **Current Oncology**, v. 18, n. 1, p. 18-25, 2011.

ALMEIDA, E. R.; *et al*. Molecular dynamics of carbon nanohorns and their complexes with cisplatin in aqueous solution. **Journal of Molecular Graphics and Modelling**, v. 89, p. 167-177, 2019.

ALMEIDA, E. R.; *et al*. Chemically Modified Carbon Nanohorns as Nanovectors of the Cisplatin Drug: A Molecular Dynamics Study. **Journal of Chemical Information and Modeling**, v. 60, n. 2, p. 500-512, 2020.

ALMEIDA, E. R.; *et al*. Carbon nanohorns as nanocontainers for cisplatin: insight into their interaction with the plasma membranes of normal and breast cancer cells. **Physical Chemistry Chemical Physics**, v. 23, p. 16376-16389, 2021.

ALMEIDA, E. R.; *et al*. Unveiling the Releasing Processes of Pt(II)-Based Anticancer Drugs from Oxidized Carbon Nanohorn: An In Silico Study. **Journal of Physical Chemistry B**, v. 126, n. 23, p. 4246-4260, 2022.

ALMEIDA, E. R. & DOS SANTOS, H. F. Nanoconfinement effect on the hydrolysis of cisplatin. **Chemical Physics Letters**, v. 811, n. 140247, p. 1-7, 2023.

ALMEIDA, E. R.; *et al*. Modeling the cellular uptake of functionalized carbon nanohorns loaded with cisplatin through a breast cancer cell membrane. **Molecular Pharmaceutics**, 2023 *(in press)*. DOI: https://doi.org/10.1021/acs.molpharmaceut.3c00379

ALMEIDA, E. R.; *et al*. Translocation processes of Pt(II)-based drugs through human breast câncer cell membrane: in silico experiments. **Journal of Chemical Information and Modeling**, 2023 (accepted for publication).

ALVES, A. C.; *et al*. Biophysics in Cancer: The Relevance of Drug-Membrane Interaction Studies. **Biochimica et Biophysica Acta**, v. 1858, n. 9, p. 2231-2244, 2016.

ANAND, P.; *et al.* Cancer is a Preventable Disease that Requires Major Lifestyle Changes. **Pharmaceutical Research**, v. 25, n. 9, p. 2097-2116, 2008.

ANAND, U.; *et al*. Cancer chemotherapy and beyond: Current status, drug candidates, associated risks and progress in targeted therapeutics. **Genes & Diseases**, https://doi.org/10.1016/j.gendis.2022.02.007.

ANDOH, Y.; *et al*. Molecular dynamics study of lipid bilayers modeling the plasma membranes of normal murine thymocytes and leukemic GRSL cells. **The Journal Physical Chemistry**, v.144, p. 1-14, 2016.

ANTHONY, E. J.; *et al*. Metallodrugs are unique: opportunities and challenges of discovery and development. **Chemical Science**, v. 11, p. 12888-12917, 2020.

ARNOLD, M.; *et al.* Current and future burden of breast cancer: Global statistics for 2020 and 2040. **The Breast**, v. 66, p. 15-23, 2022.

ATTIA, M. F.; *et al*. An overview of active and passive targeting strategies to improve the nanocarriers efficiency to tumour sites. **Journal of Pharmacy and Pharmacology**, v. 71, p. 1185-1198, 2019.

BANCROFT, D.P.; LEPRE, C. A.; LIPPARD, S. J. Platinum-195 NMR kinetic and mechanistic studies of cis- and trans-diamminedichloroplatinum(II) binding to DNA. **Journal of the American Chemical Society**, v. 112, n. 19, p. 6860-6871, 1990.

BERGAMO, A.; DYSON, P. J.; SAVA, D. The mechanism of tumor cell death by metal-based anticancer drugs is not only a matter of DNA interactions. **Coordination Chemistry Reviews**, v. 360, p. 17-33, 2018.

BERNARDES, N. & FIALHO, A. M. Perturbing the Dynamics and Organization of Cell Membrane Components: A New Paradigm for Cancer-Targeted Therapies. **International Journal of Molecular Science**, v. 19, n. 3871, p. 1-19, 2018.

BUZAID, A. C.; *et al*. Challenges in the journey of breast cancer patients in Brazil. **Brazilian Journal of Oncology**, v. 16, p. 1-10, 2020.

CASTEIGNAU, F.; *et al*. Synthesis of Carbon Nanohorns by Inductively Coupled Plasma. **Plasma Chemistry and Plasma Processing**, v. 42, p. 465-481, 2022.

CHANADAY, N. L. & KAVALALI, E. T. Time course and temperature dependence of synaptic vesicle endocytosis. **Federation of European Biochemical Societies**, v. 592, p. 3606-3614, 2018.

CHAKRABORTY, S.; *et al*. How cholesterol stiffens unsaturated lipid membranes. **Proceedings of the National Academy of Sciences**, v. 117, n. 36, p. 21896-21905, 2020.

CHERNIAVSKYI, Y. K.; RAMSEYER, C.; YESYLEVSKYY, S. O. Interaction of C_{60} fullerenes with asymmetric and curved lipid membranes: a molecular dynamics study. **Physical Chemistry Chemical Physics**, v. 18, p. 278-284, 2015.

CURCIO, M.; *et al*. Carbon Nanohorns as Effective Nanotherapeutics in Cancer Therapy. **C – Journal of Carbon Research**, v. 7, n. 3, p. 1-18, 2021.

DAS, C. G. A.; *et al*. Nanomaterials in anticancer applications and their mechanism of action -A review. **Nanomedicine: Nanotechnology, Biology, and Medicine**, v. 47, n. 102613, p. 1-23, 2023.

DE SOUZA, L. A.; *et al*. DFT study of cisplatin@carbon nanohorns complexes. **Journal of Inorganic Biochemistry**, v. 129, p. 71-83, 2013.

DE SOUZA, L. A.; *et al*. Inclusion complexes between cisplatin and oxidized carbon nanostructures: a theoretical approach. **Journal of Inorganic Biochemistry**, v. 178, p. 134-143, 2018.

DE KONING, L. **Chromatin assembly factors and heterochromatin organization during cell proliferation, tumorigenesis and in quiescence**. 2009. Thesis. École Doctorale Complexité du Vivant. Université Pierre et Marie Curie, Paris VI, 2009.

DILRUBA, S. & KALAYDA, G. V. Platinum-based drugs: past, present and future. **Cancer Chemotherapy Pharmacology**, v. 77, n. 6, p. 1103-1124, 2016.

DUAN, X.; *et al*. Nanoparticle formulations of cisplatin for cancer therapy. **WIREs Nanomedicine and Nanobiotechnology**, v. 8, n. 5, p. 776-791, 2016.

ENKAVI, G.; *et al*. Multiscale Simulations of Biological Membranes: The Challenge To Understand Biological Phenomena in a Living Substance. **Chemical Reviews**, v. 119, p. 5607-5774.

FISCHER, E. G. Nuclear Morphology and the Biology of Cancer Cells. **Acta Cytologica**, v. 64, p. 511-519, 2020.

GANDIN, V.; HOESCHELE, J. D.; MARGIOTTA, N. Special Issue "Cisplatin in Cancer Therapy: Molecular Mechanism of Action 3.0". **International Journal of Molecular Sciences**, v. 24, n. 7917, p. 1-5, 2023.

GARRIGA, R.; *et al*. Toxicity of Carbon Nanomaterials and Their Potential Application as Drug Delivery Systems: In Vitro Studies in Caco-2 and MCF-7 Cell Lines. **Nanomaterials**, v. 10, n. 8, p. 1-21, 2020.

GIAQUINTO, A. N.; *et al*. Breast Cancer Statistics, 2022. **CA: Cancer Journal for Clinicians,** v. 72, n. 6, p. 524-541.

GODONE, R. L. N.; *et al*. Clinical and molecular aspects of breast cancer: Targets and therapies. **Biomedicine & Pharmacotherapy**, v. 106, p. 14-34, 2018.

GUPTA, S. & ASHKAR, R. The dynamic face of lipid membranes. **Soft Matter**, v. 17, p. 6910-6928, 2021.

HARAYAMA, T. & RIEZMAN, H. Understanding the diversity of membrane lipid composition. **Nature Reviews Molecular Cell Biology**, v. 19, p. 281-296, 2018.

HE, B.; *et al*. Single-walled carbon-nanohorns improve biocompatibility over nanotubes by triggering less protein-initiated pyroptosis and apoptosis in macrophages. **Nature Communications**, v. 9, n. 2393, p. 1-21, 2018.

HERLEM, G.; *et al*. Carbon Nanotubes: Synthesis, Characterization, and Applications in Drug-Delivery Systems. *In*: MOHAPATRA, S. S.; *et al.* **Nanocarriers for Drug Delivery: Nanoscience and Nanotechnology in Drug Delivery**. Elsevier, p. 469-529, 2019.

HINDMARSCH, K.; HOUSE, D. A.; TURNBULL, M. M. The hydrolysis products of cis-diamminedichloroplatinum(II) 9. Chloride and bromide anation kinetics for some $[Pt^{II}(N)_2(OH_2)_2]^{2+}$ complexes and the structures of $[Pt^{IV}Br_4(N)_2]$ $((N)_2$ = en, tn)[1]. **Inorganica Chimica Acta**, v. 257, n. 1, p. 11-18, 1997.

HOLLINGSWORTH, S. A.; DROR, R. O. Molecular dynamics simulation for all. **Neuron**, v. 99, n. 6, p. 1129-1143, 2019.

IIJIMA, S.; *et al*. Nano-Aggregates of Single-Walled Graphitic Carbon Nanohorns. **Chemical Physics Letters**, v. 309, p. 165-170, 1999.

INSTITUTO NACIONAL DO CÂNCER. Estimativa 2020 Incidência de Câncer no Brasil. Ministério da Saúde. Rio de Janeiro, RJ, 2019. Available on https://www.gov.br/inca/pt-br/assuntos/cancer/numeros/estimativa. Accessed on 05/04/2023.

INSTITUTO NACIONAL DO CÂNCER. Quimioterapia. Ministério da Saúde. Rio de Janeiro, RJ, 2023. Available on https://www.gov.br/inca/pt-br/assuntos/cancer/tratamento/quimioterapia. Accessed on 05/08/2023.

ISAAC, K. M.; *et al*. Functionalization of single-walled carbon nanohorns for simultaneous fluorescence imaging and cisplatin delivery in vitro. **Carbon**, v. 138, p. 309-318, 2018.

JIN, C.; *et al*. Application of Nanotechnology in Cancer Diagnosis and Therapy - A Mini-Review. **International Journal of Medical Sciences**, v. 17, n. 18, p. 2964-2973, 2020.

JOINT RESEARCH CENTRE. Cancer care in times of COVID-19: lessons for future pandemics. European Commission, JRC news. Available on https://joint-research-centre.ec.europa.eu/jrc-news/cancer-care-times-covid-19-lessons-future-pandemics-2023-02-28_en. Accessed on 05/04/2023.

JOHNSTONE, T. C.; SUNTHARALINGAM, K.; LIPPARD, S. J. The Next Generation of Platinum Drugs: Targeted Pt(II) Agents, Nanoparticle Delivery, and Pt(IV) Prodrugs. **Chemical Reviews**, v. 116, n. 5, p. 3436-3486, 2016.

JU, Y.; *et al.* Application of advances in endocytosis and membrane trafficking to drug delivery. **Advanced Drug Delivery Reviews**, v. 157, p. 118-141, 2020.

KAROUSIS, N.; *et al*. Structure, properties, functionalization, and applications of carbon nanohorns. **Chemical Reviews**, v. 116, n. 8, p. 4850-4883, 2016.

KHALILI-ARAGHI, F.; *et al*. Molecular dynamics simulations of membrane proteins under asymmetric ionic concentrations. **Journal of General Physiology**, v. 142, n. 4, p. 465-475, 2013.

KING, R. J. B. & ROBINS, M. W. **Cancer Biology**. 3rd ed., England: Pearson Education Limited, 2006.

KIRTANE, A. R.; *el al.* Nanotechnology approaches for global infectious diseases. **Nature Nanotechnology**, v. 16, p. 369-384, 2021.

KRANSZEWSKI, S.; *et al*. Insertion of Short Amino-Functionalized Single-Walled Carbon Nanotubes into Phospholipid Bilayer Occurs by Passive Diffusion. **PLoS ONE**, v. 7, p. 1-11, 2013.

LACERDA, L.; *et al*. How do functionalized carbon nanotubes land on, bind to and pierce through model and plasma membranes. **Nanoscale**, v. 5, p. 10242-10250, 2013.

LANCETA, A. M.; BOSCH, M. M.; LESMES, P. M. Single-Walled Carbon Nanohorns as Promising Nanotube-Derived Delivery Systems to Treat Cancer. **Pharmaceutics**, v. 12, n. 850, p. 1-21, 2020.

LEWARDS, E. **Computational chemistry**: Introduction to the Theory and Applications of Molecular and Quantum Mechanics. Kluwer Academic Publishers, 2003.

MAKOVEC, T. Cisplatin beyond: molecular mechanisms of action and drug resistamce development in cancer chemotherapy. **Radiology and Oncology**, v. 53, n. 2, p. 154-158, 2019.

MANUAL DE BASES TÉCNICAS BÁSICAS DA ONCOLOGIA – SIA/SUS – Sistema de Informações ambulatoriais, Sistema Único de Saúde. Brasília, DF, 2013. Available on https://bvsms.saude.gov.br/bvs/publicacoes/inca/manual_oncologia_14edicao.pdf. Accessed on 07/05/2023.

MANZANARES, D. & CEÑA, V. Endocytosis: The Nanoparticle and Submicron Nanocompounds Gateway into the Cell. **Pharmaceutics**, v. 12, n. 4, p. 1-22, 2020.

MARQUES, N. P.; *et al*. Cancer diagnosis in Brazil in the COVID-19 era. **Seminars in Oncology**, v. 48, n. 2, p. 156-159, 2021.

MARRINK, S. J.; *et al*. Computational Modeling of Realistic Cell Membranes. **Chemical Reviews**, v. 119, p. 6184-6226, 2019.
MATSUMURA, S.; *et al*. Ultrastructural localization of intravenously injected carbon nanohorns in tumor. **International Journal of Nanomedicine**, v. 9, p. 3499-3508, 2014.

MEJRI, A.; *et al*. Encapsulation into Carbon Nanotubes and Release of Anticancer Cisplatin Drug Molecule. **The Journal of Physical Chemistry B**, v. 119, p. 604-611, 2015.

MEJRI, A.; *et al*. Confinement of the antitumoral drug cisplatin inside edge-functionalized carbon nanotubes and its release near lipid membrane. **The European Physical Journal D**, v. 75, n. 99, p. 1-10, 2021.

MIYAWAKI, J.; *et al*. Toxicity of single-walled carbon nanohorns. **ACS Nano**, v. 2, p. 213-226, 2008.

MORGON, N. H. Computação em química teórica: informações técnicas. **Química Nova**, v. 24, n. 5, p. 676-682, 2001.

MURAKAMI, T.; *et al*. Drug-Loaded Carbon Nanohorns: Adsorption and Release of Dexamethasone in Vitro. **Molecular Pharmaceutics**, v. 1, n. 6, p. 399-405, 2004.

MURATA, K.; *et al*. Nanowindow-induced molecular sieving effect in a single-wall carbon nanohorn. **The Journal of Physical Chemistry B**, v. 106, n. 49, p. 12668-12669, 2002.

NAKAJIMA, H.; *et al*. Outer-Surface Covalent Functionalization of Carbon Nanohorn Spherical Aggregates Assessed by Highly Spatial-Resolved Energy-Dispersive X-ray Spectrometry in Scanning Electron Microscopy. **The Journal of Physical Chemistry C**, v. 124, n. 45, p. 25142-25147, 2020.

NATIONAL CANCER INSTITUTE. What is cancer? National Institutes of Health – USA.gov. U.S., 2023. Available on https://www.cancer.gov/about-cancer/understanding/what-is-cancer. Accessed on 05/06/2023.

NATIONAL CANCER INSTITUTE. Types of Cancer Treatment. National Institutes of Health – USA.gov. U.S., 2023. Available on https://www.cancer.gov/about-cancer/treatment/types. Accessed on 05/08/2023.

NELSON, D. L. & COX, M. M. **Lehninger Principles of Biochemistry**. W. H. Freeman, fourth edition, p. 369, 2004.

NELSON, D. L. & COX, M. M. **Princípios de Bioquímica de Lehninger**. Artmed, sixth edition, p. 415, 2014.

NENCLARES, P. & HARRINGTON, K. J. The biology of cancer. **Medicine**, v. 48, n. 2, p. 67-72, 2020.

NICOLSON, G. L. & MATTOS, G. F. A Brief Introduction to Some Aspects of the Fluid–Mosaic Model of Cell Membrane Structure and Its Importance in Membrane Lipid Replacement. **Membranes**, v. 11, n. 12, p. 1-19, 2021.

OBRESHKOVA, D.; IVANOVA, S.; YORDANOVA-LALEVA, P. Influence of chemical structure and mechanism of hydrolysis on pharmacological activity and toxicological profile of approved platinum drugs. **Pharmacia**, v. 69, n. 3, p. 645-653.

OUN, R.; MOUSSA, Y. E.; WHEATE, N. J. The side effects of platinum-based chemotherapy drugs: a review for chemists. **Dalton Transactions**, v. 47, n. 19, p. 6645-6653, 2018.

PATEL, S.; *et al*. Brief update on endocytosis of nanomedicines. **Advanced Drug Delivery Reviews**, v. 144, p. 90-111, 2019.

PATHAK, C.; *et al*. Insights of Endocytosis Signaling in Health and Disease. **International Journal of Molecular Sciences**, v. 24, n. 3, p. 1-23, 2023.

PAVELKA, M.; *et al*. On the Hydrolysis Mechanism of the Second-Generation Anticancer Drug Carboplatin. **Chemistry A European Journal**, v. 13, n. 36, p. 10108-10116, 2007.

PERAMO, A.; *et al*. Squalene versus cholesterol: Which is the best nanocarrier for the delivery to cells of the anticancer drug gemcitabine? **Comptes Rendus Chimie**, v. 21, n. 10, p. 974-986, 2018.

PERSIL, E.; *et al*. Systems analysis of intracellular pH vulnerabilities for cancer therapy. **Nature Communications**, v. 9, n. 2997, p. 1-11, 2018.

PEYRONE, M. Ueber die Einwirkung des Ammoniaks auf Platinchlorür [On the action of ammonia of platinum chloride]. **European Journal of Organic Chemistry**, v. 51, n. 1, p. 1-29, 1844.

PORTO, A. B.; *et al*. Oxidation of single-walled carbon nanotubes under controlled chemical conditions. **Journal of the Brazilian Chemical Society**, v. 29, n. 11, p. 2387-2396, 2018.

QIN, Z.; *et al*. Systemic Evaluation on the Pharmacokinetics of Platinum-Based Anticancer Drugs From Animal to Cell Level: Based on Total Platinum and Intact Drugs, **Frontiers in Pharmacology**, v. 10, n. 1485, p. 1-11, 2020.

RACZYŃSKI, P.; et al. On the impact of nanotube diameter on biomembrane indentation – Computer simulations study. **Biochimica et Biophysica Acta (BBA) – Biomembranes**, v. 1860, n. 2, p. 310-318, 2018.

RENNICK, J. J.; *et al*. Key principles and methods for studying the endocytosis of biological and nanoparticle therapeutics. **Nature Nanotechnology**, v. 16, p. 266-276, 2021.

RIVEL, T.; RAMSEYER, C.; YESYLEVSKYY. The asymmetry of plasma membranes and their cholesterol content influence the uptake of cisplatin. **Scientific Reports**, v. 9, n. 5627, p. 1-14, 2019.

ROSENBERG, B.; VANCAMP, L.; KRIGAS, T. Inhibition of cell division in Escherichia coli by electrolysis products from a platinum electrode. **Nature**, v. 205, n. 4972, p. 698-699, 1965.

ROSS, G. A.; *et al*. Biomolecular Simulations under Realistic Macroscopic Salt Conditions. **The Journal of Physical Chemistry B**, v. 122, n. 21, p. 5466-5486, 2018.

RUSESKA, I. & ZIMMER, A. Internalization mechanisms of cell-penetrating peptides. **Beilstein Journal of Nanotechnology**, v. 11, p. 101-123, 2020.

SHAH, S. S.; *et al*. Present Status and Future Prospects of Jute in Nanotechnology: A Review. **The Chemical Record**, v. 21, p. 1-36, 2021.

SHI, Y.; *et al*. Biodistribution Survey of Oxidized Single-Wall Carbon Nanohorns Following Different Administration Routes by Using Label-Free Multispectral Optoacoustic Tomography. **International Journal of Nanomedicine**, v. 14, p. 9809-9821, 2019.

SHIMADA, M.; ITAMOCHI, H.; KIGAWA, J. A cisplatin derivative in cancer chemotherapy. **Cancer Management and Research**, v. 5, p. 67-76, 2013.

SHINDE, V. R.; *et al*. Enhanced permeability and retention effect: A key facilitator for solid tumor targeting by nanoparticles. **Photodiagnosis and Photodynamic Therapy**, v. 39, n. 102915, p. 1-12, 2022.

SIEGEL, R. L.; *et al*. Cancer statistics, 2023. **CA: Cancer Journal for Clinicians**, v. 73, n. 1, p. 17-48, 2023.

SIGMA-ALDRICH. Single-Walled Carbon Nanohorn Properties & Applications. Available on: https://www.sigmaaldrich.com/BR/pt/technical-documents/technical-article/materials-science-and-engineering/electron-microscopy/single-walled-carbon-nanohorns. Accessed on 05/14/2023.

SINGER, S. J & NICOLSON, G. L. The fluid mosaic model of the structure of cell membranes. **Science**, v. 175, p. 720-731, 1972.

SINGHVI, G.; *et al.* Nanocarriers as Potential Targeted Drug Delivery for Cancer Therapy. *In*: DAIMA, H. K.; *et al*. **Nanoscience in Medicine vol.1**. Springer, p. 51-88, 2020.

SOARES, S.; *et al*. Nanomedicine: Principles, Properties, and Regulatory Issues. **Frontiers in Chemistry**, v. 6, n. 360, p. 1-15, 2018.

SOUZA, G. F.; WLODARCZKL, S. R.; MONTEIRO, G. Carboplatin: molecular mechanisms of action associated with chemoresistance. **Brazilian Journal of Phamaceutical Sciences**, v. 50, n. 4, 693-701, 2014.

STILLWELL, W. Membrane transport. *In*: STILLWELL, W. **An introduction to biological membranes: composition, structure and function**. Elsevier, p. 423-451, 2016.

SUDHAKAR, A. History of Cancer, Ancient and Modern Treatment Methods. **Journal of Cancer Science & Therapy**, v. 1, n. 2, 1-4.

SUNG, H.; *et al*. Global cancer statistics 2020: GLOBOCAN estimates of incidence and mortality worldwide for 36 cancers in 185 countries. **CA: Cancer Journal for Clinicians**, v. 71, n. 3, p. 209-249, 2021.

TABARI, S. H.; JAMALI, Y.; POURSALEHI, R. Multi-Scale Simulation of Carbon Nanotubes Interactions with Cell Membrane: DFT Calculations and Molecular Dynamic Simulation. **Procedia Materials Science**, v. 11, p. 423-427, 2015.

TAHARA, Y.; *et al*. Histological assessments for toxicity and functionalization-dependent biodistribution of carbon nanohorns. **Nanotechnology**, v. 22, n. 26, p. 265106-265140, 2011.

TCHOUNWOU, P. B., *et al*. Advances in Our Understanding of the Molecular Mechanisms of Action of Cisplatin in Cancer Therapy. **Journal of Experimental Pharmacology**, v. 13, p. 303-328, 2021.

TOMAR, N.; HASHMI, M. A.; HASHMI, A. Multifunctional Nanomedicine. *In*: ISLAM, S. U.; HASHMI, A. A.; KHAN, S. A. **Advances in Metallodrugs: Preparation and Applications in Medicinal Chemistry**. Scrivener Publishing LLC, p. 363-402, 2020.

WALLACE, E. J. & SANSOM, M. S. P. Molecular Dynamics Studies of the Interactions Between Carbon Nanotubes and Biomembranes. *In*: SANSOM, M. S. P. & BIGGIN, P. C. **Molecular Simulations and Biomembranes: from biophysics to funtion**. Royal Society of Chemistry Biomolecular Science, n. 20, p. 287-305, 2010.

WELSH, J. Animal Models for Studying Prevention and Treatment of Breast Cancer. *In*: CONN, P. M. **Animal Models for the Study of Human Disease**. Elsevier, p. 997-1018, 2013.

WHITE, K. A.; GRILLO-HILL, B. K.; BARBER, D. L. Cancer cell behaviors mediated by dysregulated pH dynamics at a glance. **Journal of Cell Science**, v. 130, p. 663-669, 2017.

WORLD HEALTH ORGANIZATION. Cancer, 2022. Available on https://www.who.int/news-room/fact-sheets/detail/cancer. Accessed on 05/07/2023.

WU, Y.; *et al*. Retrospective study of the efficacy and toxicity of lobaplatin in combined chemotherapy for metastatic breast cancer. **OncoTargets and Therapy**, v. 12, p. 4849-4857, 2019.

YAMAMOTO, A.; *et al*. Efficacy and Adverse Events of Carboplatin Desensitisation Therapy for Gynaecological Cancer: A Retrospective Study. **Medicines**, v. 9, n. 4, p. 1-22, 2022.

YESYLEVSKYY, S. O.; RIVEL, T.; RAMSEYER, C. The influence of curvature on the properties of the plasma membrane. Insights from atomistic molecular dynamics simulations. **Scientific Reports**, v. 7, n. 16078, p. 1-13, 2017.

ZHANG, M.; *et al*. Biodegradation of carbon nanohorns in macrophage cells. **Nanoscale**, v. 7, p. 2834-2840, 2015.

ZHOU, J.; *et al*. The Drug-Resistance Mechanisms of Five Platinum-Based Antitumor Agents. **Frontiers in Pharmacology**, v. 11, n. 343, p. 1-17, 2020.

ZHU, W.; *et al*. Nanomechanical mechanism for lipid bilayer damage induced by carbon nanotubes confined in intracellular vesicles. **Proceedings of the National Academy of Sciences of the United States of America**, v. 133, n. 1, p. 12374-12379, 2016.

2 CHAPTER 2

Theoretical methods

The MD was the central method employed in this work to study the dynamical and energetic behavior of the inclusion complexes drug@CNH (Pt(II)-based drugs encapsulated in CNHs) in aqueous solution and near to cell membranes. Methods of free energy were also used to calculate the potentials of mean force (PMF) and the binding free energies of the systems drug --- CNH and drug@CNH --- membranes. In this sense, before presenting the results, this section will focus on a summary of the main details referring to the simulation methods applied in this work.

2.1 CLASSICAL MOLECULAR DYNAMICS

The MD is a simulation method based on the fundamentals of classical mechanics that provides the description of time evolution of a many-body system by numerically solving the equations of motion with appropriate boundary conditions (TUCKERMAMN & MARTYNA, 2000). This method is classified as deterministic, since the definition of the initial conditions of a system, which are characterized by dynamical parameters at a given time, and the interaction forces between the system entities provide the simulation of the dynamical history referring to a system, *i.e.* the positions and momenta of all particles at any instant of time (HAILE, 1997).

In the MD method, the molecules are treated as many-body systems formed by N particles (atoms) with masses m_1, m_2, …, m_N moving under internal forces which are the interaction potentials. Each particle has Cartesian (position in x, y, and z) and kinetic (momentum p_x, p_y, and p_z) coordinates, which form the generalized coordinates $g_1(t)$, $g_2(t)$…, $g_N(t)$. The space defined by these particles is known as phase space, which represent all possible states for a classical system (TUCKERMAMN & MARTYNA, 2000). The aim of a MD simulation is to compute a set of generalized coordinates of a system along the phase space forming the so-called trajectory.

In MD, the classical motion of a system formed by N particles is described by Newton's second law:

$$F_i(t) = m_i \ddot{r}_i(t) \tag{2.1}$$

where F_i refers to the applied force F to the atom i due to the N-1 atoms of the system, m_i is the atomic mass, and $\ddot{r}_i$ is the second derivative of the position with respect to time, *i.e.* the acceleration of the atom i:

$$\ddot{r}_i(t) = \frac{\partial^2 r_i(t)}{\partial t^2} = a_i(t) \tag{2.2}$$

The velocity and position functions can be derived from the acceleration (equation 2.2) as:

$$a_i(t) = \frac{dv_i}{dt} \tag{2.3}$$

$$v_i(t) = \frac{dr_i}{dt} \tag{2.4}$$

Since the force on each particle of the system is a function of the N position variables, $F_i = F_i(r_1, r_2, \dots, r_N)$, the Equation 2.1 actually involves a set of 3N coupled second-order differential equations. Therefore, by choosing a set of initial conditions $\{r_1(0), \dots, r_N(0); v_1(0), \dots v_N(0)\}$ for the Equation 2.1, one can calculate the full set of positions and velocities as function of time referring to the classical motion. If the molecular system is conservative, it is possible to obtain the force from the negative gradient of potential energy of the system (V(r)):

$$F_i(t) = m_i \ddot{r}_i(t) = -\frac{\partial V(r^N)}{\partial r_i} \tag{2.5}$$

where r^N involves the set of atomic coordinates of all atoms of the system ($r^N = r_1, r_2, \dots, r_N$). The result of a MD simulation, which is the trajectory of a system, is the product of the numerical resolution of the Equation 2.5. The equation 2.1 has also a Hamiltonian form, where the Hamiltonian $\mathcal{H}(p, r)$ of a system formed by N particles under interparticle interactions is:

$$\mathcal{H}(p, r) = \mathcal{H}(p_1, \dots, p_N, r_1, \dots, r_N) = \sum_{i=1}^{N} \frac{p_i^2}{2m_i} + V(r_1, \dots, r_N) \tag{2.6}$$

where p is the linear momenta of the particle and r is the position of a particle. The Equation 2.1 can be derived from equation 2.6 by using the Hamilton's equations (TUCKERMAMN & MARTYNA, 2000):

$$\dot{r}_i = \frac{\partial \mathcal{H}}{\partial p_i} = \frac{p_i}{m_i} \tag{2.7}$$

$$\dot{p}_i = -\frac{\partial \mathcal{H}}{\partial r_i} = -\frac{\partial V}{\partial r_i} = F_i(r_1, \dots, r_N) \tag{2.8}$$

If we take the time derivative of both sides of Equation 2.7 and we substitute into Equation 2.8, we arrive at Equation 2.1. This way, in the Hamiltonian approach, the full set of positions and momenta grouped in a single vector $x = (p_1, \dots, p_N, r_1, \dots, r_N)$ is named as phase space vector, which exists in the N-dimensional phase space (TUCKERMAMN & MARTYNA, 2000).

Unlike kinetic energy that is defined in Equation 2.6 from the masses and velocities of the particles, the potential energy ($V(r_1, \dots, r_N)$) has specific forms that characterize the nature of the atomic interactions in a molecular system. The general form used in this thesis and details of this potential energy function will be presented in the next subsection.

2.1.1 Force field

The term $V(r^N)$ in Equation 2.5 is known as potential energy surface (PES) or force field in the MD's vocabulary. In a molecular system, this multidimensional function describes the energy of a molecule in terms of its nuclear positions, *i.e.*, the atomic positions. Thus, each point in the PES corresponds to a set of atoms that are subjected to the interaction potentials, which define the molecule, thereby composing a specific molecular structure (LEWARDS, 2003).

The force fields used in MD simulations are commonly composed by pairwise additive potentials, where the harmonic oscillator model is the simplest and most used approximation to describe molecular vibrations. In this model, the potential energy function $V(r)$ is partitioned into bonded contributions, which model the covalent bonds composing the intramolecular potential $V_{intra}(r)$, and non-bonded contributions, which account for the electrostatic and van der Waals interactions composing the intermolecular potential $V_{inter}(r)$:

$$V(r) = \sum V_{intra}(r) + \sum V_{inter}(r) \tag{2.9}$$

In the present thesis, we used the AMBER force field that has the following format (CASE, *et al*. 2016):

$$\begin{aligned} V(r) = & \sum_{i \in bonds} K_{bi}(b_i - b_i^0)^2 + \sum_{i \in angles} K_{\theta i}(\theta_i - \theta_i^0)^2 \\ & + \sum_{i \in dihedrals} \sum_{n} \left(\frac{K_{i,n}}{2}\right)[1 + \cos(n\phi_i - \gamma_i)] \\ & + \sum_{nonb\ i<j} \left(\frac{A_{ij}}{R_{ij}^{12}} - \frac{B_{ij}}{R_{ij}^{6}}\right) + \sum_{nonb\ i<j} \left(\frac{q_i q_j}{R_{ij}}\right) \end{aligned} \tag{2.10}$$

where the parameters b_i^0, θ_i^0, and ϕ_i are the equilibrium values for the bonds, bond angles and dihedral angles respectively, and K_{bi}, $K_{\theta i}$, and $K_{i,n}$ are the force constants for bond stretching, angle bending, and bond torsion, respectively. The parameter n refers to the periodicity of the torsional angle and γ_i describe the phase angle of the ith torsional angle. In the last two terms of Equation 2.10, R_{ij} is the interatomic distance between the atoms i and j, $q_i$and q_j are the atomic charges of the atoms i and j modeled by the Coulomb potential, and A_{ij} and B_{ij} are the parameters that describe the van der Walls interactions modeled by the Lennard-Jones (LJ) potential (see Equation 2.11).

$$V(r) = 4\epsilon_{ij}\left[\left(\frac{\sigma_{ij}}{R_{ij}}\right)^{12} - \left(\frac{\sigma_{ij}}{R_{ij}}\right)^{6}\right] \tag{2.11}$$

where ϵ_{ij} is the potential well depth referring to the non-bonded atoms i and j, and σ_{ij} is the distance at which the potential energy between the two non-bonded atoms i and j is zero. This last parameter is also defined as the van der Waals radius. Still regarding Equation 2.10, while A_{ij} accounts for the repulsion, B_{ij} refers to the attractive term. The parameters A_{ij} and B_{ij} include the parameters ϵ_{ij} and σ_{ij} by the relations: $A_{ij} = 4\epsilon_{ij}{\sigma_{ij}}^{12}$ and $B_{ij} = 4\epsilon_{ij}{\sigma_{ij}}^{6}$ (NAMBA, *et al.*, 2008).

In order to conduct a MD simulation, an important step is the determination of the parameters that compose the force field, such as the ones presented in Equation 2.10 (b_i^0, θ_i^0,

ϕ_i, K_{bi}, $K_{\theta i}$, $K_{i,n}$, R_{ij}, q_i, A_{ij}, and B_{ij}). The set of theoretical and experimental procedures involved in the calculation of these parameters is known as force field parameterization. In the present work, we used specific AMBER force fields for representing organic molecules, lipids, water molecules, and ions (CASE, *et al*. 2016), for Pt complexes, the intra- and intermolecular parameters were parametrized. In view of both concept and analytical expression of the force field $V(r)$, it is possible to describe the algorithm of a MD simulation in the next subsection.

2.1.2 Algorithm of a classical MD simulation

The basic algorithm of a MD simulation involves the following steps (MARTÍNEZ, *et al*., 2007):

a) determine initial configuration of the system;
b) calculate forces, acceleration, potential energy, and kinetic energy;
c) move the atoms of the system;
d) increment the time step over N steps up to the simulation time.

The first step of this algorithm is the determination of the initial configuration of the system, which basically consist in the atomic coordinates (r_i) and linear momenta (p_i, $p_i = m_i v_i$) of the system at time t = 0. Concerning the atomic coordinates of a system, these data can be obtained from spectroscopic techniques, such as X-ray diffraction and nuclear magnetic resonance (NMR), and from theoretical methods based on molecular modeling, including the softwares PACKMOL (MARTÍNEZ, *et al.*, 2009) and Avogadro (HANWELL, *et al.*, 2012). The initial structures of macromolecules can be also available in molecules database, such as the Protein Data Bank (PDB) that has structures and data of biological macromolecules, including proteins and nucleic acids (BERMAN, *et al.*, 2000). When it comes to the linear momenta, the masses correspond to the atomic masses, and the initial velocities can be either considered null, where the system evolves form the rest, or derived from different approaches, such as the attribution from random seeds and from the Maxwell-Boltzmann distribution (MARTÍNEZ, *et al*., 2007). The velocity (and kinetic energy) is related to the temperature by the equipartition theorem:

$$\sum_{i=1}^{N} \frac{1}{2} m_i v_i^2 = \frac{3}{2} N k_B T \tag{2.12}$$

where N is the number of particles, m_i is the mass of the particle i, v_i is the velocity of the particle i, k_B is the Boltzmann's constant, and T is the temperature.

The second step of the MD algorithm is the calculation of the forces F_i as the negative gradient of the potential, which has the form indicated in Equation 2.10 (in this work), according to Equation 2.5. The potential energy of the molecular system is also computed by truncating the sum of atomic interactions according to the condition $R_{ij} > R_C$, where R_C stands for the cutoff radius. After obtaining the forces, the acceleration a_i of each particle is directly calculated with Equation 2.5. Since the positions, velocities, and acceleration are in Cartesian coordinates and both force and potential are in spherical polar coordinates, it is necessary to carry out a conversion from spherical polar coordinates to Cartesian coordinates. Therefore, the components of acceleration a_i of each particle is given by the following set of equations:

$$a_{xi} = \frac{F_{xi}}{m_i};\ a_{yi} = \frac{F_{yi}}{m_i};\ a_{zi} = \frac{F_{zi}}{m_i} \tag{2.13}$$

After obtaining the initial conditions of the system, including positions (x_0, y_0, z_0), velocities (v_{x0}, v_{y0}, v_{z0}), forces (F_{x0}, F_{y0}, F_{z0}), and accelerations (a_{x0}, a_{y0}, a_{z0}) for the N atoms of the system, the next step of the MD algorithm involves the motion of the system for obtaining the new conditions of positions (x_1, y_1, z_1), velocities (v_{x1}, v_{y1}, v_{z1}), forces (F_{x1}, F_{y1}, F_{z1}), and accelerations (a_{x1}, a_{y1}, a_{z1}) of the N particles. As it was explained in the beginning of this subsection, the Equation 2.1 refers to a set of 3N coupled second-order differential equations, and the conventional solution of this set of equations involves the application of finite-difference methods (MARTÍNEZ, *et al*., 2007). In these numerical methods, the differentials (dx and dt) are replaced by finite differences (Δx and Δt), thereby converting differential equations into finite-difference equations, where the rate is constant over a small but finite time Δt (HAILE, 1997). In summary, the total time of the simulation in these integration algorithms is discretized in time intervals Δt, also known as time step, so that from the initial conditions (positions x_0 and velocities v_0) at t = 0 it is possible to compute the same parameters at the time t + Δt.

In this context, there is a series of integration methods for numerically solving the equations of motions, such as the Verlet algorithm (HAILE, 1997; MARTÍNEZ, *et al*., 2007),

Beeman algorithm (BEEMAN, 1976), and the Runge Kutta algorithms (HAILE, 1997). Since the MD software AMBER (CASE, *et al.*, 2016; CASE, *et al.*, 2020) employed in this thesis uses the leapfrog algorithm (HINCHLIFFE, 2003), the details of this method will be presented here.

The leapfrog algorithm is a modification of the Verlet algorithm with a higher precision, where the velocities are explicitly calculated in half the time step (Δt/2) (MARTÍNEZ, *et al.*, 2007). Thus, the Taylor expansion for $v_i(t)$ is:

$$v_i\left(t+\frac{\Delta t}{2}\right) = v_i(t) + \left(\frac{dv_i}{dt}\right)_t \frac{\Delta t}{2} + \frac{1}{2}\left(\frac{d^2 v_i}{dt^2}\right)_t \left(\frac{\Delta t}{2}\right)^2 + \cdots \tag{2.14}$$

$$v_i\left(t-\frac{\Delta t}{2}\right) = v_i(t) - \left(\frac{dv_i}{dt}\right)_t \frac{\Delta t}{2} + \frac{1}{2}\left(\frac{d^2 v_i}{dt^2}\right)_t \left(\frac{\Delta t}{2}\right)^2 + \cdots \tag{2.15}$$

The velocity update equation in the leapfrog algorithm can be obtained by subtracting and rearranging Equation 2.14 and 2.15:

$$v_i\left(t+\frac{\Delta t}{2}\right) = v_i\left(t-\frac{\Delta t}{2}\right) + \Delta t\, a_i(t) \tag{2.16}$$

In Equation 2.16, the acceleration a_i is calculated from the force. The velocities at $t + \Delta t/2$ are employed to calculate the positions at $t + \Delta t$. By following the same procedure for the Taylor expansion for the positions r(t), the position update expression is:

$$r_i(t+\Delta t) = r_i(t) + v_i\left(t+\frac{\Delta t}{2}\right)\Delta t + \cdots \tag{2.17}$$

The leapfrog algorithm is based on the Equations 2.16 and 2.17. In summary, the velocities of the particles are first computed at time $t + \Delta t/2$. These velocities are employed to calculate the positions of the particles at time $t + \Delta t$ and so on (HINCHLIFFE, 2003). By following this iterative procedure, Equations 2.16 and 2.17 are solved step by step up to the total simulation time, thereby providing a trajectory, *i.e.* a set of atomic coordinates and velocities as function of time, in the phase space of the molecular system.

In order to calculate the macroscopic properties from a molecular system, the MD simulations also consider a key ingredient in the statistical thermodynamics – the so-called ensembles that will be discussed in the next subsection.

2.1.3 Ensembles

The calculation of experimental properties of macroscopic systems from a molecular approach goes back to a major impasse in thermodynamics in the middle of the 20th century, which gave rise to the statistical thermodynamics: how to treat real systems since they are formed by a number of particles in the order of 10^{23}? (HILL, 1987) For instance, if we consider that a thermodynamic property X is determined by the dynamical states of the molecular system, it is possible to write the relation X = X(r,p), where r and p are the coordinates and momenta of the particles referring to this system. The experimental measurement of this property X, beginning at $t = t_0$, to give the observable X (X_{obs}), actually involves an observation of X(r,p) over a period of time τ. Thus, the value of X_{obs} is given by the following equation:

$$X_{obs} = \frac{1}{\tau}\int_{t_0}^{\tau+t_0} X(r,p)dt \tag{2.18}$$

The Equation 2.18 shows that the X_{obs} is a time average that is solved by computing the dynamical states of the system formed by about 10^{23} particles. However, this approach is mechanically impractical, since the complexity of this problem involves the resolution of about 10^{23} equations (HILL, T. L.; 1987). The works of the physicists Ludwig Boltzmann, James Clerk Maxwell, and Josiah Willard Gibbs, solved this problem by averaging over dynamics states. The physicist Gibbs introduced the idea of ensemble in the so-called Ensemble Method of Gibbs that established the relation between the desired time average of a mechanical variable (*e.g.* pressure, energy, volume, number of molecules, etc.) with the ensemble average of the same property. The validity of this idea that connects theory and experiments is confirmed by experimental evidences (HILL, T. L.; 1987).

Specifically, the ensemble is a mental collection of a very large number η of systems, which are replicas of the thermodynamic levels of the actual thermodynamic system being analyzed. From the thermodynamic point of view, these replicas are identical, but this is not true in a molecular level, due to the fact that each replica is also compartmentalized in a series

of quantum states. For example, in the pressure calculation of a system, the instantaneous pressure is different for each quantum states. The ensemble average of the pressure is computed over these instantaneous values, considering the same weight to each replica in the ensemble (HILL, T. L.; 1987).

The ensemble method of Gibbs is based on two fundamental postulates (HILL, T. L.; 1987):

First postulate: The time average (for a long time) of a mechanical variable M in the thermodynamic system of interest is equal to the ensemble average of M in the limit $\eta \rightarrow \infty$*, provided that the systems of the ensemble replicate the thermodynamic state and environment of the actual system.*

Second postulate: In an ensemble ($\eta \rightarrow \infty$*) representative of an isolated thermodynamic systems, the replicas (systems) in the ensemble are distributed uniformly, i.e., with equal probability or frequency over the possible quantum states with specified values of N (number of particles), V (volume), and E (energy).*

In summary, these postulates propose that the time average referring to a property of the macroscopic system given by Equation 2.18 can be replaced by an instantaneous average over a large number of theoretical replicas of the system, which compose the ensemble. In order to calculate a X_{obs} of a macroscopic system from a molecular system using the ensemble method, Gibbs proposed the calculation of the ensemble average ($\langle X \rangle$)with the inclusion of a distribution function $f(r,p)$ according to the equation (HILL, 1987):

$$X_{obs} = \overline{X_\tau} = \int f(r,p)X(r,p)drdp \ = \langle X \rangle \tag{2.19}$$

Where $\langle X \rangle$ is the ensemble average of a variable X, $\overline{X_\tau}$ is the time average connected to X_{obs} (in contrast to the Equation 2.18) for a microscopically long time τ, and dS is the surface element of an arbitrary volume in phase space (TUCKERMAN, 2010). In addition to be independent of time, the distribution function $f(r,p)$, which has different forms depending of the conditions of the thermodynamics system, is a constant of the motion. Therefore, by using the ensemble method with $\eta \rightarrow \infty$, it is possible to simulate the real system in equilibrium state (HILL, T. L.; 1987).

In the context of MD simulations, a thermodynamic property Y is computed from averages over the M configurations that compose the trajectories. The following equation indicates these averages (MARTÍNEZ, *et al*., 2007):

$$\bar{Y} = \frac{1}{M}\sum_{t=1}^{M} Y_t(r^N, p^N) \tag{2.20}$$

where r, p, and N correspond to the coordinates, the linear momenta, and the number of particles.

Since there are different ways to express the state of a thermodynamic system, depending on the thermodynamic variables, there are different types of ensembles with specific distribution functions f(r,p) (HILL, T. L.; 1987). The main ensembles and the ones used in the MD simulations carried out in this work will be briefly described here:

Canonical ensemble (NVT)

In this ensemble, the system has a fixed volume V, fixed number N of particles, and fixed temperature T by means of its immersion in a very large heat bath. The very large heat bath is in line with the number of replicas $\eta \rightarrow \infty$ as suggested by the first postulate. Therefore, the representative ensemble of the experimental system can be imagined as η macroscopic systems (replicas), each one with fixed N and V organized in a lattice (see Figure 2.1).

Figure 2.1 – Scheme of a canonical ensemble (NVT) of η systems, each one with N and V.

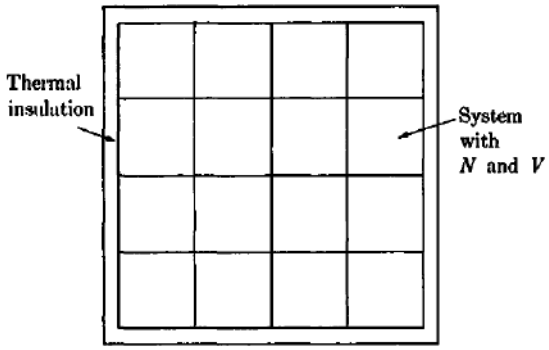

Source: HILL (1987).

In Figure 2.1, the walls between the different systems (replicas) in the ensemble are heat conducting and impermeable to all molecules. As it was previously mentioned, all these systems are immersed in a heat bath at temperature T. After reaching the equilibrium, the thermal insulation is placed on the borders of the ensemble, thereby forming an isolated system with volume ηV, number of molecules ηN, and a total energy E_T. In this new system called supersystem, all possible quantum states are equally probable. If we define n_j as the distribution of systems in the ensemble found in state E_j, all distributions n_j must satisfy the following relations (HILL; 1987):

$$\sum_j n_j = \eta \tag{2.21}$$

$$\sum_j n_j E_j = E_j \tag{2.22}$$

The number of states of the supersystem $\Omega_t(n)$, which is consistent with a distribution n_1, n_2 ,…, is given by:

$$\Omega_t(n) = \frac{(n_1 + n_2 + \cdots)!}{n_1!\, n_2! \ldots} = \frac{\eta!}{\prod_j n_j!} \tag{2.23}$$

The probability P of a state E_j is given by the Boltzmann distribution:

$$P_j = \frac{n_j}{\eta} = \frac{e^{-\beta E_j(N,V)}}{\sum_i e^{-\beta E_j(N,V)}} \tag{2.24}$$

Equation 2.24 is also called canonical distribution and the denominator is the canonical partition function Z(N,V,T), where $\beta = 1/k_B T$. The thermodynamic properties of a system modeled by the canonical ensemble can be derived from Equation 2.24 (HILL; 1987).

Microcanonical Ensemble (NVE)

In this ensemble, the system has a fixed number N of particles, fixed volume V, and fixed energy E. The microcanonical ensemble is a degenerated canonical ensemble where all

systems have the same energy and all states have the same probability (BRAGA, 2021). In this ensemble, entropy S is the central thermodynamic property for the variables N, V and E:

$$S(N,V,E) = k_B ln\Omega(\mathrm{N,V,E}) \tag{2.25}$$

The Equation 2.25 is the basic equation of the microcanonical distribution. In this ensemble, there are fluctuations between kinetic and potential energies, but the total energy is constant (MARTÍNEZ, *et al*., 2007).

Isothermal-isobaric ensemble (NPT)

In this ensemble, the system has a fixed number N of particles, fixed pressure P, and fixed temperature T. The isothermal-isobaric distribution is Δ = Δ(N, P, T) and the isothermal-isobaric partition function Δ(N, P, T) is (HILL, T. L.; 1987):

$$\Delta(N,P,T) = \frac{k_B T}{PV}\left(\frac{k_B T}{P\Lambda^3}\right)^N, \qquad \Lambda = \frac{h}{(2\pi m k_B T)^{1/2}} \tag{2.26}$$

In Equation 2.26, N is the number of particles and h is the Planck's constant. This is a widely used ensemble in simulations, since it considers the conventional conditions of most experiments in the laboratory, which are conducted under constant temperature and pressure (MARTÍNEZ, *et al*., 2007).

2.1.4 Stages of a conventional MD simulation

The conventional MD simulations, including the ones conducted in this work, involves computational stages such as energy minimization, heating, equilibration, and production, to prepare and simulate molecular systems at the conditions of interest. In the present work, the simulations were carried out at the conditions of the physiological medium (temperature T of 310 K and pressure P of 1 atm). The details of these stages will be discussed below:

Energy minimization

The first stage of a MD simulations involves the energy minimization of the system, which provides the molecular relaxation of the newly built system by correcting the unstable contacts/interactions and distortions in bonds and bond angles (NAMBA, *et al*., 2008). This procedure is conducted via optimization algorithms of functions, such as the Steepest Descent (SD) and the Conjugated Gradient (CG) methods (CASE, *et al*., 2019).

In the SD algorithm, a series evaluations of a function $f(x)$ are performed in the negative gradient direction. Specifically, the first derivative of the potential energy V with respect to the coordinates is employed to search the minimum in this function, which represent the optimized structure of the system. The general idea is to calculate a step along a given search direction d_k (MEZA, 2010):

$$x_{k+1} = x_K + \alpha_k d_k \ , k = 0, 1, \ldots \tag{2.27}$$

where α_k is the step length:

$$\alpha_k = \arg\min f(x_k + \alpha d_k) \tag{2.28}$$

where arg min stands for the argument of the minimum of a function. In the SD method, the search direction is the negative gradient $d_k = -\nabla f(x_K)$. In each step of the algorithm the difference between $f(x_k)$ and $f(x_{k-1})$ is evaluated and compared to a convergence tolerance value. In the MD simulations, the function $f(x)$ is the potential energy function (Equation 2.10). However, the SD method presents some problems, such as oscillations around the minimum path, especially for long narrow valleys. In addition to the reduction of the rate of convergence as the minimum is approached, this method can also find local minima (JENSEN, 2007).

When it comes to the CG method, the algorithm is more refined and efficient that the SD, since it is applied not along the current gradient, but along a line of gradients that is constructed, thereby conjugating the current search direction with the previous ones. The first step of this method is a SD step, but the next step (the subsequent searches) is performed along a line formed by the mixture involving the current negative gradient and the previous search direction according to the equation:

$$d_i = -g_i + \beta_i d_{i-1} \tag{2.29}$$

The term β_i has different forms associated to different methods of gradient combination. Although the convergence of the CG method is superior to the SD method, it also has a tendency to find local minima (JENSEN, 2007).

Heating and equilibration

After the energy minimization of the system, the next stage is the so-called heating stage, in which the temperature T of the system is increased up to the value of interest (310 K in this work). This temperature control requires the use of algorithms called thermostats. In the most basic thermostat, the velocities of all particles are rescaled in each step of the simulation aiming to adjust the kinetic energy of the system with the temperature of interest (NAMBA, *et al*., 2008). Specifically, the velocities are multiplied by a coefficient α:

$$\alpha = \sqrt{\frac{T^{ref}}{T(t)}} \tag{2.30}$$

This coefficient is applied at each simulation step, so that the instantaneous temperature T(t), which is obtained from Equation 2.12, progressively converges to the reference temperature T^{ref} (MARTÍNEZ, *et al*., 2007). There are other sophisticated thermostats used in MD softwares such as the Berendsen thermostat, Andersen thermostat, Nosè-Hoover thermostat, and Langevin thermostat (KE, *et al*., 2022). In the present work, the Langevin thermostat was employed to regulate the temperature of the systems. This stochastic thermostat, which is initiated by a random number seed, modifies the momenta p in the equation of motion at each time step Δt :

$$\Delta p_i = \left(\frac{\partial V(r)}{\partial r_i} - \gamma p_i + \delta p\right)\Delta t \tag{2.31}$$

where r is the coordinates, V is the potential energy function, γp_i is a term that damps the momenta due to a solvent drag force, and δp is a Gaussian distributed random number with probability:

$$\rho(\delta p) = \frac{1}{\sqrt{2\pi\sigma}} exp\left(-\frac{|\delta p|^2}{2\sigma^2}\right) \tag{2.32}$$

In Equation 2.32, the standard deviation is given by $\sigma^2 = 2\gamma m_i k_B T$. This random force represents the thermal kicks from the small particles. By using the Langevin thermostat, it is possible to represent the influence of the solvent on the dynamics of the solute via not only random collisions, but also by imposing a frictional drag force on the motion of the solute immersed in the solvent. The parameter γ, also know as collision frequency or friction, defines the heat bath coupling strength. In summary, the random force in a Langevin dynamics depends on the random seed, the probability distribution based on the temperature, and the γ. The heating stage was conducted with the NVT ensemble (SINDHIKARA, *et al*., 2009).

The next stage is the system equilibration that is normally conducted with the NPT ensemble. This is an important stage to stabilize the temperature, pressure, and density. While the temperature is controlled by thermostats, the pressure is regulated by barostats. Actually, the pressure P is indirectly controlled with the regulation referring to the volume V of the system, which is based on scaling the dimensions of the simulation box by a factor β:

$$\beta = \sqrt[3]{\frac{P(t)}{P^{ref}}} \tag{2.33}$$

This factor β is applied at each simulation step, so that the instantaneous pressure P(t), which is computed in a simulation using Equation 2.34, progressively converges to the reference pressure P^{ref} (1 bar) (MARTÍNEZ, *et al*., 2007).

$$P(t) = \frac{Nk_B T}{V} - \frac{1}{3V}\sum_{i=1}^{N}\sum_{j>1}^{N} r_{ij}(t).F_{ij}(t) \tag{2.34}$$

Where $r_{ij}(t) = r_j(t) - r_i(t)$ is the position vector that connects the particles i and j, and $F_{ij}(t)$ is the intermolecular force between this pair of particles at the instant of time t. Therefore, by variating the volume of the simulation box, the distances are modified as well as the intermolecular forces, which consequently provide the pressure regulation (MARTÍNEZ, *et al*., 2007).

In this work, the Berendsen barostat was employed to maintain constant the pressure of the simulated systems with an average value of 1 bar (BERENDSEN, *et al*., 1984). In this algorithm, the system is coupled to a pressure bath in the same principle employed to the Langevin thermostat with a heat bath. Specifically, the barostat modifies the equations of motion with the inclusion of an extra term that effects the pressure change:

$$\left(\frac{dP}{dt}\right)_{bath} = \frac{P_o - P(t)}{\tau_P} \tag{2.35}$$

where P_o is the reference pressure, and P(t) is given by Equation 2.34 through scaling of interparticle distances. The pressure scaling factor μ applied in each time step is:

$$\mu(t) = \left[1 + \frac{\Delta t}{\tau_P}\beta(P_o - P(t))\right]^{1/3} \tag{2.36}$$

In Equation 2.36, β is the isothermal compressibility and τ_P is the time constant of the coupling. In summary, this barostat provides a scaling of coordinates and box length per time step. It worth mentioning that the pressure scaling factor shown in Equation 2.36 is applied to MD simulations with isotropic systems (BERENDSEN, *et al*., 1984).

Regarding the equilibration of membranes, the simulations were conducted with the NPγT, where the surface tension γ was maintained constant (value of 0 dyne/cm) by using the Berendsen barostat with a semiisotropic pressure scaling due to the non-isotropic nature of interfaces, including lipid bilayers (CASE, *et al*., 2020). The use of barostats for controlling the surface tension is connected to the fact that this property is a function of the pressure tensor. In this semiisotropic scaling, while the volume of the simulation box remains constant in x and y directions, which define the plane of the membrane, the pressure is applied along the z-axis which a free variation of the volume. The average γ is calculated according to the following equation:

$$\gamma(t) = \frac{1}{n}\int_0^{L_z}\left[P_{zz}(z,t) - \frac{P_{xx}(z,t) + P_{yy}(z,t)}{2}\right]dz \tag{2.36}$$

where L_z, n, and (P_{xx}, P_{yy} and P_{zz}) are the box length, number of faces, and the pressure tensor components with respect to the time t (BATTELL, *et al*., 2022). While P_{xx} and P_{yy} represent the tangential pressure, the P_{zz} is the normal pressure.

Production dynamics

After equilibrating the system at 310 K and 1 bar, the last stage of the simulation is the production dynamics which is a long simulation with the NPT ensemble aiming to generates the trajectories that will be indeed analyzed and employed to calculate the properties of interest according to Equation 2.20. The time scale can involve hundreds of nanoseconds to microseconds or more. In addition to the analysis of interaction mechanisms and conformational dynamics, these trajectories can be used to study, for instance, the solvation structure, formation of interactions, structural and thermodynamic stability.

Therefore, the complete algorithm of the MD simulations conducted in the present work is organized in the following steps:

a) determine initial configuration of the system (coordinates);
b) conduct the energy minimization step of the system using the SD and CG methods;
c) define the initial velocities and calculate forces, acceleration, potential and kinetic energies;
d) write the positions, velocities, and the temperature of the system in the trajectory;
e) move the atoms of the system and repeat the calculation of the forces, accelerations, velocities, potential and kinetic energies using the Langevin thermostat with the NVT ensemble;
f) repeat the steps d and e for a specific number N of simulation steps up to the temperature of interest (310 K). This stage generates the heating trajectory;
g) from the last frame of the heating trajectory, repeat steps d and e using the Berendsen barostat with the NPT ensemble for a specific number N of simulation steps up to the pressure of interest (1 bar). This stage produces an equilibrium trajectory;
h) conduct the production run with the NPT ensemble (with the equilibrated values of both temperature and pressure) over N steps up to the simulation time repeating steps d and

e. This stage generates the production trajectory of the system at both pressure and temperature of interest;

2.2 BINDING FREE ENERGY CALCULATION – MM/GBSA

The binding free energy ($\Delta_b G$) is a property that indicates the interaction affinity between two species (A and B), such as the binding strength in a noncovalently bound receptor-ligand complex. The end-point free energy methods are examples of widely used approaches to compute $\Delta_b G$ due to their good balance between computational efficiency and accuracy. As suggested by the name, these methods involve sampling of the final states of the system, which substantially reduces the computational cost (WANG, *et al*., 2019).

In the present work, one of the well-known end-point methods, the molecular mechanics generalized Born surface area (MM/GBSA), was used to calculate the $\Delta_b G$ referring to the inclusion complexes formed by cddp (ligand) and CNHs (receptor) (MILLER, *et al*, 2012). The central idea of this method involves the energetic analysis of the formation process of a complex (RL) from the association of a ligand (L) to a receptor (R) in aqueous solution:

$$L_{(aq)} + R_{(aq)} \rightarrow RL_{(aq)}$$

The $\Delta_b G$ of this process can be expressed by the following equation:

$$\Delta_b G = G_{RL} - G_R - G_L \tag{2.37}$$

Each term in the right side of Equation 2.37 can be decomposed into different contributions in line with the thermodynamic definition of the free energy:

$$\Delta_b G = \Delta H - T\Delta S = \Delta E_{MM} + \Delta G_{sol} - T\Delta S \tag{2.38}$$

where ΔH, $T\Delta S$, ΔE_{MM}, and ΔG_{sol} are the changes in the enthalpy, conformational entropy upon binding, gas-phase molecular mechanics (MM) energy, and solvation free energy, respectively. The contribution ΔE_{MM} correspond to the MM energies in gas phase (electrostatic and van der Waals contributions) from the force field (Equation 2.10):

$$\Delta E_{MM} = \Delta E_{elec} + \Delta E_{vdW} \tag{2.39}$$

In the MM/GBSA method, the term ΔG_{sol} is also composed by the electrostatic solvation energy (ΔG_{GB}) or polar contribution and the nonpolar contribution (ΔG_{SA}):

$$\Delta G_{sol} = \Delta G_{GB} + \Delta G_{SA} \tag{2.40}$$

The polar contribution (ΔG_{GB}) is calculated with the Generalized Born (GB) model, in which the atoms are represented by charged spheres with a lower internal dielectric constant than that of the environment. The canonical GB equation with the absence of salt is:

$$\Delta G_{sol} = -\left(\frac{1}{\varepsilon_{in}} - \frac{1}{\varepsilon_{sol}}\right)\sum_{i,j}\frac{q_i q_j}{f_{GB}} \tag{2.41}$$

where q_i and q_j are the partial charges of the atoms i and j, ε_{in} is the dielectric constant of the solute ($\varepsilon_{in} = 1$), ε_{sol} is the dielectric constant of the solvent ($\varepsilon_{sol} = 80$ for water at 300 K), and f_{GB} is a smooth function that includes the nature of the atoms in the GB model:

$$f_{GB} = \sqrt{r_{ij}^2 + \alpha_{ij}^2\, exp\left(\frac{r_{ij}^2}{4\alpha_{ij}^2}\right)} \tag{2.42}$$

In the equation 2.42, r_{ij} is the distance between atoms i and j, α_{ij} is the geometric average of the efficient Born radii α_i and α_j (WANG, *et al*., 2019).

The nonpolar contribution (ΔG_{SA}) to the solvation free energy (ΔG_{sol}) (Equation 2.40) is expressed as:

$$\Delta G_{SA} = \gamma . SASA + b \tag{2.43}$$

Where γ is the surface tension constant, SASA is the solvent accessible surface area of the solute, and b is a correction constant (γ = 0.00542 kcal mol^{-1} Å^{-2} and b = 0.92 kcal mol^{-1} in the AMBER package). This contribution represents the effect of the solute cavity formation within the solvent and the van der Waals interactions solute-solvent around the cavity (WANG, *et al*., 2019).

At last, the entropic contribution ($T\Delta S$) to the $\Delta_b G$ (see Equation 2.38) is decomposed into the different molecular degrees of freedom (translational, rotational, and vibrational degrees):

$$\Delta S = \Delta S_{trans} + \Delta S_{rot} + \Delta S_{vib} \tag{2.44}$$

Since entropy calculation in the MM/GBSA method assumes that the biological systems obey rigid rotor model, the translational and rotational entropies (ΔS_{trans} and ΔS_{rot}) are computed using statistical thermodynamics formulas (MILLER, *et al*, 2012). In the canonical ensemble (NVT), the entropy is calculated from the canonical partition function Z = Z(N,V,T) using the following equation (BRAGA, 2021):

$$S = k_B T \left(\frac{\partial ln\, Z}{\partial T}\right)_{V,N} + k_B ln\, Z \tag{2.45}$$

The translational and rotational components of the entropy (Equation 2.44) are computed with the equations:

$$S_{trans} = N k_B \ln \left(\frac{(2\pi m k_B T)^{3/2}}{h^3} \frac{e^{5/2} V}{N}\right) \tag{2.46}$$

$$S_{rot} = N k_B \ln \left[\frac{\pi^{1/2} e^{3/2}}{\sigma} \left(\frac{8\pi^2 I_A k_B T}{h^2}\right)^{1/2} \left(\frac{8\pi^2 I_B k_B T}{h^2}\right)^{1/2} \left(\frac{8\pi^2 I_C k_B T}{h^2}\right)^{1/2}\right] \tag{2.47}$$

where σ and (I_A, I_B, and I_C) are the symmetry number and the three components of the moment of inertia, respectively. The calculation of the vibrational entropy contribution (ΔS_{vib}) in Equation 2.44 depends on the values of the vibrational frequencies ν_i of the system. In the AMBER software, this calculation can be conducted with the normal modes analysis method and with the quasi-harmonic approximation (MILLER, *et al*, 2012). The vibrational frequencies data can be finally used to calculate the ΔS_{vib} using the equation:

$$S_{vib} = N k_B \ln \sum_{i=1}^{3N-6} \left[\frac{h\nu_i}{k_B T} \frac{1}{e^{\frac{h\nu_i}{k_B T}} - 1} - \ln\left(1 - e^{\frac{h\nu_i}{k_B T}}\right)\right] \tag{2.48}$$

2.3 FREE ENERGY CALCULATIONS USING ENHANCED SAMPLING METHODS

The MD method described in the subsection 2.1 provides an exploration of the configurational space referring to a molecular system. By using this sampling, it is possible to compute thermodynamics properties, including enthalpy difference (ΔH) and Gibbs (ΔG) and Helmholtz (ΔA) free energies differences. In particular, the free energy is a relevant property in biomolecular processes, since it not only drives all molecular processes, such as chemical reactions, molecular associations, protein folding, but also quantifies the spontaneity of these events (WANG, *et al*., 2019). The absolute free energy (G) of molecular processes conducted under isothermal-isobaric conditions (NPT ensemble) is defined as:

$$G = -k_B T \ln Z \tag{2.49}$$

where Z is the isothermal-isobaric partition function of the system expressed as:

$$Z = \frac{1}{V_o N!\, h^{3N}} \int exp\left(-\frac{PV}{k_B T}\right) dV \iint exp\left(-\frac{\mathcal{H}(p,r)}{k_B T}\right) dp\, dr \tag{2.50}$$

In Equation 2.50, V_o is a constant with units of volume, N is the number of particles, h is the Planck's constant, P is the pressure of the system, V is the volume of the system, and $\mathcal{H}$ is the Hamiltonian of the system as function of momenta p and coordinates r (WANG, *et al*., 2019). However, the absolute free energy of large systems with complex interactions cannot be computed using Equation 2.49, since there are not analytical expressions for the partition functions involving these macrosystems. In most cases, the calculation of the free energy difference (ΔG) for an event or the relative free energy of two states is more convenient in practical situations, including computational methods. By using the statistical mechanical definition of G (Equation 2.49), the free energy difference between two states A and B is:

$$\Delta G_{BA} = G_B - G_A = -k_B T \ln \frac{Z_B}{Z_A} = -k_B T \ln \frac{\rho_B}{\rho_A} \tag{2.51}$$

where ρ_B and ρ_A refer to the probabilities of the system is in state B and in state A. In order to calculate the ΔG_{BA}, three basic ingredients need to be defined (CHRIST, *et al*., 2010):

a) a model Hamiltonian;
b) a sampling protocol to generate an ensemble of molecular configurations;
c) a method to estimate the free energy difference.

In the context of MD simulations, the Hamiltonian $\mathcal{H}$ is formed by the force field and the kinetic energy of the particles (Equation 2.6). Additionally, the simulation trajectories can be interpreted as the sampling over different minima on the potential energy landscape referring to the system of interest. Finally, the end-point free energy methods, such as the MM/GBSA (subsection 2.2), are examples of free energy estimators.

However, the sampling protocol for a free energy calculation is not trivial for MD simulations of all biological systems due to their complex potential energy landscapes which can result in the problem of quasi-nonergodicity. To understand this problem, it is necessary to revisit the statistical mechanics' postulates and the calculation of thermodynamic properties from a MD simulation (subsection 2.1.3). Based on the first postulate, a macroscopic property X (an observable) can be derived from a molecular system by means of the ensemble method as indicated in the Equation 2.19 represented below:

$$X_{obs} = \overline{X_\tau} = \int f(r,p)X(r,p)drdp \ = \langle X \rangle$$

The ingredient that provides the connection between time average of a property X ($\overline{X_\tau}$) and ensemble average of this property X ($\langle X \rangle$) is a distribution function $f(r,p)$, which is the probability density $\rho(r,p)$ of configurations of the system given by the following equation in the canonical ensemble (CHRIST, *et al*., 2010):

$$\rho(r,p) = \frac{e^{-\beta\mathcal{H}(p,r)}}{\iint e^{-\beta\mathcal{H}(p,r)}\, dpdr} \tag{2.52}$$

By considering a separable Hamiltonian $\mathcal{H}$ in p (momenta) and r (coordinates), the configurational probability density ($\rho(r)$) is:

$$\rho(r) = \frac{e^{-\beta V(r)}}{\int e^{-\beta V(r)}\, dr} \tag{2.53}$$

where $V(r)$ is a potential energy function. A set of configurations that is organized in line with this probability density is characterized as the Boltzmann distribution. By using this definition of $\rho(r)$, the average ensemble ($\langle X \rangle$) for a property X in Equation 2.19 is defined as (CHRIST, *et al*., 2010):

$$\langle X \rangle = \int X(r)\, \rho(r)\, dr \tag{2.54}$$

A MD is a popular method to generate Boltzmann distributed ensembles of configurations, where the properties are computed as time averages ($\bar{X}$) over all these configurations. The assumption presented in the first postulate of the statistical mechanics that points out that the time average ($\bar{X}$) equals the ensemble average $\langle X \rangle$ is called the ergodic hypothesis (CHRIST, *et al*., 2010):

$$\bar{X} = \langle X \rangle \tag{2.55}$$

The systems that obey the ergodic hypothesis are represented by a microcanonical distribution (ensemble NVE), where all microstates have constant energy E. In a MD simulation, since the equations of motion are propagated with conservation of the Hamiltonian ($\mathcal{H}(x)$), the trajectory generates configurations belonging to the microcanonical ensemble NVE with energy E (TUCKERMAN, 2010). However, the ergodic behavior is not present in most systems, especially in the ones with many degrees of freedom. For instance, if all configurations with significant probability $\rho(r)$ are visited in a simulation, then the ergodic hypothesis is a first approximation. On the other hand, if there are regions of high probability $\rho(r)$ in the configurational space that are separated by high energy barriers, it is unlikely that a MD simulation will sample all important configurations of a system. This behavior is known as the problem of quasi-nonergodicity, where the ergodic hypothesis breaks down locally (CHRIST, *et al*., 2010). This problem is connected to the fact that in a conventional MD simulation, the average kinetic energy per degree of freedom, which is defined by the equipartition principle, is $k_B T/2$ as well as for the average potential energy defined by harmonic potentials (TUCKERMAN, 2010; BRAGA, 2001). Specifically, $k_B T$ in units of energy per mol is:

$$k_B T = k_B T \cdot N_A = \left(1.380\ x\ 10^{-23}\frac{J}{K}\right) \cdot (310.15\ K) \cdot \left(6.022\ x\ 10^{23}\frac{1}{mol}\right) =$$

$$= 2.58\ \frac{kJ}{mol} \cdot \left(\frac{0.24\ kcal}{kJ}\right) = \ 0.62\ kcal/mol$$

where N_A is the Avogadro's number. This small energy sampled in a MD simulation indicates that if a particular state has a high energy barrier to surmount, a very long time will be required to promote barrier-crossing from the energy accumulation through fluctuations in this configurational mode (TUCKERMAN, 2010). This inability to visit important configurations during MD simulations appears in studies involving complex biological systems with slow domain motion such as proteins, membranes, and slow biophysical processes.

In this context, the enhanced sampling methods were developed to overcome the problem of quasi-nonergodicity and, therefore, to sample high probability states separated by high energy regions along the potential energy surface. These enhanced sampling methods are classified in two categories: collective variable based and collective variable free methods. While the collective variable based methods use a predefined reaction coordinates or collective variables, the collective variable free methods involve a modification of the probability distribution aiming to enrich the sampling of the potential energy. Some examples of collective variable based methods include umbrella sampling, adaptive biasing force, and hyperdynamics, whereas examples of collective variable free methods comprise replica exchange molecular dynamics, accelerated molecular dynamics simulations, and enveloping distribution sampling (YANG; *et al*., 2019).

In the present work, the drug release process from CNHs and the transmembrane transport of drugs and CNHs are examples of systems characterized by a quasi-nonergodic behavior. The simulation of these events was treated using the steered molecular dynamics (SMD) simulations coupled to the umbrella sampling (US) method, which provided the calculation of the free energy profiles referring to these processes. This approach will be discussed in the following subsections.

2.3.1 Steered molecular dynamics

The umbrella sampling method is based on a bias potential with the predefinition of a reaction coordinate ξ (collective variable) that connects configurational states of interest referring to a system. The reaction coordinates can also be represented as a low dimensional function $\xi(r)$ of the atomic coordinates r of a molecular system (YANG; *et al*., 2019). In the present work, the reaction coordinate that was defined to the drug release from CNHs was a parallel axis to the

main axis of this carbon nanostructure, where the initial point corresponded to the encapsulated drug at the center of mass of this nanovector and the last point indicated the free drug in the bulk phase. The other reaction coordinate employed in this work was the perpendicular axis to the plane of a cell membrane to simulate the permeation processes of platinum drugs and CNHs through these biological barriers. These reaction coordinates were obtained in this thesis by means of SMD simulations.

A SMD simulation is a method that involves nonequilibrium calculations based on the application of a time-dependent external potential to the potential that drives the system over the reaction coordinate of interest. This time-dependent perturbation along a reaction path ξ has the following form:

$$V_{rest}(t) = \frac{1}{2}K[x - x_0(t)]^2 \tag{2.56}$$

where the time-dependent harmonic potential ($V_{rest}(t)$) is characterized by a force constant K, in which x can be a distance or an angle between atoms or groups of atoms. By using this potential, the system is restrained to a particular center that changes according to a constant velocity during the simulation from ξ_0 (initial point in the reaction coordinate) to ξ_f (final point in the reaction coordinate) (CASE, *et al*., 2020; TUCKERMAN, 2010).

This nonequilibrium method can be used to calculate the free energy difference between two likely states (ΔG_{AB}) according to the Jarzynski equality (JARZYNSKI, 1997). Before presenting this equality, it is important to recapitulate the work-free-energy inequality:

$$W_{AB} \geq \Delta G_{AB} \tag{2.57}$$

If the transformation of a system from state A to B is carried out along a reversible path (reversible work W), the equality holds in this relation (Equation 2.57), thereby indicating an equilibrium condition. On the other hand, if the path to transform state A to state B involves an irreversible process (irreversible W), the system is driven out of the equilibrium. Since W_{AB} is a thermodynamic property, it can also be derived from an ensemble average performed over a particular path x of conversion from state A to state B ($W_{AB}(x)$). Therefore, the work-free-energy inequality (Equation 2.57) can be written as:

$$W_{AB} = \langle W_{AB}(x_0)\rangle_A \geq \Delta G_{AB} \tag{2.58}$$

where $\langle W_{AB}(x_0)\rangle_A$ is the ensemble average involving the initial distribution of microstates x_0 belonging to state A. In 1997, the physicist Christophe Jarzynski demonstrated that irreversible work can be used to calculate the free energy differences by using an average of $exp[-\beta W_{AB}(x_0)]$ over a canonical distribution instead of calculating $\langle W_{AB}(x_0)\rangle_A$. This relation called the Jarzynski equality (TUCKERMAN, 2010):

$$e^{-\beta \Delta G_{AB}} = \langle e^{-\beta \Delta W_{AB}(x_0)}\rangle_A \tag{2.59}$$

$$\Delta G_{AB} = -k_B T\, ln\langle e^{-\beta \Delta W_{AB}(x_0)}\rangle_A \tag{2.60}$$

In summary, the Jarzynski equality is the basis of the nonequilibrium free energy methods, since it provides the extraction of equilibrium information (ΔG) from the ensemble of nonequilibrium measurements (JARZYNSKI, 1997). The use of this equality in MD simulations requires, therefore, the repetition of a series of simulations using different initial conditions to calculate the free energy difference.

In the present work, the SMD simulations were employed to generated a series of configurations of the systems along a reaction coordinate ξ. These snapshots were finally employed in the US method to estimate the free energy profiles referring to the processes of interest.

2.3.2 Umbrella Sampling method

The umbrella sampling (US) method was proposed by the physicists Torrie and Valleau (TORRIE & VALLEAU, 1977) as a sampling enrichment approach of a system, which is based on the application of a biasing potential energy, aiming to calculate its free energy along a reaction coordinate (KÄSTNER, 2011). It is important to emphasize that this method requires prior knowledge of the reaction coordinate ξ of a process, *e.g.* $A \rightarrow B$ (Figure 2.2A), which is not captured by a conventional MD simulation (unbiased simulation), thereby suggesting the existence of high energy barriers ($\Delta V^{\ddagger}$) that prohibit the sampling of this event.

Figure 2.2 – Procedures of the umbrella sampling method: prior knowledge of the reaction coordinate ξ referring to a specific process (A), definition of the simulation windows from the partition of the reaction coordinate ξ (B), application of the bias potential (C), and representation of the biased probability distribution $\rho^b(\xi)$ calculated from a simulation window $\xi_{0,x}$ (D).

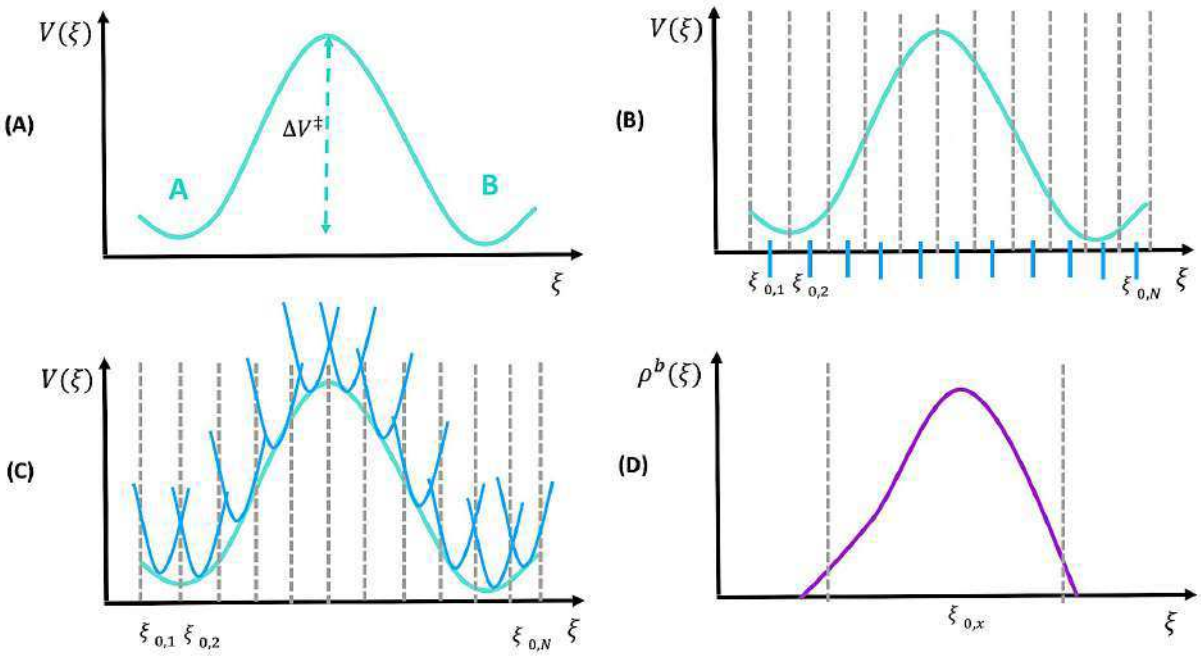

Reference: Own author (2023).

Although the reaction coordinate ξ for the process $A \rightarrow B$ is known, the free energy profile (green line in Figure 2.2A) is unknown and the idea of the US method is exactly to calculate this curve. The first step in this method is to generate several configurations of the system along this path ξ which are called simulation windows. The initial configurations of these windows can be obtained from SMD simulations as described in the last subsection. Thus, each window i is simulated with the application of an artificial potential $\omega_i(\xi)$, which is included in the potential energy of the system forming the biased potential V^b (KÄSTNER, 2011):

$$V^b = V^u + \omega_i(\xi) \tag{2.61}$$

Equation 2.61 shows that the biased potential V^b is formed by the sum of the unbiased potential V^u with the artificial potential $\omega_i(\xi)$, which normally involves a harmonic potential as indicated in Equation 2.62 and Figure 2.2C:

$$V^b = V^u + K_i(\xi_i - \xi_i^{ref})^2 \quad (2.62)$$

where K_i is a force constant that represents the strength of the harmonic bias and ξ_i^{ref} is the the reference point of the respective window i along the reaction coordinate. In these biased simulations, the term V^b is used in the equations of motion (Equation 2.5).

The biased simulations of these N windows generate N ensembles of configurations referring to the system (process $A \rightarrow B$) that sample all the regions along the reaction coordinate ξ. Data from each simulation window can be used to compute the biased probability distributions ($\rho^b(\xi)$) referring to each window as shown in Figure 2.2D for a generic window x. The representation of all $\rho^b(\xi)$ over the reaction coordinate is presented in Figure 2.3. These probability distribution histograms indicate the count of the number of visited states per window along ξ.

Figure 2.3 – Representation of the biased probability distributions ($\rho^b(\xi)$) referring to each simulation window using the umbrella sampling method with a reaction coordinate ξ.

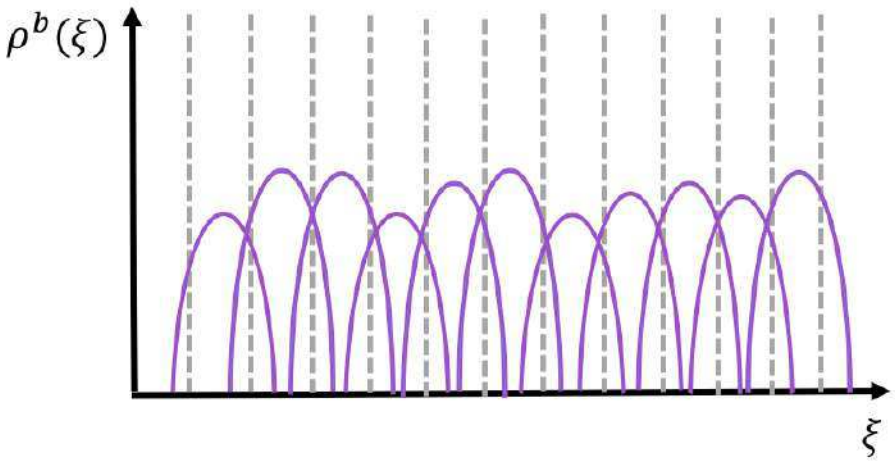

Reference: Own author (2023).

Once it is known the probability distribution $\rho^b(\xi)$, it is possible to calculate the unbiased free energy along the ξ in equilibrium conditions ($G^u(\xi)$), also called potential of mean force (PMF):

$$PMF = G^u(\xi) = f(\rho^b(\xi)) \quad (2.63)$$

In Equation 2.63, the form the function $f(\rho^b(\xi))$ is related to the thermodynamic definition of free energy as indicated in Equation 2.51. In the canonical ensemble (NVT), the Helmholtz free energy (A) can be calculated from the probability distribution ρ (KÄSTNER, 2011):

$$A^u(\xi) = -k_B T ln \rho^u(\xi) = -\frac{1}{\beta} ln\, \rho^u(\xi) \tag{2.64}$$

When it comes to the isothermal-isobaric ensemble (NPT), the Gibbs free energy can be also computed from the probability distribution ρ:

$$G^u(\xi) = -\frac{1}{\beta} ln\, \rho^u(\xi) \tag{2.65}$$

The probability distribution ρ of the system along the reaction coordinate ξ can be computed by integrating out all degrees of freedom but ξ (KÄSTNER, 2011):

$$\rho^u(\xi) = \frac{\int \delta[\xi(q) - \xi] e^{-\beta V^u(q)} dq}{\int e^{-\beta V^u(q)} dq} \tag{2.66}$$

where the term $[\xi(q) - \xi]$ is used to compute $\rho^u(\xi)$ for a given reaction coordinate value $\xi(q)$ with the following behavior:

$\delta[\xi(q) - \xi] = 1$, when $\xi(q) = \xi$,
$\delta[\xi(q) - \xi] = 0$, when $\xi(q) \neq \xi$,

Therefore, in order to calculate $G^u(\xi)$ (PMF) (Equation 2.65), we need to calculate $\rho^u(\xi)$, but the US simulations of the N windows generate $\rho^b(\xi)$. Thus, it is necessary to obtain a relation between these two probability distributions ($\rho^b(\xi)$ and $\rho^u(\xi)$). In fact, $\rho^b(\xi)$ can be calculated in the same idea as shown in Equation 2.66 for the $\rho^u(\xi)$ with the addition of the artificial potential $\omega\big(\xi(q)\big)$ (Equation 2.62) (KÄSTNER, 2011):

$$\rho^b(\xi) = \frac{\int \delta[\xi(q) - \xi] e^{-\beta[V^u(q) + \omega(\xi(q))]} dq}{\int e^{-\beta[V^u(q) + \omega(\xi(q))]} dq} \tag{2.67}$$

Since the artificial potential depends only on ξ:

$$\rho^b(\xi) = \frac{\int \delta[\xi(q) - \xi] e^{-\beta V^u(q)} e^{-\beta\omega(\xi(q))} dq}{\int e^{-\beta[V^u(q)+\omega(\xi(q))]} dq} \tag{2.68}$$

$$\rho^b(\xi) = e^{-\beta\omega(\xi)} \frac{\int \delta[\xi(q) - \xi] e^{-\beta V^u(q)} dq}{\int e^{-\beta[V^u(q)+\omega(\xi(q))]} dq} \tag{2.69}$$

By using Equations 2.66 and 2.69, we can evaluate the relation $\rho^u(\xi)/\rho^b(\xi)$:

$$\frac{\rho^u(\xi)}{\rho^b(\xi)} = \frac{\int \delta[\xi(q) - \xi] e^{-\beta V^u(q)} dq}{\int e^{-\beta V^u(q)} dq} \frac{\int e^{-\beta[V^u(q)+\omega(\xi(q))]} dq}{e^{-\beta\omega(\xi)} \int \delta[\xi(q) - \xi] e^{-\beta V^u(q)} dq} \tag{2.70}$$

$$\frac{\rho^u(\xi)}{\rho^b(\xi)} = e^{\beta\omega(\xi)} \frac{\int e^{-\beta[V^u(q)+\omega(\xi(q))]} dq}{\int e^{-\beta V^u(q)} dq} \tag{2.71}$$

$$\rho^u(\xi) = \rho^b(\xi) e^{\beta\omega(\xi)} \frac{\int \boldsymbol{e^{-\beta\omega(\xi(q))} e^{-\beta V^u(q)} dq}}{\int \boldsymbol{e^{-\beta V^u(q)} dq}} \tag{2.72}$$

In Equation 2.72, the term in bold corresponds the ensemble average of $e^{-\beta\omega(\xi(q))}$ as shown in Equation 2.54. Thus:

$$\rho^u(\xi) = \rho^b(\xi) e^{\beta\omega(\xi)} \langle \boldsymbol{e^{-\beta\omega(\xi(q))}} \rangle \tag{2.73}$$

By using Equation 2.73 in the definition of the $G^u(\xi)$ (Equation 2.65):

$$G^u(\xi) = -\frac{1}{\beta} ln\, \rho^u(\xi) = -\frac{1}{\beta} \ln [\rho^b(\xi) e^{\beta\omega(\xi)} \langle e^{-\beta\omega(\xi(q))} \rangle] \tag{2.74}$$

$$G^u(\xi) = -\frac{1}{\beta} \ln \rho^b(\xi) - \frac{1}{\beta} \ln e^{\beta\omega(\xi)} - \frac{1}{\beta} \ln \langle e^{-\beta\omega(\xi(q))} \rangle \tag{2.75}$$

$$G^u(\xi) = -\frac{1}{\beta} \ln \rho^b(\xi) - \omega(\xi) - \frac{1}{\beta} \ln \langle e^{-\beta\omega(\xi(q))} \rangle \tag{2.76}$$

In Equation 2.76, $\rho^b(\xi)$ is collected from the US simulations (simulations of the N windows), $\omega(\xi)$ has an analytical form (Equation 2.62), and the last term will be defined as F:

$$G^u(\xi) = -\frac{1}{\beta}\ln \rho^b(\xi) - \omega(\xi) + F \tag{2.77}$$

The Equation 2.77 demonstrates that it is possible to calculate the free energy as function of the reaction coordinate (PMF) referring to unbiased processes using data from biased simulations by means of the US method. This equation is applied for the N windows, which provides the calculation of $G_i^u(\xi)$ for each window i. Thus (KÄSTNER, 2011):

$$G_i^u(\xi) = -\frac{1}{\beta}\ln \rho_i^b(\xi) - \omega_i(\xi) + F_i \tag{2.78}$$

The global $G^u(\xi)$, which is the free energy profile or PMF, involves the combination of each $G_i^u(\xi)$ and, consequently, the calculation of the terms F_i. One of the most popular methods to combine data from multiple US simulations and calculate the term F_i in order to finally obtain the PMF is the Weighted Histogram Analysis method (WHAM) (CHRIST, *et al.*, 2010; KUMAR, *et al*., 1992; KUMAR, *et al*., 1995; ROUX, 1995).

The WHAM method is an extension of the US method that provides the optimal estimative of the PMF with minimal statistical errors linking probability distribution histograms of a series of US simulations (KUMAR, *et al*., 1992). In Equation 2.78, the term F_i can be expressed as:

$$F_i = -\frac{1}{\beta}\ln\langle e^{-\beta\omega(\xi)}\rangle \tag{2.79}$$

$$-\beta F_i = \ln\langle e^{-\beta\omega(\xi)}\rangle \tag{2.80}$$

$$e^{-\beta F_i} = \langle \boldsymbol{e^{-\beta\omega(\xi)}}\rangle \tag{2.81}$$

where the highlighted term represents the definition of ensemble average (Equation 2.54):

$$e^{-\beta F_i} = \langle e^{-\beta\omega_i(\xi)}\rangle = \int \rho^u(\xi)\, e^{-\beta\omega_i(\xi)} d\xi \tag{2.82}$$

In the WHAM method, the idea is to calculate the global distribution $\rho^u(\xi)$ from a weighted average of the probability distributions of each window i (KÄSTNER, 2011):

$$\rho^u(\xi) = \sum_i^{N_w} p_i(\xi)\, \rho_i^u(\xi) \tag{2.83}$$

where N_w is the number of windows, $\rho_i^u(\xi)$ is the unbiased probability distribution of each window i, and $p_i(\xi)$ is the statistical weight for each window. The values of this weight $p_i(\xi)$ are calculated by minimizing the statistical error of $\rho_i^u(\xi)$:

$$\frac{\partial \sigma^2(\rho^u(\xi))}{\partial p_i(\xi)} = 0 \tag{2.84}$$

under the condition $\sum_i^{N_w} p_i(\xi) = 1$. The expression of $p_i(\xi)$ is:

$$p_i(\xi) = \frac{a_i(\xi)}{\sum_j^{N_w} a_j} \quad , \qquad a_i(\xi) = N_i e^{-\beta\omega_i(\xi)+\beta F_i} = N_i \frac{\rho_i^b}{\rho_i^u} \tag{2.85}$$

where N_i is the total number of steps sampled in window i. In summary, to calculate F_i (Equation 2.82), we need to compute the global $\rho^u(\xi)$ (Equation 2.83), which depends on $p_i(\xi)$ and $a_i(\xi)$ (Equation 2.85). However, this last term $a_i(\xi)$ also has a dependency on F_i, which is the factor that we intend to calculate. In the WHAM method, these equations are solved iteratively until convergence, thereby yielding F_i and, finally, the PMF ($G^u(\xi)$ in Equation 2.77) (KÄSTNER, 2011). To summarize, by using the WHAM method, it is possible not only to estimate the statistical uncertainty of the unbiased probability distribution from biased distributions, but also to compute the PMF with the smallest uncertainty (HUB, *et al*., 2010).

REFERENCES

BATTEL, W.; *et al*. Remediation of pharmaceuticals from wastewater via computationally selected molecularly imprinted polymers. **Molecular Systems Design & Engineering**, v. 7, p. 196-204, 2022.

BEEMAN, D. Some multistep methods for use in molecular dynamics calculations. **Journal od Computational Physics**, v. 20, n. 2, p. 130-139, 1976.

BERENDSEN, H. J. C.; *et al*. Molecular dynamics with coupling to an external bath. **The Journal Chemical Physics**, v. 81, p. 3684-3690, 1984.

BERMAN, H. M.; *et al*. The protein data bank. **Nucleic Acids Research**, v. 28, n. 1, p. 235-242, 2000.

BRAGA, J. P. O colapso da equipartição da energia. **Química Nova**, v. 24, n. 5, p. 693-699, 2001.

BRAGA, J. P. **Fundamentos de Química Quântica**. Ed. UFV, 2007.

BRAGA, J. P. **Termodinâmica Estatística de Átomos e Moléculas**. Livraria da Física, 2ed, 2021.

CASE, D. A.; *et al*. **AMBER 2016**, University of California, San Francisco, 2016.

CASE, D. A.; *et al.* **AMBER 2020**, University of California, San Francisco, 2020.

CHRIST, C. D.; *et al*. Basic Ingredients of Free Energy Calculations: A review. **Journal of Computational Chemistry**, v. 31, n. 8, 2010.

CHUNG, L. W.; *et al*. The ONIOM method and its applications. **Chemical Reviews**, v. 115, p. 5678-5796, 2015.

GEORG, H. & CANUTO, S. Métodos Híbridos para Modelagem do Ambiente Molecular. *In*: MORGON, N. H. & COUTINHO, K. **Métodos de Química Teórica e Modelagem Molecular**. Editora Livraria da Física, 1a ed, 2007.

HAILE, J. M. **Molecular Dynamics Simulations: Elementary Methods**. Wiley-Interscience, 1 ed., 1997.

HANWELL, M. D.; *et al*. Avogadro: An advanced semantic chemical editor, visualization, and analysis platform. **Journal of Cheminformatics**, v. 4, n. 17, 2012.

HILL, T. L. **An Introduction to Statistical Thermodynamics**. Dover Publications, 1987.

HILL, T. L. **Statistical Mechanics: Principles and Selected Applications**. Dover Publications, 1987.

HINCHLIFFE, A. **Molecular Modelling for Beginners**. Wiley, 2ed, 2003.

HUB, J. S.; *et al*. g_whams-A Free Weighted Histogram Analysis Implementation Including Robust Error and Autocorrelation Estimates. **Journal of Chemical Theory and Computation**, v. 6, p. 3713-3720, 2010.

JARZYNSKI, C. Nonequilibrium Equality for Free Energy Differences. **Physical Review Letters**, v. 78, n. 14, 1997.

JENSEN, F. **Introduction to Computational Chemistry**, John Wiley & Sons, 2nd edition, Chichester, UK, 2007

KÄSTNER, J. Umbrella Sampling. **WIREs Computational Molecular Science**, v. 1, p.932-942, 2011.

KE, Q.; *et al*. Effects of thermostats/barostats on physical properties of liquids by molecular dynamics simulations. Journal of Molecular Liquids, v. 365, 120116, 2022.

KUMAR, S.; *et al.* The weighted histogram analysis method for free-energy calculations on biomolecules. I. The method. **Journal of Computational Chemistry**, v. 13, n. 8, p. 1011-1021, 1992.

KUMAR, S.; *et al.* Multidimensional free-energy calculations using the weighted histogram analysis method. **Journal of Computational Chemistry**, v. 16, n. 11, p. 1339-1350, 1995.

LEWARDS, E. **Computational Chemistry**: Introduction to the Theory and Applications of Molecular and Quantum Mechanics. Kluwer Academic Publishers, 2003.

MARTÍNEZ, L.; BORIN, I. A.; SKAF, M. S. Fundamentos de Simulação por Dinâmica Molecular. *In*: MORGON, N. H. & COUTINHO, K. **Métodos de Química Teórica e Modelagem Molecular**. Editora Livraria da Física, 1a ed, 2007.

MARTÍNEZ, L.; *et al*. PACKMOL: a package for building initial configurations for molecular dynamics simulations. **Journal of Computational Chemistry**, v. 30, n. 12, p. 2157-2164, 2009.

MEZA, J. C. Steepest descent. **Wiley Interdisciplinary Reviews: Computational Statistics**, v. 2, p. 718-722, 2010.

MILLER, B. R.; *et al*. MMPBSA.py: An Efficient Program for End-State Free Energy Calculations. **Journal of Chemical Theory and Computation**, v. 8, p. 3314-3321, 2012.

NAMBA, A. M.; DA SILVA, V. B.; DA SILVA, C. H. T. P. Dinâmica molecular: Teoria e aplicações em planejamento de fármacos. **Eclética Química**, v. 33, n. 4, p. 13-24, 2008.

ROUX. B. The calculation of the potential of mean force using computer simulations. **Computer Physics Communications**, v. 91, n. 1-3, p. 275-282, 1995.

SINDHIKARA, D. J.; *et al*. Bad Seeds Sprout Perilous Dynamics: Stochastic Thermostat Induced Trajectory Synchronization in Biomolecules. **Journal of Chemical Theory and Computation**, v. 5, p. 1624-1631, 2009.

TORRIE, G. M. & VALLEAU, J. P. Nonphysical Sampling Distributions in Monte Carlo Free-Energy Estimation: Umbrella Sampling. **Journal of Computational Physics**, v. 23, n. 2, p. 187-199, 1977.

TUCKERMAN, M. E. & MARTYNA, G. J. **Journal of Physical Chemistry B**, v. 104, p. 159-178, 2000.

TUCKERMAN, M. E. **Statistical Mechanics: Theory and Molecular Simulation**. Oxford University Press, 1ed, 2010.

VREVEN, T.; *et al*. Combining quantum mechanics methods with molecular mechanics methods in ONIOM. **Journal of Chemical Theory and Computation**, v. 2, n. 3, p. 815-826, 2006.

WANG, E.; *et al*. End-Point Binding Free Energy Calculation with MM/PBSA and MM/GBSA: Strategies and Applications in Drug Design. **Chemical Reviews**, v. 119, p. 9478-9508, 2019.

YANG, Y. I.; SHAO, Q.; ZHANG, J.; YANG, L.; GAO, Y. Q. Enhanced sampling in molecular dynamics. **The Journal of Chemical Physics**, v. 151, 070902, 2019.

3 CHAPTER 3

Carbon nanohorns as nanocontainers for cisplatin: insight into their interaction with the plasma membranes of normal and breast cancer cells

3.1 INTRODUCTION

Over the years, breast cancer (BC) has been pointed out as the most common cancer type and the second leading death cause in women worldwide (HARBECK, *et al.*, 2019; WAKS & WINER; 2019). As a result of the high heterogeneity and variability of the BC genomes, this disease encompasses diversity in terms of subtypes and aggressive behaviors, which also require both application and development of specialized treatments (GODONEA, *et al*., 2018; FENG, *et al.*, 2018). Despite the severe side effects and the propensity to tumor resistance, the chemotherapy based on Pt-drugs, including the well-known cisplatin (cddp, cis-diamminedichloroplatinum-(II)) and carboplatin (*cis*-diammine-1,1-cyclobutane dicarboxylate platinum (II)), is still a routinely used therapeutic alternative for BC. Over the last 40 years, several studies (AL-BAHLANI, *et al.*, 2017; DILRUBA, & KALAYDA, 2016; DUAN, *et al.*, 2016) showed the effectiveness of these compounds in the treatment of many cancers' types, such as lung, bladder, testicular, and ovarian cancers. A strategy that potentially reduces toxicity and resistance in tumors is the encapsulation of Pt(II)-based metallodrugs into drug delivery systems (DDS). It can protect the chemotherapeutic agents from side reactions in the physiological environment and provide their slow and targeted release to the tumor sites (CHEN, *et al.*; 2017; DUAN, *et al*., 2016).

In this context, the incorporation of cddp into carbon nanohorns (CNH) (CURCIO, *et al.*, 2021; VECLANI, *et al.*, 2020) has been pointed out as a potential nanoparticle-based formulation of cddp, even for BC, since the very first experimental studies published by Iijima *et al.* (IIJIMA, *et al.,* 1999; MURATA, *et al.*, 2002; MURAKAMI, *et al.*, 2004; AJIMA, *et al*., 2005; AJIMA, *et al*., 2006, AJIMA, *et al*., 2008). While a conical tip forms typical structures of CNH with a cone angle of 20º connected to a tubular section with 40-50 nm in length and 2-5 nm in diameter, during their synthesis, thousands of these singular structures assemble together to form spherical aggregates known by their dahlia-like shape with about 100 nm of diameter (NAKAMURA, *et al*., 2011; KAROUSIS, *et al*., 2016). In addition to the presence of suitable cavities to accommodate clusters of therapeutic molecules, the relevance of these carbon-based nanomaterials as drug carriers is related to their current mass production with

high purity (LANCETA, *et al*., 2020), low toxicity (MIYAWAKI, *et al.*, 2008), better dispersibility and biodistribution when chemically functionalized (TAHARA, *et al*., 2011), biodegradation by the macrophages (ZHANG, *et al.*, 2015), and better biocompatibility and nanosafety compared to the carbon nanotubes (CNT) (HE, *et al*., 2018).

Regarding the recent studies involving inclusion complexes formed by CNH loaded with cddp molecules, henceforth identified as cddp@CNH, Isaac *et al*. (ISAAC, *et al*., 2018) proposed the use of CNH decorated with amide thiol groups as nanotheranostic vehicles of this drug based on a hybridization scheme with quantum dots (CdSe/ZnS core/shell). By incubating this hybrid DDS with rat bladder carcinoma cells (AY-27), the authors demonstrated the cellular internalization using fluorescence imaging, followed by a notable tumor cell death. They also showed the cddp release during 72 h characterized by inhibitory concentration (IC_{50}) that was, on average, 65 times greater than the one referring to the application of free cddp. Additionally, Yang and coworkers (YANG, *et al*., 2018) demonstrated that the CNH presented high efficiency and stability in the physiological environment, a long blood half-life, and selectivity for the tumor sites. They obtained these results by studying a chemo-photothermal therapy based on chemically modified CNH loaded with cddp and doxorubicin drugs to treat breast and lung tumors.

In these studies, the presence of nanowindows on the surface of the CNH is an important topological characteristic since it constitutes routes for the permeation and release of the cddp molecules (AJIMA, *et al*., 2006). For instance, these holes can be formed by oxidation treatments using O_2 atmosphere at high temperature (KAROUSIS, *et al*., 2016). Recently, Stevic *et al.* (STEVIC, *et al*., 2020) evaluated the use of Cu phthalocyanine as a catalyst for the oxidation process of CNH, which produced uniform nanowindows with a size smaller than 0.5 nm.

Moreover, theoretical studies on structure, stability, and spectroscopy of the cddp@CNH complexes have also been explored in the light of quantum mechanical calculations (DE SOUZA, *et al*., 2013; DE SOUZA, *et al*., 2018) and molecular dynamics (MD) simulations (ALMEIDA, *et al*., 2019; ALMEIDA, *et al*., 2020). While in 2014, Dos Santos *et al*. (DOS SANTOS, *et al.*, 2014) conducted a density-functional tight-binding (DFTB) study focusing on a series of pristine CNH topologies, we recently modeled oxidized (CNHox) and reduced (CNHh) structures and then, we highlighted both formations of nanowindows and insertion of polar functional groups onto their surface as relevant post-synthesis strategies to improve the biocompatibility of this DDS (ALMEIDA, *et al*., 2020).

Another central issue to the nanomedicine field is to understand the cellular uptake mechanism of drug nanocarriers into tumor tissues (HARE, *et al.*, 2017). Unlike CNH, the interactions of other C nanomaterials with plasma membranes have been addressed in several theoretical studies. For instance, a MD study conducted by Kraszewski *et al*. (KRASZEWSKI, *et al.*, 2012) demonstrated that the passive diffusion mechanism of amino-functionalized CNT models in a phospholipid bilayer (POPC: 1-palmitoyl-2-oleoyl-sn-glycero-3-phosphocholine) involves several steps, such as landing and floating, penetration in the polar head regions of lipids, and actual sliding into the membrane. By combining data from both MD simulations and transmission electron microscopy (TEM), Lacerda and coworkers (LACERDA, *et al.*, 2013) evidenced an improvement of the interactions between CNT and lipid bilayers (POPC) due to the presence of polar functional groups inserted on the surface of the CNT. In 2015, MD simulations conducted by Mejri *et al*. (MEJRI, *et al*., 2015) indicated a favored release of cddp molecules from the interior of CNT when near to a cell membrane model (POPC). Recently, Mejri and coworkers (MEJRI, *et al*., 2021) showed that the gradual release of cddp molecules from edge-functionalized CNT with hydroxyls groups takes place only when this nanovector tries to insert itself in the lipid bilayer (POPC). To our knowledge, despite the promising properties of CNH for biomedical applications outlined herein, associated with experimental evidence of a cellular internalization characterized by a moderate membrane disturbance compared to the CNT (HE, *et al.*, 2018; MATSUMURA, S.; *et al.*, 2014), no prior research has addressed the molecular interaction mechanism between cddp@CNH complexes and cell membranes.

When it comes to the membrane models that interact with a nanomaterial, there is also a lack of studies including realistic biomembrane models that encompass characteristics of tumor cells. Recent studies have taken into account both asymmetric lipid composition and a realistic cholesterol concentration, such as the one conducted by Yesylevskyy *et al.* (YESYLEVSKYY, *et al.*, 2017), who analyzed the influence of lipid bilayer curvature on the properties of a realistic plasma membrane model of mammalian cells. In 2019, Rivel and coworkers (RIVEl, *et al.*, 2019) evaluated the permeation process of cddp through realistic membrane models referring to normal and cancer cells. Besides verifying a decrease of drug permeability by increasing the cholesterol molar ratio, the authors observed a decrease in the drug permeability through cancer membranes due to the loss of lipid asymmetry commonly detected in cancer cells. Furthermore, by conducting MD simulations involving plasma membrane prototypes of mouse hepatocytes and hepatomas, Andoh *et al.* (ANDOH, *et al.,*

2016) showed a reduction in fluidity and an increase in lateral ordering of these lipid bilayers due to hepatic carcinogenesis.

In view of the literature gap referring to the biomedical application of CNH as DDS, a question that naturally arises is how this potential nanomaterial loaded with cddp molecules interacts and translocate through membranes of breast cancer cells? Understanding these molecular events is a challenge and relevant research topic since the superior biocompatibility of CNH in comparison to CNT may induce a significant reduction of both cddp resistance and secondary effects, commonly observed in chemotherapies for this frequent cancer (SALAS-TREVINO, *et al.*, 2018). In this sense, the present study involves modeling the 3cddp@CNHox complexes (three cddp molecules included in the CNHox cavity) immersed in a physiological environment containing realistic plasma membrane models of normal and BC cells and the analysis of the system by MD simulation.

3.2 METHODS

3.2.1 Molecular models

Concerning the CNH, by starting from a pristine structure ($C_{360}H_{24}$) investigated in our previous papers (ALMEIDA, *et al*., 2019; DOS SANTOS, *et al.*, 2014), we built an oxidized structure based on our previously studied oxidation mechanism of CNT and CNH with O_2 and H_2O summarized as CNH + $2O_2$ + H_2O → CNHox (DE SOUZA, *et al*., 2017; DA SILVA, *et al*., 2009). In the present work, we distributed the oxidation functional groups to all pentagons on the surface of the CNH, aiming to reproduce the concomitant oxidation of these reactive sites. Additionally, due to the reactivity of the opened end edge of the nanostructure, all C-H bonds were replaced by C-OH bonds. Due to the drastic nature of this heat treatment with O_2 gas, we also applied the oxidation mechanism in random hexagons located at the tubular region of the CNH structure.

Another important aspect that was taken into account in the CNHox prototype was the inclusion of nanowindows on the surface of this nanomaterial as a result of the oxidation reaction. The relevance of these holes is connected to the fact that they represent the main pathways for the slow release of the encapsulated cddp molecules (AJIMA, *et al*., 2006; AJIMA, *et al.*, 2008). In this context, by using the aforementioned oxidation process at high temperatures (843-853 K), Ajima *et al.* (AJIMA, *et al.*, 2004) reported that the highest frequency of adsorbed fullerenes (C_{60}) molecules into the cavity of CNHox occurred through

nanowindows with a diameter of around 10-15 Å, located at the tip region of this nanomaterial. Based on this experimental result, we opened a nanowindow on the surface of the CNHox model with an average diameter of 11 Å, which was compatible with the effective size of a cddp molecule (~7.8 Å) (ALMEIDA, *et al.*, 2020). Still regarding this nanowindow, we included H-terminated edges to model the reduction process (H_2 gas flow at 1473 K for 3 h) employed to deactivate these holes chemically (AJIMA, *et al.*, 2006) Figure 3.1A-B presents the CNHox model ($C_{280}H_{54}O_{41}$) built in this work.

Figure 3.1 - Structures of the CNHox model ($C_{280}H_{54}O_{41}$) and its inclusion complex with three cddp molecules (3cddp@CNHox) studied in this work: side view of the CNHox model (A), frontal view from the tip of the CNHox model (B), side view of the 3cddp@CNHox (C), and the frontal view from the oxidized end of the CNHox (D). The L, De, and D_n parameters correspond to average values of the length, the diameter of the open edge, and the diameter of the nanowindow. All distances take into account the van der Waals radii of the atoms.

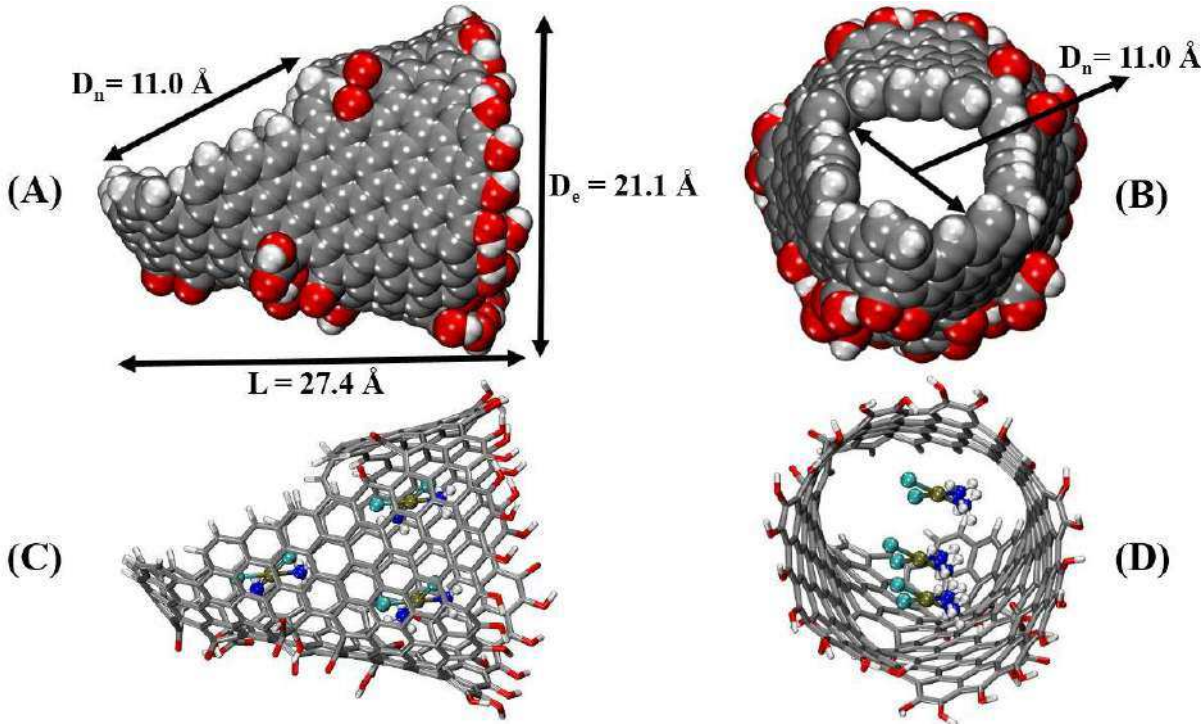

Reference: Own author (2021).

The proposed CNHox structure was optimized at the semiempirical Austin Model 1 (AM1) method (DEWAR, *et al.*, 1985) in an aqueous solution by using the polarizable continuum model (PCM) with the integral equation formalism (IEF) variant (CANCÈS, *et al.*, 1997).

Since high-resolution TEM images revealed the incorporation of cddp clusters with a size in the range of 10-50 Å inside the cavities of CNH (AJIMA, *et al*., 2006; AJIMA, *et al*., 2008), we encapsulated in the CNHox model three cddp molecules forming, in turn, the inclusion complex prototype labeled as 3cddp@CNHox. This last notation indicated an inclusion complex formed by one CNHox host loaded with three cddp guests. The choice of the number of confined molecules was connected to the size of the CNHox structure, which, in turn, represents only the tip region of the real CNH structures (AJIMA, *et al.*, 2008). In the initial structure of the 3cddp@CNHox model, while one cddp molecule was positioned near to the nanowindow, the other two were arranged close to the center of mass of the CNHox (see Figure 3.1C-D).

We built two realistic models to represent the plasma membrane of human breast cells: one based on the composition of the main lipids identified in the MCF-7 BC cells (TODOR, *et al.*, 2012) and another based on the content of the main lipids expressed in normal breast tissue cells (MERCHANT, *et al*., 1991). Henceforth, while the membrane model of a BC cell will be named as C_memb, the membrane model of a normal breast cell will be termed as N_memb. Table 3.1 shows the composition and distribution of lipids in each of the two monolayers of our lipid bilayer models. The specific numbers of lipid molecules referring to these models are organized in Table A1.

The two membrane models described in Table 3.1 included aspects experimentally identified, such as the asymmetric distribution of lipids between the two monolayers that compose the plasma membranes of normal cells, in contrast to the loss lipidic asymmetry in membranes of cancer cells (BERNARDES, *et al*., 2018). Additionally, the overexpression of the PS and PE lipids at the outer leaflet of lipid bilayers referring to cancer cells was also integrated into the C_memb model (SHARMA & KANWAR, 2018). It is worth mentioning that the selection of the lipids indicated in Table 3.1 also took into account the availability of this class of biomolecules parameterized in the AmberTools19 program (CASE, *et al.*, 2019) (see the structures in Figure A1). Based on all data in Table 3.1, we used the membrane builder tool from CHARMM-GUI website (JO, *et al.*, 2008; LEE, *et al.*, 2020) to build the N_memb and C_memb models (Figure 3.2).

Still regarding the data from Table 3.1, we solvated the system with 0.15 M of dissociated NaCl, aiming to mimic a physiological environment. It was assumed that this concentration was the same for the two membranes. These systems were also neutralized with Na^+ ions due to the presence of anionic lipids (DOPS and DOPG). Lastly, after the equilibration stages of isolated models (3cddp@CNHox, C_memb, and N_memb), the central axis of the

inclusion complex was aligned with the axis normal to the membrane plane so that the nanocarrier remained at the extracellular medium.

Table 3.1 - Lipid composition (%) and ionic concentration (M) of the plasma membrane models referring to N_memb and C_memb.

Components	**N_memb[a]**		**C_memb[b]**	
Lipids	**Membrane lipid composition / %**			
	outer monolayer	inner monolayer	outer monolayer	inner monolayer
DOPC	39.4	19.8	23.2	23.2
DOPE	2.3	8.2	9.7	9.7
DOPG	0.9	0.9	2.8	2.8
DOPS	0	13.4	4.0	4.0
CHL	8.0[c]	8.0[c]	10.3	10.3
Ions	**Ionic concentration / M**			
Na^+	0.15		0.15	
Cl^-	0.15		0.15	

[a]Lipid composition based on a normal breast tissue cell. [b]Lipid composition based on the MCF-7 cell line. [c]The cholesterol concentration referring to the normal breast cell was collected from the Reference (JOWET, 1931) DOPC: 1,2-dioleoyl-*sn*-glycero-3-phosphocholine. DOPE: 1,2-dioleoyl-*sn*-glycero-3-phosphoethanolamine. DOPG: 1,2-dioleoyl-*sn*-glycero-3-[phospho-rac-(1-glycerol)]. DOPS: 1,2-dioleoyl-*sn*-glycero-3-phospho-L-serine. CHL: cholesterol.
Reference: Own author (2021).

The distance between the last atom of the inclusion complex facing the membrane and the geometric center of the membrane surface was set as ~7.0 Å resulting, in turn, in the 3cddp@CNHox>C_memb and 3cddp@CNHox>N_memb models (Figure 3.3). These procedures were conducted using the software PyMOL 1.8 (THE PyMOL, 2009-1015).

3.2.2 Force field parameterizations

Regarding the CNHox model, while the intramolecular and Lennard-Jones (LJ 12-6) potential parameters were selected from the General AMBER Force Field (GAFF2) (WANG, *et al*., 2004), the atomic charges were calculated by using the ChelpG approach (BRENEMAN & WIBERG, 1990) at the HF/6-31G(d,p) level of theory in aqueous solution (PCM).

When it comes to the cddp molecule, we used the same parameterization scheme employed previously (ALMEIDA, *et al.,* 2019; ALMEIDA, *et al*., 2020). In this conventional procedure, the set of intramolecular parameters of cddp was derived from its optimized geometry in aqueous solution (PCM) at the MP2/LANL2DZ/6-31G(d,p) level (MØLLER & PLESSET, 1934 ; HEHRE, *et al.*, 1975 ; HAY & WADT, 1985). The force constants for the bond stretching (Kb) and angle bending (Ka) were extracted by using the Visual Force Field Toolkit (VFFDT) (ZHENG, *et al*., 2016).

Figure 3.2 - Initial structures of the plasma membrane models referring to a normal breast cell (A) and a BC cell (MCF-7) (B). The blue, red, yellow, green, magenta, white, cyan, and orange spheres correspond to the DOPC, DOPE, DOPS, DOPG, CHL, OL, Cl^-, and Na^+ species, respectively.

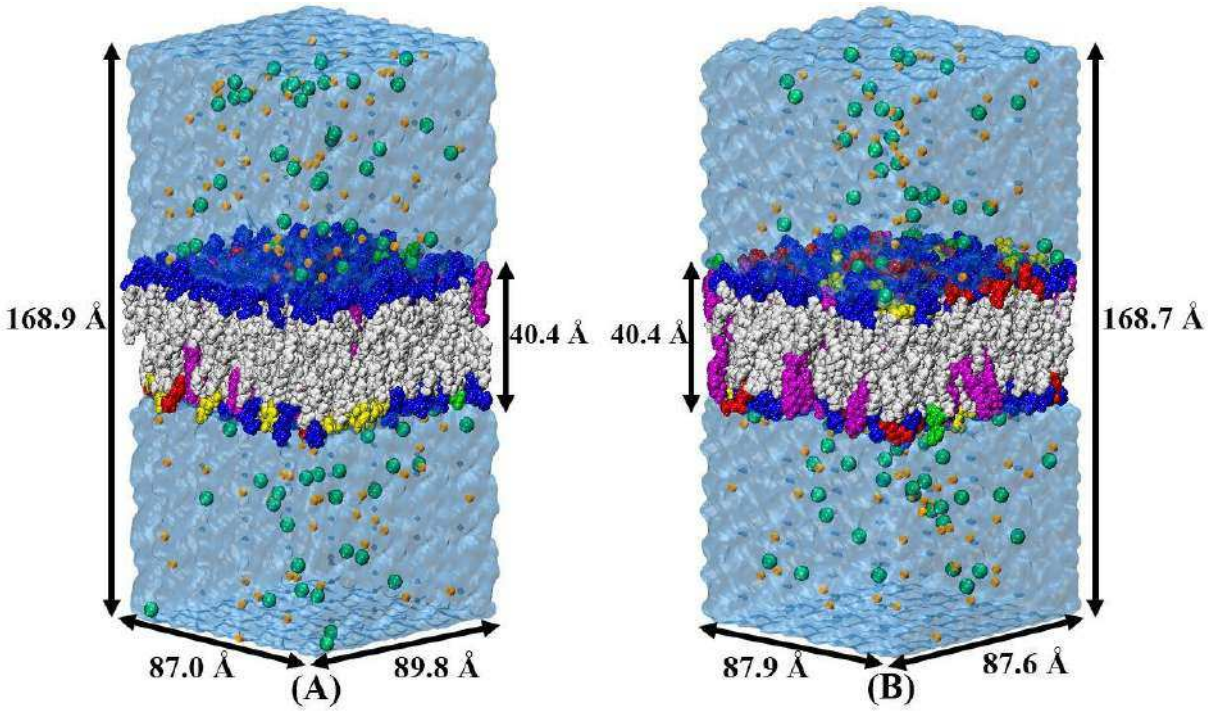

Reference: Own author (2021).

Concerning the intermolecular parameters, while the LJ 12-6 potential parameters referring to the Pt atom were collected from previous work (LOPES, *et al*., 2008), the same parameters for the nonmetal atoms (Cl, N, and H) were selected from the GAFF (WANG, *et al*, 2004). The atomic charges using the ChelpG fitting procedure were computed at the HF/6-31G(d,p)/LANL2DZ level in aqueous solutions (PCM). All quantum mechanics calculations were carried out with the Gaussian-09 release D.01 program (FRISCH, *et al*., 2009).

At last, the plasma membrane models (C_memb and N_memb) were described by the parameters of the Lipid17 force field, which is an updated version of the previous Lipid11 (SKJEVIK, *et al*., 2012) and Lipid14 (DICKSON, C. J.; *et al*., 2014; MADEJ, *et al.*, 2015) force fields for lipids. All water molecules were represented by the TIP3P model (JORGENSEN, *et al*., 1983), and the Na^+ and Cl^- ions were described by the parameters proposed by Li and coworkers (LI, *et al.,* 2015).

Figure 3.3 - Initial structures of two systems formed by the 3cddp@CNHox complex located either near to a plasma membrane model of a normal breast cell, named as 3cddp@CNHox>N_memb model (A), or near to a plasma membrane prototype of a BC cell (MCF-7), referenced as 3cddp@CNHox>C_memb model (B). The blue, red, yellow, green, magenta, white, lime, and orange correspond to the DOPC, DOPE, DOPS, DOPG, CHL, OL, Cl^-, and Na^+ species, respectively.

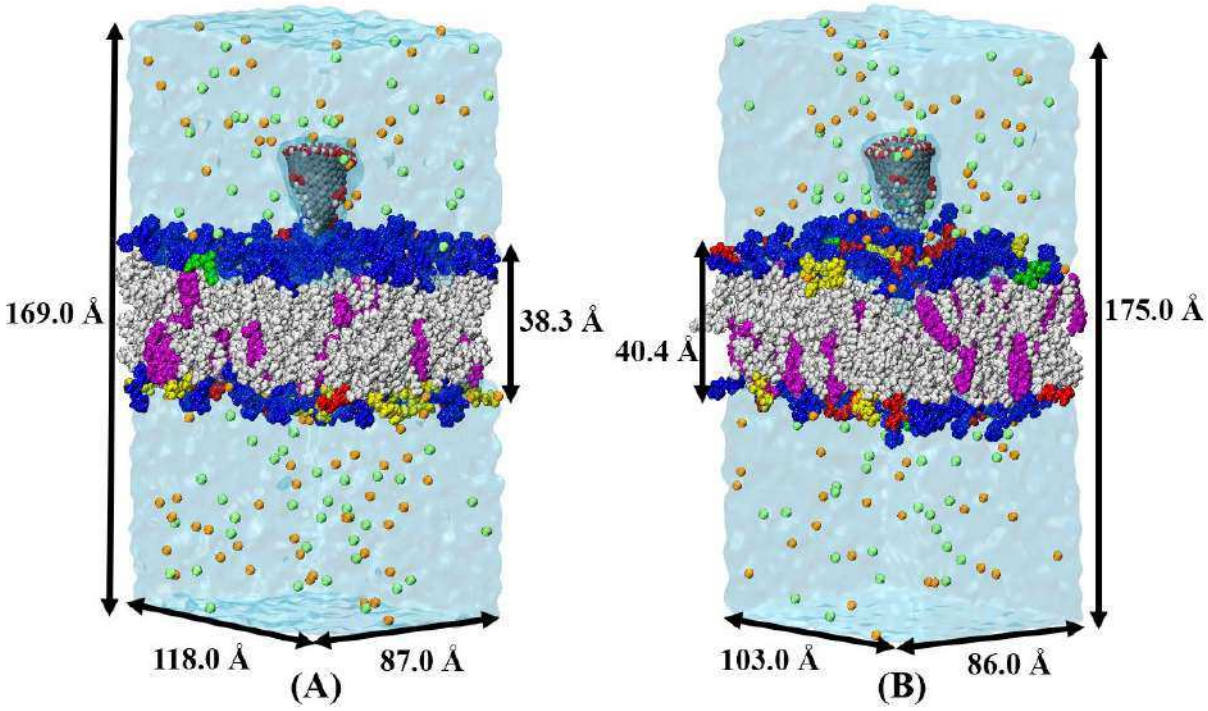

Reference: Own author (2021).

3.2.3 MD simulation details

All MD simulations were performed using the pmemd CUDA implementation (SALOMON-FERRER, *et al.*, 2013) of the AMBER 16 software package (CASE, *et al.*, 2016), and the trajectories were analyzed with the CPPTRAJ module (ROE & CHEATHAM, 2013).

Concerning the isolated 3cddp@CNHox structure simulation, we placed the inclusion complex at the center of a simulation box characterized by a truncated octahedral shape with an average length of 84.3 Å. We solvated the system with TIP3P water molecules and 0.15 M of dissociated NaCl. We performed two cycles of energy minimization using the steepest descent (SD) method (JENSEN, 2007) for the first 4500 cycles and the conjugate gradient (CG) method (HESTENES & STIEFEL, 1952) for the last 4500 cycles. These cycles were executed in two steps, initially for the energy minimization of the solvent followed by the minimization of the entire system. After that, by applying a weak positional restraint with force constant of 10.0 kcal mol-1 $Å^2$ on the solute, the system was gradually heated from 283 K to 310 K in the canonical ensemble (NVT) for 10 ns, using the Langevin thermostat (UBERUAGA, *et al.*, 2004) with a collision frequency of 1.0 ps^{-1}. To equilibrate the system and the density, a 200 ns simulation of the free system was performed in the isothermal-isobaric ensemble (NPT), employing the Berendsen barostat (BERENDSEN, *et al.*, 1984) with a relaxation time of 1.0 ps in order to maintain an average pressure of 1.0 bar.

Considering the simulations of the C_memb and N_memb models, the first step was the energy minimization of the solvent with the solute atoms restrained by applying a force constant of 500.0 kcal mol-1 $Å^2$. The first 30000 cycles were performed with the SD method and the last 30000 cycles with the CG method. The energy minimization of the entire system was the next step, with 6000 cycles for the SD method and more extra 6000 cycles for the CG method. Then, the membrane models were heated from 283 K to 310 K considering a weak positional restraint to the solute atoms characterized by a force constant of 10.0 kcal mol^{-1} $Å^2$. This stage was performed for 20 ns in the NVT ensemble with temperature regulation using the Langevin thermostat with a collision frequency of 1.0 ps^{-1}. After the heating step, we equilibrated the systems at 310 K and 1.0 bar for 400 ns using the Berendsen barostat, with a relaxation time of 1.0 ps, an anisotropic pressure scaling, and no positional restraints in the NPT ensemble.

The production MD was carried out with the 3cddp@CNHox>C_memb and 3cddp@CNHox>N_memb systems built using the equilibrated models (3cddp@CNHox, C_memb, and N_memb). This step involved a simulation time of 800 ns in the NPT ensemble with temperature and pressure controlled by the Langevin thermostat and Berendsen barostat. All MD simulations conducted in this work are summarized in Table 3.2.

Regarding all MD simulations described in Table 3.2, since the bonds involving H atoms were constrained using the SHAKE algorithm (RYCKAERT, *et al.*, 1977), a 2.0 fs time step was employed. The LeapFrog method was used for the numerical integration of Newton's equations of motion. By using three-dimensional periodic boundary conditions, both van der

Waals (vdW) interactions and the electrostatic interactions (elec), which were calculated by the Particle Mesh Ewald (PME) method (DARDEN, *et al*., 1993), were truncated at a cutoff of 10.0 Å. When it comes to the 3cddp@CNHox>C_memb and 3cddp@CNHox>N_memb systems, the cutoff was 11.0 Å. The number of H bonds was calculated by following geometric criteria of a donor (D-H)–acceptor (A) distance of 3.0 Å and D–H–A angle cutoff of 135°. Finally, using conformational ensembles of the host-guest systems, the binding free energies ($\Delta_b G$) were calculated based on the Molecular Mechanics Generalized Born Surface Area (MM/GBSA) method (MILLER III, *et al*., 2012). Since vibrational frequencies calculations are computationally demanding for lipid bilayers, the entropic contribution to the $\Delta_b G$ was neglected in these calculations.

Table 3.2 - Summary of the MD simulations conducted at 310 K, 1.0 bar, and 0.15 M NaCl concentration.

System[a]	N_a [b]	L_{box} / Å [c]	N_m^{wat} [d]	N_L^{mem} [e]	N_L^l [f]	t_{equi} / ns [g]	t_{sim} / ns [h]
3cddp@CNHox	33309	89x89x89	10947	-	-	200	200
C_memb	96496	103x86x175	24200	196	98	400	400
N_memb	101707	118x87x169	25551	198	99	400	400
3cddp@CNHox>C_memb	95961	103x86x175	23887	196	98	100	800
3cddp@CNHox>N_memb	101177	118x87x169	25239	198	99	100	800

[a]3cddp@CNHox>C_memb: structure of the 3cddp@CNHox complex with the C_memb membrane model. 3cddp@CNHox>N_memb: structure of the 3cddp@CNHox complex with the N_memb membrane model. [b]N_a: Total number of atoms, including both solute and solvent. [c]L_{box}: Dimensions of the simulation box (x y z) in Å. [d]N_m^{wat}: total number of water molecules. [e]N_L^{mem}: number of lipids per membrane. [f]N_L^l: Number of lipids per leaflet. [g]t_{equi}: simulation time for the equilibration stage in nanoseconds (ns) after the heating stage. [h]t_{sim}: total simulation time in ns after the heating stage.
Reference: Own author (2021).

3.3 RESULTS AND DISCUSSION

3.3.1 Simulation of the free 3cddp@CNHox inclusion complex

The simulation of the isolated 3cddp@CNHox (Figure 3.1C-D) in an aqueous solution of 0.15 M NaCl was monitored by temporal variation of the temperature, pressure, density, and volume. The system was equilibrated during the first 50 ns of the 200 ns trajectory (see Figure A.2). The equilibrium was also verified when we evaluated the potential, kinetic, and total energies during this time (Figure A.3). When considering only the solute (3cddp@CNHox), the temporal

variations presented in Figure A.4 and the standard deviation shown in Table A.2 (in the range of 4.9%) reinforce that all components of the total potential energy of the solute converged over 200 ns simulation.

Regarding the structure of the inclusion complex, we observed a structural variation during the 200 ns simulation time with an averaged RMSD of 3.12 ± 0.94 Å relative to the first structure of the equilibration stage. This variation is related to the reorientation of the cddp cluster inside the cavity of the CNHox (Figure 3.4) forming a stable triangular configuration after 50 ns (Figure 3.4B), characterized by the dynamical interaction between the plane defined by the square planar geometry of this drug and the walls of the nanostructure. The snapshots at 20 ns intervals obtained from the 200 ns MD trajectory of the 3cdd@CNHox complex were organized in Figure A.5.

Figure 3.4 - Temporal variation of the RMSD of the 3cddp@CNHox complex calculated over the 200 ns simulation referring to the first structure of the trajectory (A). The green line represents the moving average calculated for sets of 350 frames. Equilibrium triangular arrangement of the 3cddp cluster inside the CNHox cavity (B).

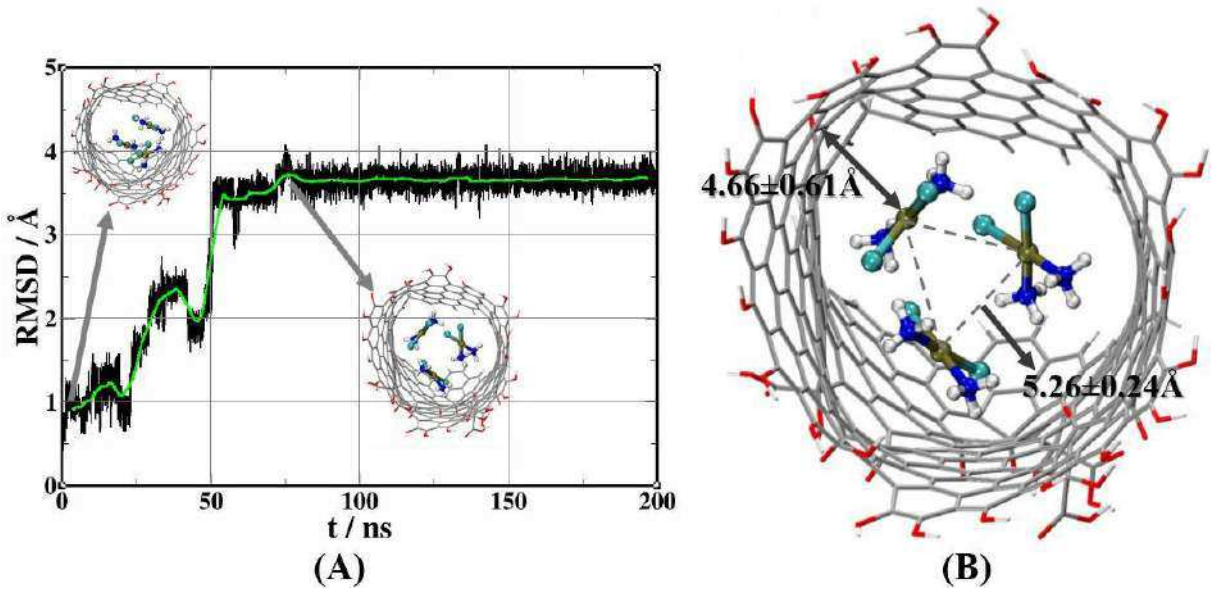

Reference: Own author (2021).

The spatial distribution of the three cddp molecules incorporated into the CNHox cavity (see Figure A.6) reinforced the confinement of this cluster throughout the 200 ns trajectory suggesting a strongly favorable interaction between this carbon nanocarrier and the cddp drug, as also reported in our previous study (ALMEIDA, *et al*., 2020).

Concerning the interaction with solvent molecules, the radial distribution function (RDF) defined between the center of mass (CM) of the CNHox model and the O atoms (Ow) of the water molecules, namely g(r) CM--Ow, indicated the presence, on average, of seven water molecules inside the cavity of the CNHox (see Figure A.7). Moreover, analyzing the RDF defined between the cddp cluster and the water molecules, data from Figure A.8 revealed that the Pt--O_w and NH--O_w interactions were the most intense with the first solvation shell centered, on average, at 4.35 Å (seven water molecules) and 2.85 Å (two water molecules), respectively.

To analyze the evolution of the different energetic contributions related to the cddp drug during the 200 ns simulation, we computed the pair interaction energies composed by vdW and electrostatic interactions within a 10 Å cutoff distance (Figure 3.5). It is possible to notice that the system reached a stable configuration after 50 ns, as seen in the RMSD analysis (Figure 3.4). In Figure 3.5A, we also verify that the main energetic contribution came from the interaction between the cddp cluster and the water molecules (3cddp--WAT) with an average value equal to -233.2 kcal mol^{-1} mainly related to electrostatic interactions (~92%). A similar result (~-200 kcal mol^{-1}) was also reported by Mejri *et al*. (MEJRI, *et al*., 2015; MEJRI, *et al*., 2021) when they analyzed the same interaction in complexes formed by either pristine CNT or CNT with edges functionalized by -OH groups, both loaded with four cddp molecules. By considering only the inner solvation shell of the complex, which was composed of seven water molecules (see Figure A.7), in the calculation of the 3cddp--WAT pair energy with a cutoff distance equal to 5.0 Å, it was possible to obtain average inner solvation energy equal to -83.8 kcal mol^{-1}, that also contributed for the stability of the 3cddp@CNHox complex.

The second most important contribution came from the 3cddp--CNHox interaction (see Figure 3.5A, black line), with an average value of -162.9 kcal mol^{-1}, mainly of the vdW nature (~74%). This energy came from the interaction of three cddp molecules with the CNHox structure within a 10 Å cutoff, representing, in turn, 2.3 times lower than the value presented by Mejri and coworkers for the 4cddp@CNT (our notation) complex (MEJRI, *et al.*, 2015). More recently, Mejri *et al*. (MEJRI, *et al*., 2021) have found a value of -80.0 kcal mol^{-1} for the interaction involving four cddp molecules and a hydroxyl-terminated CNT (17,0), with a retention time superior to 14.0 ns.

The strong 3cddp--CNHox interaction explains the confinement of the Pt(II) drug inside the nanocarrier model during all the 200 ns simulation. Recently, by analyzing the release of cddp from a CNTox model using a semi-rigid scan calculation of the potential energy surface (PES), we verified that this process required an energy barrier of 58.4 kcal mol^{-1}, even though it was also exergonic (~ -25 kcal mol^{-1}) (DE SOUZA, *et al.*, 2021).

Figure 3.5 - Evolution of the pair interaction energy (moving average) over the 200 ns simulation referring to the components of the inclusion complex formed by a cluster of three cddp molecules incorporated into one CNHox structure: pair energy between the cddp cluster and the CNHox, ions, waters, other cddp species (A), and the decomposition of the total pair energy (E_{total}) of the 3cddp@CNHox complex into the vdWs (E_{vdW}) and the electrostatic (E_{elec}) components (B). The moving averages were calculated for sets of 350 frames.

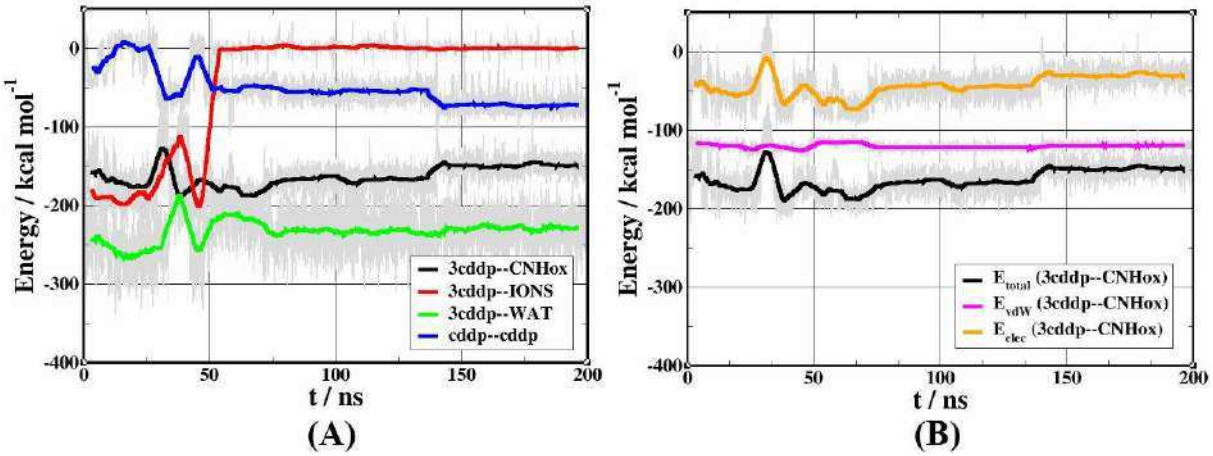

Reference: Own author (2021).

In order to evaluate the dynamical behavior of the 3cddp@CNHox inclusion complex near to plasma membranes, the influence of a lipid bilayer on the energies, and the dynamics of the encapsulated drugs, we selected from the 200 ns trajectory the structure in which one of the cddp molecules presented the closest position to the nanowindow region. It occurred at 26 ns of DM simulation (see Figure A.9).

3.3.2 Simulation of the plasma membrane models

The two membrane models (N_memb and C_memb) were initially simulated for 400 ns to equilibrate their structures and densities in an aqueous solution. The moving average of the temperature, pressure, density, and volume presented in Figures A.10-A.11, indicated the convergence of these macroscopic properties. When it comes to the kinetic, potential, and total energies, their temporal variation represented in Figures A.12-A.14 also pointed out the equilibration of both models. When one decomposed the potential energy of the solutes (C_memb and N_memb) into their components, it was possible to notice that the short-range electrostatic energy ($E_{elec1\text{-}4}$) was the main contribution to the total potential energy of these

models, as shown in Figure A.14 and Table A.3. This result was expected mainly because our membrane models are composed of anionic lipids (DOPS and DOPG), especially in the N_memb that is more enriched with these lipids than the C_memb model. However, while the well-known PS exposure in the two leaflets of the membranes referring to cancer cells may be contributing to the negative value of the E_{elec} term, the PS concentration only in the inner monolayers of membranes verified in normal cells probably resulted in the positive value of the E_{elec} term.

In order to evaluate the stability referring to the solvated structures of the membrane models, the structural properties, such as area per lipid (A_L), are per molecule (A_M), volume per lipid (V_L), and bilayer thickness (D_B), were calculated as average values over the last 100 ns of the 400 ns simulation (see Table 3.3). In Table 3.3, the A_L and A_M parameters were computed from the oscillations of the membrane surface area (A_{xy}) as shown in Equation 3.1-3.2, where n_{lipid} and n_{CHL} stand for the number of phospholipids and cholesterol molecules, respectively.

$$A_L = \frac{A_{xy}}{n_{lipid}} \tag{3.1}$$

$$A_M = \frac{A_{xy}}{n_{lipid} + n_{CHL}} \tag{3.2}$$

Temporal variation of the A_L shown in Figure A.15 and the small oscillations (in the range of 0.86 $Å^2$ - Table 3.3) evidenced the structural stability of the two membrane models. Similar behavior was observed by evaluating the V_L property (see Equation 3.3), which presented variations around 0.43% of the average value for the two lipid bilayers. The volume per lipid (V_L) and the volume per molecule (V_M) were calculated as average values over the last 100 ns of the 400 ns simulation by taking into account the volume of the simulation box (V_{xyz}), the volume of a TIP3P water molecule (V_w), and the total number of water (n_w), lipids (n_{lipid}), and cholesterol (n_{CHL}) molecules, as shown in Equation 3.3-3.4.

$$V_L = \frac{V_{xyz} - n_w V_w}{n_{lipid}} \tag{3.3}$$

$$V_M = \frac{V_{xyz} - n_w V_w}{n_{lipid} + n_{CHL}} \tag{3.4}$$

Table 3.3 - Structural properties of the membrane models referring to a normal breast cell (N_memb) and a BC cell (C_memb) calculated as averages values over the last 100 ns of the 400 ns simulation at 310 K, 1.0 bar, and 0.15 M NaCl.

Property / unit	**N_memb**	**C_memb**
	Average ± Std.[a]	**Average ± Std.**
A_{xy} / Å^2	5986.99±62.95	5569.42±72.70
A_L / Å^2	72.13±0.76 (72.5)[b]	73.28±0.96 (72.5)[b]
A_M / Å^2	60.47±0.64	56.83±0.74
V_{xyz} / Å^3	1009760.00±963.50	957486.00±931.62
V_L / Å^3	1403.67±5.88 (1303)[b]	1441.74± 6.13 (1303)[b]
V_M / Å^3	1174.50±4.92	1118.08± 4.75
D_B / Å	38.33±0.44 (36.9)[b]	40.44±0.17 (36.9)[b]

The parameters A_{xy}, A_L, A_M, V_{xyz}, V_L, V_M, D_B correspond to the membrane surface area in Å^2, the area per lipid in Å^2, the area per molecule in Å^2, the total membrane volume in Å^3, the volume per lipid in Å^3, the volume per molecule in Å^3, the bilayer thickness in Å, respectively. [a]The symbol Std. refers to the standard deviation. [b]Experimental data referring to a DOPC membrane at 298.15 K collected from Reference (NAGLE, *et al*., 2000).

Reference: Own author (2021).

As reported for membranes of hepatocyte and hepatoma cells (ANDOH, *et al.*, 2016), the C_memb model proposed here also experienced a decrease of ~7.0% in its surface area (A_{xy}) compared to the N_memb model. This result was a consequence of the lipid composition, such as the increase of 37.5% in the cholesterol content presented in our C_memb model. By comparing the A_L and V_L with A_M and V_M, we also noticed the condensing effect of lipid bilayers due to the presence of cholesterol molecules, as discussed by Hung *et al*. (HUNG, *et al.*, 2007)

Still regarding Table 3.3, the D_B parameter was estimated from the electron density profiles along the z axis of the two membrane models (Figure 3.6), where z = 0 corresponds to the CM of these prototypes. Precisely, the D_B parameter was calculated as the peak-to-peak distance from the total electron density profile (black lines in Figure 3.6), which consisted of the average distance between the polar head groups of the lipids located in the two leaflets of the lipid bilayer models.

Figure 3.6 - The total and decomposed electron density profiles calculated for the plasma membrane models referring to a normal breast cell (N_memb) and a BC cell (C_memb) calculated as average values over the last 100 ns of the 400 ns equilibration stage: N_memb (A) and C_memb (B). The electron density is defined here as the difference between the atomic number and the fixed charge.

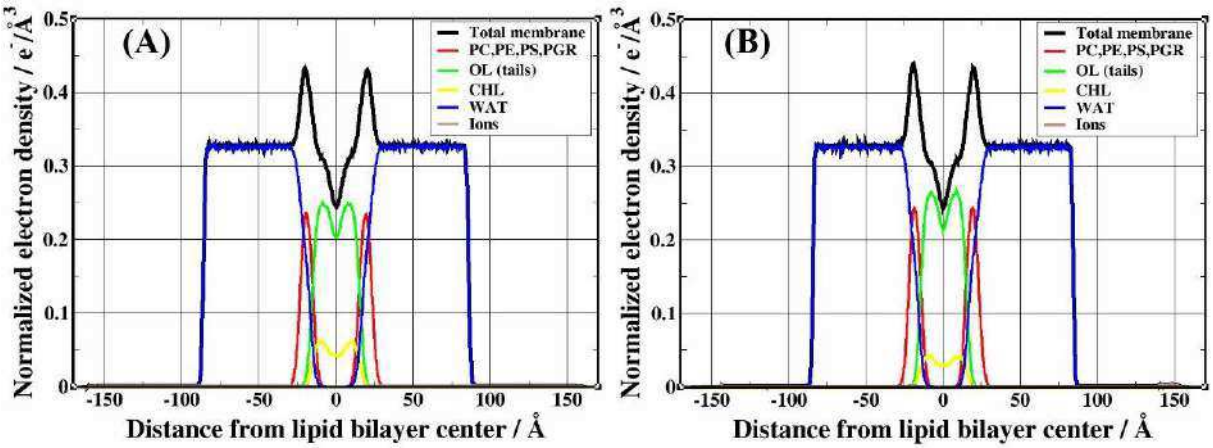

Reference: Own author (2021).

In general, the symmetric profiles shown in Figure 3.6 corroborated that both membrane models reached structural stability during the last 100 ns of the entire simulation time (400 ns). The difference of ~2.11 ± 0.31 Å in the D_B of model C_memb relative to N_memb may be connected to the larger cholesterol content included in the biomembrane model C_memb.

In summary, the energetic and structural properties discussed herein confirmed the efficiency of the simulation protocol in providing equilibrated membrane models for the subsequent study involving the interactions with the 3cddp@CNHox complex.

3.3.3 Interaction of the 3cddp@CNHox complex with plasma membrane models

Regarding the MD simulations of the inclusion complex near to the plasma membrane models presented herein, the analysis of the simulation properties, such as temperature, pressure, volume, density, kinetic, potential, and total energy as a function of time (see Figure A.16-A.18) indicated that these systems were equilibrated during the first 100 ns of the 800 ns simulation. The snapshots collected every 100 ns along the 800 ns trajectories were organized in Figure A.19 (3cddp@CNHox>C_memb) and Figure A.20 (3cddp@CNHox>N_memb). Moreover, we have sketched in Figure 3.7 the main stages of the interaction mechanism referring to these systems.

Figure 3.7 - The main stages of the interaction mechanism (over 800 ns) between the inclusion complex formed by a cluster of three cddp molecules incorporated into the CNHox structure and the plasma membrane models of cancer (C_memb) and normal (N_memb) cells of a human breast. (A) and (B): approach, (C) and (D): landing, (E) and (F): insertion, (G) and (H): penetration.

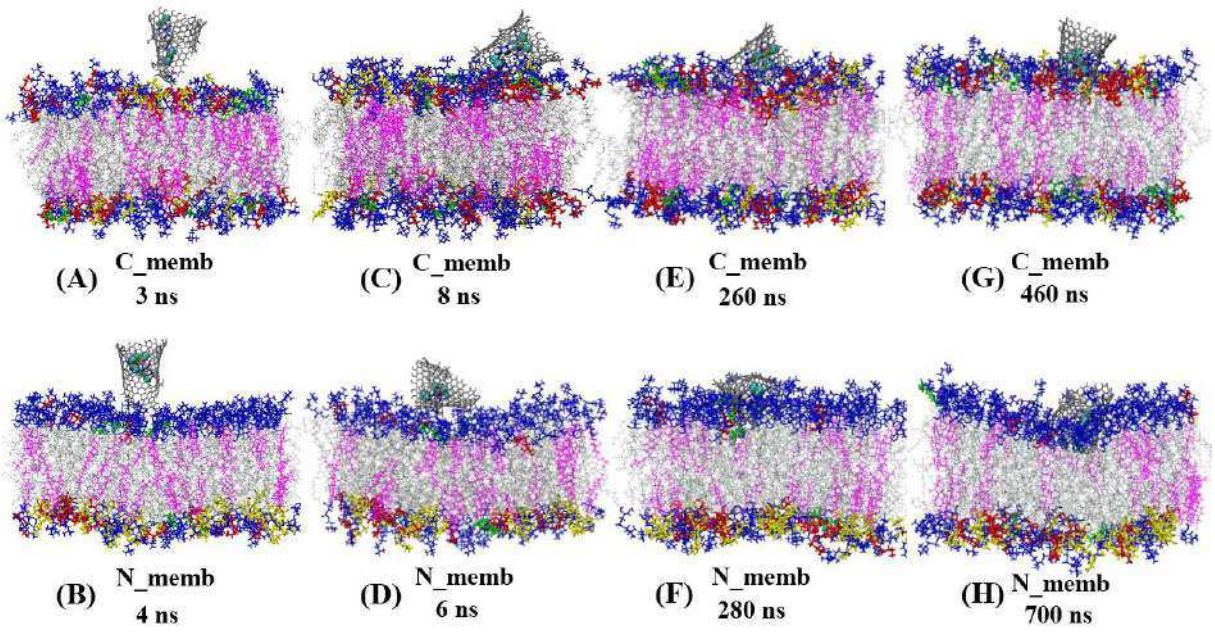

Reference: Own author (2021).

The first stage of the mechanism involved the approach of the 3cddp@CNHox complex to the lipid bilayers. Figure 3.7A-B revealed that although the central axis of the nanocontainer remained in the normal direction in relation to the plane of both membranes, this fast stage took about 3 ns and 4 ns for the C_memb and N_memb models, respectively.

The cddp cluster remained confined inside the CNHox as well as reported for the 4cddp@CNTox (our notation) (MEJRI, *et al*., 2021). Next, we observed a gradual tilt (by 90°) of the CNHox that culminated in its landing upon the surface of the biomembranes (Figure 3.7C-D). While this stage is characterized by the alignment between the central axis of the CNHox and the plane of the membranes starting about 8 ns for the C_memb, the same occurred approximately 6 ns for the N_memb model. Lacerda *et al*. (LACERDA, *et al*., 2013) also showed a landing step (at ~50 ns) in the interaction mechanism of amino-functionalized CNT models and a POPC membrane. Also, by reporting a similar stage for the 4cddp@CNTox, Mejri and coworkers (MEJRI, *et al.*, 2021) verified the progressive release of the cddp molecules at 26, 60, 112, and 141 ns from the CNTox laid down on the surface of a POPC membrane.

After the landing stage, it was verified an insertion of the inclusion complex in the headgroups region of the membranes about 260 ns and 280 ns for the C_memb and N_memb

models, respectively (Figure 3.7E-F). However, while the 3cddp@CNHox complex is inserted into the C_memb by the nanowindow region, the same inclusion complex is inserted into the N_memb by the opened end with -OH groups at the edges (Figure A.21). This behavior is related to the different lipid composition between the two biomembranes. Unlike the C_memb model with overexpression of anionic lipids in the outer leaflet, the high homogeneity of the N_memb in terms of concentration of DOPC lipids in the outer monolayer may have contributed to the H bonds with the -OH groups located at the edge of the CNHox. This stage was also highlighted by insertions of one polar head (PC group) of the DOPC lipid from both membrane models into the cavity of the CNHox (see Figure A.21).

Despite the presence of this headgroup, the cddp molecules were not expulsed from the nanovector. Figure 3.7G-H illustrates the beginning of the last stage, which involved the penetration of the inclusion complex inside the biomembranes. In both membranes, the central axis of the 3cddp@CNHox complex slowly returned to the normal direction in relation to the membranes' plane. Nonetheless, while the complex started the penetration by the nanowindow region in the C_memb, the same complex tried to penetrate in the N_memb model by the oxidized edge of that nanostructure. Due to the strong repulsions between this oxidized region of the CNHox and hydrophobic tails of the membrane (OL tails), the process resulted in a deformation of the lipid bilayer plane that took at least 700 ns (Figure 3.7H). In contrast, this process was much faster in the C_memb (~460 ns), which also involved favorable interactions between the lipid tails and the nanowindow with H-terminated edges.

The energetic path of the interaction mechanism shown in Figure 3.7 was also monitored by calculating the pair interaction energies involving all species, namely, CNHox, cddp, membranes, waters, and ions. In the first 150 ns, Figure 3.8A-B shows that when the 3cddp@CNHox approached both membranes, the CNHox--WAT pair interaction energy increases (~42% for the C_memb and ~51% for the N_memb), since the CNHox--membrane pair interaction becomes increasingly prominent. Moreover, by comparing the interactions between the 3cddp@CNHox and the two biomembranes (yellow line in Figure 3.8) over the first 150 ns, we noticed that the energy decrease for the 3cddp@CNHox--N_memb system was more significant than with the 3cddp@CNHox--C_memb system, with a difference of ~80 kcal mol^{-1}. This result suggests that the inclusion complex--N_memb interactions were favorable during the approach and landing stages presented in Figure 3.7. This behavior may be connected with the orientation of the complex with the -OH-terminated edge facing the polar groups of the N_memb model, which consequently favored the interactions in that region.

When it comes to the 4cddp@CNTox complex near to a POPC-type membrane studied by Mejri and coworkers (MEJRI, *et al.*, 2021), the authors reported that the last stage of their interaction mechanism at 140 ns was the landing of the CNT on the biomembrane followed by the progressive release of cddp in the extracellular region of this lipid bilayer. Instead of that, in our system, the drug molecules remained encapsulated into the CNHox at 140 ns (landing stage), and we observed two new stages in the interaction mechanism (see Figure 3.7E-H).

Figure 3.8 - Evolution of the pair interaction energy (moving average) over the 800 ns simulation referring to the interactions between the 3cddp@CNHox inclusion complex and plasma membrane models, and the decomposition of these pair energies (E_{total}) into the vdW (E_{vdW}) and the electrostatic (E_{elec}) components. Pair energies related with the C_memb model: (A) and (C), and pair energies related with the N_memb model: (B) and (D). The moving averages were calculated for sets of 350 frames.

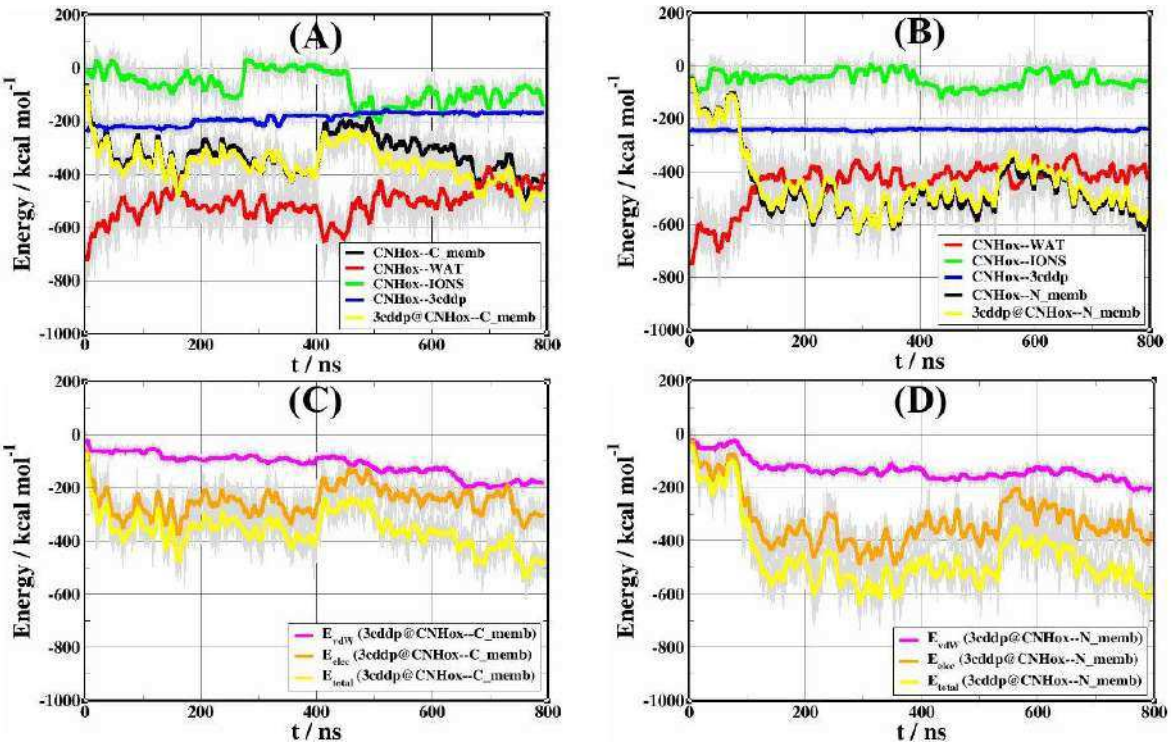

Reference: Own author (2021).

After 200 ns, the increase of the pair energy CNHox--WAT highlighted in Figure 3.8B also indicated a more significant insertion of the complex in the head groups region of the N_memb model relative to the C_memb model, followed by destabilization of the interactions with the solvent molecules. Concerning the CNHox--3cddp pair, we verified a stable behavior over all 800 ns simulation time, mainly in the N_memb model with average pair energy equals

to -242.0 ± 7.5 kcal mol^{-1}, whereas in the C_memb, it was -190.1 ± 24.1 kcal mol^{-1}. Figure 3.8C-D reveals that the 3cddp@CNHox--membrane dynamics (yellow line) was mainly dominated by coulombic interactions (orange line). For instance, while the interaction of the complex with the N_memb model was composed by about 71% of E_{elec}, the same interaction with the C_memb model was composed by ~67% of E_{elec}.

The host-guest affinities involving the 3cddp@CNHox complex and the membrane models were also analyzed by computing the binding free energies (Δ_bG) based on the MM/GBSA method (see Table 3.4). In particular, we investigated the stability of the 3cddp@CNHox complex in solution and when inserted in the membrane models, in addition to the interaction between this complex and the biomembranes.

By evaluating the data from Table 3.4 referring to the free inclusion complex, it was possible to note that the inclusion of a cluster formed by three cddp molecules into the CNHox cavity was still thermodynamically favorable, as well as the inclusion of either a dimer or monomer of this drug discussed in our last work (ALMEIDA, *et al.*, 2020). The thermodynamic stability of the 3cddp@CNHox system was also investigated when it was inserted with the plasma membrane models.

Our results showed that the presence of biomembranes provided an intensification of the complex stability. Specifically, when the complex was inserted into the C_memb model, the energy decreased by 23.7 kcal mol^{-1}, on average, relative to the free form. In contrast, the complex stability increased by 72.9 kcal mol^{-1} when it was interacting with the N_memb model. These results are interesting since they suggest that the complex is less stable in the presence of C_memb than N_memb and, therefore, the drug release would be facilitated in the presence of cancer cells relative to normal cells. In addition, the overall affinity between the 3cddp@CNHox and the membrane models was also evaluated (the last two processes in Table 3.4). Our results showed that, on average, the interaction between the 3cddp@CNHox complex and the C_memb model (Δ_bG = -116.9 ± 35.4 kcal mol^{-1}) was slightly more favorable on average than the one involving the N_memb model (Δ_bG = -110.6 ± 25.3 kcal mol^{-1}).

In order to determine the preferential interactions between either the cddp cluster or the 3cddp@CNHox complex and the different lipids that compose the membrane models, we computed the number of H bonds (HB) established over the 800 ns trajectories (Figure 3.9).

Table 3.4 - Comparison of the average values for the binding free energies (Δ_bG) referring to the inclusion complex (3cddp@CNHox) formed by a cluster of three cddp molecules encapsulated into one CNHox structure interacting with plasma membrane models of normal (N_memb) and cancer cells (C_memb) of the human breast.

Process	$\Delta_b G$ / kcal mol^{-1} [a]		
	Average	**Std.**[b]	**Err.**[c]
3cddp@CNHox [d]			
3cddp + CNHox → 3cddp@CNHox	-62.96	3.73	0.17
3cddp@CNHox inserted in the C_memb			
3cddp + CNHox → 3cddp@CNHox	-86.63	8.64	0.45
3cddp@CNHox inserted in the N_memb			
3cddp + CNHox → 3cddp@CNHox	-135.84	2.70	0.28
Interaction of the 3cddp@CNHox with the C_memb and N_memb models			
3cddp@CNHox + C_memb → 3cddp@CNHox>C_memb	-116.87	35.35	1.76
3cddp@CNHox + N_memb → 3cddp@CNHox>N_memb	-110.59	25.25	1.25

[a]Binding free energies calculated by using the molecular mechanics energies combined with the generalized Born and surface area continuum solvation (MM/GBSA) method. [b]Standard deviation value. [c]Standard error of mean reflects how precise the mean value is as an estimate of the true mean. [d]Inclusion complex in its free form as discussed in section 3.1. All average values refer to the last 200 ns of each simulation by taking into account a set of 384 frames for the systems involving membranes and a set of 1000 structures for the free complex.
Reference: Own author (2021).

Data from Figure 3.9 reveals that the number of HB formed between the inclusion complex and the C_memb model was substantially greater than that formed with the N_memb model, with a notable difference equal to 43,389 HB. When one considers only the cddp cluster, we verified the same behavior, in a less extension, where the number of HB formed with the C_memb model was about 43 times greater than the one involving the membrane of a healthy breast cell (N_memb). These findings are relevant since they suggest a selectivity degree of the 3cddp@CNHox model by the membranes of tumor cells. Moreover, it was noticed that 77% and 13% of the HB came from the interactions involving the polar groups PC and PE of neutral lipids. The presence of the anionic lipids was not significant to the formation of HB with either the complex or the drug molecules.

Figure 3.9 - The total number of HB formed between either the 3cddp@CNHox complex or the cddp cluster and the lipids that compose the C_memb and N_memb models during the 800 ns simulations.

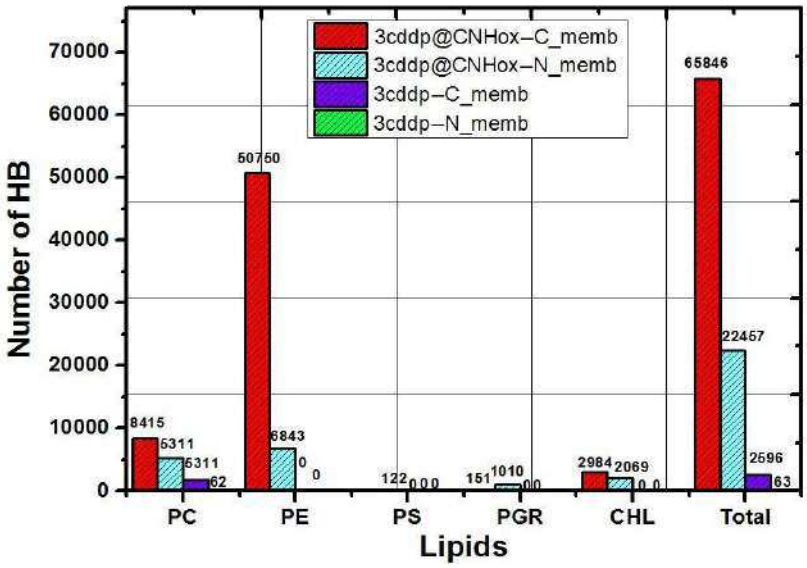

Reference: Own author (2021).

At last, the complete translocation of the 3cddp@CNHox throughout the two membrane models followed by the cddp release from the cavity of the CNHox was not observed over the 800 ns simulation time. The results suggest that these processes are both active and slow with high free energy barriers. Based on experimental data, Panczyk and coworkers (PANCZYK, *et al.*, 2013) estimated an energy barrier equal to 85 kJ mol^{-1} for the release of cddp from CNT (L = 200 Å and D = 100 Å) capped by magnetic nanoparticles. Using the Fick's first law, the authors also estimated that the release of 5% of the cddp would take 15 μs to complete. In order to overcome this energetic barrier and improve the cddp targeting effect to the tumor cells, the application of external agents, such as the near infrared (NIR) irradiation (CURCIO, *et al*., 2021; LANCETA, *et al.*, 2020) and external magnetic field (CURCIO, *et al*., 2021) have been pointed out as a promising alternative due to the photothermal properties of CNH.

It is worth to mention that our approach has some limitations, such as the use of only unbiased MD simulations to describe the events and the free energies related with our systems. In this sense, the application of enhanced sample methods, such as steered MD (BOUBETA, *et al.,* 2019), umbrella sampling simulations (KÄSTNER, 2011), metadynamics (BUSSI & LAIO, 2020), and Markov state model (HUSIC & PANDE, 2018), would also be a relevant topic, since it could not only improve the statistical validity of our results, but also provide the potentials of mean force referring to the processes described in this work. Another alternative to enhance our results would be to conduct simulation replicas, such as the triplicates with different random

seeds. Despite these limitations, the simulations provide an initial exploration of the interactions between CNH-based carriers loaded with cddp molecules and biomembranes model of human breast cells. Future studies will cover the applications of enhanced sample methods in order to derive the free energy profile for the cddp release from CNH and the permeation through the membranes.

In summary, the present study described a molecular interaction mechanism between CNHox as nanocontainers of cddp molecules and plasma membrane models of normal and cancer cells of a typical human breast. The insights raised by this work may not only fill up the gap of studies related to the behavior of these carbon nanomaterials in biological systems but also impulse the development of experimental protocols for pre-clinical trials in the context of cancer treatment.

3.4 CONCLUSIONS

In this work, we performed an analysis based on MD simulations of the interactions between CNHox loaded with cddp molecules, 3cddp@CNHox, and plasma membrane models of cancer and normal cells. Two realistic membrane models (C_memb and N_memb) were built based on experimental data referring to both composition and distribution of lipids in a typical human breast. The simulation of the free 3cddp@CNHox complex in an aqueous solution verified that the three cddp molecules, which formed a stable cluster inside the cavity of the CNHox, remained encapsulated into this functionalized nanomaterial during the simulation time. The favorable interactions with the inner part of the CNHox cavity explain the high stability of this complex, mainly due to the vdW contributions. When the loaded CNHox was in the presence of plasma membranes, the results demonstrated the interaction mechanism between the 3cddp@CNHox complex and these biological systems, which involved the approach, landing, insertion, and penetration stages. While the penetration stage into the C_memb model initiated at ~400 ns, the same stage in the N_memb started at ~700 ns accompanied by a deformation of the lipid bilayer. The MM-GB/SA interaction energy indicated a stable behavior of the inclusion complex interacting with the biomembranes over the 800 ns trajectories. Moreover, this analysis suggested that the cddp releasing from the CNHox cavity would be more favorable in the presence of C_memb than N_memb. Besides, the complex affinity by C_memb was 6.3 kcal mol^{-1} more favorable than by N_memb due to the large number of H-bonds. In summary, the present in study led to two important conclusions suggesting the potentiality of the CNHox-based DDS for cddp: (i) the interaction of the DDS with cancer cells would be faster and slightly

more favorable than with healthy cells, and (ii) once in the presence of cancer cell, the cddp releasing would be more favorable compared with the normal cells. Although this *in silico* study requires more investigations regarding the interactions and effects on healthy cells, the aforementioned conclusions reinforce some desirable aspects of the CNH loaded with cddp molecules in the context of breast cancer treatments.

REFERENCES

AJIMA, K.; *et al*. Material storage mechanism in porous nanocarbon. **Advanced Materials**, v. 16, p. 397-401, 2004.

AJIMA, K.; *et al*. Carbon nanohorns as anticancer drug carriers. **Molecular Pharmaceutics**, v. 2, n. 6, p. 475-480, 2005.

AJIMA, K.; *et al.* Effect of functional groups at hole edges on cisplatin release from inside single-wall carbon nanohorns. **Journal of the Physical Chemistry B**, v. 110, n. 11, p. 5773-5778, 2006.

AJIMA, K. *et al*. Enhancement of In Vivo Anticancer Effects of Cisplatin by Incorporation Inside Single-Wall Carbon Nanohorns. **ACS Nano**, v. 2, n. 10, p. 2057-2064, 2008.

AL-BAHLANI, S.; *et al*. Platinum-Based Drugs Differentially Affect the Ultrastructure of Breast Cancer Cell Types. **BioMed Research International**, v. 2017, n. 3178794, p. 1-13, 2017.

ALMEIDA, E. R.; *et al*. Molecular dynamics of carbon nanohorns and their complexes with cisplatin in aqueous solution. **Journal of Molecular Graphics and Modelling**, v. 89, p. 167-177, 2019.

ALMEIDA, E. R.; *et al*. Chemically Modified Carbon Nanohorns as Nanovectors of the Cisplatin Drug: A Molecular Dynamics Study. **Journal of Chemical Information and Modeling**, v. 60, n. 2, p. 500-512, 2020.

ANDOH, Y.; *et al*. Molecular dynamics study of lipid bilayers modeling the plasma membranes of normal murine thymocytes and leukemic GRSL cells. **The Journal Physical Chemistry**, v.144, p. 1-14, 2016.

BERENDSEN, H. J. C.; *et al*. Molecular dynamics with coupling to an external bath. **The Journal Chemical Physics**, v. 81, p. 3684-3690, 1984.

BERNARDES, N. & FIALHO, A. M. Perturbing the Dynamics and Organization of Cell Membrane Components: A New Paradigm for Cancer-Targeted Therapies. **International Journal of Molecular Science**, v. 19, n. 3871, p. 1-19, 2018.

BOUBETA, F. M.; *et al*. Lessons learned about steered molecular dynamics simulations and free energy calculations. **Chemical Biology & Drug Design**, v. 93, p. 1-10, 2019.

BRENEMAN, C. M. & WIBERG, K. B. Determining atom-centered monopoles from molecular electrostatic potentials. The need for high sampling density in formamide conformational analysis. **Journal of Computational Chemistry**, v. 11, n. 3, 1990.

BUSSI, G. & LAIO, A. Using metadynamics to explore complex free-energy landscapes. **Nature Reviews Physics**, v. 2, p. 200-212, 2020.

CASE, D. A.; *et al*. **AMBER 2016**, University of California, San Francisco, 2016.

CASE, D. A.; *et al*. **AMBER 2019**, University of California, San Francisco, 2019.

CANCÈS, E.; MENNUCCI, B.; TOMASI, J. A new integral equation formalism for the polarizable continuum model: theoretical background and applications to isotropic and anisotropic dielectrics. **The Journal of Chemical Physics**, v. 107, p. 3032-3041, 1997.

CHEN, J.; *et al*. Inorganic Nano-Targeted Drugs Delivery System and Its Application of Platinum-Based Anticancer Drugs. **Journal of Nanoscience and Nanotechnology**, v. 17, n. 1, p. 1-17, 2017.

CURCIO, M.; *et al*. Carbon Nanohorns as Effective Nanotherapeutics in Cancer Therapy. **C – Journal of Carbon Research**, v. 7, n. 3, p. 1-18, 2021.

DARDEN, T.; YORK, D.; PEDERSEN, L. An N·log(N) Method for Ewald Sums in Large Systems. **The Journal of Chemical Physics**, v. 98, n. 12, p. 10089-10092, 1993.

DA SILVA, A. M..; *et al*. New insights on chemical oxidation of single-wall carbon nanotubes: a theoretical study. **The Journal of Physical Chemistry C**, v. 113, p. 10079-10084, 2009.

DE SOUZA, L. A.; *et al*. DFT study of cisplatin@carbon nanohorns complexes. **Journal of Inorganic Biochemistry**, v. 129, p. 71-83, 2013.

DE SOUZA, L. A.; *et al*. Oxidized single-walled carbon nanotubes and nanocones: a DFT study. **Royal Society of Chemistry Advances**, v. 7, p. 13212-13222, 2017.

DE SOUZA, L. A.; *et al*. Inclusion complexes between cisplatin and oxidized carbon nanostructures: a theoretical approach. **Journal of Inorganic Biochemistry**, v. 178, p. 134-143, 2018.

DE SOUZA, L. A.; *et al*. Cisplatin release from inclusion complex formed by oxidized carbon nanotube: A DFT study. **Chemical Physics Letters**, v. 774, p. 138619-138626, 2021.

DEWAR, M. J. S.; *et al.* Development and use of quantum mechanical molecular models. 76. AM1: a new general purpose quantum mechanical molecular model. **Journal of the American Chemical Society**, v. 107, n. 13, p. 3902-3909, 1985.

DICKSON, C. J.; *et al*. Lipid14: The Amber Lipid Force Field. **Journal of Chemical Theory and Computation**, v. 10, p. 865-879, 2014.

DOS SANTOS, H. F.; *et al.* Structure, Stability, and Infrared Spectrum of Capped Carbon Cones: A DFTB Study. **The Journal of Physical Chemistry C**, v. 118, n. 42, p. 24761-24768, 2014.

DILRUBA, S. & KALAYDA, G. V. Platinum-based drugs: past, present and future. **Cancer Chemotherapy and Pharmacology**, v. 77, n. 6, p. 1103-1124, 2016.

DUAN, X; *et al*. Nanoparticle formulations of cisplatin for cancer therapy. **WIREs Nanomedicine and Nanobiotechnology**, v. 8, n. 5, p. 776-791, 2016.

FENG, Y.; *et al*. Breast cancer development and progression: Risk factors, cancer stem cells, signaling pathways, genomics, and molecular pathogenesis. **Genes Diseases**, v. 5, n. 2, p. 77-106, 2018.

FRISCH, M. J.; *et al*. Gaussian 09, revisão D.01.; Gaussian, Inc.: Wallingford, CT, 2009.

GODONEA, R. L. N.; et al. Clinical and molecular aspects of breast cancer: Targets and therapies. **Biomedicine & Pharmacotherapy**, v. 106, p. 14-34, 2018.

HARE, J. I.; *et al.* Challenges and strategies in anti-cancer nanomedicine development: An industry perspective. **Advanced Drug Delivery Reviews**, v. 108, p. 25-38, 2017.

HARBECK, N.; *et al*. Breast Cancer. **Nature Reviews Disease Primers**, v. 5, n. 66, p. 1-31, 2019.

HAY, P. J. & WADT, W. R. Ab initio effective core potentials for molecular calculations. Potentials for K to Au including the outermost core orbitals. **The Journal of Chemical Physics**, v. 82, p. 299-310, 1985.

HE, B.; *et al*. Single-walled carbon-nanohorns improve biocompatibility over nanotubes by triggering less protein-initiated pyroptosis and apoptosis in macrophages. **Nature Communications**, v. 9, n. 2393, p. 1-21, 2018.

HEHRE, W. L. ; DITCHFIELD, R. ; POPLE, J. A. Self-Consistent Molecular Orbital Methods. XII. Further Extensions of Gaussian-Type Basis Sets for Use in Molecular Orbital Studies of Organic Molecules. **Journal of Chemical Physics**, v. 56, n. 5, p. 2257-2261, 1972.

HESTENES, M. R. & STIEFEL, E. Methods of Conjugate Gradients for Solving Linear Systems. **Journal of Research of the National Bureau of Standards**, v. 49, p. 409-436, 1952.

HUNG, W. C.; *et al*. The condensing effect of cholesterol in lipid bilayers. **Biophysical Journal**, v. 92, p. 3960-3967, 2007.

HUSIC, B. E. & PANDE, V. S. Markov state models: from an art to a science. **Journal of the American Chemical Society**, v. 140, n. 7, 2018.

IIJIMA, S.; *et al*. Nano-Aggregates of Single-Walled Graphitic Carbon Nanohorns. **Chemical Physics Letters**, v. 309, p. 165-170, 1999.

ISAAC, K. M.; *et al*. Functionalization of single-walled carbon nanohorns for simultaneous fluorescence imaging and cisplatin delivery in vitro. **Carbon**, v. 138, p. 309-318, 2018.

JENSEN, F. **Introduction to Computational Chemistry**, John Wiley & Sons, 2nd edition, Chichester, UK, 2007

JO, S.; *et al*. CHARMM-GUI: A Web-based Graphical User Interface for CHARMM. **Journal of Computational Chemistry**, v. 29, p. 1859-1865, 2008.

JORGENSEN, W. L.; *et al*. Comparison of Simple Potential Functions for Simulating Liquid Water. **The Journal of Chemical Physics**, v. 79, p. 926-935, 1983.

JOWET, M. The phosphatide and cholesterol contents of normal and malignant human tissues. **Biochemical Journal**, v. 25, p. 1991–1998, 1931.

KAROUSIS, N.; *et al*. Structure, properties, functionalization, and applications of carbon nanohorns. **Chemical Reviews**, v. 116, n. 8, p. 4850-4883, 2016.

KRASZEWSKI, S.; *et al*. Insertion of Short Amino-Functionalized Single-Walled Carbon Nanotubes into Phospholipid Bilayer Occurs by Passive Diffusion. **PLoS ONE**, v. 7, p. 1-11, 2012.

LACERDA, L.; *et al*. How do functionalized carbon nanotubes land on, bind to and pierce through model and plasma membranes. **Nanoscale**, v. 5, p. 10242-10250, 2013.

LANCETA, A. M.; BOSCH, M. M.; LESMES, P. M. Single-Walled Carbon Nanohorns as Promising Nanotube-Derived Delivery Systems to Treat Cancer. **Pharmaceutics**, v. 12, n. 850, p. 1-21, 2020.

LEE, J.; *et al*. CHARMM-GUI supports the Amber force fields. **The Journal of Chemical Physics**, v. 153, n.3, p.1-9, 2020.

LI, P.; *et al*. Systematic Parameterization of Monovalent Ions Employing the Nonbonded Model. **Journal of Chemical Theory and Computation**, v. 11, n. 4, p. 1645-1657, 2015.

LOPES, J. F.; *et al.* Theoretical study of the potential energy surface for the interaction of cisplatin and their aquated species with water. **Journal of Chemical Physical**, p. 128, n. 16, p. 16510-165117, 2008.

KÄSTNER, J. Umbrella Sampling. **WIREs Computational Molecular Science**, v. 1, p.932-942, 2011.

MADEJ, B. D.; GOULD, I. R.; WALKER, R. C. A Parameterization of Cholesterol for Mixed Lipid Bilayer Simulation within the Amber Lipid14 Force Field. **The Journal of Physical Chemistry B**, v. 119, p. 12424-12435, 2015.

MATSUMURA, S.; *et al*. Ultrastructural localization of intravenously injected carbon nanohorns in tumor. **International Journal of Nanomedicine**, v. 9, p. 3499-3508, 2014.

MEJRI, A.; *et al*. Encapsulation into Carbon Nanotubes and Release of Anticancer Cisplatin Drug Molecule. **The Journal of Physical Chemistry B**, v. 119, p. 604-611, 2015.

MEJRI, A.; *et al*. Confinement of the antitumoral drug cisplatin inside edge-functionalized carbon nanotubes and its release near lipid membrane. **The European Physical Journal D**, v. 75, n. 99, p. 1-10, 2021.

MERCHANT, T. E.; *et al*. ^{31}P Magnetic resonance phospholipid profiles of neoplastic human breast tissues. **British Journal of Cancer**, v. 63, p. 693-698, 1991.

MILLER III, B. R.; *et al*. MMPBSA.py: An Efficient Program for End-State Free Energy Calculations. **Journal of Chemical Theory and Computation**, v. 8, n. 9, p. 3314-3321, 2012.

MIYAWAKI, J.; *et al*. Toxicity of Single-Walled Carbon Nanohorns. **ACS Nano**, v. 2, n. 2, p. 213-226, 2008.

MØLLER, C. & PLESSET, M. S. Note on an Approximation Treatment for Many-Electron Systems. **Physical Review**, v. 46, p. 618-622, 1934.

MURAKAMI, T.; Drug-loaded carbon nanohorns: adsorption and release of dexamethasone in vitro. **Molecular Pharmaceutics**, v. 1, n. 6, p. 399-405, 2004.

MURATA, K.; *et al*. Nanowindow-Induced Molecular Sieving Effect in a Single-Wall Carbon Nanohorn. **The Journal of Physical Chemistry B**, v. 106, n. 49, p. 12668-12669, 2002.

NAGLE, J. F. & TRISTAM-NAGLE, S. Structure of lipid bilayers. **Biochimica et Biophysica Acta**, v. 1469, n. 3, p. 159-195, 2000.

NAKAMURA, M.; *et al.* Single-walled carbon nanohorns as drug carriers: adsorption of prednisolone and anti-inflammatory effects on arthritis. Nanotechnology, v. 22, n. 46, p. 465102-465110, 2011.

PANCZYK, T.; *et al*. Molecular dynamics study of cisplatin release from carbon nanotubes capped by magnetic nanoparticles. **The Journal of Physical Chemistry C**, v. 117, p. 17327-17336, 2013.

ROE, D. R. & CHEATHAM. III. PTRAJ and CPPTRAJ: Software for Processing and Analysis of Molecular Dynamics Trajectory Data. **Journal of Chemical Theory and Computation**, v. 9, p. 3084-3095, 2013.

RIVEL, T.; RAMSEYER, C.; YESYLEVSKYY. The asymmetry of plasma membranes and their cholesterol content influence the uptake of cisplatin. **Scientific Reports**, v. 9, n. 5627, p. 1-14, 2019.

RYCKAERT, J. P.; CICCOTTI, G.; BERENDSEN, H. J. C. Numerical integration of the Cartesian equations of motion of a system with constraints: Molecular dynamics of n-alkanes. **Journal of Computational Physics**, v. 23, n. 3, p.327-341, 1977.

SALAS-TREVINO, D.; et al. Carbon nanotubes: An alternative for platinum-based drugs delivery systems. **Journal of the Balkan Union of Oncology**, v. 23, n. 3, p. 541-549, 2018.
SALOMON-FERRER, et al. Routine Microsecond Molecular Dynamics Simulations with AMBER on GPUs. 2. Explicit Solvent Particle Mesh Ewald. **Journal of Chemical Theory Computational**, v. 9, p. 3878-3888, 2013.

SHARMA, B & KANWAR, S. S. Phosphatidylserine: A cancer cell targeting biomarker. **Seminars in Cancer Biology**, n. 52, p. 17-25, 2018.

SKJEVIK, Å. A.; et al. LIPID11: A Modular Framework for Lipid Simulations Using Amber. **The Journal of Physical Chemistry B**, v. 116, p. 11124-11136, 2012.

STEVIC, D.; *et al*. Cu-phthalocyanine-mediated nanowindow production on single-wall carbon nanohorn. **Molecular Physics**, 2020, DOI: https://doi.org/10.1080/00268976.2020.1815883.

TAHARA, Y.; *et al.* Histological assessments for toxicity and functionalization-dependent biodistribution of carbon nanohorns. **Nanotechnology**, v. 22, p. 265106-265114, 2011.

The PyMOL Molecular Graphics System, Version 1.8 Schrödinger, LLC, 2009-2015.

TODOR, I. N.; LUKYANOVA, N. Y.; CHEKHUN, V. F. The lipid content of cisplatin- and doxorubicin resistant mcf-7 human breast cancer cells. **Experimental Oncology**, v. 34, n. 2, p. 97-100, 2012.

UBERUAGA, B. P.; ANGHEL, M.; VOTER, A. F. Synchronization of trajectories in canonical molecular-dynamics simulations: Observation, explanation, and exploitation. **The Journal of Chemical Physics**, v. 120, p. 6363-6374, 2004.

VECLANI, D. TOLAZZI, M; MELCHIOR, A. Molecular Interpretation of Pharmaceuticals' Adsorption on Carbon Nanomaterials: Theory Meets Experiments. **Processes**, v. 8, n. 642, 2020.

WAKS, A. G. & WINER, E. P. Breast Cancer Treatment: A Review. **Journal of the American Medical Association**, v. 321, n. 3, p. 288-300, 2019.

WANG, J.; *et al*. Development and testing of a general amber force field. **Journal of Computational Chemistr**y, v. 25, n. 9, p. 1157-1174, 2004.

YANG, J.; *et al*. Dual Chemodrug-Loaded Single-Walled Carbon Nanohorns for Multimodal Imaging-Guided Chemo-Photothermal Therapy of Tumors and Lung Metastases. **Theranostics**, v. 8, n. 7, p. 1966-1984, 2018.

YESYLEVSKYY, S. O.; RIVEL, T.; RAMSEYER, C. The influence of curvature on the properties of the plasma membrane. Insights from atomistic molecular dynamics simulations. **Scientific Reports**, v. 7, n. 16078, p. 1-13, 2017.

ZHANG, M; *et al*. Biodegradation of Carbon Nanohorns in Macrophage Cells. **Nanoscale**, v. 7, p. 2834-2840, 2015.

ZHENG, S.; *et al*. VFFDT: a new software for preparing AMBER force field parameters for metal-containing molecular systems. **Journal of Chemical Information and Modeling**, v. 56, p. 811-818, 2016.

4 CHAPTER 4

Unveiling the releasing processes of Pt(II)-based anticancer drugs from oxidized carbon nanohorn: an in silico study

4.1 INTRODUCTION

The carbon nanohorns (CNH) consist in a class of carbon allotropes that has been attracting a growing attention over the last 22 years, due to the potential applications in the context of energy conversion (ZHANG, *et al*., 2015), catalysis (KAGKOURA & TAGMATARCHIS, 2020), gas storage (SANO, *et al*., 2014), biosensors (FORD, *et al.*, 2019), biomaterials (SELVAM, *et al*., 2020) and drug delivery systems (DDS) (KOKUBUN, *et al*., 2018). Typical structures of such carbonaceous nanomaterial present a tubular section with a length of 30-50 nm coupled to a cone-shaped tip with an average cone angle of 20° (IIJIMA, *et al*., 1999). By variating pressure and buffer gas conditions during the synthesis, thousands of these nanostructures form spherical aggregates with a diameter of 80-100 nm in two possible forms: dahlia-like and bud-like forms (KASUYA, *et al*., 2002).

The promising aspects of the CNH are connected with their large-scale production with high purity, thermal stability, semiconductor properties, large surface area, porosity, and the capacity to encapsulate clusters of small drug molecules (KAROUSIS, *et al*., 2016). Furthermore, in the nanomedicine field, the CNH represent an attractive DDS since their hydrophobicity and poor dispersibility in aqueous solution can be reduced by means of chemical functionalization, such as the oxidation reactions and the non-covalent decoration with metal nanoparticles, porphyrins, and pyrene units (CURCIO, *et al.*, 2021). These post-synthesis treatments also contribute to the outstanding biocompatibility of these carbon-based nanovectors, which is, in turn, superior to the one related to the carbon nanotubes (CNT) (HE, *et al*., 2018).

Recently, using multispectral optoacoustic tomography imaging, Shi and coworkers (SHI, *et al*., 2019) conducted a broad study involving the biodistribution of oxidized CNH (CNHox) in live mice. The authors demonstrated that while the intravenous injection of CNHox resulted in their accumulation in the spleen and liver, oral gavage led to a concentration in the gastrointestinal tract, and hypodermic and intramuscular applications caused a distribution around the injection region. In addition to the low toxicities (MIYAWAKI, *et al*., 2008; MORENO-LANCETA, *et al*., 2020), the *in vitro* study conducted by Zhang and coworkers

(ZHANG, *et al*., 2015) shows that 30% of the CNH were biodegraded in macrophage cells, and 60% were degraded by an oxidation process catalyzed by the myeloperoxidase enzyme.

Concerning the use of CNH as nanovectors in cancer therapy, the encapsulation of the well-known cisplatin (*cis*-diaminedichloroplatinum(II)), named herein as cddp (see Figure 4.1A), into this carbon nanomaterial has been a widely studied strategy (AJIMA, *et al*., 2005; AJIMA, *et al*., 2006; AJIMA, *et al*., 2008; MATSUMURA, *et al*., 2007; DEWITT, *et al.*, 2014).

Figure 4.1 - Structures of the three worldwide approved Pt(II)-based drugs: cisplatin (A), carboplatin (B), and oxaliplatin (C).

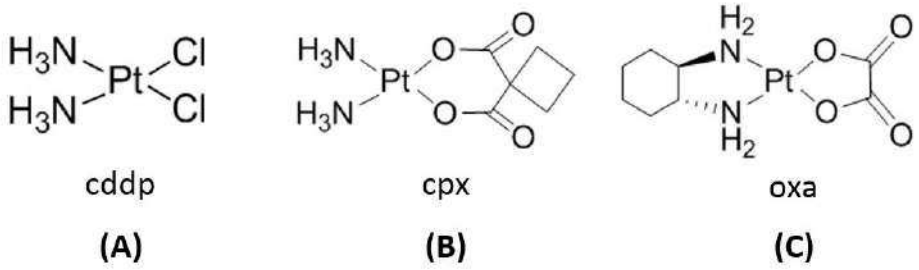

Reference: Own author (2022).

It occurs due to the strong antitumor activity of this drug and the possibility to reduce its severe side effects (CURCIO, *et al*., 2021; OUN, *et al*., 2018). In this context, Lucío and coworkers (LUCÍO, *et al*., 2017) developed a selective CNH-based nanocarrier with cddp molecules as prodrug species for killing prostate cancer cells. The efficiency of this DDS in selectively targeting the tumor cells was achieved due to the attachment of the monoclonal antibody D2B, which presented a selectivity for prostate-specific membrane antigen (PSMA), onto the surface of these nanomaterials. Moreover, some strategies for cancer treatment consider the usage of CNH as nanocontainers for cddp molecules, such as cancer theranostics (ISAAC, *et al*., 2018), multi-drug synergism (YANG, *et al*., 2018), and phototherapy (DEWITT, *et al*., 2014).

In addition to the medication with cddp, the other two Pt(II)-based drugs used worldwide for the treatment of many solid tumors are the carboplatin (*cis*-diammine(1,1-cyclobutane dicarboxylato)platinum(II)), named herein as cpx (see Figure 4.1B), and the oxaliplatin (*cis*-oxalato-trans-l-1,2-diaminocyclohexaneplatinum(II)), henceforth named as oxa (see Figure 4.1C) (DILRUBA & KALAYDA, 2016). Since these metallodrugs also induce tumor cell resistance and a number of side effects, such as the myelosuppression by cpx and the

neurotoxicity by oxa (OUN, *et al.*, 2018), their encapsulation in carbon nanomaterials may also represent a promising strategy to overcome adverse effects. In this sense, numerous experimental (ARLT, *et al*., 2010; WU, *et al*., 2013; BALAS, *et al.*, 2016; SALAS-TREVIÑO, *et al*., 2019) and theoretical (MAHDAVIFAR & MORIDZADEH, 2014; KHATTI & HASHEMIANZADEH, 2015; EL KHALIFI, *et al.*, 2015; KHATTI, *et al.*, 2018) studies have demonstrated the potential of CNT as DDS for cpx and oxa by providing drug protection and a slow and concentrated drug delivery to the tumor sites. Similarly, the incorporation of cpx into boron nitride nanotubes (BNNT) has also been investigated in the light of molecular dynamics (MD) simulations and density functional theory (DFT) calculations (BENTIN, *et al*., 2019; EL KHALIFI, *et al.*, 2016; EL KHALIFI, *et al.*, 2015). However, presumably, there are no previous theoretical studies in the literature on the encapsulation of either oxa or cpx into CNH.

When it comes to the drug release from CNH, Iijima and coworkers (AJIMA, *et al*., 2006; AJIMA, *et al*., 2006) demonstrated that the holes, also known as nanowindows (MURATA, *et al.*, 2002), formed on the surface of these nanovectors during the oxidation treatment, represent the main routes for this process. In order to protect these nanowindows from the plug effect, where the -COOH and -OH groups located at the hole edges are replaced by -COONa and -ONa, Iijima and coworkers (AJIMA, *et al*., 2006) proposed a reduction reaction involving flow of H_2 gas at 1,200°C for 3 h. Using this chemical treatment, the authors showed an increase of 55% in the quantity of cddp released from the CNH with less oxygenated groups at the nanowindows edges. In a more recent study, Stevic and coworkers (STEVIC, *et al.*, 2021) proposed a method for a controlled formation of uniform nanowindows of about 0.5 nm in size on the walls of CNH by using copper phthalocyanine. In addition to adsorbing on the CNH surface, the authors demonstrated that this compound catalyzed the oxidation process conducted in O_2 at high temperature (~573 K).

In spite of being reported by experimentalists, the drug release from the CNH cavity is not promptly achieved using unbiased MD simulations, since this process seems to involve energy barriers superior to the thermal energy. Furthermore, the energy barrier is probably even higher in the conical part of the CNH due to the strong confinement effect in this region, as described by Furmaniak and coworkers (FURMANIAK, *et al.*, 2018). By using reactive Monte Carlo simulations, these authors showed an intensification of the interactions between the reacting molecules and the carbon wall located at the conical section of CNH. This confinement effect due to the strong interactions between the encapsulated molecules and the CNH cavity was also discussed in in our last works (ALMEIDA, *et al.*, 2019; ALMEIDA, *et al.*, 2020), when we evaluated the structure and stability of this nanomaterial acting as nanovectors of the

cddp. By using pristine and chemically modified topologies of CNH with small nanowindows, we showed that the cddp clusters, formed by two cddp molecules, remained trapped in the cavity during the simulation time (200 ns). More recently (ALMEIDA, *et al*., 2021), we reported an average pair interaction energy of -162.9 kcal mol^{-1} for the 3cddp@CNHox complex (three cddp molecules encapsulated into a CNHox), which also supported the high stability of this inclusion complex. Panczyk and coworkers (PANCZYK, *et al*., 2013) pointed out that the release of cddp molecules from multiwalled CNT capped by magnetic nanoparticles involved energy barriers that were not achieved using conventional MD simulations. In order to provide a controlled release of cddp, the authors performed MD simulations in which they applied an external magnetic field of 9.3 T along the perpendicular direction to the CNT axis.

In addition to the application of magnetic and electric fields in MD simulations, the use of enhanced sampling methods, such as the Steered Molecular Dynamics (SMD) (BOUBETA, *et al.*, 2019) and Umbrella Sampling (US) (KÄSTNER, 2011) simulations, consist of robust alternatives for describing the drug release thermodynamics in terms of the potentials of mean force (PMF). These biased methods are relevant since they provide a broad sampling of the phase space, including the high energy states with significant probabilities, which would not be approached by unbiased simulations (COVA, *et al.*, 2017). Recently, by using the adaptive biasing force (ABF) method, Mejri and coworkers (MEJRI, *et al*., 2021) computed the free energy profiles for the cddp release from CNT models with carbon (CNT-C), hydrogen (CNT-H), and oxygen (CNT-OH) atoms at the edges of these tubes. The authors demonstrated that the energy barrier for the drug release from the CNT-H was 1.1 kcal mol^{-1}, whereas the barriers for the CNT-H and CNT-OH models were 2.3 kcal mol^{-1} and 3.3 kcal mol^{-1}. From semi-rigid scan calculations of the potential energy surface at the B3LYP/LANL2DZ/6-31G (gas phase) level, our group also demonstrated that the cddp release from a nanowindow of a CNTox model was thermodynamically favorable (~-25 kcal mol^{-1}), and kinetically unfavorable with a free energy barrier of 58.4 kcal mol^{-1} (DE SOUZA, *et al.*, 2021).

To the best of our knowledge, previous studies have not provided a detailed molecular description of the releasing process of Pt(II)-based drugs approved worldwide from the nanowindows of CNH. Therefore, the present study intends to fill this gap by presenting an analysis focused on the energy profiles of the inclusion and adsorption processes involving Pt(II) anticancer drugs (cddp, cpx, and oxa) and a CNHox model. This systematic analysis was based on unbiased and biased MD simulations performed in aqueous solution considering the physiological environment conditions. The results reported in this study are relevant, since they

may reinforce the promising application of the CNH in the context of more effective therapies in oncology.

4.2 METHODS

4.2.1 Molecular models

Regarding the CNH structure, we employed the same oxidized topology ($C_{280}H_{54}O_{41}$) reported in our last paper (ALMEIDA, *et al.*, 2021) with average length and diameter of 27.4 Å and 9.0 Å. In brief, this model, henceforth termed CNHox, has hydroxyl, carbonyl, and carboxyl groups on its surface due to the oxidation mechanism with O_2 and H_2O (DE SOUZA, *et al.*, 2017; DA SILVA, *et al.*, 2009). In addition to the presence of hydroxyls at the open end, this prototype includes a nanowindow with an average diameter of 11 Å on its surface, which agrees with the experimental data from this oxidation process (AJIMA, *et al.*, 2004). Moreover, the carbon atoms at the nanowindow edge were modelled with C-H bonds to reproduce the product provided by the reduction reaction (H_2 gas flow, 1,200°C) (AJIMA, *et al.*, 2006). Thus, the CNHox structure was optimized at the Austin Model 1 (AM1) semiempirical level in aqueous solution, using the polarizable continuum model (PCM) with the integral equation formalism (IEF) variant (DEWAR, *et al.*, 1985; CANCÈS, *et al*., 1997).

The structures of the three Pt(II)-based drugs (Figure 4.1) were also optimized in aqueous solution (PCM) (CANCÈS, *et al*., 1997) at the MP2/6-31G(d,p)/LANL2DZ level of theory (MØLLER & PLESSET, 1934 ; HEHRE, *et al*., 1972 ; HAY & WADT, 1985). By using the optimized geometries of the CNHox and the three Pt(II)-containing drugs (cddp, cpx, and oxa), we built three inclusion complexes labeled as cddp@CNHox, cpx@CNHox, and oxa@CNHox, in which each anticancer drug was positioned at the center of mass (CM) of the nanostructure. Additionally, to study the adsorption processes, we also built three adsorption complexes named as cddp>CNHox, cpx>CNHox, and oxa>CNHox, where the drugs interact with the outside CNHox surface. Figure 4.2 presents the chemical structures of these six complexes.

By considering the three inclusion complexes (Figure 4.2A-4.2C), we proposed two drug release modes, as represented in Figure 4.3, representing the most likely configurations for this process based on the size of both nanowindow and Pt(II) drugs. Index 1 in the nomenclature of these complexes indicates Mode 1 (cddp1@CNHox, cpx1@CNHox, and oxa1@CNHox), whereas index 2 indicates the Mode 2 (cddp2@CNHox, cpx2@CNHox, and

oxa2@CNHox). This difference related to drug release mode was taken into account only in the biased MD simulations.

Figure 4.2 - Initial structures of the inclusion and adsorption complexes: cddp@CNHox (A), cpx@CNHox (B), oxa@CNHox (C), cddp>CNHox (D), cpx>CNHox (E), and oxa>CNHox (F). The silver, red, white, green, blue, and golden colors refer to the C, O, H, Cl, N, and Pt atoms.

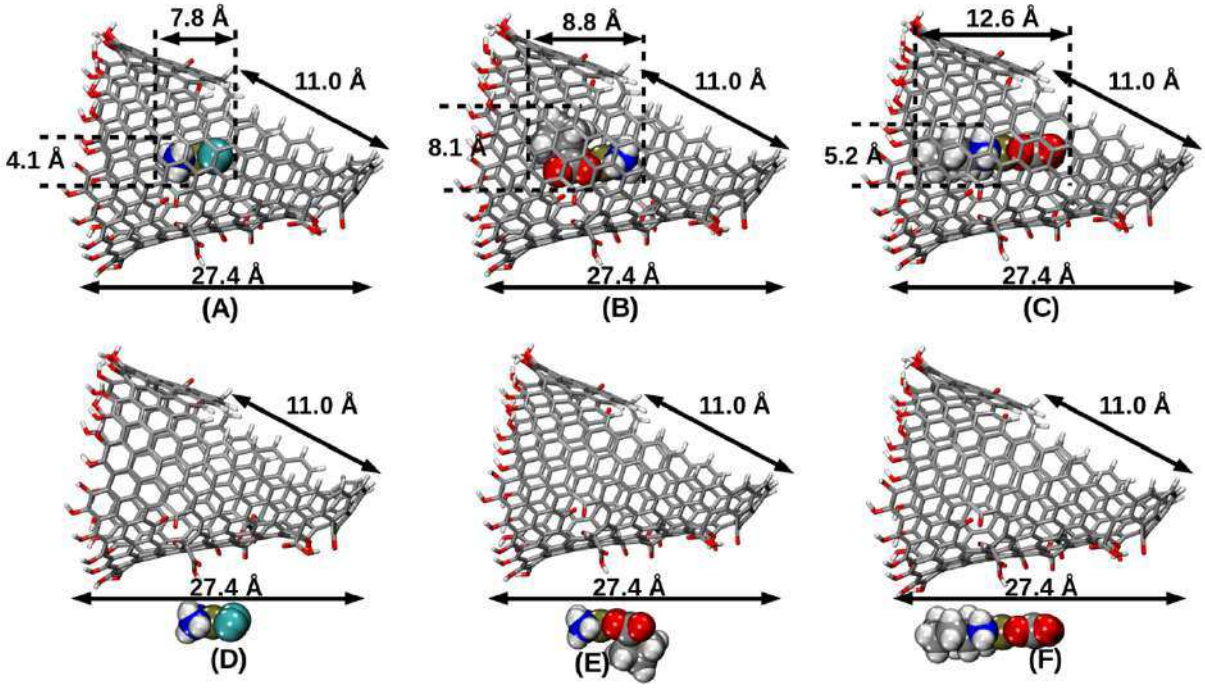

Reference: Own author (2022).

4.2.2 Force field parameterizations

With regard to the CNHox model, the GAFF2 (WANG, *et al.*, 2004) was used to describe the intramolecular and 12-6 Lennard Jones potential (12-6 LJ) parameters. By using the ChelpG procedure (BRENEMAN & WIBERG, 1990), the atomic charges were computed at the HF/6-31G(d,p) level of theory in aqueous solution using the PCM with the IEF variant (CANCÈS, *et al.*, 1997).

About the Pt(II)-based drugs, we employed the conventional parameterization procedure described in our last papers (ALMEIDA, *et al.,* 2019; ALMEIDA, *et al.,* 2020; ALMEIDA, *et al.,* 2021). In this scheme, the intramolecular parameters were calculated from the optimized structures at the MP2/6-31G(d,p)/LANL2DZ level of theory. The force constants for bonds and angles were derived using the Visual Force Field Toolkit (ZHENG, *et al.*, 2016).

Figure 4.3 - The two drug release modes from the CNHox model evaluated in the biased MD simulations. Mode 1: (A), (B), and (C). Mode 2: (D), (E), and (F). The dashed blue arrows indicate the direction of drug release.

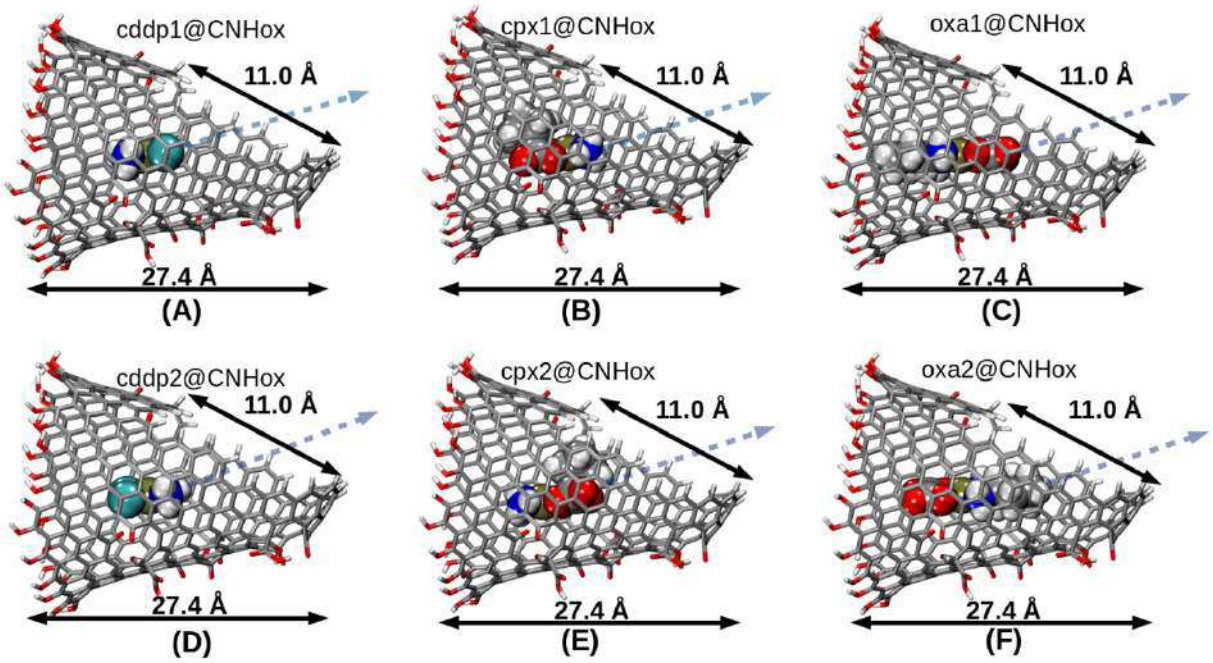

Reference: Own author (2022).

While the 12-6 LJ parameters for the Cl, N, O, H and C atoms were collected from GAFF2, the same set for the Pt atom of cddp was selected from a previous study (LOPES, *et al*., 2008), and the set for the Pt atom in the cpx and oxa drugs was collected from a recent work (SANTANA, 2019). At last, atomic charges were also calculated at the HF/6-31G(d,p)/LANL2DZ level in aqueous solution (PCM).

4.2.3 Computational details

While all MD simulations were conducted with the pmemd CUDA implementation (SALOMON-FERRER, *et al.*, 2013) of the AMBER 16 software package (CASE, *et al*., 2016), quantum mechanical calculations were carried out with the Gaussian-09 release D.01 program (FRISCH, *et al.,* 2009).

Concerning the unbiased MD simulations, the six complexes were firstly placed at the center of a truncated octahedral simulation box with an average length of 89.3 Å. The first stage was the energy minimization of these systems with restraint of 500 kcal mol^{-1} $Å^{-1}$ on the solute, followed by the entire system without constraint. Specifically, this stage involved 5,000 cycles

with steepest descent method (JENSEN, 2007) and 5,000 cycles with the conjugate gradient method (HESTENES & STIEFEL, 1952). After that, the heating from 283 K to 310 K for 500 ps was the second stage. The solute was weakly restricted (force constant 10 kcal mol^{-1} $Å^{-1}$), considering the Langevin thermostat and the canonical ensemble (NVT). Next, the systems were equilibrated at 310 K and 1.0 bar for 2.7 ns with no restraints on the solutes, using the Berendsen barostat and the isothermal-isobaric ensemble (NPT). The last stage was the production run with the NPT ensemble for 200 ns. Finally, we performed all unbiased MD simulations in triplicate with different random seeds for the Langevin thermostat, and the results, in turn, were presented as averages values of these replicas.

When it comes to the biased simulations, we conducted SMD simulations followed by US to calculate the PMF related to the drug release process from the nanowindow of the CNHox model. For these simulations, the complexes were placed at the center of a rectangular simulation box with dimensions 68x69x157 Å (x,y,z). We used the same protocol described for the unbiased simulations until the equilibration stage. After that, we weakly restrained the metallodrugs at the CM of the CNHox. This positional restraint was gradually reduced from 20 to 5 kcal mol^{-1} $Å^{-1}$ for 2.8 ns. The reaction coordinate for the drug release was defined as a distance of 30 Å from the CM of the CNHox model along the main axis of this nanovector (z axis) towards the bulk. Thus, a pulling step of the drug along this reaction coordinate was conducted for 32 ns using SMD simulations. After that, we partitioned this path of 30 Å into 30 windows, representing the 30 configurations of the system selected in intervals of 1 Å. Each window was simulated for 20 ns with the NPT ensemble, and a harmonic bias potential (force constant of 2.5 kcal mol^{-1} $Å^{-1}$) was applied to the solute. Therefore, these independent simulations added up to ~650 ns for each inclusion complex. We computed the PMF for each complex using the Weighted Histogram Analysis Method (WHAM) (KUMAR, *et al.*, 1992; GROSSFIELD).

Finally, each simulation box was filled up with TIP3P water molecules and 150 mM of dissociated NaCl, aiming to reproduce the physiological conditions. By using periodic boundary conditions, the electrostatic interactions were treated by the Particle Mesh Ewald (PME) method (DARDEN, *et al.*, 1993), and the van der Waals (vdW) interactions were spherically truncated at 10 Å. Besides, the shake algorithm (RYCKAERT, *et al.*, 1977) was employed to impose constraints for all bonds containing hydrogen atoms, which allowed the use of a 2.0 fs time step. The binding free energies ($\Delta_b G$) were calculated with the Molecular Mechanics Generalized Born Surface Area (MM/GBSA) method (MILLER III, *et al.*, 2012). Table 4.1 summarizes the main details of all MD simulations carried out in this work.

Table 4 1 - Summary of the MD simulations performed at 310 K, 1.0 bar, and 150 mM NaCl concentration.

Simulations	System	N_{tot} [a]	N_{wat} [b]	V_{box} / Å^3 [c]	t_{equi} / ns [d]	t_{tot} / ns [e]
Unbiased	cddp@CNHox	33395	10982	367395	3 x 2.7	3 x 202.7
	cpx@CNHox	33385	10974	367269	3 x 2.7	3 x 202.7
	oxa@CNHox	33407	10980	367604	3 x 2.7	3 x 202.7
	cddp>CNHox	32681	10744	361324	3 x 2.7	3 x 202.7
	cpx>CNHox	34365	11300	379991	3 x 2.7	3 x 202.7
	oxa>CNHox	33434	10989	368761	3 x 2.7	3 x 202.7
Biased[f]	cddp1@CNHox	69316	22929	811047	2.8	647.8
	cpx1@CNHox	69315	22924	811046	2.8	647.8
	cxa1@CNHox	69307	22920	811047	2.8	647.8
	cddp2@CNHox	69316	22927	811047	2.8	647.8
	cpx2@CNHox	69315	22925	811047	2.8	647.8
	oxa2@CNHox	69307	22920	811047	2.8	647.8

[a]Total number of atoms. [b]Number of water molecules. [c]Volume of the simulation box. [d]Simulation time for the equilibration stage in nanoseconds (ns). [e]Total simulation time in ns after the heating stage. [f]Steered Molecular Dynamics followed by Umbrella Sampling simulations. In the nomenclature of the inclusion complexes, while the index 1 indicated the drug release Mode 1, the index 2 corresponds to the drug release Mode 2. The unbiased MD simulations were conducted in triplicates.

Reference: Own author (2022).

4.3 RESULTS AND DISCUSSION

4.3.1 Unbiased molecular dynamics

Regarding the unbiased simulations of the inclusion and adsorption complexes (see Figure 4.2), we analyzed the temporal variation of the temperature, density, volume, kinetic energy, potential energy, and total energy (Figure B.1). The stable moving averages indicate that these systems were equilibrated in 2.7 ns. Furthermore, we verified the same behavior for all simulation replicas. In Table B.1, the standard deviation values of the energies in the order of 0.31%, in relation to the average values, reinforce the energetic stability and the convergence

of the simulations. In order to characterize the structural variation of the complexes, we also evaluated the root mean square deviation (RMSD) as a function of time during the equilibration stages of 2.7 ns (see Table 4.2).

Table 4.2 - Statistics of the root mean square deviation (RMSD) related to the 2.7 ns equilibration runs of the inclusion and adsorption complexes studied in this work. Each temporal average was calculated from the simulation triplicates.

Complex	**Equilibration stage (2.7 ns)**	
	RMSD / Å	
	<RMSD>	**Std.**
cddp@CNHox	0.14	0.02
cpx@CNHox	0.83	0.18
oxa@CNHox	0.17	0.03
cddp>CNHox	0.14	0.02
cpx>CNHox	0.57	0.06
oxa>CNHox	0.14	0.02

*The terms <RMSD> and Std. refer to the average value and standard deviation.

Reference: Own author (2022).

Based on Table 4.2, it is possible to observe that all complexes achieved a structural stability in 2.7 ns, with average RMSD ~0.33 Å with oscillations in the range of 0.06 Å (see also Figure B.2). Henceforth, the analysis will be covering only the production runs and their replicas. Figures B.3-B.5 present the final snapshots of the unbiased trajectories referring to the six complexes. Despite the presence of two releasing routes, the final frames of the inclusion complexes show the confinement of the metallodrugs during the simulation time (200 ns). It is important to note that we obtained the same results in our last paper involving the inclusion complex with three cddp molecules named 3cddp@CNHox (ALMEIDA, *et al*., 2021). By comparing the frames of these inclusion complexes with the initial ones shown in Figure 4.2A-C, it is possible to see that the cpx is the only drug with an inversion in its initial orientation characterized by the cyclobutyl group facing the nanowindow at the end of simulation. When it comes to the adsorption complexes, the final frames (Figure B.3-B.5D,E-F) reinforce the potentiality of the CNH as nanocarriers, since the drugs remained attached to the CNHox

surface at the end of 200 ns. Moreover, the position of the drugs suggests that the oxa presented the minor mobility during the simulations.

To get insights into the dynamics of the drugs through the trajectories, we analyzed the spatial distributions of the anticancer drugs during the 200 ns, as shown in Figure 4.4 and Figure B.6 and B.7 for the other two replicas. With regard to the inclusion complexes, the spatial distributions (Figure 4.4) emphasize the restricted mobility of the metallodrugs inside the CNH cavity along the 200 ns trajectories. By analyzing the dynamical behavior of the encapsulated drugs, it is possible to confirm that the cddp drug had the most significant mobility (Figure 4.4A), which is more evident in Figures B.6A and B.7A.

Figure 4.4 - Spatial distribution of the Pt(II)-based drugs in the inclusion and adsorption complexes during the 200 ns production run (replica 1). The green, blue, red, silver, and golden colors indicate the mobility of the Cl, N, O, C, and Pt atoms.

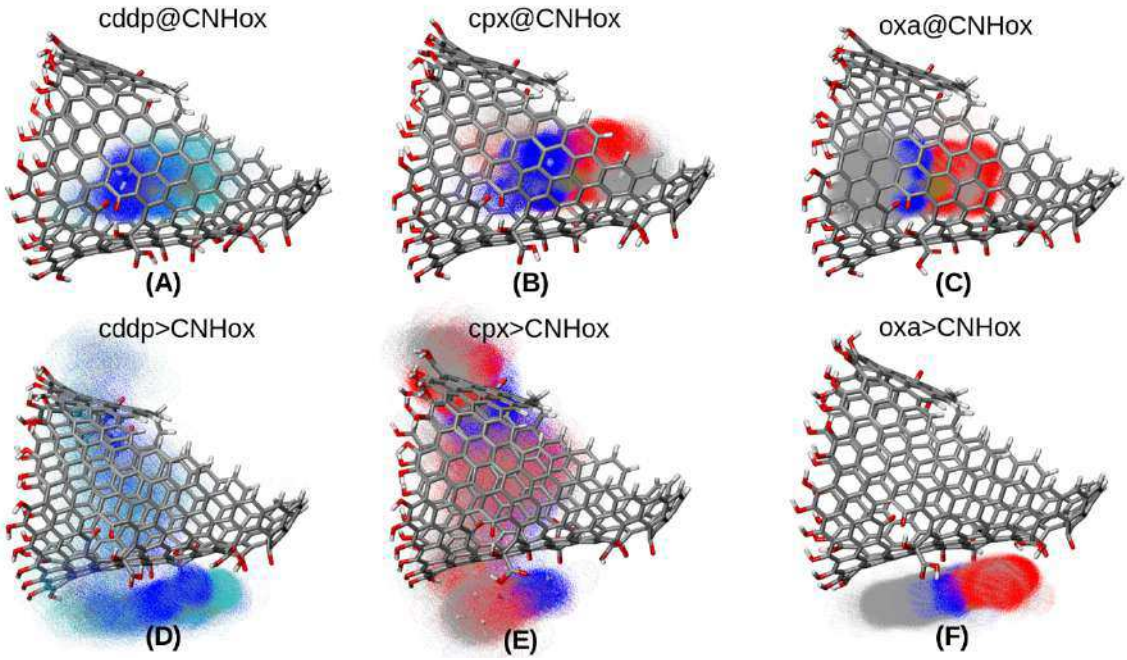

Reference: Own author (2022).

Concerning the adsorption complexes, the more dispersed distributions represented in Figure 4.4 indicate that the vectorization based on the drug adsorption on the surface of the CNHox provided, on average, a greater freedom for mapping this nanostructure, especially in the case of cddp and cpx. On the other hand, the mobility of the adsorbed oxa was, on average, reduced despite their freedom of movement. This result may be related with the less bulky

diaminocyclohexane ligand in oxa that favors a more significant number of contacts between the drug and the CNHox surface.

The solute-solvent interactions were also analyzed by computing the radial distribution functions (RDF) defined between the CM of the carbon nanostructure and the oxygen atoms of the water molecules, henceforth termed as g(r) CM--O_w (see Figure B.8). In this figure, the peaks between 0 Å and 5 Å point out the presence of inner solvation shells (waters inside the cavity). We also reported in our last papers for complexes including pristine, oxidized and reduced CNH prototypes (ALMEIDA, *et al*., 2019; ALMEIDA, *et al*., 2020; ALMEIDA, *et al*., 2021). Regarding the inclusion complexes (Figure B.8A), while the RDF referring to cddp@CNHox and cpx@CNHox complexes present three peaks centered at 0.45 Å, 2.85 Å, and 3.75 Å and 0.15 Å, 2.85 Å, and 3.75 Å, respectively, the oxa@CNHox complex presents only two peaks centered at 2.85 Å and 4.35 Å. The smallest number of peaks in the g(r) CM--O_w of the oxa@CNHox model associated with the distance of its first peak suggests that the volume occupied by the oxa molecule in the cavity of the CNHox reduced the access of solvent molecules. The number of waters referring to these solvation shells was extracted from the integral of these RDF, and the results are organized in Table 4.3 in the column named coordination number (CN). These data confirmed that the oxa drug expulsed, on average, three water molecules compared to the cddp and cpx drugs.

Additionally, despite the similarities between the average positions of the inner solvation shells in the cddp@CNHox and cpx@CNHox, the RDF shown in Figure B.8A also evidenced a greater intensity in the peaks for the complex involving the cpx molecule. These results reflect a significant solvent-solute interaction within the cavity when one includes this Pt(II) drug. Unlike the encapsulated formulations, differences in the inner solvation shells of the adsorption complexes were not observed since the cavity of the carbon-based nanovector was empty. On average, these last complexes accommodated 22 water molecules in their cavities.

Still regarding the solute-solvent interactions, we present in Table 4.3 the results referring to the analysis of hydrogen bonds (HB) formed between the complexes and the water molecules throughout the production runs (200 ns for each replica). This table indicates that the complexes involving cpx and oxa formed more HB than those with cddp during all simulations, regardless of the formulation.

Table 4.3 - Coordination number (CN) of the inner solvation shell and the solute-solvent hydrogen bonds (HB) calculated during the 200 ns production runs.

Systems	<CN>[a]	<HB>[b]	<HB/frame>[c]	<Dist>/Å[d]	<a>/° [e]	<HB-drug>[f]
cddp@CNHox	18.8±0.3	118585±823	23.72±0.17	2.78±0.01	157.48±0.02	9228±114
cpx@CNHox	18.8±0.4	134760±3176	26.95±0.63	2.78±0.01	157.43±0.03	21558±581
oxa@CNHox	15.5±0.1	132670±132	26.53±0.02	2.79±0.00	156.80±0.03	25300±101
cddp>CNHox	22.2±0.0	117620±1153	23.52±0.23	2.80±0.00	157.37±0.30	9081±66
cpx>CNHox	22.2±0.1	129683±3261	25.94±0.01	2.78±0.01	157.55±0.30	22412±1445
oxa>CNHox	22.3±0.1	128336±2496	25.80±0.73	2.78±0.00	157.70±0.09	23533±2458

[a]Average coordination number found in the inner solvation shell of the CNHox. [b]Average number of HB. [c]Average number of HB per frame. [d]Average distance of HB in Å (D-H---A, where D and A are the donor and acceptor of HB). [e]Average angle in degrees (D-H---A). [f]Average number of HB formed between the drug and the water molecules. *Each average and standard deviation value was calculated from the simulation triplicates.

Reference: Own author (2022).

Compared to the nanocarriers loaded with cddp, it is possible to observe an increase in the average number of hydrogen bonds (<HB>) of about 14% and 12% for the cpx@CNHox and oxa@CNHox complexes. In contrast, the increase for the cpx>CNHox and oxa>CNHox complexes is approximately 10% and 9%. Similar behavior is also verified in the average number of HB per frame (<HB/frame>) formed in the systems, including the cpx and oxa drugs. On average, while we observe an average increase of three HB/frame for the cpx@CNHox and oxa@CNHox complexes compared to cddp@CNHox, the average increase of the same property for the cpx>CNHox and oxa>CNHox systems relative to the cddp>CNHox is two HB/frame. When it comes to the HB geometrical parameters, the differences relative to the Pt(II)-based drugs and the formulations (adsorption and inclusion) did not influence the average distance and angle. Lastly, by focusing on the number of HB involving the metallodrugs, data from the <HB-drug> column in Table 4.3 reinforce the results mentioned above (<HB> column) of these hydrogen interactions with the cpx and oxa drugs compared to cddp. Specifically, the <HB-drug> is 2.3 and 2.7 times greater for cpx and oxa in the inclusion complexes, whereas it is 2.5 and 2.6 times greater for the same drugs in the adsorption complexes, resulting from the carbonyl groups in the cpx and oxa complexes.

We have also performed an energetic analysis of the six complexes studied in this section based on the calculation of the pair energies as function of time, considering only the

electrostatic (elec) and vdW components within a cutoff distance of 10 Å, as shown in Figure 4.5 and Figure B.9.

Figure 4.5 - Temporal variation of the pair energies during the 200 ns simulations (production runs, replica 1) referring to the inclusion complexes (A) and the adsorption complexes (B).

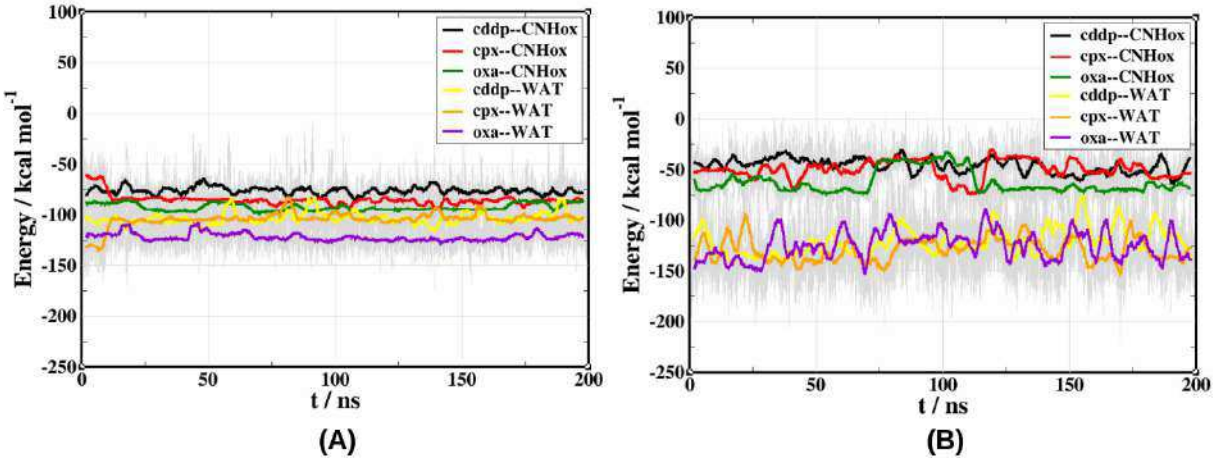

Reference: Own author (2022).

By evaluating the drug--CNH interactions in Figure 4.5, we notice that the pair energies became more negative as the drug size increased due to the maximization of the number of interactions. For instance, the average pair energy for the oxa@CNHox is -92.65±6.27 kcal mol^{-1}; for the cpx@CNHox and cddp@CNHox complexes, it is -85.42±8.93 kcal mol^{-1} and -76.34±11.31 kcal mol^{-1}, respectively (Figure 4.5A). In contrast, the pair energies for the adsorption complexes are less negative, with an increase in the range of about 40%, 42%, and 33% for the cddp>CNHox, cpx>CNHox, and oxa>CNHox, respectively (Figure 4.5B). This behavior reflects a reduction on the number of interactions between the drugs and the nanocarrier in the adsorbed formulations. Moreover, the drug--CNHox pair energies are mainly composed by vdW interactions, as we also concluded for the 3cddp@CNHox complex (ALMEIDA, *et al*., 2021). Recently, Mejri and coworkers (MEJRI, *et al*., 2021) reported a pair energy value of -80.0 kcal mol^{-1} for an inclusion complex formed by four cddp molecules encapsulated into a hydroxyl-terminated CNT (4cddp@CNT in our notation). In that work, if we consider the value of -20.0 kcal mol^{-1} for the case of a complex loaded with only one cddp molecule (cddp@CNT in or notation), we could state that the interaction energy for cddp@CNHox is 3.8 times lower (more negative) than the one reported by these authors.

When it comes to the pair energy related to the interactions between the drugs and water molecules (drug--WAT), Figure 4.5 demonstrates that these energies are, on average, more

negative than the ones referring to the drug--CNH energy. This behavior was expected due to many solute-solvent interactions (79, 73, and 73 water molecules in a cutoff distance of 10 Å relative to the CM of cddp, cpx, and oxa in the inclusion complexes). This behavior is more evident in the case of the adsorption complexes (111, 109, and 106 water molecules in the same measure with cddp, cpx, and oxa) (see g(r) Pt--O_w in Figure B.10). Specifically, while this pair energy is about -110.12±14.35 kcal mol^{-1} for the inclusion complexes, this energy for the adsorption complexes is -125.23±25.87 kcal mol^{-1}. In relation to the composition of this pair energy, it was dominated by electrostatic interactions (~90 %).

To study the degree of spontaneity relative to the formation of the six nanoformulations presented herein, we have calculated the binding free energies (Δ_bG) employing the MM/GBSA method. The average values of the Δ_bG considering the simulation triplicates for each system are presented in Table 4.4.

Table 4.4 - Average values of the binding free energies ($<\Delta_bG>$) referring to the 200 ns run of the inclusion and adsorption complexes.

Complex	**$<\Delta_bG>$ / kcal mol^{-1} [a]**	**Std.[b]**	**Err.[c]**
cddp@CNHox	-32.88	3.12	0.10
cpx@CNHox	-28.57	2.26	0.08
oxa@CNHox	-35.95	2.13	0.07
cddp>CNHox	-24.59	2.71	0.09
cpx>CNHox	-20.64	2.40	0.07
oxa>CNHox	-19.06	2.26	0.08

[a]These energies were calculated by means of the Molecular Mechanics Generalized Born Surface Area (MM/GBSA) method considering a set of 900 frames selected from each simulation replica (total of 2700 frames). [b]Standard deviation value. [c]Standard error of the mean.
Reference: Own author (2022).

Overall, the negative values of the free energies shown in Table 4.4 indicate that the CNHox model forms stable complexes with cddp, as we recently reported it (ALMEIDA, *et al*., 2021), and cpx and oxa. This behavior is also graphically represented by the green bars in Figure 4.6. By comparing the stability between inclusion and adsorption complexes, it is verified that the encapsulated formulations are more stable than the adsorbed ones, by ~11.04 kcal mol^{-1}. This result evidences the favorable interactions involving the Pt(II)-based drugs and the inner surface of the CNHox, in addition to suggesting a substantial drug protection in aqueous

solution. When it comes to the metallodrugs, data from Table 4.4 point out that while the oxa@CNHox complex is the most stable (<Δ_bG> = -35.95±2.13 kcal mol^{-1}) among the inclusion complexes, the oxa>CNHox complex is the least stable (<Δ_bG> = -19.06±2.26 kcal mol^{-1}) among the adsorption complexes. Besides, the systems involving cddp are considerably stable in both encapsulated and adsorbed forms. The small values of standard deviation (Std.) and standard error of the mean (Err.) reinforce the convergence of these results in the simulation replicas.

Figure 4.6 - Average values of the binding free energy (Δ_bG) components referring to the 200 ns simulations of the inclusion and adsorption complexes. Each value was calculated based on the simulation triplicates. The error bars indicate the standard deviation values.

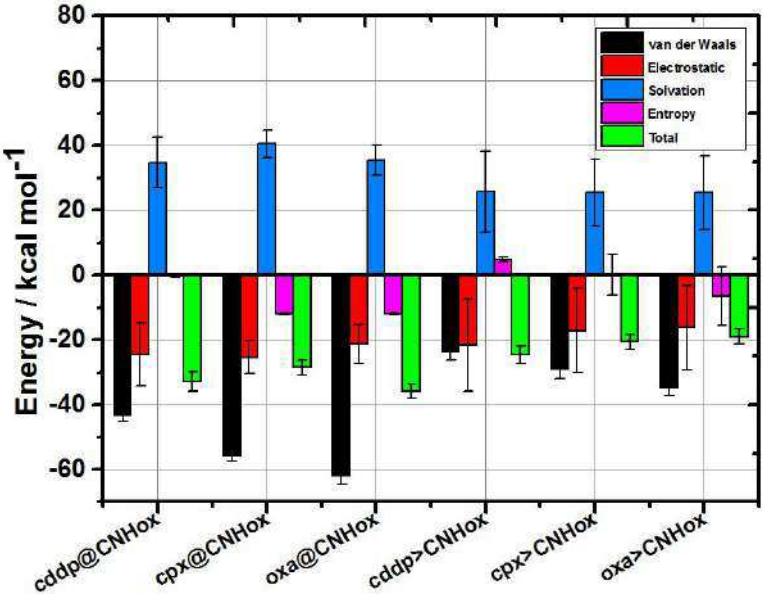

Reference: Own author (2022).

Still regarding Figure 4.6, the black bars clearly show that the main contribution to stability of the six complexes comes from the vdw. In particular, these interactions are more important in the inclusion complexes than in the adsorption ones. The encapsulated formulations are approximately 30% more favorable than the adsorbed ones when considering the electrostatic component (red bars in Figure 4.6). On the other hand, while the entropic contributions (pink bars in Figure 4.6) do not play a substantial role to the Δ_bG, when we consider the implicit solvation treated by the GB model, the positive values of the solvation free energy (blue bars in Figure 4.6) indicate a destabilization of all systems. This result is a result of the fact that the solvation energy of the complex ($G_{complex}$) is about the solvation energy of the CNH (G_{CNH}), thereby resulting in $\Delta G_{solv} = G_{complex} - (G_{CNH} + G_{drug}) \sim G_{drug}$.

By studying nanovectors for cpx based on pristine and functionalized CNT and pristine silicon carbide nanotube, Khatti and coworkers (KHATTI & HASHEMIANZADEH, 2015; KHATTI & HASHEMIANZADEH, 2018) also verified this instability related with the polar contribution to the solvation free energy using the MM/PBSA (molecular mechanics/Poisson-Boltzmann surface area) method. Despite this contribution, the energy balance of the $\Delta_b G$ ensured the stable formation of the six complexes.

We did not observe the spontaneous release of the Pt(II)-based drugs from the CNHox cavity using unbiased MD simulations. However, this confinement effect, which may be explained by the notable stability demonstrated in the free energy calculations (see Table 4.4), suggests that the drug release process involves high energies barriers, especially if one considers the inclusion complexes. In fact, studies involving MD simulations of similar systems described the existence of energetic barriers for the cddp release from CNT (PANCZYK, *et al.,* 2013; MEJRI, *et al.*, 2021).

4.3.2 Biased MD simulations

This section covers the results of the biased MD simulations of the six inclusion complexes shown in Figure 4.3 and Table 4.1. After the 2.8 ns equilibration runs, the SMD simulations were carried out to reproduce the release of the Pt(II)-based drugs from the cavity of the CNHox prototype. The main snapshots of these six trajectories are represented in Figure B.11-B.16. In these figures, it is possible to verify the drug release within 32 ns through the nanowindow region of the CNHox. In order to characterize the releasing stage of the drugs, the maximum force needed to unbind these anticancer molecules from the CNHox, also known as the rupture force (F_{max}) (DO, *et al*., 2018), was collected from the SMD runs. The values of F_{max} for each inclusion complex are presented in Table 4.5.

Since the F_{max} predicts the binding affinity (DO, *et al*., 2018), the highest value (7.08 kcal mol^{-1} $Å^{-1}$ on average) for the complexes involving the oxa indicates that these systems have the highest affinity ligand-receptor among the inclusion complexes. This result was also verified in the $\Delta_b G$ calculations (oxa@CNHox in Table 4.4) that confirmed the high stability of this system. Additionally, by comparing the average F_{max} between the complexes with oxa and the complexes including cddp (6.43 kcal mol^{-1} $Å^{-1}$) and cpx (6.51 kcal mol^{-1} $Å^{-1}$), we can speculate that the small size of these last two Pt(II) drugs facilitates the dissociation process from the CNH due to their reduced number of interactions with this nanocarrier.

Table 4.5 - Rupture force (F_{max}), process free energy (ΔG_p), free energy barrier ($\Delta\Delta G^{\ddagger}$), enthalpy barrier ($\Delta\Delta H^{\ddagger}$), and entropic contribution to the energy barrier ($T\Delta\Delta S^{\ddagger}$) for the Pt(II)-based drugs release from the cavity of the CNHox model.

Complex	F_{max} [a] kcal mol^{-1} Å^{-1}	ΔG_p [b] kcal mol^{-1}	$\langle\Delta\Delta G^{\ddagger}\rangle$ [c] kcal mol^{-1}	$\langle\Delta\Delta H^{\ddagger}\rangle$ [d] kcal mol^{-1}	$\langle T\Delta\Delta S^{\ddagger}\rangle$ [e] kcal mol^{-1}
cddp1@CNHox	6.19	18.22	19.92 ± 2.45	22.99 ± 2.45	3.07
cddp2@CNHox	6.67	20.15	16.51 ± 2.37	20.68 ± 2.37	4.17
cpx1@CNHox	5.85	9.66	16.82 ± 2.75	17.36 ± 2.75	0.56
cpx2@CNHox	7.16	19.79	17.97 ± 1.94	23.81 ± 1.94	5.84
oxa1@CNHox	6.97	23.99	26.18 ± 2.32	37.30 ± 2.32	11.12
oxa2@CNHox	7.18	21.17	21.18 ± 3.23	37.09 ± 3.23	15.91

[a]Rupture force applied in the pulling stage of the Steered Molecular Dynamics (SMD) simulations. [b]Process free energy defined as the energy difference between the final (free drug) and initial (encapsulated drug) states of the inclusion complexes calculated from the potentials of mean force. [c]Average value of the free energy barrier to the drug release. [d]Average value of the enthalpy barrier to the drug release. [e]Average value of the entropic contribution to the energy barrier referring to the drug release. *The $\Delta\Delta G^{\ddagger}$, $\Delta\Delta H^{\ddagger}$, and $T\Delta\Delta S^{\ddagger}$ were calculated as the energy difference between the higher energy state and the initial state of the inclusion complexes by using the Molecular Mechanics Generalized Born Surface Area (MM/GBSA) method.

Reference: Own author (2022).

The time defined by the F_{max} in the trajectory, henceforth named biased release time (t_{rel}), can be interpreted as the moment when the drug starts its release from the CNH and diffuses to the bulk. A summary of the key moments referring to the drug release mechanisms for each inclusion complex is schematized in Figure 4.7.

In Figure 4.7, concerning the complexes involving the cddp drug (cddp1@CNHox and cddp2@CNHox), we do not observe significant differences by comparing the two release modes, since the small size of cddp provided unrestricted rotations inside the cavity of the CNHox. However, Figure B.11 and Figure B.14 show that Mode 1 (two chloride groups of the cddp facing the nanowindow – Figure B.11) is the preferential drug release mode, since the cddp in the cddp2@CNHox rotates during the trajectory (Figure B.14) and assumes the orientation of the Mode 1 before its release from the nanocarrier.

Figure 4.7 - The main steps of the drug release mechanism from the CNHox during the 32 ns SMD simulations by taking into account the drug release Mode 1 (A) and the drug release Mode 2 (B). The biased release time (t_{rel}) is defined by the rupture force (F_{max}) during the trajectory. The two modes for each drug are show in the columns named Start.

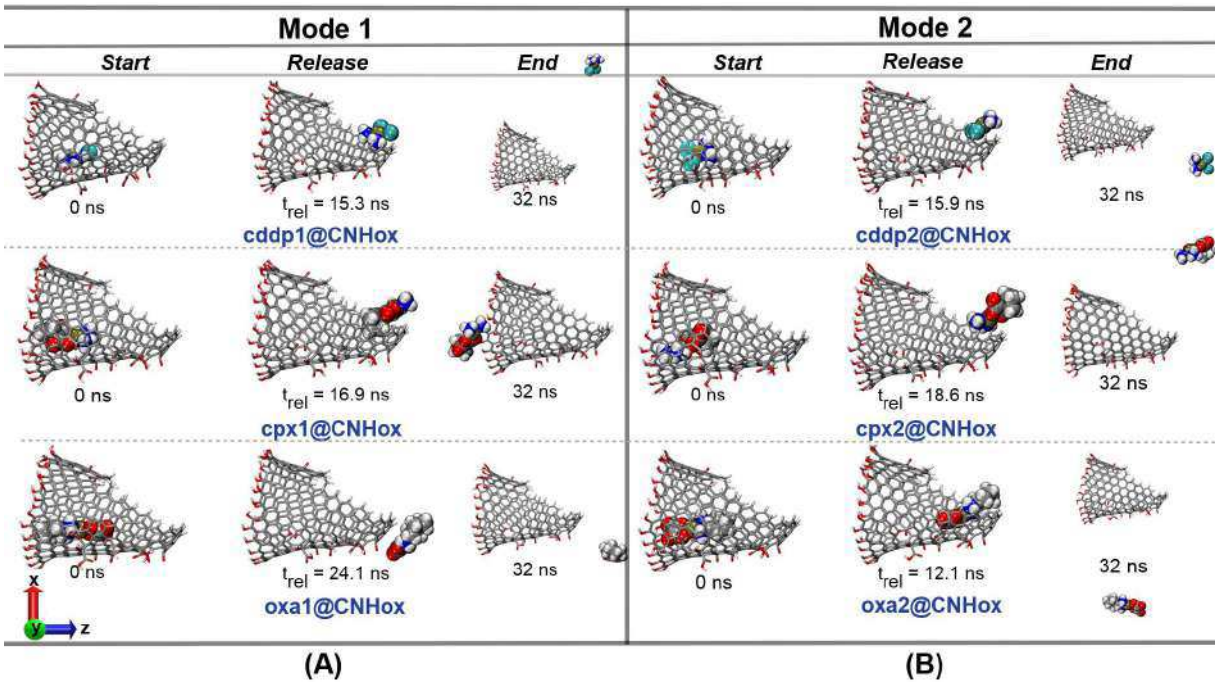

Reference: Own author (2022).

The cddp dissociation process from the CNH via Mode 1 is slightly faster (difference of 0.3 ns) than the one observed in Mode 2. When it comes to the systems with cpx (cpx1@CNHox and cpx2@CNHox), Figure 4.7 demonstrates that the drug release event through the Mode 2 is slower than the one involving Mode 1, with a difference of 1.7 ns. Since the cyclobutyl group forms favorable interactions with the hydrophobic cavity of the CNH, this behavior may represent a substantial resistance to the cpx release starting from this group (Mode 2). Finally, by evaluating the inclusion complexes with oxa (oxa1@CNHox and oxa2@CNHox), we verify that the release Mode 2 is faster than the Mode 1 by 12 ns, which may be associated with favorable interactions between the diaminocyclohexane ligand and the inner surface of the CNH.

The energetic profiles of the drug release processes summarized in Figure 4.8 were also obtained by calculating the PMF from the US simulations. Figure 4.8 presents the profiles, and Figure B.17 shows the histograms of the probability distributions through the reaction coordinate.

Figure 4.8 - Potentials of mean force (PMF) in kcal mol^{-1} referring to the drug release process from the cavity of the CNHox model through its nanowindow for the inclusion complexes: cddp1@CNHox and cddp2@CNHox (A), cpx1@CNHox and cpx2@CNHox (B), and oxa1@CNHox and oxa2@CNHox (C). The distance along the z axis corresponds to the coordinate reaction for the drug release process from the CNHox. The dashed lines indicate the biased release time (t_{rel}) of the drugs.

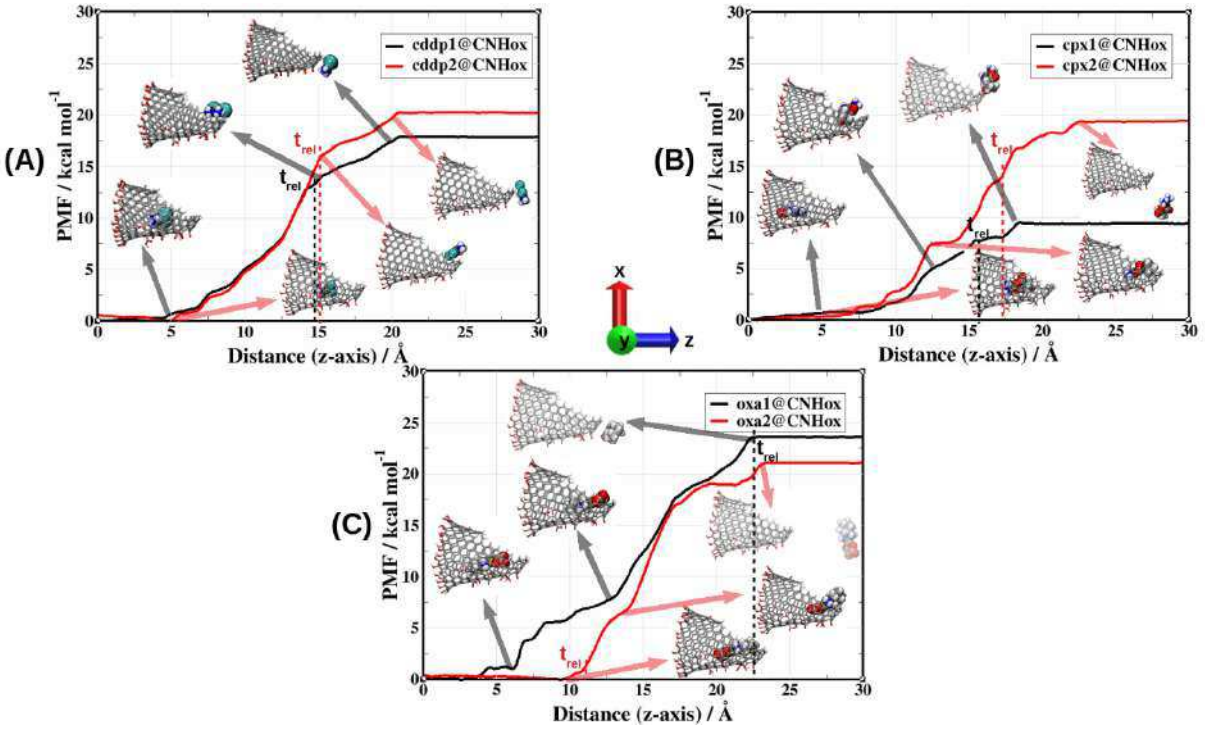

Reference: Own author (2022).

In Figure B.17, it is possible to confirm the convergence of the US simulations due to the overlap of the probability distributions that, in turn, indicate a complete sampling along the reaction path. Regarding the PMF, Figure 4.7 points out the endothermic character of all releasing processes with some differences related to release mode and metallodrug type. In order to quantify these non-spontaneous events, we defined the process free energy (ΔG_P) as the energy difference between the plateau of constant energy, which represents the drug diffusion in bulk, and the first window (first structure) of the reaction coordinate. These values in kcal mol^{-1} units are also organized in Table 4.5.

When it comes to the complexes containing the cddp (cddp1@CNHox and cddp2@CNHox), we notice in Figure 4.8A and Table 4.5 that the release Mode 2 required more energy than the release Mode 1. The energy difference of 1.93 kcal mol^{-1} might be attributed to the inversion of the cddp orientation along the reaction coordinate, as represented in Figure 4.7 and Figure B.14. It is worth noting in Figure 4.8A that the cddp in the releasing Mode 2 starts leaving the CNHox cavity around 14.8 Å. At this distance, the molecule was orientated with

the amino groups towards the nanowindow, which was higher in energy than the opposite orientation with the chlorides facing the surface hole. Comparing the snapshots in Figure 4.8A around 5 and 15 Å, we conclude that cddp has significant mobility inside the cavity; however, once it reaches the nanowindow the mobility decreases due to the steric hindrance, and the releasing occurs with that orientation.

The PMF for the cpx1@CNHox and cpx2@CNHox release processes shows a significant difference in energy variation between Modes 1 and 2 (Figure 4.8B). The release Mode 2 was more unfavorable than Mode 1 with a notable difference in energy of 10.1 kcal mol^{-1}, as indicated in Table 4.5. This low spontaneity related with the cpx2@CNHox complex (Mode 2) reinforces the larger t_{rel} compared to the one of the cpx1@CNHox (Mode 1) shown in Figure 4.7. The interaction between cyclobutyl group of the cpx and CNHox was stronger than the one involving the amino groups. A similar analysis made for cddp applies to the cpx complexes, although the larger size of cpx implies lower mobility inside the cavity. Besides, the cpx is a non-planar molecule with the cyclobutene-1,1-dicarboxylic acid ligand found out of the square-planar Pt(II) plane. Therefore, in Figure 4.8B we note that at about 9.0 Å, the energies become different for Modes 1 and 2, and the cpx is at the nanowindow in distinct orientations. For Mode 2, the bulky cyclobutane-1,1-dicarboxylic acid ligand is directed to the open hole, whereas for Mode 1, the amino groups are outside the cavity. Due to the steric hindrance, the arrangement in Mode 2 is higher in energy than that in Mode 1. Concerning the release modes for oxa complexes, the PMF (Figure 4.8C) emphasizes that Mode 1 (oxa1@CNHox) was less spontaneous than Mode 2 (oxa2@CNHox), as suggested during the analysis of the release mechanisms in Figure 4.7. Different from cpx, the diaminocyclohexane ligand is not very bulky compared to the oxalate ligand, and the PMF is similar regardless of the oxa orientation (see the snapshots ~16.2 Å in Figure 4.8C).

In order to obtain the energy barriers required for the Pt(II)-based drug release from the CNHox, we have also characterized the free energy profiles by calculating the $\Delta_b G$ with the MM/GBSA method for each window referring to the US simulations. While the graphical representation of these profiles is presented in Figure 4.9, the values of the free energy barriers ($\Delta\Delta G^{\ddagger}$) and their enthalpic and entropic components can be found in Table 4.5.

Figure 4.9 - Variation of the binding free energy (Δ_bG) referring to the windows of the US simulations, which describes the drug release process from the CNHox for the inclusion complexes: cddp1@CNHox and cddp2@CNHox (A), cpx1@CNHox and cpx2@CNHox (B), and oxa1@CNHox and oxa2@CNHox (C). These Δ_bG were calculated using the Molecular Mechanics Generalized Born Surface Area (MM/GBSA) method. The $\Delta\Delta G^{\ddagger}$ values, which are defined as the difference in free energy between the most unstable structure and the first structure of the trajectory, refer to the energy barrier for the drug release processes.

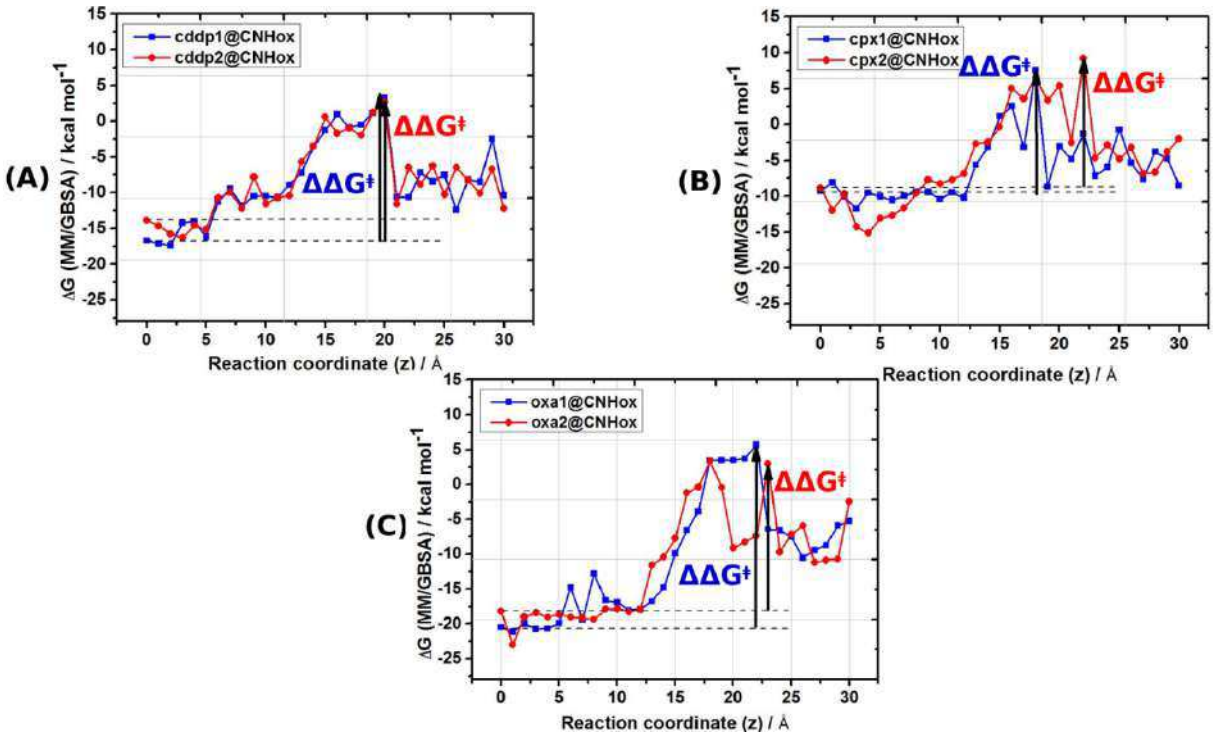

Reference: Own author (2022).

From Figure 4.9, it is possible to confirm the progressive destabilization of all complexes over the drug release trajectories, as also shown in the PMF (Figure 4.8). In particular, the most unfavorable processes involve the inclusion complexes with the oxa (Figure 4.9C), since they present the highest energy barriers with an average value of 23.68 ± 1.77 kcal mol^{-1} (see Table 4.5), which is related to the high stability of the inclusion complexes. On average, the $\Delta\Delta G^{\ddagger}$ is 36% and 30% larger than those related with the systems cpx and cddp, respectively.

As theoretical data for the release process of both cpx and oxa from the CNH are not avaliable, we conducted some comparisons with the literature by taking into account the cddp1@CNHox and cddp2@CNHox complexes. In this context, De Souza and coworkers (DE SOUZA, *et al*., 2021) obtained a value of 58.4 kcal mol^{-1} for the energy barrier, referring to the release event of cddp from the cavity of a CNTox model. The notable difference of 40.19 kcal

mol^{-1} in relation to the two complexes involving cddp presented herein (see Table 4.5) is probably an effect of the high steric hindrance of the nanowindow (diameter of ~4.13Å) in the CNTox prototype, which made it difficult the diffusion of this Pt(II) drug (diameter of ~7.75 Å) through this release pathway. In 2021, by using a biased MD method (ABF method), Mejri and coworkers (MEJRI, *et al.*, 2021) reported an energy barrier of 3.3 kcal mol^{-1}, referring to the release of cddp along the main axis of a CNTox model. This small energetic barrier is probably connected not only with the size of the open end, which correspond to the diameter of the CNTox model (13 Å), but also with the symmetry of the reaction coordinate that coincides perfectly with the longitudinal axis of the nanotube. In our CNHox model, the drug release path is not parallel to the main axis of this nanovector due to the irregularity of the structure and the position of the nanowindow (see Figure 4.3). We speculate that this structural asymmetry of the CNHox induced the high values of the $\Delta\Delta G^{\ddagger}$ relative to the release of drugs. Nonetheless, the above comparisons are not quite reasonable, since the cited works involve different methods, force fields and carbon nanocarriers. At last, the average value of the $\Delta\Delta G^{\ddagger}$ (17.40 kcal mol^{-1}) for the cpx1@CNHox and cpx2@CNHox complexes indicates that the cpx release from the CNHox is the most kinetically favorable process, mainly when one considers the release Mode 1.

By decomposing the $\Delta\Delta G^{\ddagger}$ into the enthalpic ($\Delta\Delta H^{\ddagger}$) and entropic ($T\Delta\Delta S^{\ddagger}$) barriers, the data in Table 4.5 reveal that the energetic barriers to the Pt(II) drugs release from the CNHox are mostly enthalpic with an average entropic contribution of 34% considering all complexes. By using quantum calculations based on semi-rigid scan, in addition to showing a slight contribution of the entropy (~0.1 kcal mol^{-1}), De Souza and coworkers (DE SOUZA, *et al*., 2021) showed that ~95% of the free energy barrier referring to the cddp release from a CNTox prototype was composed by enthalpic contribution ($\Delta\Delta H^{\ddagger}$ = 55.5 kcal mol^{-1}). In order to determine the energetic components that govern the $\Delta\Delta H^{\ddagger}$, Figure B.18 presents the profiles of the vdW and elec contributions of the $\Delta_b G$ for all processes. In this figure, it is possible to observe that the drug escape from the CNHox is accompanied by destabilization of all systems. Furthermore, the vdW interactions play the central stabilizing role in all inclusion complexes, as seen in Figure 4.6 and in other works for similar carbon nanovectors (KHATTI & HASHEMIANZADEH, 2015; KHATTI & HASHEMIANZADEH, 2018; ALMEIDA, *et al.*, 2019; ALMEIDA, *et al.,* 2020; ALMEIDA, *et al.,* 2021). Specifically, the vdW contributions to the $\Delta\Delta H^{\ddagger}$ ($\Delta\Delta E_{vdw}^{\ddagger}$) were about 0.9, 6.0, and 1.9 times greater than the elec contributions ($\Delta\Delta E_{elec}^{\ddagger}$), considering the complexes with cddp, cpx, and oxa, respectively. The high value for

cpx (52.24 kcal mol^{-1} on average) reflects the strong interaction between the cyclobutyl group of this drug and the hydrophobic cavity of the CNHox.

From the $\Delta\Delta G^{\ddagger}$ values we estimated the mean residence time (t_{res}) of the Pt(II)-based drugs inside the CNHox employing the theoretical procedure reported by Panczyk and coworkers (PANCZYK, *et al*., 2016), who studied DDS formed by doxorubicin encapsulated into CNT models. According to these authors, the probability of drug release from the nanocarrier, herein named as P_{rel}, is given by the Boltzmann factor (exp $(-E/RT)$), where E, R, and T are the energy barrier, the ideal gas constant, and the temperature, respectively. Moreover, the time involved in the one-dimensional diffusion of the drug along the nanotube length is given by $t = L^2/4D$, where L is the length nanostructure and D is the translational diffusion coefficient (D) of the drug. These authors proposed that the t_{res} can be computed by using the following equation based on the transition state theory.

$$t_{res} = \frac{L^2}{4D} \exp\left(\frac{\Delta\Delta G^{\ddagger}}{RT}\right) \quad (4.1)$$

The values of P_{rel}, D, and t_{res} for each drug incorporated into the six complexes are included in Table 4.6. Concerning the P_{rel}, data from Table 4.6 indicate that the higher the $\Delta\Delta G^{\ddagger}$ (see Table 4.5), the lower the probability of this molecular event. For instance, since the oxa release from the oxa1@CNHox involves the highest energy barrier ($\Delta\Delta G^{\ddagger}$ = 26.18 kcal mol^{-1}), this process is the least likely (P_{rel} = 3.48 x 10^{-19}). By comparing the D of the drugs inside the CNHox with the ones obtained in experimental studies, we verified a reduction of one order of magnitude for this dynamic property considering the encapsulated form of the cddp drug (D = 2.1 x 10^{-5} cm^2 s^{-1}) (PANCZYK, *et al*., 2013). The same behavior was also reported by us (ALMEIDA, *et al*., 2020) and Nejad and coworkers (NEJAD & URBASSEK, 2019), associated with restricted mobility of the drug inside nanomaterials. On the other hand, an increase of one order of magnitude in the diffusivity of the cpx drug was observed if one compared with the experimental value (7.8 x 10^{-6} cm^2 s^{-1}) (PAMPEL, *et al.*, 2002).

Finally, it is possible to note that the t_{res} is strictly connected with the $\Delta\Delta G^{\ddagger}$, *i.e*., inclusion complexes with the highest energy barriers for the drug escape provided the longest t_{res} inside the carbon nanocontainer. In particular, the t_{res} of the oxa drug in the oxa1@CNHox complex was four orders of magnitude higher than the oxa2@CNHox system. In addition to reinforce the high stability of this complex demonstrated by the ΔG_p and $\Delta\Delta G^{\ddagger}$ values in Table

4.5, this result points out that this drug will not be released within a reasonable time. In contrast, the short t_{res} for the complexes involving the cpx drug (less than 1 h), suggested that these systems are more unstable and susceptible to quick releases of this drug.

Table 4.6 - Probability of the drug release from the CNHox cavity (P_{rel}), diffusion coefficients (D) of the Pt(II)-based drugs, and the residence time (t_{res}) of the drugs inside the nanocarrier through the biased MD simulations at 310 K of the inclusion complexes.

Complex	P_{rel} [a]	D / cm^2 s^{-1} [b]	t_{res} / s [c]
cddp1@CNHox	9.02 x 10^{-15}	1.96 x 10^{-6}	1.06 x 10^{6}
cddp2@CNHox	2.29 x 10^{-12}	3.43 x 10^{-6}	2.39 x 10^{3}
cpx1@CNHox	1.38 x 10^{-12}	5.59 x 10^{-5}	2.43 x 10^{2}
cpx2@CNHox	2.13 x 10^{-13}	2.97 x 10^{-5}	2.95 x 10^{3}
oxa1@CNHox	3.48 x 10^{-19}	4.95 x 10^{-5}	1.09 x 10^{9}
oxa2@CNHox	1.17 x 10^{-15}	9.65 x 10^{-5}	1.67 x 10^{5}

[a]Probability of the drug release from the CNHox given by the Boltzmann factor exp $(-\Delta\Delta G^{\ddagger}/RT)$, where $\Delta\Delta G^{\ddagger}$, R, and T are the energy barrier, the ideal gas constant, and the temperature. [b]Translational diffusion coefficients of the Pt(II)-based drugs inside the carbon nanocarrier given by the Einstein relation $D = \frac{1}{2d}\lim_{t\to\infty}\frac{\langle x^2\rangle}{t}$, where d stands for the dimensionality of the system (n = 3 in this study), the t term stands for the observation time, and $\langle x^2\rangle$ refers to the mean-square displacement. [c]Residence time of the Pt(II) drug inside the CNHox given by $t_{res} = \frac{L^2}{4D}\exp(\Delta\Delta G^{\ddagger}/RT)$.

Reference: Own author.

It is worth to emphasize that the energy barriers shown in Table 4.5 and Figure 4.9 were calculated for 1:1 inclusion complexes (drug:CNH), which may be the least conducive stoichiometry to the dissociation and subsequent release of drugs. Indeed, by evaluating the experimental studies (AJIMA, *et al.,* 2005; AJIMA, *et al.,* 2006; AJIMA, *et al.,* 2008; MATSUMURA, *et al*., 2007) it is suggested that the release process of cddp molecules from CNH structures is gradual, since it includes clusters of this anticancer drug. Knowing this, we speculate whether the spontaneous release of cddp from the CNHox in these studies is an effect of the saturation of this drug inside the nanovectors that may progressively reduce, in turn, the energy barriers referring to the expelling of units of this molecule. In this sense, the (1:1) inclusion complexes presented herein represent a limit case of these experiments, in which the drug remains encapsulated for a long period. Besides, even for the limit case considered here,

the releasing time is strongly dependent on the mechanism, which is mainly associated with the drug orientation inside the cavity. To illustrate, for cddp, t_{res} was 294 h for Mode 1 and only 0.6 h for Mode 2. It is important to note that these releasing modes are defined for biased MD, once the process is not spontaneous at normal temperature. However, for small molecules such as cddp, both orientations should be accessible, and the drug release follows the lowest energy path. What calls our attention was the short t_{res} for cpx drug, regardless the mechanism: 4 and 49 min. for Modes 1 and 2, respectively. Using the hypothesis that an orientational equilibrium exists for the drug inside the CNHox cavity, we conclude that t_{res} = 4 min for cpx is much shorter than for cddp, 36 min. Lastly, the release of oxa is predicted to be slow, with t_{res} = 46 h. Therefore, future studies should involve the biased MD simulations considering the encapsulation of Pt(II)-based drugs clusters. In spite of that, this study represents an essential step towards understanding the dynamics of CNH as potential carriers of Pt(II) drugs for treatment of cancers at the molecular level.

4.4 CONCLUSIONS

In this study, we described a theoretical analysis of the stability and dynamics of the CNHox acting as nanocarriers of the three Pt(II)-based drugs (cddp, cpx, and oxa) approved worldwide by using unbiased and biased MD simulations. While the unbiased simulations involved three inclusion complexes (cddp@CNHox, cpx@CNHox, and oxa@CNHox) and three adsorption complexes (cddp>CNHox, cpx>CNHox, and oxa>CNHox), the biased simulations involved six inclusion complexes (cddp1@CNHox, cpx1@CNHox, oxa1@CNHox, cddp2CNHox, cpx2@CNHox, and oxa2@CNHox) that distinguished by the drug release mode. Concerning the unbiased simulations, the drugs remained either confined in the CNH or adsorbed on its surface during the simulation time, 200 ns. Calculations of the $\Delta_b G$ indicated that the complexes based on the encapsulated formulations of the drugs were more stable than the adsorbed ones, with and average difference of ~11 kcal mol^{-1}. For instance, although the oxa drug formed the most stable inclusion complex ($<\Delta_b G>$ = -35.95±2.13 kcal mol^{-1}), the same drug formed the least stable adsorption complex ($<\Delta_b G>$ = -19.06±2.26 kcal mol^{-1}). With regard to the biased MD simulations, it was possible to map aspects of the drug release process from the CNHox. PMF analysis reinforced the endothermic character of the processes with slight differences related to the drug and the release mode. Due to the high stability of the complexes with oxa, the release events of this drug required the highest ΔG_P (22 kcal mol^{-1} on average). Additionally, the average releasing barrier ($\Delta\Delta G^{\ddagger}$) for the oxa complex was about 30-36% higher than found

for cpx and cddp derivatives. These energy barriers were mainly related with the complex stabilization due to the vdW interactions. At last, the high stability of the complexes with oxa was also confirmed, since they exhibited the longest t_{res} (~46 h), followed by cddp (t_{res} = 36 min) and cpx (t_{res} = 4 min). Our results are relevant because they reinforce the potentially of the Pt(II)-based drugs nanovetorization in CNHox by forming thermodynamically stable complexes. These complexes provide protection relative to the side reactions in the physiological environment and a controlled release of these anticancer molecules in the target site.

REFERENCES

AJIMA, K.; *et al*. Material storage mechanism in porous nanocarbon. **Advanced Materials**, v. 16, p. 397-401, 2004.

AJIMA, K.; *et al*. Carbon nanohorns as anticancer drug carriers. **Molecular Pharmaceutics**, v. 2, n. 6, p. 475-480, 2005.

AJIMA, K.; *et al.* Effect of functional groups at hole edges on cisplatin release from inside single-wall carbon nanohorns. **Journal of the Physical Chemistry B**, v. 110, n. 11, p. 5773-5778, 2006.

AJIMA, K.; *et al*. Optimum hole-opening condition for cisplatin incorporation in single-wall carbon nanohorns and its release. **The Journal of Physical Chemistry B**, v. 110, n. 39, p. 19097-19099, 2006.

AJIMA, K. *et al*. Enhancement of In Vivo Anticancer Effects of Cisplatin by Incorporation Inside Single-Wall Carbon Nanohorns. **ACS Nano**, v. 2, n. 10, p. 2057-2064, 2008.

ALMEIDA, E. R.; *et al*. Molecular dynamics of carbon nanohorns and their complexes with cisplatin in aqueous solution. **Journal of Molecular Graphics and Modelling**, v. 89, p. 167-177, 2019.

ALMEIDA, E. R.; *et al*. Chemically Modified Carbon Nanohorns as Nanovectors of the Cisplatin Drug: A Molecular Dynamics Study. **Journal of Chemical Information and Modeling**, v. 60, n. 2, p. 500-512, 2020.

ALMEIDA, E. R.; *et al*. Carbon nanohorn as nanocontainer for cisplatin: insights on the interaction with plasma membranes of normal and breast cancer cells. **Physical Chemistry Chemical Physics**, v. 23, n. 30, p. 16376-16389, 2021.

ARLT, M.; *et al*. Delivery of carboplatin by carbon-based nanocontainers mediates increased cancer cell death. **Nanotechnology**, v. 21, n. 33, p. 335101-335110, 2010.

BALAS, M.; *et al*. Fabrication and toxicity characterization of a hybrid material based on oxidized and aminated MWCNT loaded with carboplatin. **Toxicology in Vitro**, v. 37, p. 189-200, 2016.

BENTIN, J.; Duverger, E. Picaud, F. Influence of nanotube section on carboplatin confinement. **Journal of Molecular Modeling**, v. 25, n. 3, p. 1-9, 2019.

BOUBETA, F. M.; *et al*. Lessons learned about steered molecular dynamics simulations and free energy calculations. **Chemical Biology & Drug Design**, v. 93, p. 1-10, 2019.

BRENEMAN, C. M. & WIBERG, K. B. Determining atom-centered monopoles from molecular electrostatic potentials. The need for high sampling density in formamide conformational analysis. **Journal of Computational Chemistry**, v. 11, n. 3, 1990.

CANCÈS, E.; MENNUCCI, B.; TOMASI, J. A new integral equation formalism for the polarizable continuum model: theoretical background and applications to isotropic and anisotropic dielectrics. **The Journal of Chemical Physics**, v. 107, p. 3032-3041, 1997.

CASE, D. A.; *et al*. **AMBER 2016**, University of California, San Francisco, 2016.

COVA, T. F.; NUNES, S.C.C.; PAIS, A. C. Free-energy patterns in inclusion complexes. The relevance of non-included moieties in the stability constants. **Physical Chemistry Chemical Physics**, v. 19, n.7, p. 5209-5221, 2017,

CURCIO, M.; *et al*. Carbon Nanohorns as Effective Nanotherapeutics in Cancer Therapy. **C – Journal of Carbon Research**, v. 7, n. 3, p. 1-18, 2021.

DARDEN, T.; YORK, D.; PEDERSEN, L. An N·log(N) Method for Ewald Sums in Large Systems. **The Journal of Chemical Physics**, v. 98, n. 12, p. 10089-10092, 1993.

DA SILVA, A. M..; *et al*. New insights on chemical oxidation of single-wall carbon nanotubes: a theoretical study. **The Journal of Physical Chemistry C**, v. 113, p. 10079-10084, 2009.

DE SOUZA, L. A.; *et al*. Cisplatin release from inclusion complex formed by oxidized carbon nanotube: A DFT study. **Chemical Physics Letters**, v. 774, p. 138619-138626, 2021.

DE SOUZA, L. A.; *et al*. Oxidized single-walled carbon nanotubes and nanocones: a DFT study. **Royal Society of Chemistry Advances**, v. 7, p. 13212-13222, 2017.

DE SOUZA, L. A.; *et al*. Cisplatin release from inclusion complex formed by oxidized carbon nanotube: a DFT study. **Chemical Physics Letters**, v. 774, n. 42, p. 138619-138626, 2021.

DEWITT, M.; *et al*. Influence of hyperthemia on efficacy and uptake of carbon nanohorn-cisplatin conjugates. **Journal of Biomechanical Engineering**, v. 136, n. 2, 2014.

DEWAR, M. J. S.; *et al.* Development and use of quantum mechanical molecular models. 76. AM1: a new general purpose quantum mechanical molecular model. **Journal of the American Chemical Society**, v. 107, n. 13, p. 3902-3909, 1985.

DILRUBA, S. & KALAYDA, G.V. Platinum-based drugs: past. present and future. **Cancer Chemotherapy and Pharmacology**, v. 77, n. 6, p. 1103-1124, 2016.

DO, P-C.; LEE, E. H.; LE, L. T. Steered Molecular Dynamics Simulation in Rational Drug Design. **Journal of Chemical Information and Modeling**, v. 58, n. 8, p. 1473-1482, 2018.

DUAN, X; *et al*. Nanoparticle formulations of cisplatin for cancer therapy. **WIREs Nanomedicine and Nanobiotechnology**, v. 8, n. 5, p. 776-791, 2016.

EL KHALIFI, *et al*. Theoretical study of interaction between carbon nanotubes and carboplatin anticancer molecules. **Analytical Methods**, v. 7, n. 24, p. 10145-10150, 2015.

EL KHALIFI, M.; *et al*. Theoretical demonstration of the potentiality of boron nitride nanotubes to encapsulate anticancer molecule. **Physical Chemistry Chemical Physics**, v. 17, n. 44, p. 30057-30064, 2015.

EL KHALIFI, M.; *et al*. Encapsulation capacity and natural payload delivery of an anticancer drug from boron nitride nanotube. **Physical Chemistry Chemical Physics**, v. 18, n. 36, p. 24994-25001, 2016.

FORD, R.; *et al*. Carbon nanohorn modified platinum electrodes for improved immobilization of enzyme in the design of glutamate biosensors. **Analyst**, v. 144, n. 17, p. 5299-5307, 2019.

FRISCH, M. J.; *et al*. Gaussian 09, revisão D.01.; Gaussian, Inc.: Wallingford, CT, 2009.

FURMANIAK, S.; *et al*. Carbon nanohorns as reaction nanochambers – a systematic Monte Carlo study. **Scientific Reports**, v. 8, p. 15407-15416, 2018.

GROSSFIELD. Alan. "WHAM: the weighted histogram analysis method". version 2.0.10.1. http://membrane.urmc.rochester.edu/wordpress/?page_id=126.

HAY, P. J. & WADT, W. R. Ab initio effective core potentials for molecular calculations. Potentials for K to Au including the outermost core orbitals. **The Journal of Chemical Physics**, v. 82, p. 299-310, 1985.

HE, B.; *et al*. Single-walled carbon-nanohorns improve biocompatibility over nanotubes by triggering less protein-initiated pyroptosis and apoptosis in macrophages. **Nature Communications**, v. 9, n. 2393, p. 1-21, 2018.

HEHRE, W. L. ; DITCHFIELD, R. ; POPLE, J. A. Self-Consistent Molecular Orbital Methods. XII. Further Extensions of Gaussian-Type Basis Sets for Use in Molecular Orbital Studies of Organic Molecules. **Journal of Chemical Physics**, v. 56, n. 5, p. 2257-2261, 1972.

HESTENES, M. R. & STIEFEL, E. Methods of Conjugate Gradients for Solving Linear Systems. **Journal of Research of the National Bureau of Standards**, v. 49, p. 409-436, 1952.

IIJIMA, S.; *et al*. Nano-Aggregates of Single-Walled Graphitic Carbon Nanohorns. **Chemical Physics Letters**, v. 309, p. 165-170, 1999.

ISAAC, K. M.; *et al*. Functionalization of single-walled carbon nanohorns for simulations fluorescence imaging and cisplatin delivery in vitro. **Carbon**, v. 138, n. 7, p. 309-318, 2018.

JENSEN, F. **Introduction to Computational Chemistry**, John Wiley & Sons, 2nd edition, Chichester, UK, 2007

KAGKOURA, A. & TAGMATARCHIS, N. Carbon nanohorn-based electrocatalysts for energy conversion. **Nanomaterials**, v. 10, n. 7, p. 1407-1433, 2020.

KÄSTNER, J. Umbrella Sampling. **WIREs Computational Molecular Science**, v. 1, p.932-942, 2011.

KASUYA, D.; *et al*. Selective production of single-wall carbon nanohorn aggregates and their formation mechanism. **The Journal of Physical Chemistry B**, v. 106, n. 19, 2002.

KAROUSIS, N.; *et al*. Structure, properties, functionalization, and applications of carbon nanohorns. **Chemical Reviews**, v. 116, n. 8, p. 4850-4883, 2016.

KHATTI, Z. & HASHEMIANZADEH, S. M. Investigation of thermodynamic and structural properties of drug delivery system based on carbon nanotubes as a carboplatin drug carrier by molecular dynamics simulations. **Journal of Inclusion Phenomena Macrocyclic Chemistry**, v. 83, n. 1-2, p. 131-140, 2015.

KHATTI, Z.; HASHEMIANZADEH, S. M.; SHAFIEI, S. A. A molecular study on drug delivery system based on carbon nanotube for encapsulation of platinum-based anticancer drug. **Advanced Pharmaceutical Bulletin**, v. 8, n. 1, p. 163-167, 2018.

KOKUBUN, K.; *et al*. Immobilization of a carbon nanomaterial-based localized drug-release system using a bispecific material-binding peptide. **International Journal of Nanomedicine**, v. 13, p. 1643-1652, 2018.

KUMAR, S.; *et al.* The weighted histogram analysis method for free-energy calculations on biomolecules. I. The method. **Journal Computational Chemistry**, v. 13, n. 8, p. 1011-1021, 1992.

LOPES, J. F.; *et al.* Theoretical study of the potential energy surface for the interaction of cisplatin and their aquated species with water. **Journal of Chemical Physical**, p. 128, n. 16, p. 16510-165117, 2008.

LUCÍO, M. I.; *et al*. Targeted killing of prostate cancer cells using antibody-drug conjugated carbon nanohorns. **Journal of Materials Chemistry** B, v. 5, n. 44, p. 8821-8832, 2017.

MAHDAVIFAR, Z. & MORIDZADEH, R. Theoretical prediction of encapsulation and adsorption of platinum-anticancer drugs into single-walled boron nitrite and carbon nanotubes. **Journal of Inclusion Phenomena and Macrocyclic Chemistry**, v. 79, n. 3-4, p. 443-457, 2014.

MATSUMURA, S.; *et al*. Dispersion of cisplatin-loaded carbon nanohorns with a conjugated comprised of an artificial peptide aptamer and polyethylene glycol. **Molecular Pharmaceutics**, v. 4, n. 5, p. 723-729, 2007.

MEJRI, A.; *et al*. Confinement of the antitumoral drug cisplatin inside edge-functionalized carbon nanotubes and its release near lipid membrane. **The European Physical Journal D**, v. 75, n. 99, p. 1-10, 2021.

MIYAWAKI, J.; *et al*. Toxicity of single-walled carbon nanohorns. **ACS Nano**, v. 2, n. 2, 2008.

MØLLER, C. & PLESSET, M. S. Note on an Approximation Treatment for Many-Electron Systems. **Physical Review**, v. 46, p. 618-622, 1934.

MORENO-LANCETA, A.; *et al*. Single-walled carbono nanohorns as promising nanotube-derived delivery systems to treat cancer. **Pharmaceutics**, v. 12, n. 9, p. 850-871, 2020.

MURATA, K.; *et al*. Nanowindow-Induced Molecular Sieving Effect in a Single-Wall Carbon Nanohorn. **The Journal of Physical Chemistry B**, v. 106, n. 49, p. 12668-12669, 2002.

NEJAD, M. A.; URBASSEK, H. M. Adsorption and diffusion of cisplatin molecules in nanoporous materials: a molecular dynamics study. **Biomolecules**, v. 9, n. 5, p. 1-10, 2019.

OUN, R.; *et al*. The side effects of platinum-based chemotherapy drugs: a review for chemists. **Dalton Transactions**, v. 47, n. 19, p. 6645-6653, 2018.

PAMPEL, A.; MICHEL, D.; RESZKA, R. Pulsed field gradient MAS-NMR studies of the mobility of carboplatin in cubic liquid-crystalline phases. **Chemical Physics Letters**, v. 357, n. 1-2, p. 131-136, 2002.

PANCZYK, T.; *et al*. Molecular dynamics study of cisplatin release from carbon nanotubes capped by magnetic nanoparticles. **The Journal of Physical Chemistry C**, v. 117, p. 17327-17336, 2013.

PANCZYK, T.; WOLSKI, P.; LAJTAR, L. Coadsorption of Doxorubicin and Selected Dyes on CarbonNanotubes. Theoretical Investigation of Potential Application as a pH-Controlled Drug Delivery System. **Langmuir**, v. 32, n. 12, p. 4719-4728, 2016.

RYCKAERT, J. P.; CICCOTTI, G.; BERENDSEN, H. J. C. Numerical integration of the Cartesian equations of motion of a system with constraints: Molecular dynamics of n-alkanes. **Journal of Computational Physics**, v. 23, n. 3, p.327-341, 1977.

SALAS-TREVIÑO, D.; *et al*. Hyaluronate functionalized multi-wall carbon nanotubes filled with carboplatin as a novel drug nanocarrier against murine lung cancer cells. **Nanomaterials**, v. 9, n. 11, p. 1572-1583, 2019.

SALOMON-FERRER, *et al*. Routine Microsecond Molecular Dynamics Simulations with AMBER on GPUs. 2. Explicit Solvent Particle Mesh Ewald. **Journal of Chemical Theory Computational**, v. 9, p. 3878-3888, 2013.

SANO, N.; TANIGUCHI, K.; TAMON, H. Hydrogen storage in porous single-walled carbon

nanohorns dispersed with Pd-Ni alloy nanoparticles. **The Journal of Physical Chemistry C**, v. 118, n. 7, p. 3402-3408, 2014.

SANTANA, L. C. **Desenvolvimento de Parâmetros Intermoleculares para o Estudo de Carboplatina e Oxaliplatina em Solução Aquosa**. 2019. Master's dissertation. Universidade Federal de Itajubá, 2019.

SELVAM, K. P.; *et al*. Synthesis and characterization of conductive flexible cellulose carbon nanohorn sheets for human tissue applications. **Biomaterials**, v. 24, n. 18, p. 1-12, 2020.

SHI, Y.; *et al*. Biodistribution survey of oxidized single-wall carbon nanohorns following different administration routes by using label-free multispectral optoacoustic tomography. **International Journal of Nanomedicine**, v. 14, p. 9809-9821, 2019.

STEVIC, D.; *et al*. Cu-phthalocyaninemediated nanowindow production on single-wall carbon nanohorn. **Molecular Physics**, v. 119, n. 15-16, 2021.

WANG, J.; *et al*. Development and testing of a general amber force field. **Journal of Computational Chemistr**y, v. 25, n. 9, p. 1157-1174, 2004.

WU, L.; *et al*. PEGylated multi-walled carbon nanotubes for encapsulation and sustained release of oxaliplatin. **Pharmaceutical Research**, v. 30, n. 2, p.412-423, 2013.

YANG, J.; *et al*. Dual chemodrug-loaded singlewalled carbon nanohorns for multimodal imaging-guided chemo-photothermal therapy of tumors and lung metastases. **Theranostics**, v. 8, n. 7, p. 1966-1984, 2018.

ZHANG, Z.; *et al*. Single-walled carbon nanohorns for energy applications. **Nanomaterials**, v. 5, n. 4, p. 1732-1755, 2015.

ZHANG, M.; *et al*. Biodegradation of carbon nanohorns in macrophage cells. **Nanoscale**, v. 7, n. 7, p. 2834-2840, 2015.

ZHENG, S.; *et al*. VFFDT: a new software for preparing AMBER force field parameters for metal-containing molecular systems. **Journal of Chemical Information and Modeling**, v. 56, p. 811-818, 2016.

5 CHAPTER 5

Modeling the cellular uptake of functionalized carbon nanohorns loaded with cisplatin through a breast cancer cell membrane

5.1 INTRODUCTION

Breast cancer is pointed out as the most frequent type of cancer in women and as the 5th cause of deaths among the modalities of this disease (ŁUKASIEWICZ, *et al*., 2021; GIAQUINTO, *et al.*, 2022). This malignant neoplasm has a heterogeneous and complex profile, since it involves a series of variations in terms of aggressiveness, genome, morphology, and incidence (GODONE, *et al.*, 2018). When it comes to the treatments, the *cis*-diamminedichloroplatinum(II)-based chemotherapy, also known as cisplatin, is a routine alternative due to its notable inhibition towards breast cancer cells growth and even to the prevention of metastasis (WANG, *et al*., 2021). However, the medication with this well-known platinum drug causes not only severe side effects due to the damages to healthy cells, but also the resistance in tumors as a result of the low accumulation of this metallodrug at these sites (ZHANG, *et al.*, 2022).

The use of nanomaterials as vectors of this drug is a potential strategy to circumvent these problems, since the enhanced permeability and retention effect in solid tumors can optimize both accumulation and penetration of nanoparticles in these specific sites (SHINDE, *et al.*, 2022; EJIGAH, *et al*., 2022). In this context, the carbon nanohorns (CNHs) represent a promising nanocarrier class for cisplatin (cddp) due to their potential properties for medical applications, such as biocompatibility (HE, *et al.*, 2018), hemocompatibility (ZIEBA, *et al*., 2021), low toxicity (CURCIO, *et al*., 2021), biodegradability route by the myeloperoxidase enzyme (ZHANG, *et al*., 2015), and dispersibility in physiological solutions when they are functionalized (LANCETA, *et al*., 2020). Typical structures of this carbon nanomaterial are formed by a tubular section, which has a length of 40-50 nm and a diameter of 2-3 nm, coupled to a conical end with a cone angle of ~20° by means of topological defects (IIJIMA, *et al*., 1999).

The encapsulation of cddp inside CNHs has been studied since 2005, when Ajima and coworkers reported that this nanoformulation avoided the drug dissipation by providing its slow release to the tumor site (AJIMA, *et al*., 2005). The next papers of Ajima *et al.* pointed out not only the adherence of oxidized CNH with a high cddp load to cancer cells up to 25 days, but

also a better drug release process (~70%) by chemically protecting the holes, also known as nanowindows, formed on the surface of this nanomaterial (AJIMA, *et al.*, 2006; AJIMA, *et al*., 2008). Therefore, the efficiency of CNH-based drug delivery systems (DDS) depends on post-synthesis treatments, such as oxidation and chemical functionalization, which reduce the high hydrophobicity of this nanomaterial (KAROUSIS, *et al*., 2016). Concerning the covalent decoration of CNHs, by functionalizing oxidized CNH (CNHox) with poly(ethylene glycol) diamine and cyanine 3 dye and exposing them to the human cervical cancer cell line HeLa ATCC CCL2, Hifni and coworkers (HIFNI, *et al*., 2020) reported a cellular viability of 80% of this cell line even in high concentration (20 μg/mL) of this nanomaterial. Recently, Gao and coworkers (GAO, *et al.*, 2022) discussed the preparation of CNHs as phototheranostic agents by employing a noncovalent functionalization based on the conjugation between hyaluronic acid containing an amide bond (HA-NH_2) and IR808 dye. In addition to providing a targeted tumor ablation with a simultaneous fluorescence imaging-guidance, this nanoformulation resulted in a suppression of residual cancer cells.

Our group has studied functionalized CNH (CNHf) models considering molecular dynamics (MD) simulations and quantum mechanical calculations. In 2020, we proposed a series of oxidized and reduced CNH models with encapsulated cddp based on oxidation and reduction reactions at high temperature. It was shown that the stability of the inclusion complexes could be modulated by the oxidation degree (ALMEIDA, *et al*., 2020). More recently, we studied the incorporation of cddp, carboplatin, and oxaliplatin into a CNHox prototype with a ~11 Å nanowindow, which is the typical size verified in experimental studies. The results pointed out that the drug releasing processes were endothermic with energy barriers of about 21 kcal mol^{-1} (ALMEIDA, *et al*., 2022). By using a QM/MM hybrid method, we also investigated the nanoconfinement effect on the hydrolysis reaction of cddp inside a CNHf model decorated with amide-thiol groups. We showed that the reaction in the confined regime was kinetically favorable by 4-orders of magnitude, whereas it was also less spontaneous (~7 kcal mol^{-1}) if we compared to this process in bulk solution (ALMEIDA, *et al*., 2023).

In nanomedicine, another relevant information for the applications of CNHs as cddp carriers is the understanding of their interaction and cellular uptake in human tissues. This issue was explored by Zhu and coworkers (ZHU, *et al*., 2016) that demonstrated the non-pathogenicity of pristine CNHs compartmentalized in hepatocytes, since this nanomaterial induced neither damages in lysosomes nor activation of apoptosis, unlike long and stiff carbon nanotubes (CNTs). The intracellular uptake of CNHox in both Madin-Darby canine kidney cells and nude mice was also studied by Shi and coworkers (SHI, *et al.*, 2017). In addition to

reporting a substantial bioadhesion on cells, the authors pointed out not only the occurrence of the CNHs transcytosis in these cell lines, but also a long retention of them in the intestinal tract of mice. The study conducted by He and coworkers (HE, *et al*., 2018) also indicated that the internalization of CNHs in macrophages via phagocytosis presented a lower membrane disturbance compared to CNTs. Based on the electron paramagnetic resonance (EPR) spectra using the spin probes technique, Kartel and coworkers (KARTEL, *et al*., 2020) described that the interaction of CNHox with erythrocytes of rats caused disorders in the outer leaflet of the lipid bilayers, as well as an increase of polarity in this microenvironment.

When it comes to an *in-silico* approach, we reported the interaction mechanism between the complex 3cddp@CNHox (three cddp molecules encapsulated in a CNHox model) and membrane models of cancer and normal cells referring to the human breast via MD simulations (ALMEIDA, *et al*., 2021). In contrast to the results with the healthy membrane, the simulations highlighted that the nanovector established fast and strong interactions with the cancer cell membrane, as well as a more favorable cddp release near the tumor environment. However, the translocation of the 3cddp@CNHox through the biomembranes was not completely captured by the 800 ns unbiased MD simulations. In fact, there is a lack of information regarding the CNHs permeation through cell membranes at a molecular level.

Unlike CNHs, there are some insights in literature concerning this process for CNTs (RACZYNSKI, *et al.*, 2013; RACZYNSKI, *et al.*, 2014; TABARI, *et al.*, 2015). For instance, steered molecular dynamics (SMD) simulations conducted by Raczynski and coworkers (RACZYNSKI, *et al.*, 2013) evidenced the penetration process of a membrane model formed by 1,2-dimyristoyl-*sn*-glycero-3-phosphocholine (DMPC) and cholesterol molecules with CNTs prototypes. The authors showed that the process with capped CNTs involved both energy barrier and level of deformation lower than that the one with open-ended CNTs. By using the adaptive biasing method (ABF), Tabari and coworkers (TABARI, *et al.*, 2015) reported a strong interaction (120 kcal mol^{-1}) between a CNT model with hydroxyls groups at the open ends and a 1,2-dioleoyl-*sn*-glycero-3-phosphocholine (DOPC) bilayer. Raczynski and coworkers (RACZYNSKI, *et al.*, 2018) also demonstrated the inexistence of permanent damages on the DMPC membrane model during both nanoindentation and translocation processes of CNTs.

In view of the research gap concerning the cellular uptake of CNHs, the focus of our work is to describe the dynamics and energetics referring to the permeation of functionalized CNHs carrying cddp molecules through a membrane model of breast cancer cells by using biased MD simulations. A molecular understanding of the cellular internalization of CNHs is a

key to modulate the membrane disturbance, which is also correlated with the activation of cytotoxicity cascades.

5.2 METHODS

5.2.1 Molecular models

Regarding the CNHs, we built three prototypes that take into account the most conventional chemical modifications of carbon nanostructures: an oxidized carbon nanohorn (CNHox) model, a covalently functionalized carbon nanohorn (CNHf-cov) model, and a noncovalently functionalized carbon nanohorn (CNHf-ncov) model. The CNHox topology ($C_{279}H_{52}O_{41}$, see Figure 6.1A), which was presented in our previous study (ALMEIDA, *et al*., 2021), was modeled from a pristine structure ($C_{360}H_{24}$) (DOS SANTOS, *et al.*, 2014) using as a guide the oxidation reaction with O_2 and H_2O at high temperature (DA SILVA JR, *et al.,* 2009). In addition to presenting hydroxyl, carbonyl, and carboxyl groups in all pentagons on the carbon wall, this structure includes hydroxyls at the open-end edge and a realistic nanowindow (~11 Å), which is normally formed during the oxidation process (MURATA, *et al*., 2002; AJIMA, *et al*., 2004).

Since the oxidation is generally the first step in the chemical functionalization routes of CNHs, we considered the CNHox structure as the template for modeling the CNHf-cov and CNHf-ncov topologies. By using as guide the reaction reported by Hifni and coworkers (HIFNI, *et al*., 2020) between CNHox and solutions of *N*-(3-dimethylaminopropyl)-*N*′-ethylcarbodiimide, *N*-hydroxysuccinimide, and 1,8-diamino-3,6-dioxaoctane at room temperature, we modified the carboxyls groups of the CNHox by inserting the 1,8-diamino-3,6-dioxaoctane (Fig.6.1D) in order to build the CNHf-cov ($C_{297}H_{94}N_6O_{44}$, see Figure 6.1B) model. Finally, the CNHf-ncov ($C_{308}H_{100}N_4O_{61}$, see Figure 6.1C) prototype was built by positioning a HA-NH_2 chain ($C_{29}H_{48}N_4O_{20}$, Figure 6.1E), which was formed by two repeated disaccharide units (β-D-glucuronic acid and *N*-acetyl-D-glucosamine), onto the external surface of the CNHox topology. This modification was a part of the noncovalent functionalization scheme of CNHs described by Gao and coworkers (GAO, *et al.*, 2022), who then added the photosensitizer IR808 in this nanoformulation.

The geometries of the three CNH structures were optimized in aqueous solution using the polarizable continuum model (PCM) with the integral equation formalism (IEF) (CANCÈS

& TOMASI, 1934) variant at the semiempirical method Austin Model 1 (AM1) (DEWAR, *et al.*, 1985).

Figure 5.1 - Side (top) views of the inclusion complexes and the 2D structures (bottom) of the functionalization groups. The systems are formed by three cddp molecules encapsulated into the oxidized (CNHox), covalently functionalized (CNHf-cov), and noncovalently functionalized (CNHf-ncov) carbon nanohorn models named as 3cddp@CNHox (A), 3cddp@CNHf-cov (B), and 3cddp@CNHf-ncov (C), respectively. The L, D_w, and D_e parameters indicate the average values for the length, the diameter of the nanowindow, and the diameter of the open end. The carboxyls with 1,8-diamino-3,6-dioxaoctane (D) were used as the covalent functionalization of the CNHf-cov, where the letter R refers to the CNH. The activated HA-NH_2 (E) was used as the noncovalent functionalization of the CNHf-ncov.

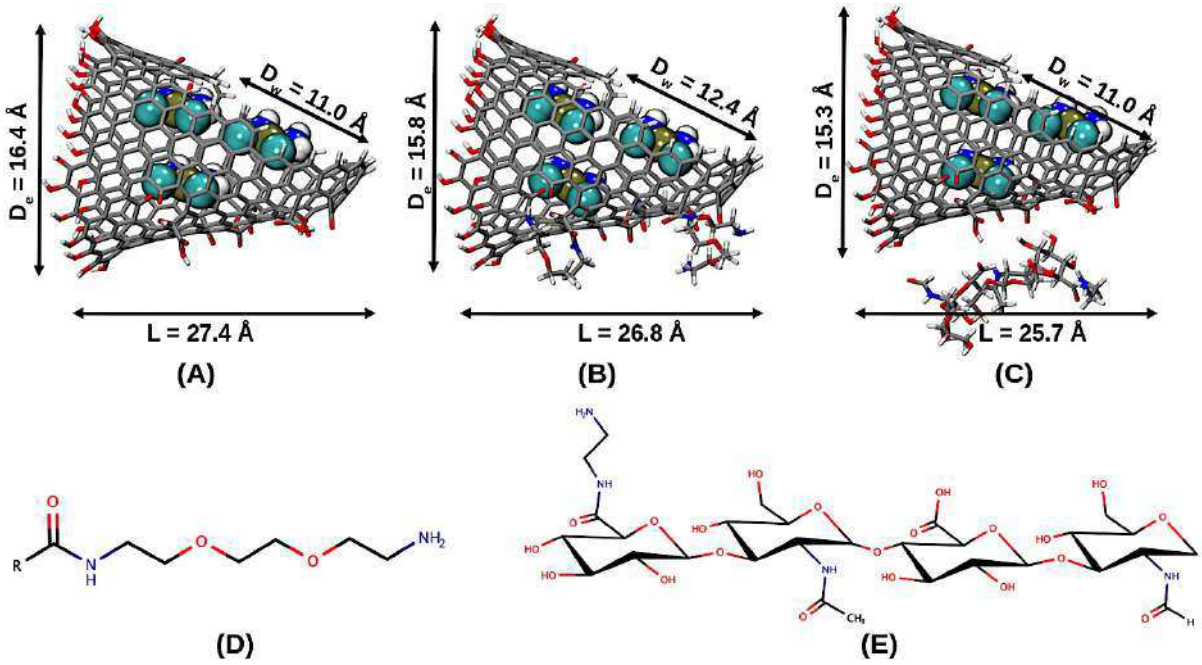

Reference: Own author (2023).

In order to build the inclusion complexes, we encapsulated three cddp molecules inside each CNH model since transmission electron microscopy (TEM) images (AJIMA, *et al.*, 2008) revealed the presence of cddp clusters with this size at the tip region of the experimental CNHs, which is the part represented by our models. The three inclusion complexes to be studied herein with the optimized CNH structures (AM1) are shown in Figure 5.1.

Concerning the biomembrane, we employed our previous model of a human breast cancer cell membrane (C_memb) (ALMEIDA, *et al.*, 2021), which was built based on the lipid

composition referring to the MCF-7 cell line (TODOR, *et al.*; 2012). The lipid composition of this model is organized in Table 5.1.

Table 5.1 - Composition and distribution of lipids and ions referring to the plasma membrane model of a breast cancer cell (C_memb) (ALMEIDA, *et al*., 2021).

Components	**Lipid composition / %**	
Lipids [a]	**outer leaflet**	**inner leaflet**
DOPC	23.2	23.2
DOPE	9.7	9.7
DOPGR	2.8	2.8
DOPS	4.0	4.0
CHL	10.3	10.3
Ions	**Ionic concentration / M** [b]	
Na^+	0.15	
Cl^-	0.15	

[a]Lipid composition based on the MCF-7 cell line (SOULE, *et al*., 1973).[37] [b]Molar concentration of ions in the physiological environment. DOPC: 1,2-dioleoyl-*sn*-glycero-3-phosphocholine. DOPE: 1,2-dioleoyl-*sn*-glycero-3-phosphoethanolamine. DOPGR: 1,2-dioleoyl-*sn*-glycero-3-[phospho-rac-(1-glycerol)]. DOPS: 1,2-dioleoyl-*sn*-glycero-3-phospho-L-serine. CHL: cholesterol.
Reference: Own author (2023).

In brief, the C_memb model takes into account the main characteristics that are observed in membrane of these cells, such as the deregulation of the lipids distribution asymmetry that produces the symmetrization of these biomolecules among the leaflets (BERNADES & FIALHO, 2018), the exposure of the phospholipid PS in the outer monolayer of the membrane (SHARMA & KANWAR, 2018), the increase of the cholesterol concentration (about 37.5%) compared to membranes of normal breast cells (BERNADES & FIALHO, 2018). It is worth to emphasize that the heterogeneity of our model includes the most abundant lipids expressed in the MCF-7 cell line. Additionally, the C_memb was generated using the membrane builder tool available on the CHARMM-GUI website (JO, *et al*., 2008; LEE, *et al*., 2020).

Lastly, we built the central systems to be evaluated in this work (see Figure 5.2) by aligning the main axis of each inclusion complex (3cddp@CNHox, 3cddp@CNHf-cov, and 3cddp@CNHf-ncov) to the perpendicular axis relative to the plane of the equilibrated C_memb. The initial distance between the surface of the C_memb and the tip region of the nanocarriers was about 14 Å. Henceforth, these three systems will be referenced as 3cddp@CNHox>C_memb, 3cddp@CNHf-cov>C_memb, and 3cddp@CNHf-ncov>C_memb.

Figure 5.2 - The initial configurations of the three systems simulated in this work: 3cddp@CNHox>C_memb (A), 3cddp@CNHf-cov>C_memb (B), and 3cddp@CNHf-ncov>C_memb (C). The violet, red, orange, tan, magenta, white, green, and yellow correspond to the DOPC, DOPE, DOPS, DOPGR, CHL, OL, Cl-, and Na+ components, respectively.

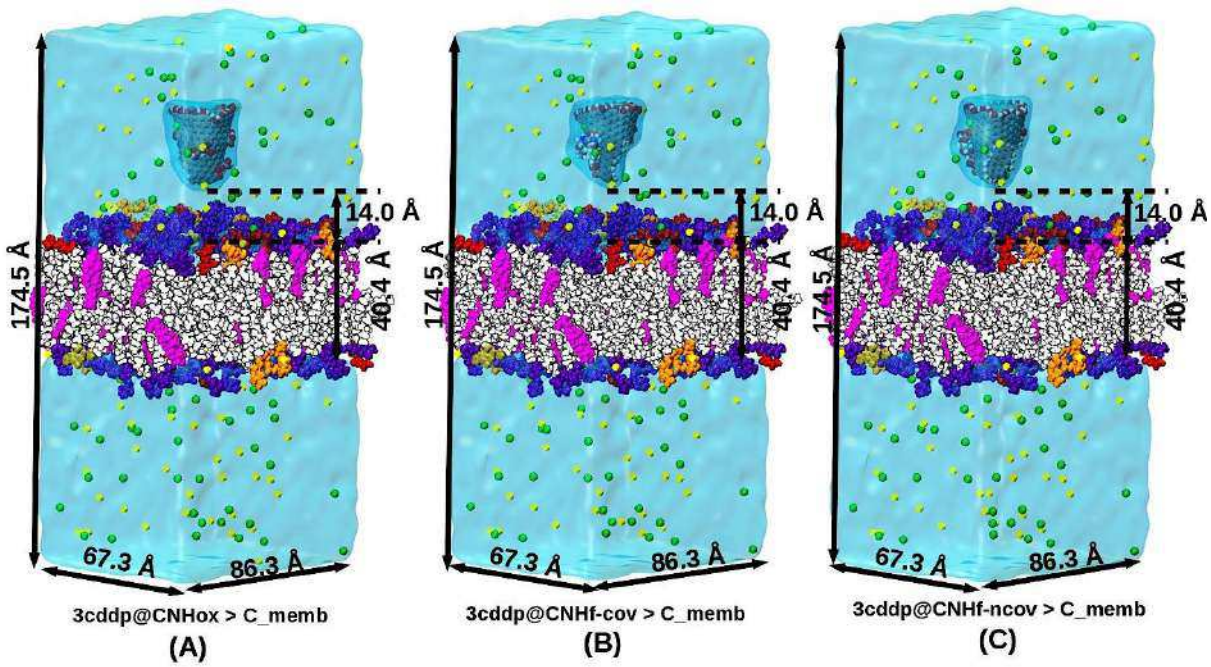

Reference: Own author (2023).

5.2.2 Force field parameterization

Regarding the three CNH models, we used the General Amber Force Field (GAFF2) (WANG, *et al*., 2004) for describing the intramolecular and intermolecular (only the Lennard-Jones (LJ) 12-6) parameters. Atomic charges were calculated using the ChelpG approach (BRENEMAN & WIBERG, 1990) at the HF/6-31G(d,p) level of theory in aqueous solution with the IEF variant of the PCM.

With regard to the cddp molecule, we employed our parameterization scheme described previously (ALMEIDA, *et al*., 2019). Basically, the intramolecular parameters were calculated from the optimized structure of cddp at the MP2/6-31G(d,p)/LANL2DZ level of theory (MØLLER & PLESSET, 1934; HEHRE, *et al*., 1972; HAY & WADT, 1985). We used the Visual Force Field Toolkit (ZHENG, *et al*., 2016) to derive the force constants referring to the bond stretching and angle bending. By applying the ChelpG method, we calculated the atomic charges at the HF/6-31G(d,p)/LANL2DZ level of theory in aqueous solution considering the PCM with the IEF variant. Lastly, while the LJ 12-6 potential parameters for the Pt atom were

collected from a previous study (LOPES, *et al*., 2008), the same set for the Cl, N, and H atoms was selected from the GAFF (WANG, *et al*., 2004).

The parameters of the lipid17 force field (CASE, *et al*., 2019) were used to represent the C_memb model as discussed in our previous paper (ALMEIDA, *et al*., 2021) We described the water molecules by means of the TIP3P model (JORGENSEN, *et al.*, 1983) and we used the parameters set reported by Li and coworkers (LI, *et al*., 2015) to model the Na^+ and Cl^- ions.

5.2.3 Computational details

The quantum mechanical calculations were performed with the Gaussian-09 release D.01 program (FRISCH, *et al*., 2009), and the MD simulations were conducted using the pmemd CUDA implementation (SALOMON-FERRER, *et al*., 2013) of the Amber 20 software (CASE, *et al*., 2020). For the analysis of MD trajectories, we used the CPPTRAJ module (ROE & CHEATHAM, 2013).

Regarding the unbiased simulations of the free inclusion complexes in aqueous solution, each solute was initially positioned at the center of a solvent box with a truncated octahedral shape and an average length of 92.0 Å, containing TIP3P water molecules. The first stage of the simulation protocol was the energy minimization of the solvent keeping a positional restraint to the solute (500 kcal mol^{-1} $Å^{-2}$) followed by the same process for the entire system. In this stage, we used the steepest descent (SD) method (JENSEN, 2007) for the first 5,000 cycles, while we employed the conjugate gradient (CG) method (HESTENES & STIEFEL, 1952) for the last 5,000 cycles. Next, we started the heating stage of the systems from 283 K to 310 K, considering the canonical ensemble (NVT) and the Langevin thermostat (UBERUAGA, *et al*., 2004). Specifically, we applied weak restraints on the solute based on the application of a 5 kcal mol^{-1} $Å^{-2}$ force constant during these 500 ps runs. After, we performed the equilibration stage for ~30 ns with no positional restraints at 310 K and 1.0 bar pressure, employing the isothermal-isobaric ensemble (NPT) and the Berendsen barostat (BERENDSEN, *et al*., 1984). Finally, the production stage was conducted for 300 ns considering the NPT ensemble. For the binding free energy ($\Delta_b G$) calculations, we used the molecular mechanics generalized Born surface area (MM/GBSA) method (MILLER III, *et al.*, 2012). We ran all unbiased MD simulations in triplicate and the results were expressed as an average of these independent runs.

The biased simulations referring to the translocation of the inclusion complexes through the C_memb (see Figure 5.2) were conducted using the SMD (BOUBETA, *et al*., 2019) and Umbrella Sampling (US) (KÄSTNER, 2011) methods. For these simulations, we defined the

reaction coordinate as a distance of 115 Å along the perpendicular axis (z axis) to the plane of the membrane. In order to precisely calculate the potential of mean force (PMF) referring to the permeation processes, we performed simulations in two directions along the reaction coordinate: from 50 Å to -65 Å and from -50 Å to 65 Å (see Figure C.1). For the protocol, we firstly conducted the energy minimization stage with the same details as described for the unbiased simulations. The next stage was the 25 ns equilibration at 310 K and 1 bar, where the inclusion complexes were held at 14 Å relative to the plane of the C_memb using a positional restraint of 2.5 kcal mol^{-1} $Å^{-2}$. In this stage, we applied a semiisotropic pressure scaling and a surface tension (γ) regulation with the NPγT ensemble. After that, we ran the pulling stage of the nanocarriers along the reaction coordinate from 50 Å to -65 Å and from -50 Å to 65 Å through the membrane (z axis) for 50 ns using the SMD method. Then, we divided the reaction coordinate into intervals of 1 Å resulting in 115 configurations of the inclusion complex through the membrane. At last, for US, each of these 115 windows was run for 30 ns using the NPγT ensemble and a harmonic bias potential with a 2.5 kcal mol^{-1} $Å^{-2}$ force constant. We calculated the PMFs and their statistical errors by means of the Weighted Histogram Analysis Method (WHAM) (KUMAR, *et al*., 1992; GROSSFIELD, 2023; KUMAR, *et al*., 2005; ROUX, 1995) and the Monte Carlo bootstrap error analysis (EFRON & TIBSHIRANI, 1994).

As general details, all simulations were conducted in periodic boundary conditions using 0.15 M dissociated NaCl, a time step of 2.0 fs and the shake algorithm (RYCKAERT*, et al*., 1977) to restrain the bonds involving H atoms. We employed the Particle Mesh Ewald (PME) method (DARDEN, *et al*., 1993) to treat the electrostatic interactions, while the van der Waals interactions were spherically truncated at 12 Å cutoff. The main details of all simulations are organized in Table 5.2.

The deuterium order parameters (S_{CD}^{i}) of each carbon atom i of the oleoyl (OL) tails were calculated according to Eq. 5.1 (VÖGELE, *et al*., 2018), where Θ_i corresponds to the angle between each C-H bond of the lipid tails and normal axis to the plane of the membrane, and the symbol < > indicates an average referring to the MD trajectories.

$$S_{CD}^{i} = \frac{1}{2}\langle 3cos^{2}\Theta_{i} - 1\rangle \tag{5.1}$$

Table 5.2 - Summary of the details referring to the MD simulations conducted in this work.

Systems	N_a [a]	N_m^{wat} [b]	N_m^{lip} [c]	N_{lip}^{l} [d]	t_{eq}/ns [e]	t_{SMD}/ns [f]	t_{US}/μs [g]	t_{tot}/μs [h]
3cddp@CNHox	33,371	10,968	-	-	3x240	-	-	3x0.300
3cddp@CNHf-cov	37,190	12,216	-	-	3x120	-	-	3x0.300
3cddp@CNHf-ncov	39,386	12,936	-	-	3x190	-	-	3x0.300
C_memb [i]	96,496	24,200	196	98	400	-	-	0.400
3cddp@CNHox>C_memb	95,903	23,867	196	98	2x25	2x50	2x3.45	2x3.525
3cddp@CNHf-cov>C_memb	95,821	23,817	196	98	2x25	2x50	2x3.45	2x3.525
3cddp@CNHf-ncov>C_memb	95,799	23,799	196	98	2x25	2x20	2x3.45	2x3.525

[a]Total numbers of atoms (solute and solvent). [b]Number of water molecules. [c]Number of lipid molecules. [d]Number of lipid molecules per leaflet. [e]Simulation time for the equilibration stage. [f]Simulation time for the pulling stage of the inclusion complexes through the membrane using the SMD method. [g]Total simulation time of the 115 windows using the US method. [h]Total simulation time. [i]Previously equilibrated model of a breast cancer cell membrane (ALMEIDA, *et al.,* 2021). The index 3x indicates the unbiased simulations that were run in triplicate, while the index 2x refers to the biased simulations that were conducted in two directions (50 Å → -65 Å and -50 Å → 65 Å) along the reaction coordinate. The production time for the free inclusion complexes (three first lines) is given by $t_{prod} = t_{tot} - t_{eq}$. Reference: Own author (2023).

5.3 RESULTS AND DISCUSSION

5.3.1 Stability of the free inclusion complexes in aqueous solution

We firstly analyzed the structural stability of the free inclusion complexes in aqueous solution containing 0.15 M NaCl after the heating stage (see the first three lines in Table 5.2). The plots referring to the temporal variation of the root mean square deviation (RMSD) along 300 ns runs (see Figure C.2) indicate that the 3cddp@CNHox (Figure C.2A) achieved structural stability in 240 ns (6,000 frames), whereas both 3cddp@CNHf-cov (Figure C.2B) and 3cddp@CNHf-ncov (Figure C.2C) achieved this state in 120 ns (3,000 frames) and 190 ns (4,750 frames), respectively. If we consider only the CNHs in the RMSD calculations, the relatively stable profiles of this measure (see Figure C.2) reveal the rigidity and the fast structural stability of these nanostructures over the simulation time. For instance, by calculating the average RMSD considering the runs in triplicate (Table C.1), we notice that both CNHox and CNHf-ncov equilibrate in ~25 ns (625 frames), since the standard deviation values of the RMSD represented slight variations of about 16% relative to the respective averages in addition to the stable moving averages illustrated in Figure C.2A and Figure C.2C during this time. In contrast, Table C.1 points out that the CNHf-cov required 40 ns (1,000 frames) to be equilibrated with

oscillations in the range of 12% of the average RMSD. If we consider the inclusion complex (CNH + three cddp molecules), it is expected to have higher variations in the RMSD over time, as we verify in Figure C.2 and Table C.1, due to the mobility of four species in contrast to two species in the calculation of the RMSD for the CNHs. The results of Table C.1 show that the RMSD values of the 3cddp@CNHf-cov were about 6 times greater than the ones of the other complexes for the equilibration stage and 4 times greater than the ones referring to the other complexes for the production stage. This notable variation for the system with the CNHf-cov is a consequence of the high mobility of the three covalent functionalization chains (backbone of 11 atoms, see Figure 1D) on the surface of this model in addition to the dynamics of the three drug molecules. The equilibration was also observed in terms of the variation of temperature, density, volume, pressure, kinetic, potential and total energies as function of time during the 300 ns simulations by evaluating the stable behavior of the running averages referring to these properties in Figure C.3. Data from Table C.2 also emphasize an energetic stability of all inclusion complexes during the equilibration stages, as we can see standard deviation values of the total energy on the order of 0.2% relative to the average values. With the equilibrated inclusion complexes, all analyses to be presented henceforth will refer to the production runs (see Table 5.2).

The host-guest affinity of the inclusion complexes during the production runs was evaluated in the light of the MM/GBSA method. The average values of the $\Delta_b G$ are presented in Table 5.3 while the energetic components are schematized in Figure 5.3.

Table 5.3 - Statistics of the binding free energies ($\Delta_b G$) referring to the formation of the three inclusion complexes studied in this work.

Process	$<\Delta_b G>$ / kcal mol^{-1} [a]	Std.[b]	Err.[c]
3cddp + CNHox → 3cddp@CNHox	-73.3	2.8	0.07
3cddp + CNHf-cov → 3cddp@CNHf-cov	-70.2	2.9	0.08
3cddp + CNHf-ncov → 3cddp@CNHf-ncov	-62.1	3.2	0.09

[a]The energies were calculated using the Molecular Mechanics Generalized Born Surface Area (MM/GBSA) method. Each value represents an average of the production runs (~117 ns, Table 2) in triplicate considering 1,500 frames per simulation. [b]Standard deviation value. [c]Standard error of the mean.
Reference: Own author (2023).

In addition to verify the thermodynamic stability of all inclusion complexes in Table 5.3, we notice that the 3cddp@CNHf-ncov is the least stable with differences in terms of $\Delta_b G$

of about 11.2 kcal mol^{-1} and 8.1 kcal mol^{-1} for the complexes 3cddp@CNHox and 3cddp@CNHf-cov, respectively. Moreover, we can conclude that the functionalization strategies for the CNHox, *i.e.*, the chemical modification processes of the CNHox to generate both CNHf-cov and CNHf-ncov, reduced the stability of the respective modified inclusion complexes. The deeper analysis (Figure 5.3) of the main terms responsible for the Δ_bG shows that the high stability of these cddp nanoformulations is mainly connected to the van der Waals (vdW) interactions.

Figure 5.3 - Binding free energy decomposition of the three inclusion complexes studied in this work. The energy differences ΔE_{vdW}, ΔE_{elec}, ΔE_{gas}, ΔE_{solv}, $T\Delta S$, and $\Delta_b G$ refer to the van der Waals energy, the electrostatic energy, the energy in gas phase, which includes the sum of the intermolecular energies ($\Delta E_{vdW} + \Delta E_{elec}$), the solvation energy, the entropic contribution, and the binding free energy. All values were calculated as averages of the production runs (~170 ns, Table 5.2) in triplicate considering 1,500 frames for each simulation.

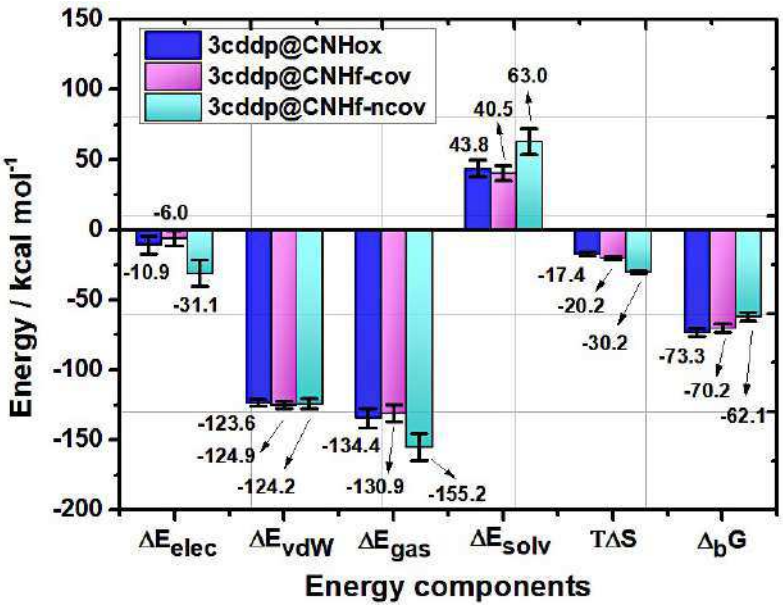

Reference: Own author (2023).

While the energetic component referring to these interactions (ΔE_{vdW}) for the 3cddp@CNHf-ncov represents 80.0% of the total energy in gas phase (ΔE_{gas}), the same component of the 3cddp@CNHf-cov and 3cddp@CNHox represents 95.4% and 79.6% of the ΔE_{gas}, respectively. The predominance of the ΔE_{vdW} component was also reported for nanoparticle formulations of carboplatin based on CNTs (KHATTI & HASHEMIANZADEH, 2015), boron nitride nanotube (KHATTI & HASHEMIANZADEH, 2016), and silicon carbide nanotube (KHATTI, *et al.*, 2018). Regarding the electrostatic component (ΔE_{elec}), the

3cddp@CNHf-ncov presented the highest contribution to its overall stability. Specifically, while the difference in terms of ΔE_{elec} between the 3cddp@CNHf-ncov and 3cddp@CNHox was 20.2 kcal mol^{-1}, the difference between 3cddp@CNHf-ncov and 3cddp@CNHf-cov was 25.1 kcal mol^{-1}.

Still regarding Figure 5.3, the same destabilizer effect by the solvation energy (ΔE_{solv}) was reported not only in our previous studies involving inclusion complexes with CNHs (ALMEIDA, *et al*., 2020; ALMEIDA, *et al*., 2022; ALMEIDA, *et al*., 2019), but also in the studies conducted by Khatti and coworkers (KHATTI & HASHEMIANZADEH, 2016; KHATTI, *et al*., 2018) with other nanocarriers for carboplatin. As we explained in a previous work (ALMEIDA, *et al*., 2019), this behavior is expected due to the notable hydrophobicity of these carbon nanomaterials, which are treated in aqueous solution by the Generalized Born (GB) implicit solvent model of the MM/GBSA method.

Besides, this is also a result of the way this quantity is calculated. The ΔE_{solv} in Figure 5.3 is in fact a relative solvation energy ($\delta\Delta E_{solv}$), *i.e*., solvation energy of products minus solvation energy of reactants: $\delta\Delta E_{solv}=\Delta E_{solv}$(3cddp@CNH)-$\Delta E_{solv}$(3cddp)-$\Delta E_{solv}$(CNH). The contributions ΔE_{solv}(3cddp@CNH) and ΔE_{solv}(CNH) are similar and cancel out, therefore, $\delta\Delta E_{solv}\sim-\Delta E_{solv}$(3cddp) that is expected to be > 0. Finally, we notice that the entropic contribution ($T\Delta S$) to the $\Delta_b G$ was unfavorable for all complexes, especially for the functionalized ones, which is an expected behavior for such associative processes (ALMEIDA, *et al*., 2020; ALMEIDA, *et al*., 2022).

5.3.2 Transmembrane transport mechanism of the inclusion complexes

In order to describe the transmembrane transport of the CNH-based nanovectors through the equilibrated C_memb (ALMEIDA, *et al*., 2021) during the SMD simulations, we plotted in Figure C.4 the temporal variation of the distance between the centers of mass of both CNHs and membrane. This figure demonstrates a complete translocation of all inclusion complexes in 50 ns through the lipid bilayer considering the two directions of the reaction coordinate (50 Å → -65Å and -50 Å → 65 Å). It is possible to verify that the 3cddp@CNHox, 3cddp@CNHf-cov, and 3cddp@CNHf-ncov complexes achieved the center of the membrane at 24.05±0.15 ns, 23.24±0.36 ns, and 23.65±0.14 ns, respectively. These results point out an average reduction of 0.605 ns in the nanoporation time of CNHf into the C_memb compared to the same process with the CNHox. In other words, the functionalization strategies slightly improve the insertion

capacity of CNHs in a cancer membrane. The detailed description of Figure C.4 is presented in Figure 5.4 and Figure C.5.

Figure 5.4 - Permeation of inclusion complexes. Main frames of the SMD simulations referring to the translocation (reaction coordinate: 50 Å → -65 Å) of the inclusion complexes through the cancer cell membrane (C_memb): 3cddp@CNHox>C_memb (A), 3cddp@CNHf-cov>C_memb (B), and 3cddp@CNHf-ncov>C_memb (C). The violet, red, orange, and green in the membrane indicate the PC, PE, PS, and PGR polar heads, while the magenta and silver colors represent the CHL and oleoyl (OL). For the nanostructures, the silver, red, blue, white, green, and ochre correspond to the C, O, N, H, Cl, and Pt atoms. Water molecules are omitted for clarity. Dashed lines delimit the states of the mechanism.

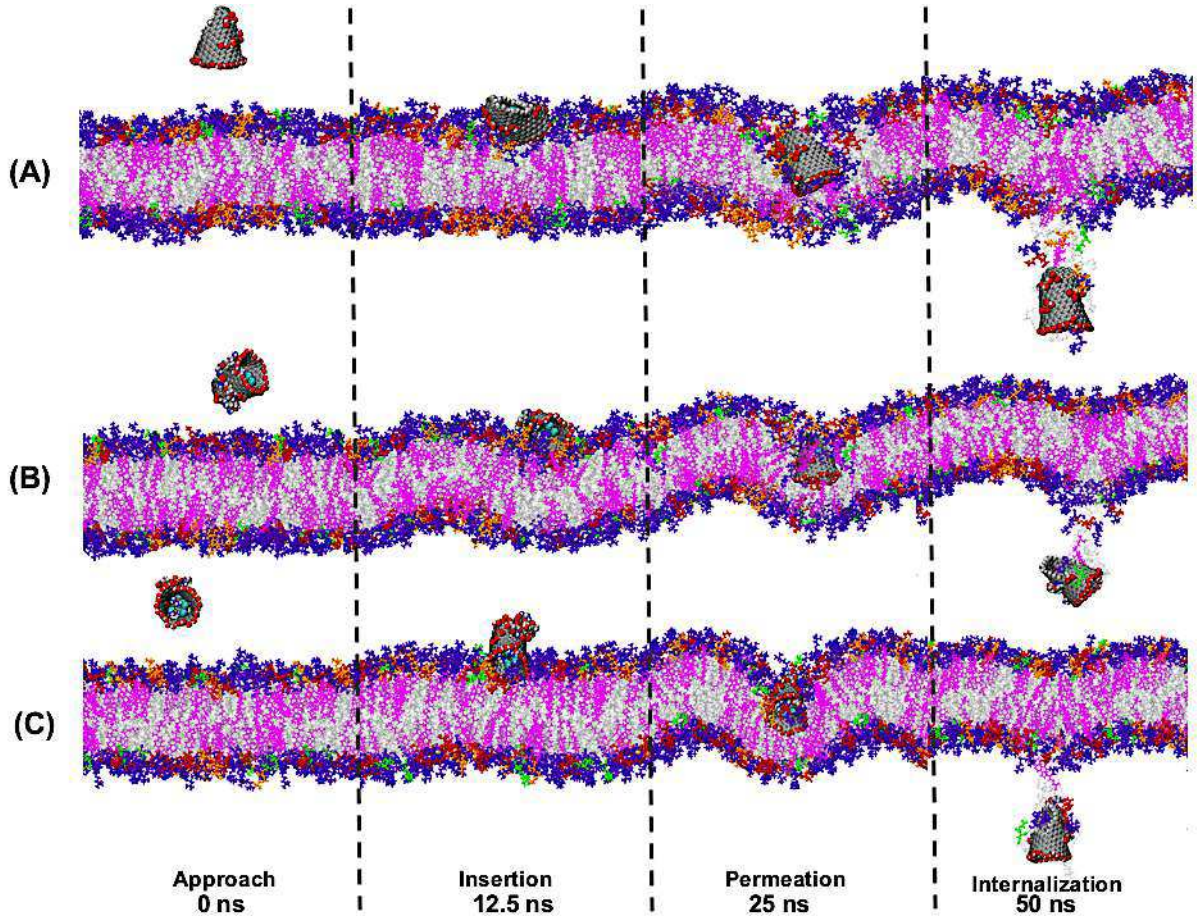

Reference: Own author (2023).

Based on the biased trajectories, we defined four main stages for the transmembrane transport of CNHs in Figure 5.4 and Figure C.5: approach, insertion, permeation, and internalization. The approach (at 0 ns) started after the equilibration step, where the center of mass of each inclusion complex was held at 14 Å from the membrane plane (see Figure 5.2).

Since there was no restriction to the rotational mobility of the complexes during the equilibration runs, the beginning of the approach stage was characterized by a reorientation of the nanocarriers, where their main axis remained parallel to the membrane plane. For the 3cddp@CNHf-cov (Figure 5.4B and Figure C.5B) and 3cddp@CNHf-ncov (Figure 5.4C and Figure C.5C) models, it is possible to verify that the functionalization groups face the biomembrane, indicating their relevance to the nanoadherence in cancer cells.

The second stage was the insertion at 12.5 ns, when the inclusion complexes interacted with the polar heads region of the lipid bilayer by mainly using the open end of the CNHs. This configuration can be explained by the favorable interactions between two hydrophilic regions: lipidic polar heads and –OH groups located at the open ends of the CNHs. These preferential interactions resulted, on average, in an inclination of the main axis of the nanostructures towards the membrane normal axis. The same inclination in order to favor the interactions between hydroxyls groups and polar heads was reported by Mejri and coworkers (MEJRI, *et al*., 2021), who studied the interactions of CNTox loaded with cddp and a membrane of POPC lipids. We did not observe significant differences among the insertion of oxidized and functionalized topologies of CNHs through the membrane. However, it was possible to notice less favorable interactions between the HA-NH_2 chain of the CNHf-ncov and the polar heads due to the greater distance of this group from the membrane during this stage.

The permeation of the inclusion complexes through the membrane was the next stage at 25 ns. In Figure 5.4, we can see that all nanocarriers penetrate the C_memb in an orientation approximately perpendicular to the surface of this biomembrane. This phase was characterized by a high deformation of the lipid bilayer regardless of the chemical modification of the CNHs. This membrane curvature is related to not only the steric hindrance, but also with the electrostatic repulsion among different groups in the CNHs models and the hydrophobic core of the membrane. Raczynski and coworkers (RACZYNSKI, *et al*., 2018) also reported a structural deformation of DMPC membranes due to the permeation of pristine CNT models. The CNHf-cov presented the fastest permeation (39.7 ns), while this stage for the CNHox and CNHf-ncov involved 41.0 ns and 43.0 ns, respectively.

The last step of the transmembrane transport mechanism shown in Figure 5.4 was the cellular internalization, when the inclusion complexes reached the intracellular environment with a simultaneous self-sealing of the C_memb. Additionally, the simulations showed the adsorption of lipids on the surface of the CNHs when they reached the cytoplasm, as also reported in other studies involving CNTs (RACZYNSKI, *et al*., 2014; RACZYNSKI, *et al*., 2018; AL-QATTAN, *et al*., 2018). This additional functionalization may improve the

biocompatibility of the CNHs in the intracellular microenvironment and may potentiate the cddp release. The lipid extraction from intracellular vesicles due to the permeation of CNTs and graphene was also described in a study conducted by Zhu and coworkers (ZHU, *et al*., 2016). By using all-atom and coarse grained simulations, these authors demonstrated that the lipid extraction was related to not only the uninterrupted contact time between nanovector and membrane, but also to the contact force and the size of the nanostructure. In our simulations, it is possible to verify that the functionalized CNHs have more types of adsorbed lipids than the CNHox. Specifically, we noticed the adsorption of lipids DOPC, DOPE, DOPGR, and CHL on the surface of both CNHf-cov and CNHf-ncov, whereas it was observed the adsorption of lipids DOPC and DOPS on the surface of CNHox. This diversity in terms of adsorbed lipids may be connected to the presence of different functional groups on the CNHf topologies. To conclude, the inclusion complexes were able to reach the cytoplasm of the cancer cell with the intact cddp load, which evidences the potential of CNH as a drug delivery system.

5.3.3 Membrane deformation

In order to quantify the deformation of the C_memb model resulting from the translocation processes of the inclusion complexes, we calculated structural properties of membranes that reveal the level of the lipidic distortions. In this sense, the effect of this transmembrane transport on the global structure of the C_memb was investigated by computing the electron density profile along the lipid bilayer shown in Figure 5.5. By comparing the profile of the free C_memb (orange line in Figure 5.5) with the profiles referring to the transmembrane transport of inclusion complexes (pink, green, and blue lines in Figure 5.5), it is possible to notice the deformation of the charges concentration located at the both hydrophilic heads and hydrophobic tails as a result of the translocation processes. Particularly, both widening and decreasing of the two main peaks in the profiles of the nanocarriers point out an increase on the dispersion of polar heads per unit of volume. For the lipid tails (OL chains), which normally have the smallest electron density in a membrane, we also observe a more dispersed distribution of these portions due to the penetration of the CNHs. When it comes to the comparison among the inclusion complexes, data from Figure 5.5 indicate a negligible influence of the CNH topologies on the deformation caused on the global structure of the membrane.

Figure 5.5 - Electron density profiles calculated from the MD simulations of both free membrane C_memb (last 100 ns of the 400 ns equilibration stage) and translocation processes (50 ns pulling stage) of the inclusion complexes (A). The same profiles focused on the central region of the membrane (B). The curves of the inclusion complexes take into account the two directions of the reaction coordinate (50 Å → -65 Å and -50 Å → 65 Å).

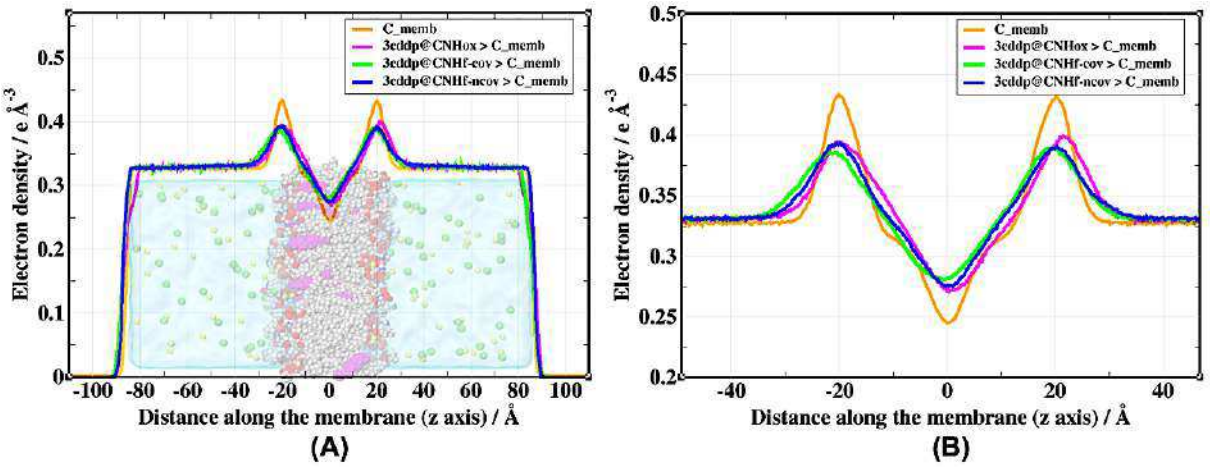

Reference: Own author (2023).

Still regarding Figure 5.5, the membrane thickness (D_{HH}) can be estimated from electron density profiles by calculating the average distance between the two main peaks (DICKSON, *et al*., 2014). These values, which may reveal the level of deformation of the membrane, are presented in Table 5.4. As expected, data from Table 5.4 indicate an average increase of 0.54 Å in the D_{HH} if we compare this property of the free membrane with the membrane during the translocation regimes. Besides, while the membrane deformation induced by the 3cddp@CNHox and 3cddp@CNHf-cov was similar, the deformation caused by the 3cddp@CNHf-ncov was the least significant, with a difference of 0.20 Å relative to the D_{HH} of the free C_memb. This result suggests that the noncovalent functionalization of CNHs may provide a less disruptive transmembrane transport. Despite these differences, the D_{HH} data are in good agreement with the experimental values (average difference of 0.98±0.29 Å), which reinforces the nondisruptive nature of the translocation processes of CNHs and the accuracy of our membrane model.

The distortion effect on the lipid tails (oleoyl, 18:1 Δ^9) of the C_memb was also evaluated by computing the S_{CD}. The reference of the 17 C atoms located at each lipid tail (OL chain) is schematized in Figure C.6, whereas the S_{CD} as function of these C atoms averaged across the SMD trajectories is graphically presented in Figure 5.6.

Table 5.4 - Structural parameters of the C_memb calculated from the SMD simulations referring to the transmembrane transport of the inclusion complexes studied herein.

Systems	$<D_{HH}>$ / Å [a]	$<S_{CD}^{C9}>$ [b]	$<S_{CD}^{C17}>$ [c]
C_memb [d]	40.44[e] (40.0)[f]	0.036±0.025 (0.045)[g]	0.021±0.025 (0.000)[g]
3cddp@CNHox > C_memb	41.15±0.50	0.028±0.030	0.017±0.026
3cddp@CNHf-cov > C_memb	41.14±0.06	0.033±0.026	0.019±0.026
3cddp@CNHf-ncov > C_memb	40.64±0.20	0.033±0.027	0.018±0.026

[a]Average thickness of the membrane calculated as the peak-to-peak distance in the electron density. [b]Average deuterium order parameter of the carbon atom C9 that is located at the double bond of the oleoyl chains. [c]Average deuterium order parameter of the carbon atom (C17) located at the end of the oleoyl chains. [d]Free membrane (ALMEIDA, *et al*., 2021) considering the last 100 ns of the 400 ns trajectory. [e]The standard deviation value was not presented since we have one trajectory. [f]Experimental values referring to a membrane composed by DOPC and 20% of CHL (MADEJ, *et al*., 2015). [g]Experimental values: DOPC membrane with 0.3 M CHL (MADEJ, *et al*., 2015). The averages consider the two directions of the reaction coordinate (50 Å → -65 Å and -50 Å → 65 Å).

Reference: Own author (2023).

The comparison between the S_{CD} values of the free C_memb (orange line in Figure 5.6) and the ones referring to the same membrane during the transmembrane transport of the inclusion complexes (pink, green and blue lines in Figure 5.6) demonstrates a decrease on this structural property during the SMD simulations. This behavior reveals a reduction of the average ordering of the lipid tails due to the translocation of the nanocarriers. In Table 5.4, by analyzing the S_{CD} of both C atom located at the unsaturation of OL chains (C9 in Figure C.6) and C atom located at the end of these lipid tails (C17 in Figure C.6), it is possible to notice an average reduction of 0.005 units in the S_{CD}^{C9} and 0.003 units in the S_{CD}^{C17} relative to the ones in the C_memb. An average reduction of 0.014±0.003 in the S_{CD}^{C17} was also observed when we compared the simulated values with the experimental one. The lowest values of both S_{CD}^{C17} and S_{CD}^{C9} for the 3cddp@CNHox>C_memb point out that the translocation of the CNHox provided a substantial disorder on the ends of the lipid chains, as well as on the most rigid part of the oleoyl molecules. In spite of the local disorder provided by the CNHox, the lowest S_{CD} values verified for the system 3cddp@CNHf-ncov>C_memb (blue line in Figure 5.6) indicate that the noncovalent functionalization of CNHs induced the highest deformation in the hydrophobic portion of the biomembrane during the translocation of this nanovector. This result may be attributed to the repulsive interactions between the HA-NH_2 chain adsorbed on the surface of the CNHf-ncov and the lipid tails (OL) of the C_memb that, in turn, distorted the lipid density around this specific nanostructure.

Figure 5.6 - Deuterium order parameters (S_{CD}) of the lipid tails (oleoyl, OL) referring to the cancer cell membrane (C_memb) calculated from the simulations of both free C_memb (last 100 ns of the 400 ns equilibration stage) and transmembrane transport (50 ns SMD runs) of the inclusion complexes. The bars indicate the standard deviation values.

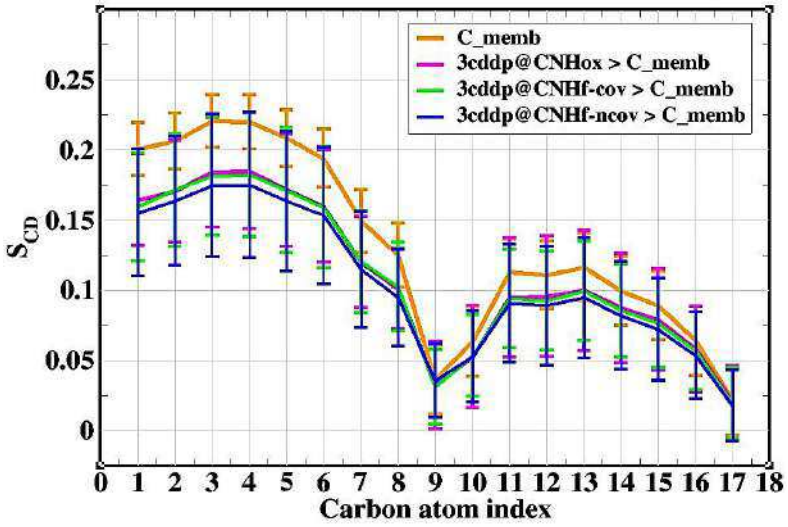

Reference: Own author (2023).

5.3.4 Interactions CNH--membrane

In order to elucidate the preferential interactions between lipids of the C_memb and our inclusion complexes during their transmembrane transport, we analyzed the number of contacts CNH---C_memb in a 3.0 Å radius per frame established during the SMD simulations. While the temporal variation of this parameter is presented in Figure 5.7, the average values are schematized in Figure 5.8. The plots in Figure 5.7 evidence that the highest numbers of CNH--lipids contacts per frame involved the PC and OL species of the C_memb. This result is expected due to the fact that the DOPC lipid is the main component of the membrane model as shown in Table 5.1.

Additionally, data from Figure 5.8 reveal that the number of contacts CNH--PC per frame of the CNHf-ncov was 17% and 23% greater than the ones involving the CNHf-cov and CNHox, respectively. Overall, the higher numbers of interactions between the CNHf (CNHf-cov and CNHf-ncov) and the PC species, emphasize the potentially of functionalization strategies for optimizing the interactions of these nanovectors and membranes of cancer cells.

Figure 5.7 - Evolution of the number of contacts per frame in a 3.0 Å radius between lipids (DOPC, DOPE, DOPS, DOPGR, and CHL) of the C_memb and CNH models referring to the inclusion complexes studied in this work during their translocation through this lipid bilayer. The symbols PC (A), PE (B), PS (C), PGR (D), CHL (E), and OL (F) stand for phosphocholine, phosphoethanolamine, phospho-L-serine, phospho-rac-(1-glycerol), cholesterol, and oleoyl, respectively. The dashed lines in gray refer to stages of insertion, permeation, and internalization of the transmembrane transport mechanism.

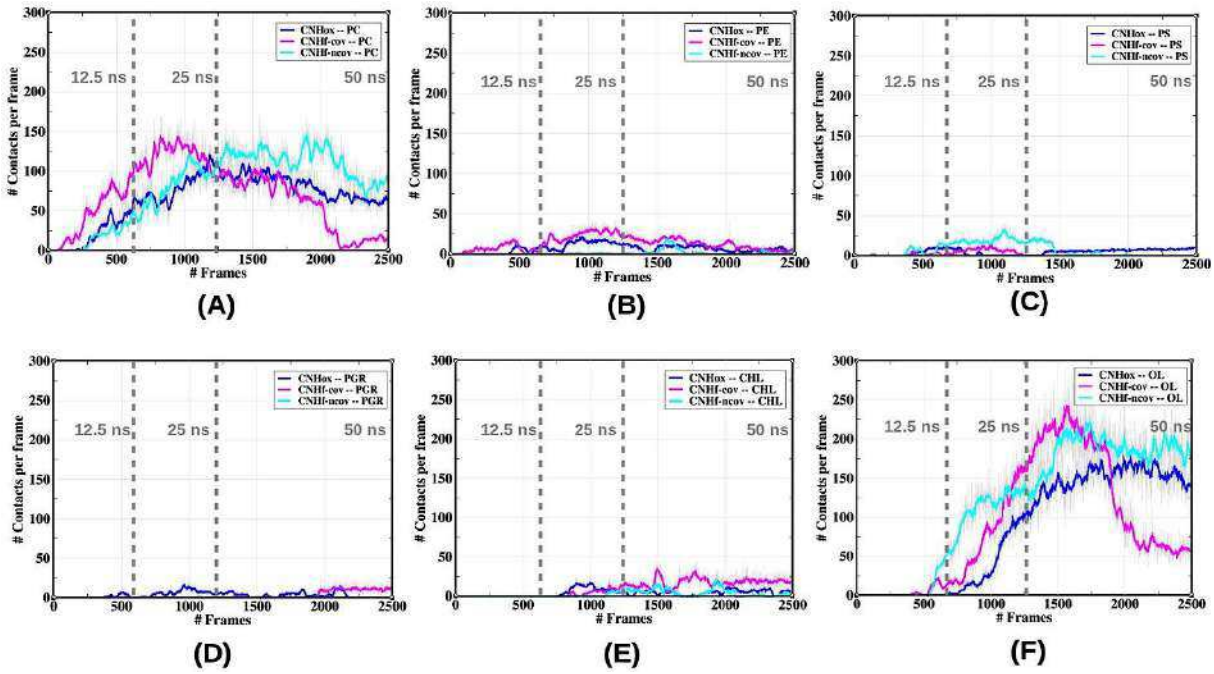

Reference: Own author (2023).

While in Figure 6.7A-D we can notice an increase of the molecular contacts during the first 25 ns, in Figure 6.7E-F we verify a significant increment of these interactions during the last 25 ns. If we consult the transmembrane transport mechanism shown in Figure 6.4, we verify that the increase in the number of contacts per frame between 0 and 25 ns (Figure 6.7A-D) reflects the approach, insertion, and initial permeation stages, where the CNHs are gradually immersed in the polar heads and lipid tails regions. Moreover, the increase of contacts/frame after 25 ns evidenced in Figure 6.7E-F suggests a high adherence of the OL and CHL molecules on the surface of the CNHs during the permeation and internalization stages (see Figure 6.4).

Figure 5.8 - Average number of molecular contacts in a 3.0 Å radius between lipids (DOPC, DOPE, DOPS, DOPGR, and CHL) of the membrane C_memb and CNH models referring to the inclusion complexes studied in this work during their translocation through the membrane (SMD runs). The average values shown above the bars take into account the SMD runs in the two directions of the reaction coordinate (50 Å → -65 Å and -50 Å → 65 Å). The bars refer to the average fluctuations of the interactions. The symbols PC, PE, PS, PGR, CHL, and OL stand for phosphocholine, phosphoethanolamine, phospho-L-serine, phospho-rac-(1-glycerol), cholesterol, and oleoyl, respectively.

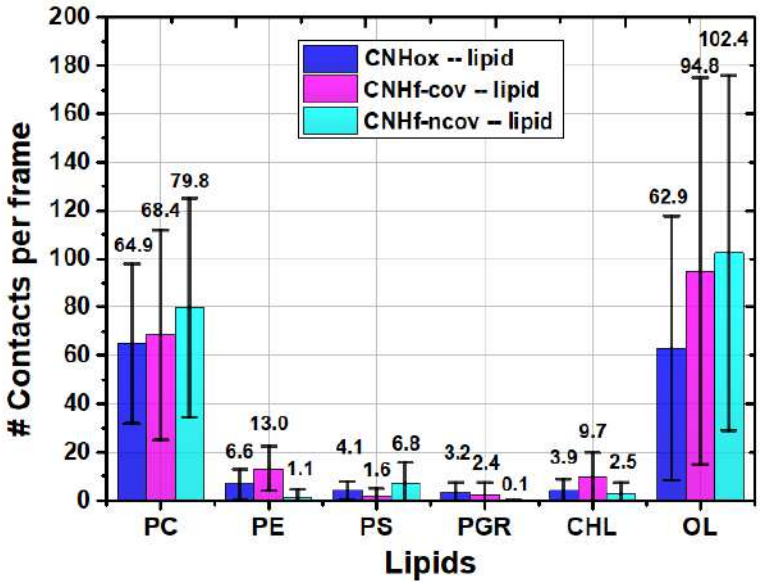

Reference: Own author (2023).

Concerning the interactions CNH--CHL, Figure 5.7E and Figure 5.8 show that the CNHf-cov formed four times more contacts with CHL than the CNHf-ncov and three times more contacts with the same lipid than the CNHox. Since breast cancer cells exhibit a notable concentration of CHL (KIM, *et al*., 2022), these results suggest that covalent functionalization in the 3cddp@CNHf-cov may favor the interactions of this specific nanocarrier with breast tumor tissues. On the other hand, both Figure 5.7C and Figure 5.8 indicate that the CNHf-ncov established the highest number of contacts per frame (6.8) with PS. Specifically, the average difference relative to the CNHox and CNHf-ncov models was about 4 contacts/frame. These favorable interactions CNHf-ncov--PS reinforce the potential of this functionalization, since the PS expression in the outer leaflet of membranes is another biomarker of cancer cells (BERNARDES & FIALHO, 2018). At last, the decrease on the number of contacts CNHf-cov--OL (Figure 5.7E) during the last 1,500 frames (last 31 ns) indicates that this nanovector loaded with cddp reaches the intracellular environment of the C_memb without a high density of OL

chains adsorbed on its surface. For instance, while the complex with the CNHf-cov reaches the cytoplasm with 71 contacts with PC and OL, the systems with CNHox and CNHf-ncov reach this region with 206 and 269 contacts with the same species. In addition to suggesting more efficient reorganization of the C_memb after the cellular internalization, the smaller number of contacts of the CNHf-cov at the intracellular region may favor the cddp release due to a less steric hindrance compared to the other CNHs. Conversely, the high number of contacts/frame (mainly with PC and OL) for both CNHox and CNHf-ncov at 50 ns may hinder drug release.

5.3.5 CNHs deformation

The deformation of the CNH prototypes was analyzed by computing their atomic fluctuations in two cases: as free inclusion complexes with cddp in aqueous solution (3cddp@CNHox, 3cddp@CNHf-cov, and 3cddp@CNHf-ncov) and as the same inclusion complexes during their transmembrane transport through the C_memb (3cddp@CNHox>C_memb, 3cddp@CNHf-cov>C_memb, and 3cddp@CNHf-ncov>C_memb). The atomic fluctuations are presented in Figure 5.9, while the average values are organized in Table 5.5. The atomic indices of the CNHs models are presented in Figure C.7-C.9.

Based on the profiles shown in Figure 5.9, it is possible to conclude that the CNHox model has the highest structural rigidity among the CNH topologies studied herein. In fact, the RMSF values of the free inclusion complexes shown in Table 5.5 indicate that the atomic fluctuations of the CNHf-cov are, on average, three times greater than the ones of the CNHox, whereas the fluctuations of the CNHf-ncov are about two times greater than the ones of the CNHox. These differences are connected with the presence of the decoration groups (HA-NH_2 and diamino chains) on the surface of the CNHf models, which have a notable structural oscillation in aqueous solution. By using as reference Figure C7-C.9, we can confirm that the RMSF values from the atomic index 373 in Figure 5.9B-C refer to the atoms of the functionalization groups in both CNHf-cov and CNHf-ncov.

In Table 5.5, the $RMSF_{373\text{-}473}$ values suggest that the structural variability of the covalent functionalization (CNHf-cov) was about two times greater than the one of the noncovalent functionalization (CNHf-ncov). Besides, Figure C.7 reveals that the highest atomic fluctuations in the CNHox (from the index 275 in Figure 5.9) come from the atoms located at the edges of both nanowindow and open end (indicated by the $RMSF_{276\text{-}372}$).

Figure 5.9 - Atomic fluctuations (root mean square fluctuation - RMSF) of the CNHs referring to both unbiased simulations of them as inclusion complexes with cddp in aqueous solution (300 ns triplicate runs) and biased simulations of them as inclusion complexes during their transmembrane transport through C_memb (50 Å → -65 Å and -50 Å → 65 Å). 3cddp@CNHox and 3cddp@CNHox>C_memb (A), 3cddp@CNHf-cov and 3cddp@CNHf-cov>C_memb (B), and 3cddp@CNHf-ncov and 3cddp@CNHf-ncov>C_memb (C). The black, silver, and red arrows indicate the central C atoms of the nanostructure, the atoms (C, H, and O) located at both open end and nanowindow, and the atoms (C, H, N, and O) located at the functionalization groups.

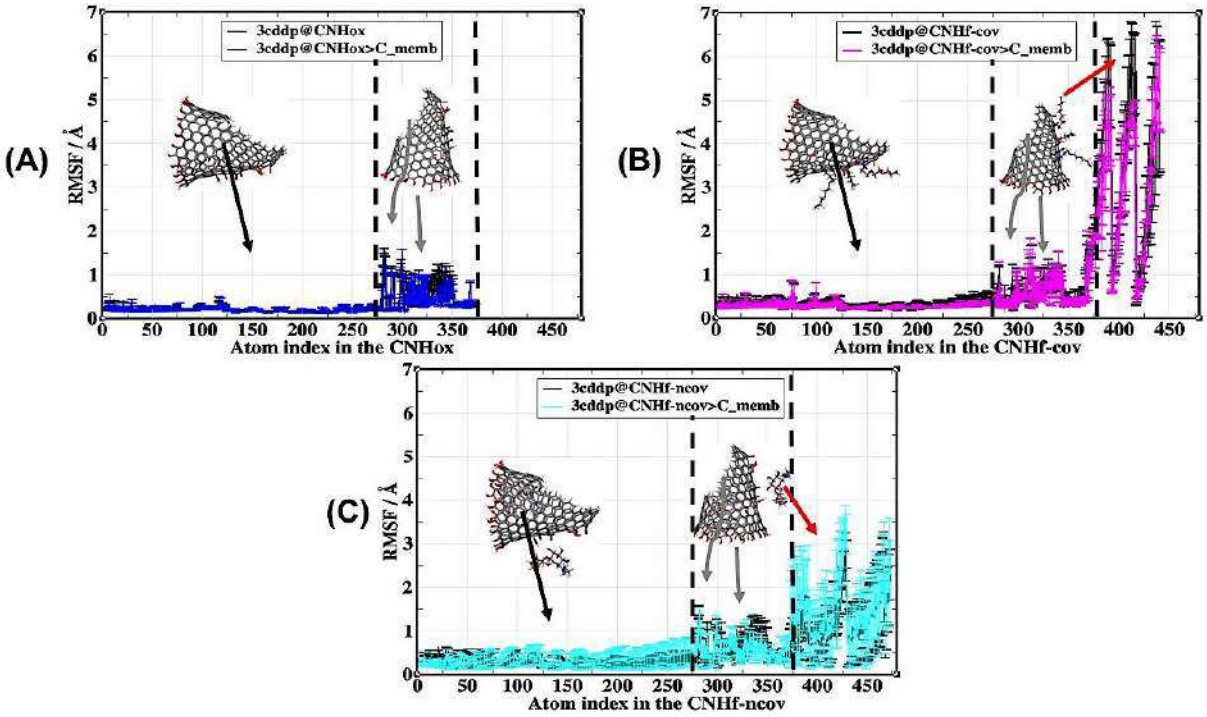

Reference: Own author (2023).

Regarding the translocation through the C_memb, Figure 5.9 shows a reduction of the structural mobility of the CNHs during these cellular uptake events. For instance, the transmembrane transport of the CNHox resulted in a decrease of 9% in the $RMSF_{276\text{-}372}$ of this topology, while the same process for the CNHf-cov resulted in a decrease of 11% in the $RMSF_{276\text{-}372}$ of this CNH model (see Table 5.5).

Table 5.5 - Root mean square fluctuations (RMSF) of the carbon nanohorn (CNH) models referring to both unbiased simulations of them as inclusion complexes with cddp in aqueous solution and biased simulations of them as the inclusion complexes during their transmembrane transport through C_memb.

Systems[a]	$RMSF_{1-275}$ / Å [b]	$RMSF_{276-372}$ / Å [c]	$RMSF_{373-473}$ / Å [d]
3cddp@CNHox	0.20±0.00	0.55±0.04	-
3cddp@CNHf-cov	0.34±0.06	1.78±0.42	3.34±0.84
3cddp@CNHf-ncov	0.30±0.08	0.92±0.31	1.22±0.53
3cddp@CNHox>C_memb	0.19±0.01	0.50±0.07	-
3cddp@CNHf-cov>C_memb	0.29±0.02	1.58±0.31	3.02±0.57
3cddp@CNHf-ncov>C_memb	0.33±0.17	1.03±0.54	1.46±0.87

[a]For the free inclusion complexes, the RMSF values were calculated from the unbiased MD simulations in triplicate, while for the transmembrane transport processes, the RMSF values were average from the SMD simulations considering the two directions of the reaction coordinate (50 Å → -65 Å and -50 Å → 65 Å). [b]Values for the central C atoms of the nanostructure. [c]Values for the atoms (C, H, and O) located at both open end and nanowindow. [d]Values for the atoms (C, H, N, and O) located at the functionalization groups. The subscripts refer to the atomic indices presented in Fig.S7-9.
Reference: Own author (2023).

This increase on the rigidity of the CNHs during the permeation processes is expected due to the steric effects experienced by these nanovectors along a reaction coordinate. Unlike the permeation of both CNHox and CNHf-cov, data from Table 5.5 point out an increase of ~11% in the atomic fluctuations of the CNHf-ncov during its transmembrane transport. This behavior is related to the dynamics of the noncovalent functionalization (see the spatial distributions in Figure C.10) during the permeation process, which presented oscillations in the range of 60% of the average $RMSF_{373-473}$ (see Table 5.5). Moreover, the highest number of contacts CNHf-ncov--OL and CNHf-ncov--PC shown in Figure 5.7-5.8 may have intensified the atomic fluctuations of the carbon-based nanocarrier.

5.3.6 Energetics of the transmembrane transport processes

In order to describe the free energy profile referring to the transmembrane transport of inclusion complexes through the C_memb, we firstly analyzed the evolution of the force applied to the nanosystems during the SMD simulations. The force profiles as a function of the reaction coordinate are graphically presented in Figure 5.10.

Figure 5.10 - Variation of the force (F) applied to the inclusion complexes (3cddp@CNHox, 3cddp@CNHf-cov, and 3cddp@CNHf-ncov) along the reaction coordinate (z axis) referring to their transmembrane transport through the breast cancer cell membrane (C_memb). The force profiles take into account SMD simulations in the two directions of the reaction coordinate: 50 Å → -65 Å (A) and -50 Å → 65 Å (B).

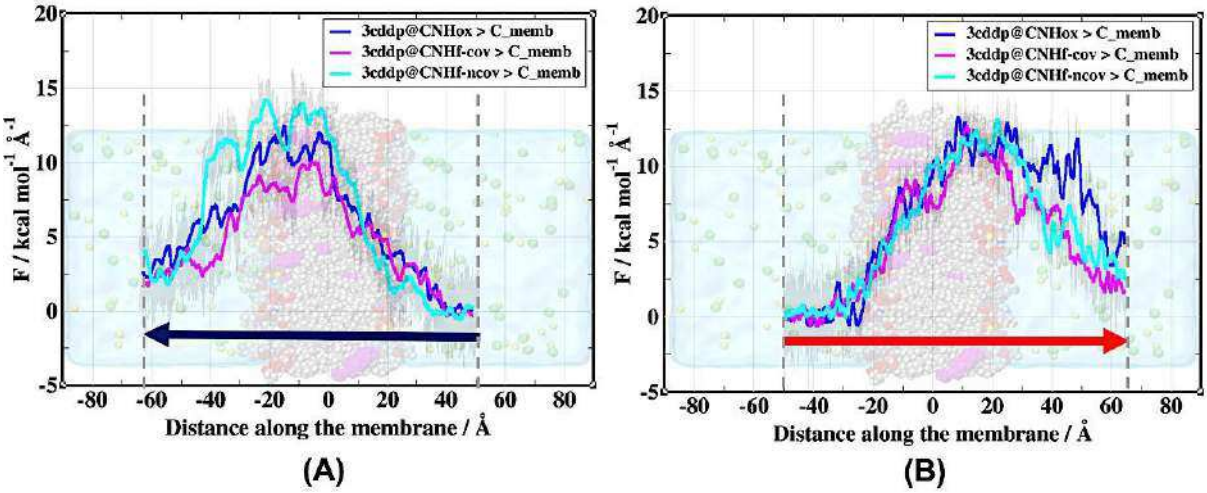

Reference: Own author (2023).

The plots in this figure show an increase of the applied force to the inclusion complexes up to the center of the biomembrane at 0 Å, and a decrease of this external force from the center of the lipid bilayer towards the bulk. This behavior is propagated in the two directions (50 Å → -65 Å in Figure 5.10A and -50 Å → 65 Å in Figure 5.10B) of the SMD runs. Moreover, the profile indicates that the first three stages of the transmembrane transport mechanism of the inclusion complexes through the C_memb (approach, insertion, and permeation in Figure 5.4 and Figure C.5) are more resistive than the last stage of this process (internalization). This high resistance experienced by these nanocarriers of cddp in the first half of the biased runs is caused by the gradual increment of the steric hindrance during the initial steps of the reaction coordinate, as the CNHs enter the C_memb. By studying both nanoidentation and extraction of CNTs through a membrane of DMPC and CHL, Raczynski and coworkers (RACZYNSKI, *et al*., 2018) also reported a profile of increasing forces until a peak located at the hydrophonic core of the lipid bilayer. When it comes to the differences between the CNH topologies, Figure 6.10 suggests that the forces required to pull the functionalized structures (CNHf-cov and CNHf-ncov) were in general greater than the ones required to the CNHox.

To differentiate the inclusion complexes in terms of experienced forces during the permeation processes, we collected the maximum force (F_{max}) applied during the SMD

simulations. The average values considering the two directions of the SMD runs are shown in Table 5.6.

Table 5.6 - Maximum force (F_{max}) and free energy barrier ($\Delta G^{\ddagger}$) calculated from the biased simulations referring to the transmembrane transport of the inclusion complexes through the breast cancer cell membrane (C_memb).

Systems	$\langle F_{max} \rangle$ [a]	$\Delta G^{\ddagger}$ [b]
	(kcal mol^{-1} Å^{-1})	(kcal mol^{-1})
3cddp@CNHox > C_memb	14.82±0.03	64.90±2.60
3cddp@CNHf-cov > C_memb	13.30±2.00	47.60±7.30
3cddp@CNHf-ncov > C_memb	15.50±1.10	53.00±1.30

[a]Maximum force applied during the SMD simulations referring to the permeation of the inclusion complexes through the membrane in the two directions of the reaction coordinate (50 Å → -65 Å and -50 Å → 65 Å). [b]Free energy barrier referring to the permeation process of the complexes through the membrane in thermodynamic equilibrium.
Reference: Own author (2023).

We can notice that the highest forces required to pull the inclusion complexes through the C_memb involve the CNHox and CNHf-ncov. The F_{max} for the translocation of the CNHf-ncov was ~17% greater than the one for the CNHf-cov, whereas this force for the CNHox was ~12% greater than the one for the CNHf-cov. This result may be a consequence of the high number of contacts CNH--OL and CNH--PC established by both CNHox and CNHf-ncov (see Figure 5.7A and Figure 5.7F), mainly after 25 ns, during the permeation and internalization stages. These numerous interactions may have induced a significant resistance to the complete extraction of both CNHox and CNHf-ncov from the C_memb towards the cytoplasm.

By using the US method, we obtained the PMFs referring to the transmembrane transport of each inclusion complex studied herein through the C_memb. Figure 5.11 displays these free energy profiles along the reaction coordinate (50 Å → -65 Å and -50 Å → 65 Å). These curves suggest that both approach and insertion stages of the transmembrane transport of inclusion complexes through the C_memb (see Figure 5.5 and Figure C.11) are spontaneous steps, since there is an average decrease in free energy during these stages of -6.4±2.6 kcal mol^{-1}, -5.8±7.3 kcal mol^{-1}, and -8.3±1.3 kcal mol^{-1} for the complexes 3cddp@CNHox, 3cddp@CNHf-cov, and 3cddp@CNHf-ncov, respectively.

Figure 5.11 - Potentials of mean force (PMFs) referring to the transmembrane transport of the inclusion complexes 3cddp@CNHox, 3cddp@CNHf-cov, and 3cddp@CNHf-ncov through the C_memb considering the two directions along the reaction coordinate of the SMD simulations (50 Å to 0 Å and -50 Å to 0 Å). The error bars refer to the 100 windows that compose each curve.

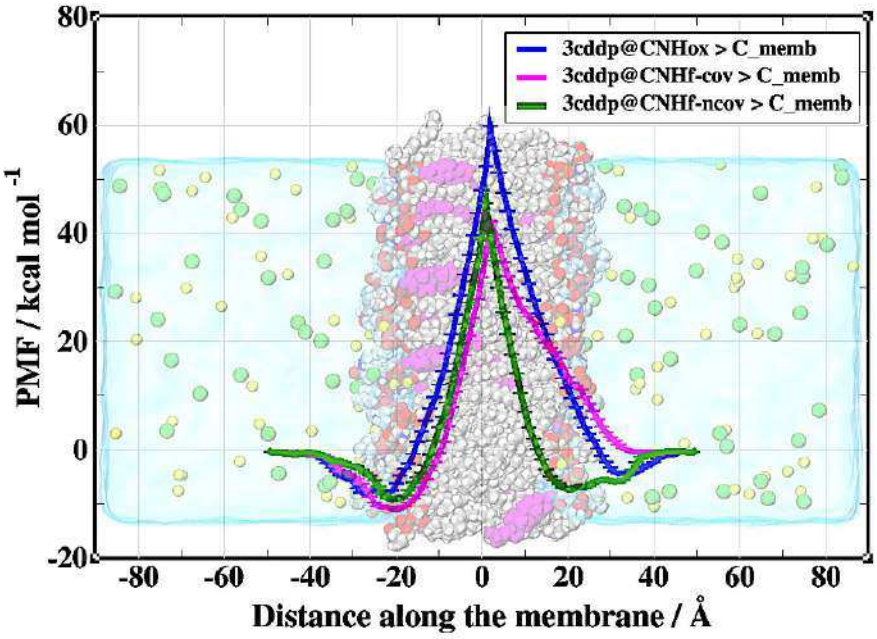

Reference: Own author (2023).

These results point out that the increasing number of contacts per frame between CNHs and polar heads illustrated in Figure 5.7, mainly composed by the interactions CNH--PC, induced a stabilization of the entire system during the approach and insertion stages. Concerning the CNH topologies, we can conclude that the CNHox and CNHf-ncov intensify their level of interaction with the biomembrane, since their potential wells are deeper by 0.6 kcal mol^{-1} and 2.5 kcal mol^{-1}, respectively, than the one referring to the transport of the CNHox. In this context, Tsukanov and Psahkie (TSUKANOV & PSAHKIE, 2016) also reported a free energy well of ~-2.4 kcal mol^{-1} in the PMF referring to the permeation of boron nitride nanotubes through a POPC membrane. After these favorable stages, the plots in Figure 5.11 show a substantial increase of the free energy as the inclusion complexes go through the lipid tails region of the C_memb. This energetic profile clearly indicates that the permeation stage of the nanocarriers (see Figure 5.4) is kinetically unfavorable. In fact, the extensive membrane restructuring, in addition to electrostatic repulsion and steric factors during this stage, may be responsible for this energy profile.

The estimated values of these $\Delta G^{\ddagger}$, which are presented in Table 5.6, evidence that the translocation events of CNHs as cddp nanocarriers through the C_memb are kinetically

unfavorable, given that they require, on average, an activation free energy of 55.1± 3.7 kcal mol^{-1}. This high energetic cost to CNHs cross biomembranes is also reported for other similar nanovectors. For instance, Pododin and Baulin (PODODIN & BAULIN, 2010) estimated energy barriers of about 100 kT (~59.30 kcal mol^{-1}) for the penetration of CNTs through DMPC membranes in the light of the single chain mean field theory. By investigating the translocation of a CNT model (length of 20 Å and diameter of 10 Å) through membranes composed by POPC and CHL molecules, Gangupomu and Capaldi (GANGUPOMU & CAPALDI, 2011) reported a barrier of 35 kcal/mol for the POPC membrane and a barrier of 50 kcal/mol for the lipid bilayer containing DOPC and 30% of CHL. According to these authors, these results agree with the estimates of energy barrier for the poration processes in membranes, which are on the order of 40-55 kcal mol^{-1}.

When it comes to the differences in terms of the CNHs prototypes, data from Table 5.6 indicate that the transmembrane transport of the 3cddp@CNHox through the C_memb required the highest free energy, 64.9±2.6 kcal mol^{-1}, among the studied inclusion complexes, with a difference of 17.3 kcal mol^{-1} and 11.9 kcal mol^{-1} relative to the 3cddp@CNHf-cov and 3cddp@CNHf-ncov, respectively. In comparison to the CNHox, this result emphasizes that the functionalization schemes of CNHs may favor the translocation of these modified nanovectors (CNHf-cov and CNHf-ncov) through biomembranes, in spite of the presence of decoration groups on the surface of the CNHf-cov and CNHf-ncov models which could induce steric effects. Despite these differences, the PMFs presented in Figure 5.11 reinforce the nonspontaneous nature of the cellular internalization of the CNH-based nanocarriers. It is worth noting that the overlap among the 115 probability distributions histograms shown in Figure C.12 corroborates the sampling efficiency over the reaction coordinate. The accuracy of the PMFs was also demonstrated by the negligible error bars shown in Figure 5.11. It is worth mentioning that the nonspontaneity of the transmembrane transport of CNHs may be circumvented with approaches based on the application of external stimuli such as ultrasound, heat, and electromagnetic fields, mainly due to the photothermal properties of this carbon nanomaterial (CURCIO, *et al*., 2021; LANCETA, *et al*., 2020; GAO, *et al.*, 2022).

5.3.7 Analysis of the cddp load

In all simulations, we did not observe the spontaneous release of cddp from the CNHs cavity regardless of their chemical modification. For instance, concerning the unbiased simulations of the free inclusion complexes in aqueous solution, the final frames (production runs) in Figure

C.13-C.15 demonstrate the encapsulation of the cddp molecules at 300 ns in all simulation replicas forming, in general, a triangular cluster inside the CNHs, as we verified in a previous work (ALMEIDA, *et al.,* 2021). The RMSD values of the cddp cluster during the production runs of the inclusion complexes (see Table C.3) evidence an increase of 56% for the encapsulated formulation inside the CNHf-cov compared to the incorporation into the CNHox, and an even more significant increase (123%) for the encapsulated formulation involving the CNHf-ncov if compared to the one with the CNHox. Unlike the higher structural stability of the cddp load transported by the CNHox, these results indicate that the functionalized nanovectors (CNHf-cov and CNHf-ncov) provided a higher mobility of the encapsulated cddp molecules, which may be relevant to reduce the energy barriers of the drug release process (ALMEIDA, *et al*., 2022).

The spatial distributions of these clusters as function of time also evidence the encapsulation of cddp into the nanocarriers during all simulations (Figure C.16-C.18). These results are in agreement with our previously reported observations (ALMEIDA, *et al*., 2022; ALMEIDA, *et al*., 2021) where we described the cddp release from a CNHox model as an endothermic process characterized by an average energy barrier of 18.2±2.4 kcal mol^{-1}. In particular, the diffuse distributions of cddp in the 3cddp@CNHf-ncov (see Figure C.16C, Figure C.17C, and Figure C.18C) indicates a wide mobility of this drug inside the cavity of the CNHf-ncov model even at the nanowindow region, where the two amino groups of the drug face the bulk region. This result may relate to the mobility of the HA-NH_2 chain that guided the cddp mapping inside the nanocarrier by means of the interactions HA-NH_2---cddp (Figure C.10). Besides, the spatial distribution of the HA-NH_2 throughout the simulations of the 3cddp@CNHf-ncov suggests the existence of high energy barriers for releasing this nonbonded group from the surface of the CNHf-ncov. We also reported a restricted mobility of the Pt(II)-based drugs adsorbed on the surface of a CNHox model (ALMEIDA, *et al*., 2022).

When it comes to the translocation of the inclusion complexes through the C_memb (Figure 5.4 and Figure C.5), the spatial distributions of these nanocontainers for cddp shown in Figure 5.12 and Figure C.19 reveal that the drugs remain encapsulated into the CNHs models during all cellular uptake processes.

Figure 5.12 - Spatial distribution of the inclusion complexes over their transmembrane transport (50 Å → -65 Å) through the breast cancer cell membrane (C_memb) as function of time during the steered molecular dynamics. The image illustrates the overlapping of only 13 frames for clarity: 3cddp@CNHox>C_memb (A), 3cddp@CNHf-cov (B), and 3cddp@CNHf-ncov (C).

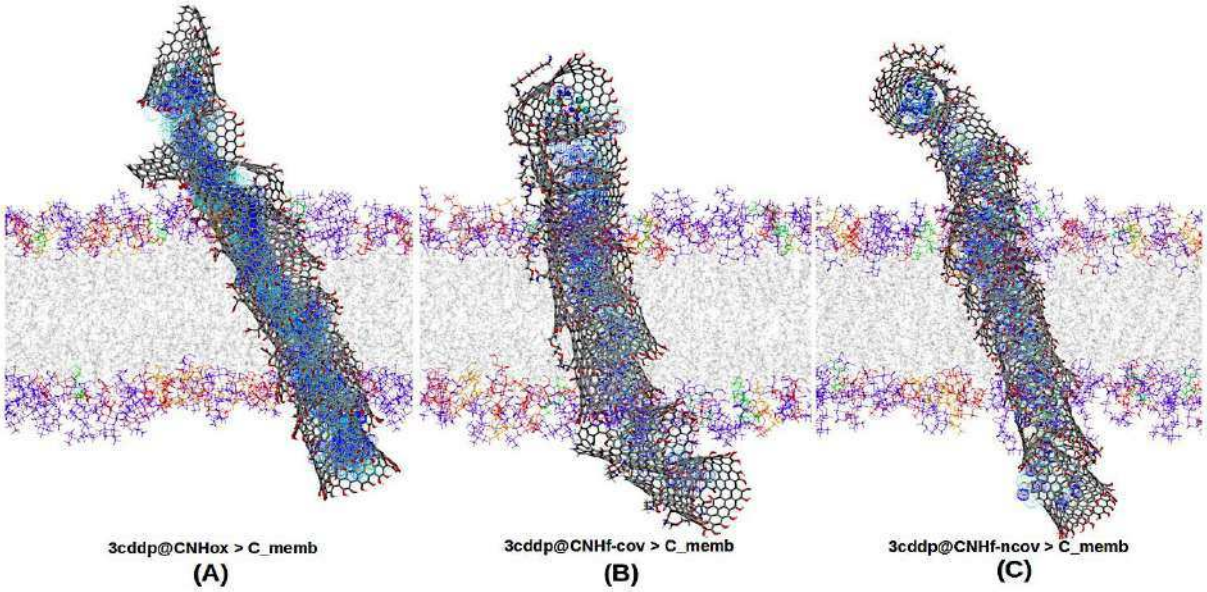

Reference: Own author (2023).

The RMSD data referring to the cddp load (see Table C.3) evidence the structural stability of this drug cluster through the translocation with a more intense mobility for the ones encapsulated in the CNHf models. Specifically, the drug mobility inside the CNHf models was about two times greater than the one inside the CNHox (Table C.3). This result suggests that the cddp release from the CNHf structures during the transmembrane transport is more susceptible than the one from the CNHox. This behavior also shows that these CNHs may protect this metallodrug in the extracellular environment and deliver its load into the cytoplasm of a breast cancer cell via an active transport (GAO, *et al*., 2022) due to the high energy barriers ($\Delta G^{\ddagger}$) shown in Table 5.6. Therefore, the most likely mechanism of cddp delivery from CNHs should involve the approach and insertion stages (see Figure 5.4 and Figure C.5), in which the insertion of these nanovectors on the C_memb is the most thermodynamically favorable process, as evidenced by the potential wells along the PMFs (Figure 5.11), especially for the 3cddp@CNHf-ncov (see Figure C.11).

After this spontaneous adsorption of the inclusion complexes on the surface of breast cancer cells, the cddp load may be slowly released in the tumor site, since there is also an energy barrier for the drug release process. Under physiological conditions (310 K, 1 bar, and 150 mM NaCl) without considering a membrane, our estimative points out that the cddp release time

from the CNHox is greater than 5.3 x 10^5 s (~6 days) (ALMEIDA, *et al*., 2022). We speculate that this kinetics of cddp release may be modified in the presence of a membrane. Ultimately, the free cddp molecules in the tumor microenvironment should finally undergo to the cellular uptake process through the membrane, which also involves an energy barrier of about 17 kcal mol^{-1} (RIVEL, *et al.*, 2019).

5.4 CONCLUSIONS

Chemically modified CNHs have been considered promising cddp delivery systems for treating cancers, including breast cancer, due to their biocompatibility and ability to both adhere and enter malignant cells. Since the cellular uptake of CNH has not been clarified at the molecular level, we used biased MD simulations to describe this process involving oxidized and functionalized CNH models carrying cddp molecules (3cddp@CNHox, 3cddp@CNHf-cov, and 3cddp@CNHf-ncov) and a breast cancer cell membrane (C_memb) prototype. The simulations unveiled the transmembrane transport mechanism of these nanocarriers which we divided in four stages: approach, insertion, permeation, and internalization. Regarding the membrane deformation, the results showed that the uptake processes were accompanied by an increase of ~0.54 Å on membrane thickness and a reduction of ~13% on the ordering of the lipid tails. This lipid disturbance was more pronounced for the 3cddp@CNHox. We also noticed the lipid adherence on carbon nanostructures, mainly on the CNHox and CNHf-ncov systems, which established three and four times more CNH--DOPC contacts/frame than the one with the CNHf-cov. The analysis of the PMFs demonstrated that permeation events of these nanovectors through a membrane are highly unfavorable with free energy barriers of ~55.2±3.7 kcal mol^{-1}. Conversely, the spontaneous adsorption of CNHs on plasma membrane of breast cancer cells, which was characterized by a potential well of about -6.8 kcal mol^{-1}, may be the most likely mechanism for delivering the cddp molecules at the tumor site. The results obtained herein demonstrate that chemical modifications on CNHs may favor not only the active transport of these nanovectors through membranes of breast cancer cells, but also their passive adsorption on these malignant cells, thereby favoring the targeted cddp delivery at these sites. In particular, the noncovalent functionalization provided the smallest membrane deformation during the active translocation, and the most favorable adsorption on the surface of the cancer cell membrane in the passive mechanism. Our study reinforces the biomedical applications of CNHs as non-disruptive nanovectors of cddp for plasma membranes, which may not only potentially accumulate on the surface of cancer cells, but also act as stimuli-responsive systems *via* active

processes. Future studies should approach the PMFs referring to the cddp release from chemically modified CNHs immersed in the tumor microenvironment.

REFERENCES

AJIMA, K.; *et al*. Material storage mechanism in porous nanocarbon. **Advanced Materials**, v. 16, p. 397-401, 2004.

AJIMA, K.; *et al*. Carbon nanohorns as anticancer drug carriers. **Molecular Pharmaceutics**, v. 2, n. 6, p. 475-480, 2005.

AJIMA, K.; *et al.* Effect of functional groups at hole edges on cisplatin release from inside single-wall carbon nanohorns. **Journal of the Physical Chemistry B**, v. 110, n. 11, p. 5773-5778, 2006.

AJIMA, K. *et al*. Enhancement of In Vivo Anticancer Effects of Cisplatin by Incorporation Inside Single-Wall Carbon Nanohorns. **ACS Nano**, v. 2, n. 10, p. 2057-2064, 2008.

ALMEIDA, E. R.; *et al*. Molecular dynamics of carbon nanohorns and their complexes with cisplatin in aqueous solution. **Journal of Molecular Graphics and Modelling**, v. 89, p. 167-177, 2019.

ALMEIDA, E. R.; *et al*. Chemically Modified Carbon Nanohorns as Nanovectors of the Cisplatin Drug: A Molecular Dynamics Study. **Journal of Chemical Information and Modeling**, v. 60, n. 2, p. 500-512, 2020.

ALMEIDA, E. R.; *et al*. Carbon nanohorn as nanocontainer for cisplatin: insights on the interaction with plasma membranes of normal and breast cancer cells. **Physical Chemistry Chemical Physics**, v. 23, n. 30, p. 16376-16389, 2021.

ALMEIDA, E. R.; *et al*. Unveiling the Releasing Processes of Pt(II)-Based Anticancer Drugs from Oxidized Carbon Nanohorn: An In Silico Study. **The Journal of Physical Chemistry B**, v. 126, n. 23, p. 4246-4260, 2022.

ALMEIDA, E. R. & DOS SANTOS, H. F. Nanoconfinement effect on the hydrolysis of cisplatin. **Chemical Physics Letters**, v. 811, n. 140247, p. 1-7, 2023.

AL-QATTAN, M. N.; DEB, P. K.; TEKADE, R. K. Molecular dynamics simulation strategies for designing carbon-nanotube-based targeted drug delivery. **Drug Discovery Today**, v. 23, n. 2, p. 235-250, 2018.

BERENDSEN, H. J. C.; *et al*. Molecular dynamics with coupling to an external bath. **The Journal Chemical Physics**, v. 81, p. 3684-3690, 1984.

BERNARDES, N. & FIALHO, A. M. Perturbing the Dynamics and Organization of Cell Membrane Components: A New Paradigm for Cancer-Targeted Therapies. **International Journal of Molecular Science**, v. 19, n. 3871, p. 1-19, 2018.

BOUBETA, F. M.; *et al*. Lessons learned about steered molecular dynamics simulations and free energy calculations. **Chemical Biology & Drug Design**, v. 93, p. 1-10, 2019.

BRENEMAN, C. M. & WIBERG, K. B. Determining atom-centered monopoles from molecular electrostatic potentials. The need for high sampling density in formamide conformational analysis. **Journal of Computational Chemistry**, v. 11, n. 3, 1990.

CASE, D. A.; *et al*. **AMBER 2019**, University of California, San Francisco, 2019.

CASE, D. A.; *et al*. **AMBER 2020**, University of California, San Francisco, 2020.

CANCÈS, E.; MENNUCCI, B.; TOMASI, J. A new integral equation formalism for the polarizable continuum model: theoretical background and applications to isotropic and anisotropic dielectrics. **The Journal of Chemical Physics**, v. 107, p. 3032-3041, 1997.

CURCIO, M.; *et al*. Carbon Nanohorns as Effective Nanotherapeutics in Cancer Therapy. **C – Journal of Carbon Research**, v. 7, n. 3, p. 1-18, 2021.

DARDEN, T.; YORK, D.; PEDERSEN, L. An N·log(N) Method for Ewald Sums in Large Systems. **The Journal of Chemical Physics**, v. 98, n. 12, p. 10089-10092, 1993.

DA SILVA, A. M..; *et al*. New insights on chemical oxidation of single-wall carbon nanotubes: a theoretical study. **The Journal of Physical Chemistry C**, v. 113, p. 10079-10084, 2009.

DEWAR, M. J. S.; *et al.* Development and use of quantum mechanical molecular models. 76. AM1: a new general purpose quantum mechanical molecular model. **Journal of the American Chemical Society**, v. 107, n. 13, p. 3902-3909, 1985.

DICKSON, C. J.; *et al.* Lipid14: The Amber Lipid Force Field. **Journal of Chemical Theory and Computation**, v. 10, n. 2, p. 865-879, 2014.

DOS SANTOS, H. F.; *et al.* Structure, Stability, and Infrared Spectrum of Capped Carbon Cones: A DFTB Study. **The Journal of Physical Chemistry C**, v. 118, n. 42, p. 24761-24768, 2014.

EFRON, B. & TIBSHIRANI, R. J. **An introduction to the Bootstrap**, Chapman and Hall/CRC, New York, 1st edn, 1994.

EJIGAH, V.; *et al*. Approaches to Improve Macromolecule and Nanoparticle Accumulation in the Tumor Microenvironment by the Enhanced Permeability and Retention Effect. **Polymers**, v. 14, p. 2601-2632, 2022.

FRISCH, M. J.; *et al*. Gaussian 09, revisão D.01.; Gaussian, Inc.: Wallingford, CT, 2009.

GANGUPOMU, V. K. & CAPALDI, F. M. Interactions of Carbon Nanotube with Lipid Bilayer Membranes. **Journal of Nanomaterials**, v. 31, p. 1-6, 2011.

GAO, C.; *et al*. Single-walled carbon nanohorns-based smart nanotheranostic: From phototherapy to enzyme-activated fluorescence imaging-guided photodynamic therapy. **Journal of Colloid and Interface Science**, v. 628, p. 273-286, 2022.

GIAQUINTO, A. N.; *et al*. Breast Cancer Statistics, 2022. **CA: A Cancer Journal for Clinicians**, v. 72, p. 524-541, 2022.

GODONE, R. L. N.; *et al*. Clinical and molecular aspects of breast cancer: Targets and therapies. **Biomedicine & Pharmacotherapy**, v. 106, p. 14-34, 2018.

GROSSFIELD, A. WHAM: Weighted Histogram Analysis Method for Analyzing Umbrella Sampling Simulation Data, version 2.0.10.1. Available online: http://membrane.urmc.rochester.edu/wordpress/?page_id=126 (accessed on February 18 2023).

HE, *et al*. Single-walled carbon-nanohorns improve biocompatibility over nanotubes by triggering less protein-initiated pyroptosis and apoptosis in macrophages. **Nature Communications**, v. 9, 2393-2414, 2018.

HEHRE, W. L. ; DITCHFIELD, R. ; POPLE, J. A. Self-Consistent Molecular Orbital Methods. XII. Further Extensions of Gaussian-Type Basis Sets for Use in Molecular Orbital Studies of Organic Molecules. **Journal of Chemical Physics**, v. 56, n. 5, p. 2257-2261, 1972.

HESTENES, M. R. & STIEFEL, E. Methods of Conjugate Gradients for Solving Linear Systems. **Journal of Research of the National Bureau of Standards**, v. 49, p. 409-436, 1952.

HIFNI, B.; *et al*. Investigation of the Cellular Destination of Fluorescently Labeled Carbon Nanohorns in Cultured Cells. **ACS Applied Bio Materials**, v. 3, p. 6790-6801, 2020.

IIJIMA, S.; *et al*. Nano-Aggregates of Single-Walled Graphitic Carbon Nanohorns. **Chemical Physics Letters**, v. 309, p. 165-170, 1999.

JENSEN, F. **Introduction to Computational Chemistry**, John Wiley & Sons, 2nd edition, Chichester, UK, 2007

JO, S.; *et al*. CHARMM-GUI: A Web-based Graphical User Interface for CHARMM. **Journal of Computational Chemistry**, v. 29, p. 1859-1865, 2008.

JORGENSEN, W. L.; *et al*. Comparison of Simple Potential Functions for Simulating Liquid Water. **The Journal of Chemical Physics**, v. 79, p. 926-935, 1983.

KAROUSIS, N.; *et al*. Structure, properties, functionalization, and applications of carbon nanohorns. **Chemical Reviews**, v. 116, n. 8, p. 4850-4883, 2016.

KARTEL, N. T.; *et al*. Study of cytotoxicity performance of carbon nanohorns by method of spin probes. **Fullerenes, Nanotubes and Carbon Nanostructures**, v. 28, p. 737-744, 2020.

KÄSTNER, J. Umbrella Sampling. **WIREs Computational Molecular Science**, v. 1, p.932-942, 2011.

KHATTI, Z. & HASHEMIANZADEH, S. M. Investigation of thermodynamic and structural properties of drug delivery system based on carbon nanotubes as a carboplatin drug carrier by molecular dynamics simulations. **Journal of Inclusion Phenomena Macrocyclic Chemistry**, v. 83, n. 1-2, p. 131-140, 2015.

KHATTI, Z. & HASHEMIANZADEH, S. M. Boron nitride nanotube as a delivery system for platinum drugs: Drug encapsulation and diffusion coefficient prediction. **European Journal of Pharmaceutical Sciences**, v. 88, p. 291-297, 2016.

KHATTI, Z.; HASHEMIANZADEH, S. M.; SHAFIEI, S. A. A molecular study on drug delivery system based on carbon nanotube for encapsulation of platinum-based anticancer drug. **Advanced Pharmaceutical Bulletin**, v. 8, n. 1, p. 163-167, 2018.

KIM, H. Y.; *et al*. Cholesterol Synthesis Is Important for Breast Cancer Cell Tumor Sphere Formation and Invasion. **Biomedicines**, v. 10, n. 8, p. 1908-1921, 2022.

KUMAR, S.; *et al.* The weighted histogram analysis method for free-energy calculations on biomolecules. I. The method. **Journal of Computational Chemistry**, v. 13, n. 8, p. 1011-1021, 1992.

KUMAR, S.; *et al.* Multidimensional free-energy calculations using the weighted histogram analysis method. **Journal of Computational Chemistry**, v. 16, n. 11, p. 1339-1350, 1995.

LANCETA, A. M.; BOSCH, M. M.; LESMES, P. M. Single-Walled Carbon Nanohorns as Promising Nanotube-Derived Delivery Systems to Treat Cancer. **Pharmaceutics**, v. 12, n. 850, p. 1-21, 2020.

LEE, J.; *et al*. CHARMM-GUI supports the Amber force fields. **The Journal of Chemical Physics**, v. 153, n.3, p.1-9, 2020.

LI, P.; *et al*. Systematic Parameterization of Monovalent Ions Employing the Nonbonded Model. **Journal of Chemical Theory and Computation**, v. 11, n. 4, p. 1645-1657, 2015.

ŁUKASIEWICZ, S.; *et al*. Breast Cancer-Epidemiology, Risk Factors, Classification, Prognostic Markers, and Current Treatment Strategies-An Updated Review. **Cancers**, v. 13, p. 4287-4317.

LOPES, J. F.; *et al.* Theoretical study of the potential energy surface for the interaction of cisplatin and their aquated species with water. **Journal of Chemical Physical**, v. 128, n. 16, p. 16510-165117, 2008.

MADEJ, B. D.; et al. A Parameterization of Cholesterol for Mixed Lipid Bilayer Simulation within the Amber Lipid14 Force Field. **Journal of Physical Chemistry B**, v. 119, p. 12424-12435.

MEJRI, A.; *et al*. Confinement of the antitumoral drug cisplatin inside edge-functionalized carbon nanotubes and its release near lipid membrane. **The European Physical Journal D**, v. 75, n. 99, p. 1-10, 2021.

MILLER III, B. R.; *et al*. MMPBSA.py: An Efficient Program for End-State Free Energy Calculations. **Journal of Chemical Theory and Computation**, v. 8, n. 9, p. 3314-3321, 2012.

MØLLER, C. & PLESSET, M. S. Note on an Approximation Treatment for Many-Electron Systems. **Physical Review**, v. 46, p. 618-622, 1934.

MURATA, K.; *et al*. Nanowindow-Induced Molecular Sieving Effect in a Single-Wall Carbon Nanohorn. **The Journal of Physical Chemistry B**, v. 106, n. 49, p. 12668-12669, 2002.

PODODIN, S. & BAULIN, V. A. Can a Carbon Nanotube Pierce through a Phospholipid Bilayer? **ACS Nano**, v. 4, n. 9, p. 5293-5300, 2010.

RACZYNSKI, P.; *et al*. Nanoindentation of biomembrane by carbon nanotubes – MD simulation. **Computational Materials Science**, v. 70, p. 13-18, 2013.

RACZYNSKI, P.; *et al*. Delivery of nitric oxide to the interior of mammalian cell by carbon nanotube: MD simulation. **Archives of Biochemistry and Biophysics**, v. 554, p. 6-10, 2014.

RACZYNSKI, P.; *et al*. On the impact of nanotube diameter on biomembrane indentation – computer simulations study. **Biochimica et Biophysica Acta (BBA) – Biomembranes**, v. 1860, n. 2, p. 310-318, 2018.

RIVEL, T. RAMSEYER, C.; YESYLEVSKYY, S. The asymmetry of plasma membranes and their cholesterol content influence the uptake of cisplatin. **Scientific Reports**, v. 9, n. 1, p. 1-14, 2019.

ROE, D. R. & CHEATHAM. III. PTRAJ and CPPTRAJ: Software for Processing and Analysis of Molecular Dynamics Trajectory Data. **Journal of Chemical Theory and Computation**, v. 9, p. 3084-3095, 2013.

ROUX. B. The calculation of the potential of mean force using computer simulations. **Computer Physics Communications**, v. 91, n. 1-3, p. 275-282, 1995.

SALOMON-FERRER, *et al*. Routine Microsecond Molecular Dynamics Simulations with AMBER on GPUs. 2. Explicit Solvent Particle Mesh Ewald. **Journal of Chemical Theory Computational**, v. 9, p. 3878-3888, 2013.

SHARMA, B & KANWAR, S. S. Phosphatidylserine: A cancer cell targeting biomarker. **Seminars in Cancer Biology**, n. 52, p. 17-25, 2018.

SHI, Y.; *et al*. The interactions of single-wall carbon nanohorns with polar epithelium. **International Journal of Nanomedicine**, v. 12, 4177-4194, 2017.

SHINDE, V. R.; *et al*. Enhanced permeability and retention effect: A key facilitator for solid tumor targeting by nanoparticles. **Photodiagnosis Photodynamic Therapy**, v. 39, p. 102915-102927, 2022.

SOULE, H. D.; *et al*. A human cell line from a pleural effusion derived from a breast carcinoma. **Journal of National Cancer Institute**, v. 51, p. 1409-1416, 1973.

TABARI, S. H.; JAMALI, Y.; POURSALEHI, R. Multi-Scale Simulation of Carbon Nanotubes Interactions with Cell Membrane: DFT Calculations and Molecular Dynamic Simulation. **Procedia Materials Science**, v. 11, p. 423-427, 2015.

TODOR, I. N.; LUKYANOVA, N. Y.; CHEKHUN, V. F. The lipid content of cisplatin- and doxorubicin resistant mcf-7 human breast cancer cells. **Experimental Oncology**, v. 34, n. 2, p. 97-100, 2012.

TSUKANOV, A. A. & PSAKHIE, S. G. Potential of mean force analysis of short boron nitride and carbon nanotubes insertion into cell membranes. **Advanced Biomaterials and Devices in Medicine**, v. 3, p. 1-9, 2016.

UBERUAGA, B. P.; ANGHEL, M.; VOTER, A. F. Synchronization of trajectories in canonical molecular-dynamics simulations: Observation, explanation, and exploitation. **The Journal of Chemical Physics**, v. 120, p. 6363-6374, 2004.

VÖGELE, M; KÖFINGER, J.; HUMMER, G. Molecular dynamics simulations of carbon nanotube porins in lipid bilayers. **Faraday discussions**, v. 209, p. 341-359, 2018.

WANG, J.; *et al*. Development and testing of a general amber force field. **Journal of Computational Chemistr**y, v. 25, n. 9, p. 1157-1174, 2004.

WANG, H.; *et al*. Cisplatin prevents breast cancer metastasis through blocking early EMT and retards cancer growth together with paclitaxel. **Theranostics**, v. 11, n. 5, p. 2442-2459, 2021.

ZHANG, M.; *et al*. Biodegradation of carbon nanohorns in macrophage cells. **Nanoscale**, v. 7, p. 2834-2840, 2015.

ZHANG, C.; *et al.* Platinum-based drugs for cancer therapy and anti-tumor strategies. **Theranostics**, v. 12, n. 5, p. 2115-2132, 2022.

ZHENG, S.; *et al*. VFFDT: a new software for preparing AMBER force field parameters for metal-containing molecular systems. **Journal of Chemical Information and Modeling**, v. 56, p. 811-818, 2016.

ZHU, W.; *et al*. Nanomechanical mechanism for lipid bilayer damage induced by carbon nanotubes confined in intracellular vesicles. **Proceedings of the National Academy of Sciences of the United States of America**, v. 113, p. 12374-12379, 2016.

ZIEBA, W.; *et al*. Nitric-Acid Oxidized Single-Walled Carbon Nanohorns as a Potential Material for Bio-Applications—Toxicity and Hemocompatibility Studies. **Materials**, v. 14, n. 6, p. 1419-1433.

6 CHAPTER 6

Translocation processes of Pt(II)-based drugs through human breast cancer cell membrane: in silico experiments

6.1 INTRODUCTION

Breast cancer is the most diagnosed cancer worldwide and one of the leading causes of female mortality, especially for black women living in low and middle-income countries (LUKASIEWICZ, *et al*., 2021; ARNOLD, *et al*., 2022). Among the different types of this malignant neoplastic disease, the invasive ductal carcinoma and the invasive lobular carcinoma account for 90-95% of all cases (FENG, *et al*., 2018). From the early diagnoses, about 30% will evolve to the metastatic modality (FENG, *et al*., 2018), which reinforces a deeper understanding of the existing treatments.

The chemotherapy based on the drugs cisplatin (cis-diaminedichloroplatinum(II) - cddp), carboplatin (*cis*-diammine(1,1-cyclobutane dicarboxylato)platinum(II) - cpx), and oxaliplatin (*cis*-oxalato-trans-l-1,2-diaminocyclohexaneplatinum(II) - oxa), remains as one of the conventional neoadjuvant strategies to treat breast cancer (GARUTTI, *et al*., 2019; KERR, *et al*., 2022). The mechanism of action of these compounds involves their interaction with the DNA of the cancer cell establishing the inter and intra-stranded crosslinks that, in turn, damage the DNA structure (KHOURY, *et al*., 2020). Ultimately, this conformational distortion activates the mechanisms of apoptosis (in case of cisplatin and carboplatin) and immunogenic cell death (in case of oxaliplatin) (ANTHONY, *et al.*, 2020). However, the cisplatin-based medication is restricted in long-term treatments due to its low selectivity for cancerous cells, thereby inducing a number of severe side effects (SCHOCH, *et al*., 2020; ZHANG, *et al*., 2022). Conversely, the administration of carboplatin results in a reduced toxicity compared to cisplatin, which is connected to the stabilizing effect of the cyclobutanedicarboxylate ligand (ZHANG, *et al*., 2022). Lastly, the application of oxaliplatin is an important alternative due to the negligible tumor resistance and efficacy in the treatment of cancers that do not present a substantial antitumor activity using either cddp or cpx (ZHOU, *et al*., 2020). Despite the series of side effects, the platinum drugs are administered in ~50% of the current schemes of chemotherapy (ANTHONY, *et al.*, 2020).

The cddp drug is also classified as a prodrug, since the active forms that will indeed bind to the DNA are its hydrolyzed species. According to the literature, the cddp undergoes to

the first hydrolysis upon entering a cell as a result of the low Cl^- concentration in the cytoplasm (~4-20 mM) compared to the extracellular medium (~100 mM) forming the monoaqua derivative *cis*-$[Pt(NH_3)_2(H_2O)Cl]^{+1}$ (cdcla, see Figure 6.1) (ZHANG, *et al.*, 2022; AHMAD, 2017; OBRESHKOVA, *et al.*, 2022).

Figure 6.1 - Hydrolysis reactions of cisplatin (*cis*-$[Pt(NH_3)_2Cl_2]$) forming the monoaqua derivative, *cis*-$[Pt(NH_3)_2(H_2O)Cl]^+$, and the diaqua derivative, *cis*-$[Pt(NH_3)_2(H_2O)_2]^{2+}$. Under alkaline media, the deprotonation of the aquated species forms the hydroxo derivatives: cis-$[Pt(NH_3)_2Cl(OH)]$, *cis*-$[Pt(NH_3)_2(H_2O)(OH)]^+$, and *cis*-$[Pt(NH_3)_2(OH)_2]$.

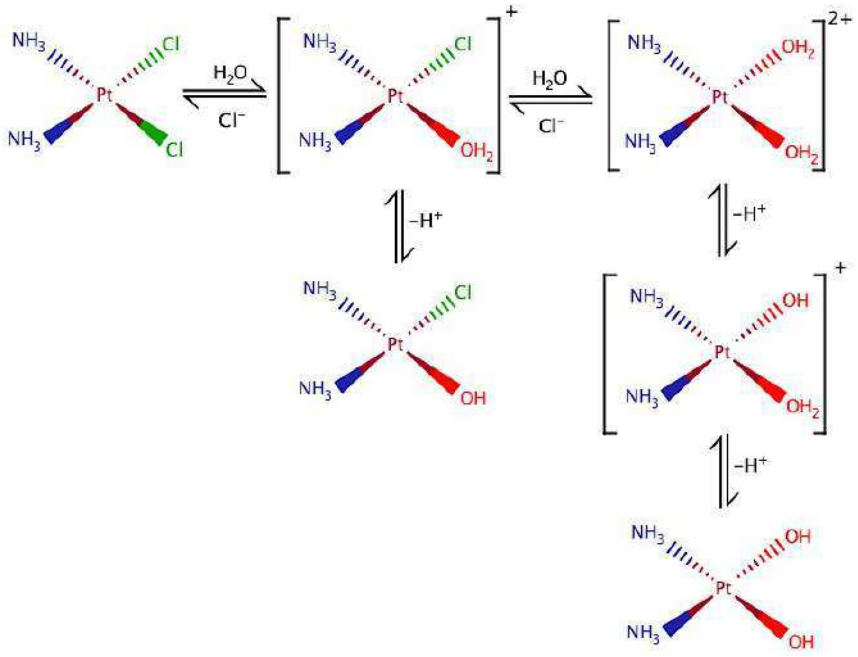

Reference: Own author (2023).

The diaqua metabolite *cis*-$[Pt(NH_3)_2(H_2O)_2]^{+2}$ (see Figure 6.1) is also generated to a notably lesser extent in the intracellular medium (AHMAD, 2017). When it comes to cancer cells, including breast cancer cells, the aqua derivatives are deprotonated in the cytosol due to the high intracellular pH (pHi > 7.4), forming the mono and di-hidroxo complexes (*cis*-$[Pt(NH_3)_2Cl(OH)]$ (cdclo) and *cis*-$[Pt(NH_3)_2(OH)_2]$) as shown in Figure 6.1 (AHMAD, 2017; LEE & SHANTI, 2021).

Unlike cddp that has good leaving groups, the presence of the carboxylate and oxalate groups in cpx and oxa makes the hydrolysis of these drugs quite slow and unfavorable. This nonspontaneity is related to not only the stabilizing effect conferred by the chelates ligands, but also to the high energy barriers referring to the ring opening (30.1 kcal mol^{-1} to cpx

(PAVELKA, *et al.*, 2007) and 28 kcal mol^{-1} to oxa (LUCAS, *et al.*, 2009)). Although the barriers for the aquation reactions are slightly reduced under acid conditions, the alkaline character expressed by the intracellular region of cancer cells considerably suppresses these chemical transformations, maintaining the neutral forms of cpx and oxa inside the malignant cells (AHMAD, 2017).

In this context, the cellular uptake of platinum drugs is the key step of their mechanisms of action. There is a consensus in the literature that the passive diffusion is one of the main cellular internalization processes for these metallodrugs, which is, in turn, modulated by their size, charge, and lipophilicity (MARTINHO, *et al.*, 2018). Arsenano and coworkers highlight that 50% of the cellular transports of cddp occurs via passive diffusion (ARNESANO, *et al.*, 2013). The Pt(II)-based drugs uptake can be also properly approached by molecular dynamics (MD) simulations, thereby providing important insights and explanations of the cellular transport. Ruano *et al* reported the permeation mechanism of cddp through a membrane model formed by 1,2-dioleoyl-*sn*-glycero-3-phosphocholine (DOPC) lipids (RUANO, *et al.*, 2021). The potential of mean force (PMF) calculated displayed a barrier of only 0.2 kcal mol^{-1} to the cddp insertion in the polar heads region of the biomembrane, and an energy barrier of 10.4 kcal mol^{-1} to reach the hydrophobic center. Nierzwick *et al* also showed for cddp, an energy barrier of 12.0 kcal mol^{-1} to enter the center of a 1,2-dimyristoyl-*sn*-glycero-3-phosphocholine (DMPC) membrane, thereby indicating a high repulsion to this drug immersed in the lipid tails region (NIERZWICK, *et al.*, 2015). The PMF referring to translocation of cddp through a DOPC membrane also reached a peak of 16.25 k_BT (~9.6 kcal mol^{-1}) at the center of the lipid bilayer, by using a flexible topology for this metallodrug based on quantum MD data (YESYLEVSKYY, *et al.*, 2015). By employing a QM/MM approach, in which the quantum region took into account 6 DOPC lipids and cddp, Cárdenas and coworkers demonstrated the prevalence of the electrostatic component of the interaction energy cddp--DOPC (quantum region) at both polar and nonpolar regions of the membrane and the overestimation of the Pauli repulsion at the lipid tails section (CÁRDENAS, *et al*., 2021).

However, the drug uptake is also dependent on the heterogeneous nature of typical plasma membranes (RUSESKA & ZIMMER, 2020; CHOE, 2020; VENEBLE, *et al*., 2019). With regard to cancer cells, the membranes present an overexpression of the phosphatidylserine at the outer leaflet (SZLASA, *et al*., 2020), a lower cholesterol concentration (BERNADES & FIALHO, 2018), a symmetrization of the lipid distribution (RIVEL, *et al*., 2019), and a dysregulated pH gradient (LEE & SHANTI, 2021). In this sense, by using asymmetric models of membranes referring to normal and cancer cells, Rivel *et al* reported a decrease of the cddp

permeability in cancer cells due to the increased content of cholesterol and the loss of lipid asymmetry, which are observed in malignant cells (RIVEL, *et al*., 2019). These authors also highlighted the overestimation of cddp permeability in DOPC membranes (5-6 orders of magnitude higher than in realistic membrane models). The same authors also showed that the membrane curvature increased the permeability coefficient of cddp, thereby indicating a more favorable cellular uptake in the curved regions of mammalian erythrocyte membranes (YESYLEVSKYY, *et al.*, 2019).

In spite of these studies, there are still some unexplored aspects to be addressed on the cellular uptake of platinum drugs in breast cancer cells, such as the effect of the asymmetry referring to the ionic concentration between intracellular and extracellular regions, the characterization of the efflux routes of these metallodrugs, and the consideration of hydrolyzed species of cddp in the cytoplasm of malignant cells. Moreover, there is also a lack of theoretical studies concerning the membrane permeability of both cpx and oxa. In this work, we analyzed the influx and efflux mechanisms of platinum drugs through a realistic model of a breast cancer cell membrane using biased MD simulations. By taking into account the asymmetric nature of breast cancer cells, we intend to provide a more accurate description of these translocation processes, presenting insights that are not fully captured by experiments, which may contribute to the improvement of the current chemotherapies.

6.2 METHODS

6.2.1 Systems

The 3D structures of the three Pt(II)-based drugs (cddp, cpx, and oxa) are represented in Figure 6.2. Concerning the plasma membrane of a breast cancer cell, we built a prototype, that includes the same lipid composition (%) used in our previous model (C_memb) (ALMEIDA, *et al.*, 2021), which was based on experimental data collected from the well-known MCF-7 cell line (SOULE, *et al.*, 1973; LEE, *et al*., 2015; TODOR, *et al.*, 2012).

In summary, the lipid content of this new membrane model, herein named as c_memb, takes into account some molecular biomarkers evidenced in breast cancer cells, such as the symmetric lipid distribution among the two leaflets of the membrane, the phosphatidylserine (PS) expression at the outer leaflet and an enriched concentration of phosphatidylethanolamine (PE) and cholesterol (CHL) in comparison to normal cells (ALMEIDA, *et al*., 2021). Both number and distribution of lipids referring to the c_memb model are organized in Table 6.1,

while the structures of each lipid are illustrated in Figure D.1. It is worth noting that this model comprises the main lipids found in plasma membranes of breast cancer cells (TODOR, *et al.*, 2012).

Figure 6.2 - 3D structures of the Pt(II)-based drugs studied in this work: (A) cisplatin - cddp, (B) carboplatin - cpx, and (C) oxaliplatin - oxa. The green, blue, white, red, silver, and ochre spheres refer to the Cl, N, H, O, C, and Pt atoms, respectively.

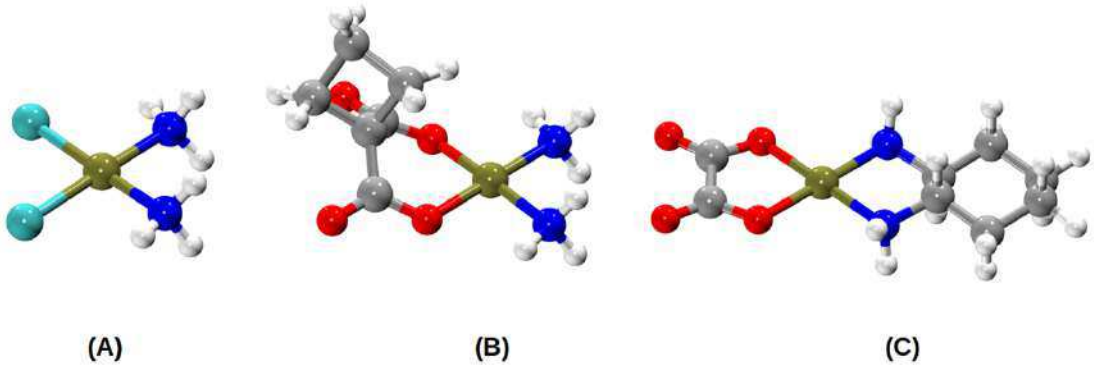

Reference: Own author (2023).

In order to represent the asymmetric concentration of the main ions (Na^+, K^+, and Mg^{2+}) existing in the intracellular and extracellular regions of a breast cancer cell, we built the c_memb as a double membrane model, which enables the separation of two solvent reservoirs, thereby mimicking the cytoplasm and extracellular compartment (see Figure 6.3). The use of this dual-membrane approach is described in literature for studying transmembrane potential gradients (SAMSON & BIGGIN, 2010; LEE, *et al.*, 2008; JO, *et al*., 2008). To neutralize our system, we added Cl^- ions and their final distribution reproduced in part the concentration gradient detected in cells. Table 6.1 also displays the distribution of ions in the c_memb model. It is worth mentioning that the two membranes in the c_memb have the same lipid composition.

The c_memb model was prepared employing the membrane builder available in the CHARMM-GUI website (JO, *et al*., 2008; LEE, *et al*., 2020) and the Packmol software (MARTÍNEZ, *et al*., 2009). By including the platinum drugs (cddp, cpx, and oxa) in the c_memb model, we built the systems that will be analyzed in this work: cddp>c_memb, cpx>c_memb, and oxa>c_memb. For the influx processes, the drugs were initially positioned at 70 Å from the center of the c_memb model, whereas for the efflux processes, the drugs were positioned at the center (0 Å) of the biomembrane (see the blue dashed lines in Figure 6.3 and Figure D.2).

Table 6.1 - Composition of lipids and ions included in the breast cancer cell membrane (c_memb) model.

Lipids[a]	**Number of lipids**[b]	
	Outer monolayer	**Inner monolayer**
DOPC	38	38
DOPE	16	16
DOPG	4	4
DOPS	6	6
CHL	18	18
Ions	**Number of ions**[c]	
	Extracellular medium	**Intracellular medium**
Na^{+} [d]	25	2
K^{+} [e]	3	15
Mg^{2+} [f]	2	0
Cl^{-}	32	17

[a]1,2-dioleoyl-*sn-glycero*-3-phosphocholine (DOPC), 1,2-dioleoyl-*sn-glycero*-3-phosphoethanolamine (DOPE). 1,2-dioleoyl-*sn-glycero*-3-[phospho-rac-(1-glycerol)] (DOPG). 1,2-dioleoyl-*sn-glycero*-3-phospho-L-serine (DOPS), and cholesterol (CHL). [b]Number of lipids (calculated from the lipid concentration (%) reported for the MCF-7 cell line (see ref.: AMARA, *et al.*, 2015). [c]Number of ions calculated from the ionic concentration referring to the intracellular and extracellular regions of a breast cancer cell. [d]See ref.: (AMARA, *et al.*, 2015). [e]See ref.: (EIL, *et al*., 2016). [f]See ref.: (PEREIRA, *et al*., 2002).
Reference: Own author (2023).

6.2.2 Force field parameterization

Regarding the drugs, we used the same parametrization procedure described in our previous work for cddp, cpx, and oxa (ALMEIDA, *et al*., 2022). In brief, the intramolecular parameters were derived from the optimized structures at the MP2/6-31G(d,p)/LANL2DZ level of theory (MØLLER, & PLESSET, 1934; HEHRE, *et al*., 1972; HAY & WADT, 1985). The polarizable continuum model (PCM) with the integral equation formalism variant was employed to consider the aqueous solution in these calculations (CANCÈS, *et al*., 1934). The force constants referring to bond stretching and angle bending were extracted from the quantum calculations using the Visual Force Field Toolkit (ZHENG, *et al*., 2016).

When it comes to the intermolecular parameters, the atomic charges were computed at the HF/6-31G(d,p)/LANL2DZ level of theory with the ChelpG approach (BRENEMAN & WIDEBERG, 1990) in aqueous solution (PCM). The Lennard-Jones 6-12 parameters for the C,

H, N, O, and Cl atoms were extracted from the General Amber Force Field (GAFF2) (WANG, *et al*., 2004), whereas the same set for the Pt atom was collected from previous studies (LOPES, *et al*., 2008; SANTANA, 2019).

Figure 6.3 - Plasma membrane model of a human breast cancer cell named c_memb. The colors violet, red, orange, tan, white, and magenta indicate the DOPC (1,2-dioleoyl-sn-glycero-3-phosphocholine), DOPE (1,2-dioleoyl-sn-glycero-3-phosphoethanolamine), DOPS (1,2-dioleoyl-sn-glycero-3-phospho-L-serine), DOPG (1,2-dioleoyl-sn-glycero-3-[phospho-rac-(1-glycerol)), OL (oleoyl chains), and CHL (cholesterol) structures, respectively. The green, yellow, pink, and gray spheres in the aqueous phases represent the Cl^-, Na^+, Mg^{2+}, and K^+ ions, respectively.

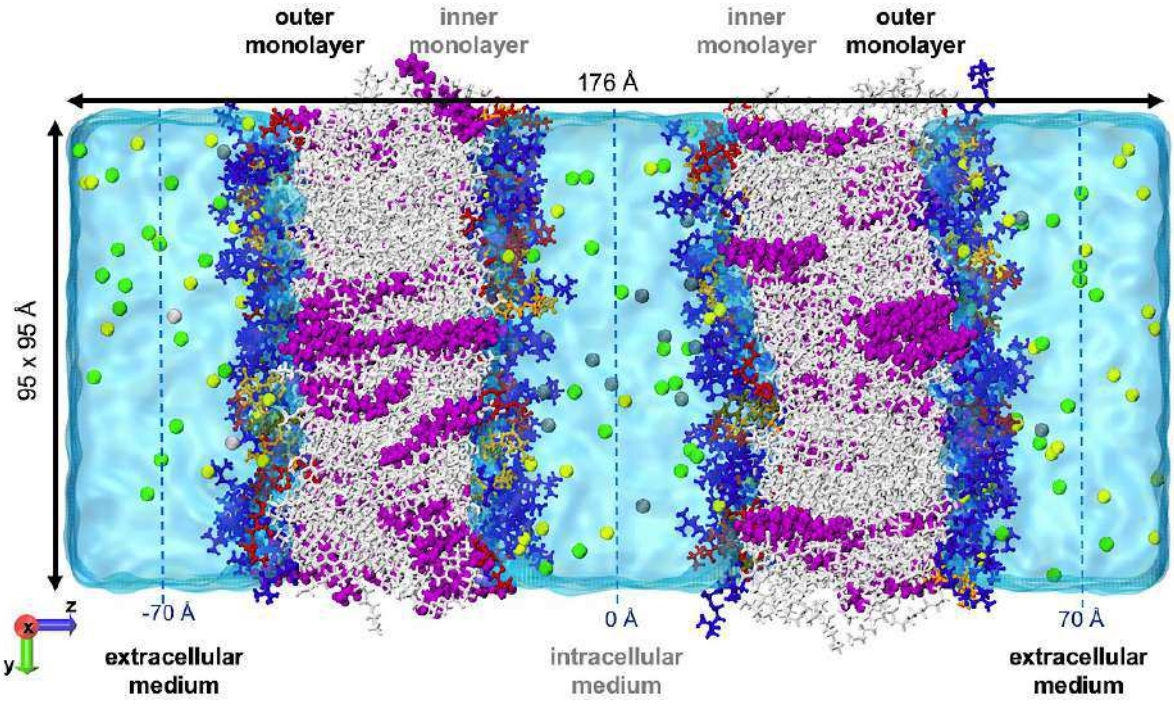

Reference: Own author (2023).

Concerning the membrane, we used the Amber force field Lipid17 for the lipids (CASE, *et al*., 2019), the TIP3P model for the water molecules (JORGENSEN, *et al*., 1983), the parameters developed by Joung and coworkers (JOUNG & CHEATHAM, 2008) for the monovalent ions (Na^+, K^+, and Cl^-), and the parameters obtained by Li and Kenneth (LI & MERZ, 2014) for the Mg^{2+} ion.

6.2.3 Computational details

The pmemd CUDA implementation (SALOMON-FERRER, *et al*., 2013; GÖTZ, *et al.,* 2012; LE GRAND, *et al*., 2013) of Amber 20 (CASE, *et al*., 2020) was employed for all MD simulations and the Gaussian-09 release D.01 program (FRISCH, *et al*., 2009) was used for the quantum mechanical calculations. The equilibration protocol for the c_memb model firstly involved the energy minimization stage of the solvent for 40,000 steps with restraints of 500 kcal mol^{-1} $Å^{-2}$ to the solute and a subsequent minimization of the entire system for 9,000 steps without applying positional restraints. While the first half of these two stages used the steepest descent method (JENSEN, 2007), the last half used the conjugate gradient method (JENSEN, 2007). The next stage was the heating from 283 K to 310 K in the NVT ensemble for 20 ns, with positional restraints to the solute of 10 kcal mol^{-1} $Å^{-2}$. The Langevin thermostat with a collision frequency of 1.0 ps^{-1} was used in this stage (UBERUAGA, *et al*., 2004). After heating, we conducted the equilibration stage in the NPT ensemble for 470 ns using the Langevin thermostat and the anisotropic Berendsen barostat (BERENDSEN, *et al*., 1984) with a reference pressure of 1.0 bar and a pressure relaxation time of 1.0 ps. The last frame of this equilibration stage was used in the simulations with the metallodrugs.

The translocation processes of the platinum drugs through the biomembrane were simulated using the steered molecular dynamics (SMD) (BOUBETA, *et al*., 2019) and umbrella sampling (US) (KÄSTNER, 2011) methods. The reaction coordinate was defined as a distance of 70 Å along the axis parallel to the membrane normal, in which the drugs were pulled out from the extracellular region to the intracellular region (influx process) and from the intracellular region to the extracellular region (efflux process, see Figure D.2). This drug pulling stage was conducted with a rate of 1.03 Å/ns for 72 ns using the semi-isotropic Berendsen barostat and a surface tension (γ) regulation in the the NPγT ensemble. Next, we extracted 71 frames every 1 Å from the SMD trajectories (influx and efflux), which corresponded to the 71 windows for the US. Each simulation window was run for 30 ns in the NPγT ensemble with the force constant of 2.5 kcal mol^{-1} $Å^{-2}$ for the biasing potential. The PMFs for each process (influx and efflux) were calculated from these 2.130 μs of sampling/drug with the Weighted Histogram Analysis Method (WHAM) (KUMAR, *et al*., 1992; GROSSFIELD, 2023; KUMAR, *et al*., 1995; ROUX, 1995). The bootstrap error analysis (GROSSFIELD, 2023; EFRON & TIBSHIRANI, 1994) was employed to compute the errors of the PMFs. The calculation of the PMFs involved two sets of sampling along the reaction coordinate (z axis): drug influx (70 Å

→ 0 Å) and efflux drug (0 Å → 70 Å). The final profiles of free energy were derived from the overlay of PMFs referring to each process (influx and efflux).

In addition to constrain all bonds involving H atoms by means of the SHAKE algorithm (RYCKAERT, *et al.*, 1977) all simulations were run with periodic boundary conditions and time step of 2 fs. The details of all simulations are organized in Table 6.2.

Table 6.2 - Summary of the main details referring to the MD simulations conducted in this study.

System[a]	N_a [b]	N_{wat} [c]	N_{lip} [d]	t_{equi}/ns [e]	t_{SMD}/ns [f]	$t_{US}/\mu s$ [g]	$t_{total}/\mu s$ [h]
c_memb	83,538	14,534	328	470	(i)	(i)	0.470
cddp>c_memb	83,549	14,534	328	2x25	2x72	2x2.13	2x2.227
cdcla>c_memb	83,483	14,511	328	2x25	2x72	2x2.13	2x2.227
cdclo>c_memb	83,476	14,510	328	2x25	2x72	2x2.13	2x2.227
cpx>c_memb	83,563	14,534	328	2x25	2x72	2x2.13	2x2.227
oxa>c_memb	83,420	14,485	328	2x25	2x72	2x2.13	2x2.227

[a]The terms c_memb, cddp, cdcla, cdclo, cpx, oxa, and > indicate the plasma membrane model of a breast cancer cell, cisplatin, mono-aqua derivative of cisplatin, mono-hydroxo derivative of cisplatin, carboplatin, oxaliplatin, and interaction drug-membrane, respectively. [b]Total number of atoms. [c]Total number of water molecules. [d]Total number of lipids considering the two lipid bilayers. [e]Simulation time for the equilibration stage. [f]Simulation time for the pulling stage of the drugs using the steered molecular dynamics (SMD) method. [g]Total simulation time for the 71 windows using the umbrella sampling (US) method. [h]Total simulation time. [i]This simulation involved only the equilibration stage of the c_memb. *The index 2x refers to the two transmembrane transports of the drugs conducted along the reaction coordinate: efflux (0 Å → 70 Å) and influx (70 Å → 0 Å).
Reference: Own author (2023).

The deuterium order parameters (S_{CD}) referring to the oleoyl (OL) chains of the lipids were computed according to Eq.6.1 (DICKSON, *et al.*, 2014). The terms *i*, Θ_i, *and* < > in eq. 6.1 denote each C atom of the OL tail, the angle between the vector that defines the C-H bond in each lipid tail and the perpendicular axis to the plane of the membrane, and the average with respect to the simulation trajectory, respectively.

$$S_{CD}^{i} = \frac{1}{2}\langle 3cos^2\Theta_i - 1\rangle \tag{6.1}$$

The permeability coefficients (*P*) of the platinum drugs were calculated using the inhomogeneous solubility-diffusion model via eq. 6.2, where $\beta = 1/k_BT$ (MARRINK & BERENDSEN, 1996). In this equation, the terms R_{eff}, *R(z)*, $\Delta G(z)$, D(z), k_B, and T correspond

to the effective resistance of the membrane, the local resistance at each z-window, the free energy at each z-window derived from the PMF, the diffusion coefficient of the drug at each z-window, the Boltzmann constant, and the temperature, respectively.

$$\frac{1}{P} = R_{eff} = \int_0^z R(z)\, dz = \int_0^z \frac{\exp\left(\beta \Delta G(z)\right)}{D(z)} dz \tag{6.2}$$

In Eq. 6.2, the position-dependent diffusion coefficients (*D(z)*) were calculated according to the method developed by Hummer (HUMMER, 2005), which used the positional variance (*var(z)*) and the position autocorrelation functions ($C_{zz}(t)$) (see Eq.6.3).

$$D_{(z=\langle z \rangle)} = \frac{var(z)^2}{\int_0^\infty C_{zz}(t)dt} \tag{6.3}$$

The $C_{zz}(t)$ in Eq. 6.3 were obtained from the time series referring to the z-position of the drugs through the membrane (see Eq. 6.4) (LEE, *et al.,* 2016) In this equation, $n_{samples}$ = 195,000 and $\delta_z(t) = z(t) - \langle z \rangle$.

$$C_{zz}(t) = \langle \delta_z(0)\delta_z(t) \rangle = \frac{1}{n_{samples}} \sum_{i=0}^{n_{samples}-1} \delta_z(i)\delta_z(t+i) \tag{6.4}$$

6.3 RESULTS AND DISCUSSION

6.3.1 Membrane equilibration

The stable behavior of the moving averages (green line in Figure D.3) referring to the temporal variation of the temperature (T), pressure (P), volume (V), and density (d) indicates the convergence of these simulation properties of the c_memb (310 K, 1 bar, and 1.02 g cm^{-3}) during the last 100 ns of the 470 ns trajectory. Figure D.4 also reflects this stabilization in terms of energy, including the kinetic, potential, and total energies of the system during the same time interval. When it comes to the decomposition of the potential energy relative to the membrane (only the solute), the components presented in Table D.1 reinforce the energetic stabilization

of the c_memb model, since the energy variations represent, on average, 0.4% of the average values of each contribution.

After characterizing the energetic stability of the c_memb, we analyzed its structure by calculating typical parameters of membranes as shown in Table 6.3. Although the experimental values are also presented in this table, they cannot be treated as quantitative references, since they involve homogeneous lipid bilayers at different temperatures.

Table 6.3 - Structural parameters of the breast cancer cell membrane (c_memb) model calculated from the last 100 ns of its 470 ns simulation at 310 K.

Property / unit	**Average ± std.[h]**	**Experimental values**
A_L / $Å^{2}$ [a]	72.8 ± 0.7	72.5[f]
V_L / $Å^{3}$ [b]	1100. ± 3.	1125.0[g]
D_{HH} / Å [c]	40.4 ± 0.2	40.0[g]
S_{CD}^{C9} / - [d]	0.038 ± 0.000	0.045[g]
S_{CD}^{C17} / - [e]	0.02 ± 0.02	0.000[g]

[a]Area per lipid. [b]Volume per lipid. [c]Membrane thickness calculated from the last 20 ns of the 470 ns. [d]Deuterium order parameter of the carbon atom C9 that is located at the double bond of the oleoyl (OL) chains. [e]Deuterium order parameter of the carbon atom C17 that is located at the ends of the two OL chains. [f]Value for a DOPC membrane at 298.15 K (see ref.: DICKSON, *et al*., 2014). [g]Value for a DOPC membrane with 0.3 molar fraction of cholesterol at 303.15 K (see ref.: MADEJ, *et al*., 2015). [h]Standard deviation.
Reference: Own author (2023).

Concerning the area per lipid (A_L), it is evidenced the low oscillation of this property (1 % of the average value) in both Figure D.5A and Table 6.3, thereby indicating the structural stability of the membrane during the simulation time (100 ns) with a good qualitative agreement with the experiment. Similarly, the stable moving average in Figure D.5B and the variation of about 0.3% in the volume per lipid (V_L) emphasize the stabilization of the c_memb model. The underestimation of the theoretical V_L compared to the experimental one is also reported in the literature with a difference of less than 5% between these values (2% in our simulation) (DICKSON, *et al*., 2014).

In order to confirm the global stability of the c_memb model and to extract the membrane thickness (D_{HH}), we calculated the electron density profile of the entire system (see Figure 6.4A). This profile evidences a symmetric and stable behavior of the two lipid bilayers that compose our model during the last 20 ns of the 470 ns run.

Figure 6.4 - Structural properties of the breast cancer cell membrane (c_memb) averaged from the last 20 ns of the 470 ns equilibration run: electron density profile (A) and deuterium order parameters (S_{CD}) of the two oleoyl (OL) tails referring to the lipids of the membrane (B).

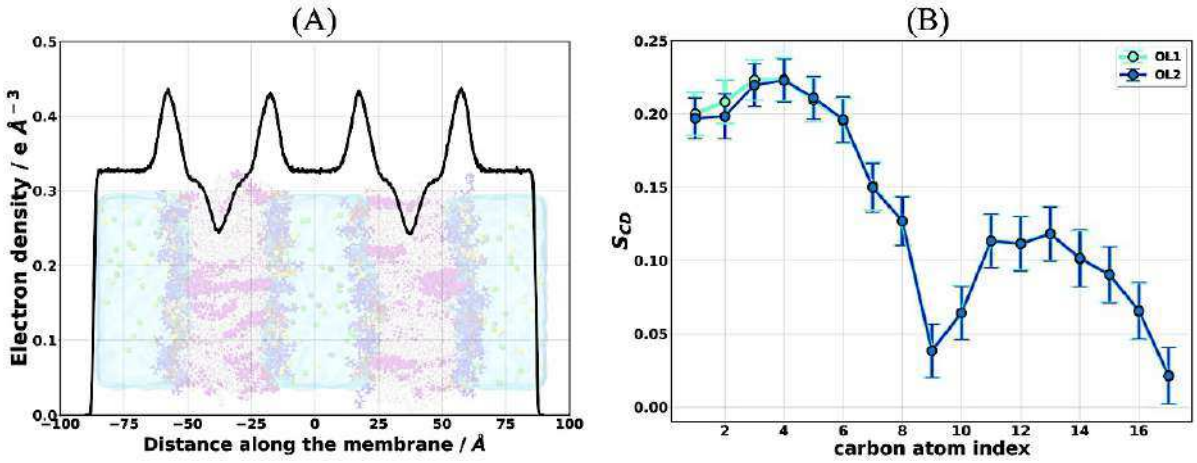

Reference: Own author (2023).

Additionally, the conventional peaks at this profile reflect the charge concentration at the polar heads region of membranes, while the two valleys indicate the lowest charge concentration among the lipid tails, which also demonstrates the hydrophobic nature of this section. From the distance between two peaks per membrane of the electron density profile, we calculated the D_{HH} values presented in Table 6.3. This latter shows a significant agreement with both the experimental data and our last study involving the membrane model C_memb that has the same lipid composition of the prototype evaluated herein.

At last, to quantify the ordering of the lipids, the S_{CD} referring to the lipid tails were calculated and graphically represented in Figure 6.4B. The general profile of these parameters is in accordance with theoretical and experimental data relative to membranes with these two acyl chains (DICKSON, *et al.*, 2014; MADEJ, *et al.*, 2015). In Figure 6.4B, the similarity between the S_{CD} of the two OL chains indicates the convergence of their dynamical behavior along the simulation time (20 ns). Moreover, the lowest S_{CD} shown in Figure 6.4B refer to the C atom located at the double bond (C9) of the OL chain and the C atom located at the end of this lipid tail (C17). The low ordering of these atoms is connected to their positions at the carbon chain that either geometrically restrict the motion as in the case of the double bond (C9) or provide a high structural variation as in the end of the tail (C17) with three C-H bonds. The S_{CD} for these two specific C atoms (S_{CD}^{C9} and S_{CD}^{C17}) are displayed in Table 6.3. Based on the analyses conducted in this section, the c_memb model was therefore equilibrated over the time of 470 ns and the last frame of this trajectory was used to study the permeation of the drugs.

6.3.2 Translocation mechanisms of the Pt(II) drugs

The mechanisms of influx and efflux of the platinum drugs through the c_memb model are presented in Figure 6.5 (influx) and Figure D.6 (efflux). In these figures, the first stage of the mechanisms is the drug insertion in the region of polar heads at 14 ns. Interestingly, the insertion mode of the drugs during both influx (Figure 6.5) and efflux (Figure D.6) are similar. Specifically, the insertion of cddp and cpx starts with the two $–NH_3$ groups facing the membrane, whereas the insertion of oxa starts with the plane of this drug facing the biomembrane. The second stage, which involves the frames at 28 ns and 42 ns, comprises the drug permeation through the lipid tails. Figure 6.5 shows that permeation mode during the influx of cddp and cpx at 28 ns is the same as the insertion mode, while the permeation mode of oxa involves the inclination of this molecule with the cyclohexanediamine group facing the polar heads of the second monolayer of lipids. In the efflux processes, Figure D.6 indicates that both cpx and oxa have similar permeation modes, while cddp has the –Cl groups facing the center of the c_memb.

Still regarding the drug permeation at 28 ns, Figure 6.6 and Figure D.7 reveal that this stage is accompanied by the deformation of the polar head region of the membrane in both influx and efflux processes. At 42 ns, we note the intensification of this deformation and the concomitant diffusion of water molecules with the drugs through the membrane (Figure 6.6 and Figure D.7). Additionally, the frames at 42 ns in Figure 6.5 indicate that while oxa keeps the same permeation mode as at 28 ns, both cddp and cpx rotate in this region, maintaining either the plane parallel to the membrane in the case of cddp or the carboxylate group facing the membrane in the case of cpx. In the efflux events at 42 ns (Figure D.6), the three drugs have similar permeation modes as we saw in the influx processes.

Next, at 56 ns, the drugs reach the polar region of the opposite monolayer with different insertion modes. Specifically, cddp and cpx enter this region with the $–NH_3$ groups facing the membrane in both influx (Figure 6.5A-B) and efflux (Figure D.6A-B), while oxa reaches the same region by the cyclohexanediamine group, with an orientation approximately parallel to the plane of the membrane, during the two transmembrane transports (Figure 6.5C, Figure 6.6C, Figure D.6C, and Figure D.7C).

Figure 6.5 - Temporal variation of the position of the Pt(II)-based drugs during their permeation (influx, 70 Å → 0 Å) through the breast cancer cell membrane (c_memb): cddp>c_memb (A), cpx>c_memb (B), and oxa>c_mem (C). The frames of the drugs, which were collected from the steered molecular dynamics simulations of 72 ns, are superimposed keeping the membrane fixed.

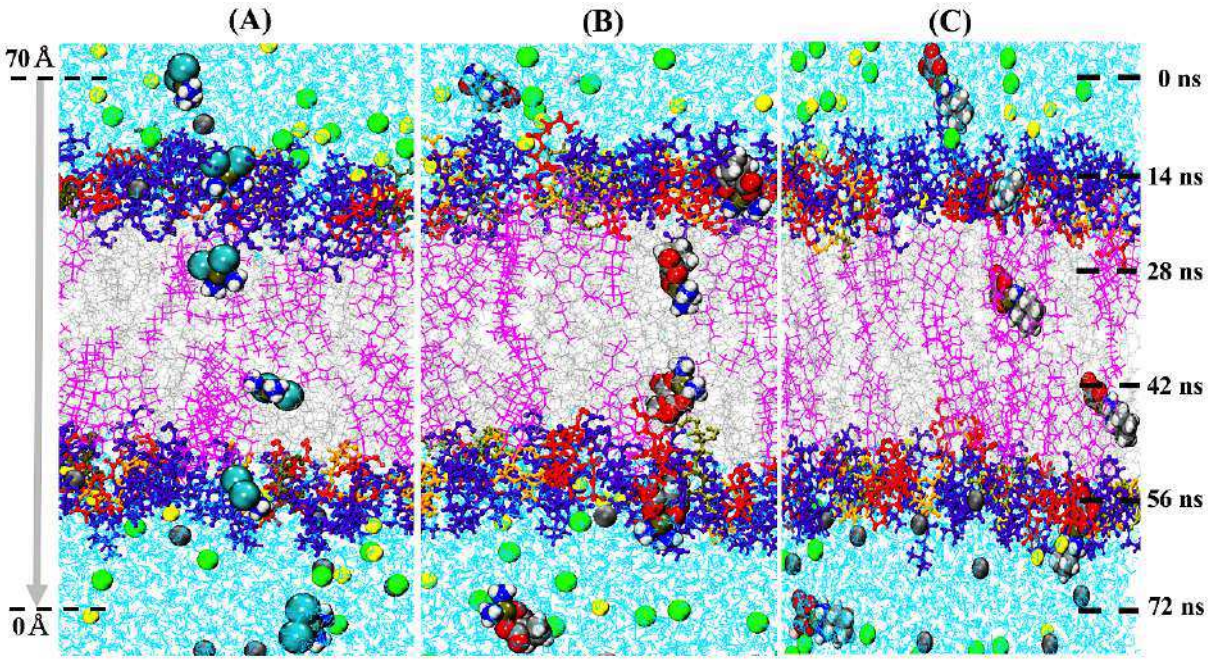

Reference: Own author (2023).

At 56 ns, we also observe the self-sealing of the membrane after the translocation processes (Figure 6.6 and Figure D.7). Finally, the drugs complete the permeation after 56 ns reaching the intracellular and extracellular media in the case of the influx and efflux processes, respectively. It is worth mentioning that a clear difference between the influx and efflux requires the development of more simulation replicas. However, this study represents a first investigation of this process aiming to describe the free energy profiles referring to the translocation of these drugs through the membrane.

6.3.3 Permeation of water and ions

To investigate the permeation of water molecules during the drug transports shown in Figure 6.6 and Figure D.7, we computed the density profiles of waters molecules along the c_memb model (see Figure D.8). This figure evidences not only the concentration of water molecules at the three reservoirs with an average number of about 460 solvent molecules along

these regions, but also the penetration of water molecules into the polar heads during the 72 ns runs.

Figure 6.6 - Influx mechanism (70 Å → 0 Å) of the Pt(II)-based drugs through the breast cancer cell membrane (c_memb) model using steered molecular dynamics (SMD) simulations: cddp>c_memb (A), cpx>c_memb (B), and oxa>c_mem (C).

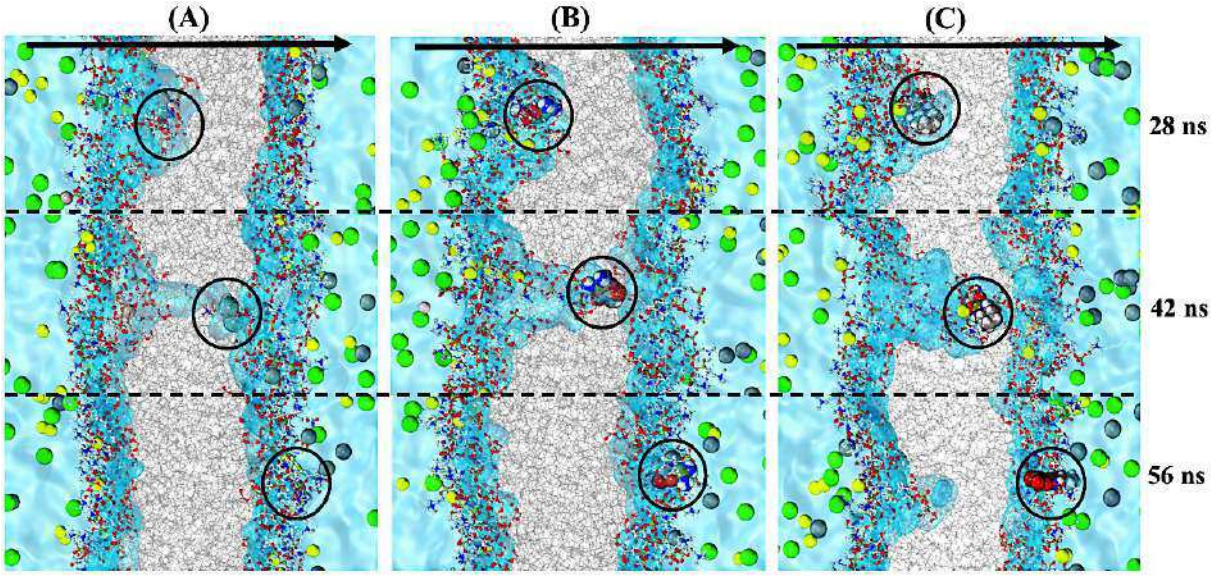

Reference: Own author (2023).

In addition to the hydrophilic nature of the polar heads that favors the interaction with the solvent, the drug permeation is also a factor that may intensify the accessibility of water molecules in this region. Conversely, the hydrophobic character of the lipid tails is also highlighted in Figure D.8 by showing a negligible density of the water molecules in this region.

In order to quantify the flow of water molecules along the OL chains, we represented in Figure 6.7 the density profiles of these molecules focusing on the hydrophobic core of the c_memb. Figure 6.7 demonstrates that, on average, there is a slight water flux during the permeation of the platinum drugs through the membrane. This flux is notably small along the region defined between 25 Å and 45 Å of the reaction coordinate, especially for cddp (Figure 6.7A,D) and cpx (Figure 6.7B,E) which present a density less than one. In contrast, the water flux due to the translocation of oxa is the greatest among the drugs, with at least two molecules for the influx (Figure 6.7C) and one molecule for efflux (Figure 6.7F).

Figure 6.7 - Profiles of the average density of water molecules (number of water molecules / Å3) along the hydrophobic core (center of the lipid bilayer) referring to the breast cancer cell membrane (c_memb) model during the permeation processes of the Pt(II)-based drugs: influx of cddp (A), influx of cpx (B), influx of oxa (C), efflux of cddp (D), efflux of cpx (E), and efflux of oxa (F). While the points indicate the average values, the shaded bands represent the standard deviation values. The term N refers to the number of molecules.

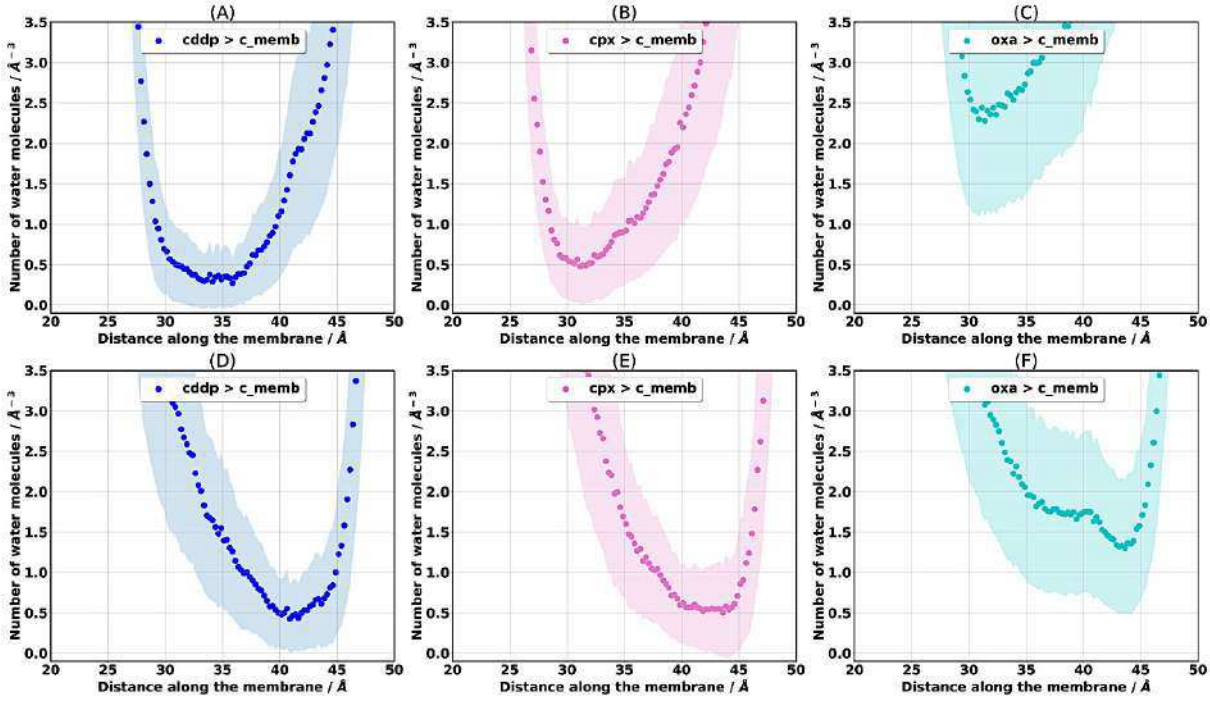

Reference: Own author (2023).

At the center of the reaction coordinate (35 Å), data from Table 6.4 reveal that the presence of water molecules during the oxa permeation is, on average, three times greater than the one related to cddp and cpx during the influx processes. When it comes to the efflux of cpx and oxa, Table 6.4 shows a slightly greater water flux compared to cddp. These differences suggest a relation with the size of the drugs, so that largest drug (oxa) cause greater membrane deformation and, in turn, induce a greater water flux during their transmembrane transport.

Regarding the ions, data from Table 6.4 highlight the inexistence of their diffusion with the drugs through the c_memb, thereby evidencing the existence of high energy barriers for this permeation. In fact, Yesylevskyy *et al* reported barriers of 24.1 kcal/mol and 24.3 kcal/mol for the permeation of Na^+ and Cl^- across an asymmetric membrane model (YESYLEVSKYY, *et al.,* 2019).

Table 6.4 - Average density of ions (Na^+, K^+, Mg^{2+}, and Cl^-) and water molecules at the center of the lipid tails referring to the breast cancer cell membrane (c_memb) model during the translocation processes of the Pt(II)-based drugs. All values represent are in units of number of species / $Å^3$.

System	Influx (70 Å → 0 Å)		Efflux (0 Å → 70 Å)	
	wat(35Å)[a]	ions(35Å)[b]	wat(35Å)	ions(35Å)
cddp	0	0	1.4±0.9	0
cpx	1.0±0.8	0	1.5±0.9	0
oxa	3.0±1.4	0	2.0±1.1	0

[a]Density of water molecules (number of water molecules / $Å^3$) at 35 Å. [b]Density of ions (number of ions / $Å^3$) at 35 Å. All values were averaged from the steered molecular dynamics (SMD) simulations (72 ns). The distance 35 Å is the average position of reaction coordinate that corresponds to the hydrophobic center of the membrane.

Reference: Own author (2023).

To access the average position of the ions inside the intracellular and extracellular regions of the membrane, we computed the density profiles of these particles from the trajectories referring to the influx and efflux of the drugs (see Figure 6.8). The plots in Figure 6.8 clearly show the permanence of the ions inside the solvent reservoirs during all simulations of 72 ns. Concerning the Na^+ ions, their concentration is larger in the polar heads regions. This preferential localization of the Na^+ ions can be explained mainly by the electrostatic interactions with the anionic lipids (DOPS and DOPG) in these hydrophilic regions. Although the behavior of the K^+ ions is slightly similar to the Na^+ ions, it is possible notice that they present a more diffused distribution inside the intracellular medium. This results suggests a greater mobility of the K^+ ions between the two polar regions that delimit this reservoir, thereby indicating a less pronounced positive charge as verified for the Na^+ ions. With regard to the Mg^{2+} ions, the low density along the reaction coordinate evidenced in Figure 6.8 is the result of its low concentration (see Table 6.1) and, consequently, its high mobility during the simulation. Overall, there is also a concentration of this divalent ion in the polar heads region.

At last, the distributions of the Cl^- ions show a more concentrated diffusion at the center of each cellular compartment. The behavior of this anion reflects the electrostatic repulsion with the negative surface of the membrane formed by polar heads. In general, when it comes to either the drugs or the transmembrane transports, there are not significant changes in the profiles shown in Figure 6.8.

Figure 6.8 - Profiles of the average density of ions (number of ions / Å^3) along the breast cancer cell membrane (c_memb) model during the permeation processes of the Pt(II)-based drugs: influx of cddp (A), influx of cpx (B), influx of oxa (C), efflux of cddp (D), efflux of cpx (E), and efflux of oxa (F). The blue, pink, and cyan colors indicate the ion profiles of the systems cddp>c_memb, cpx>c_memb, and oxa>c_memb, respectively. The black dashed lines indicate the directions of the influx (A, B, and C) and efflux (D, E, and F) processes of the drugs. The term N refers to the number of molecules.

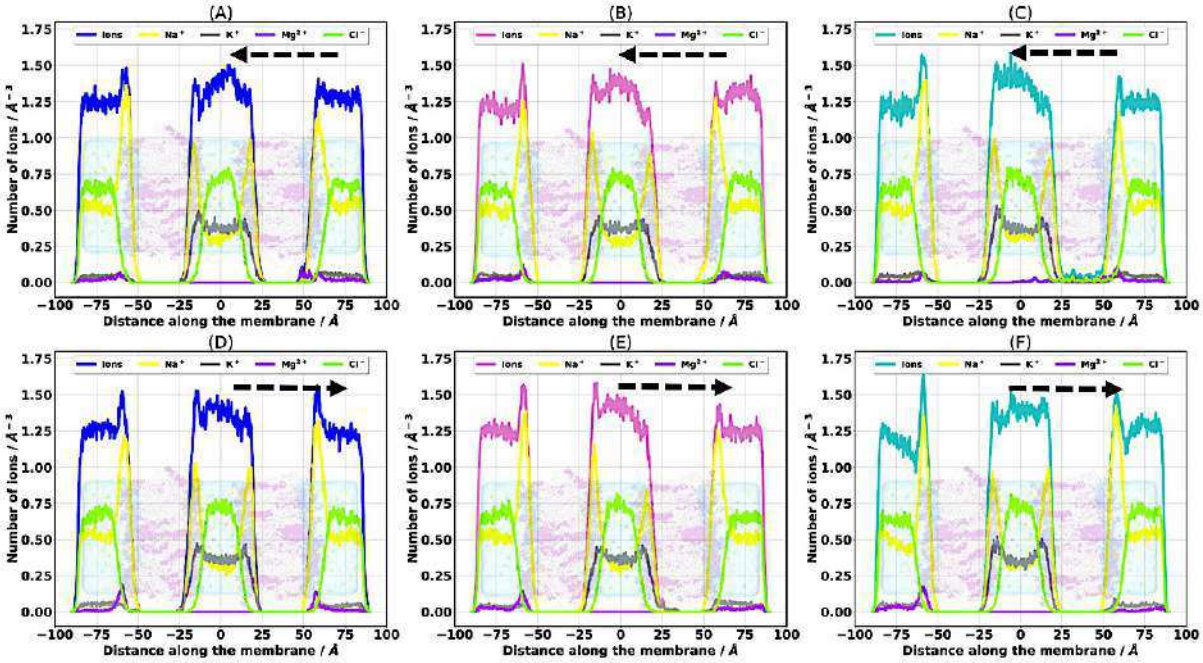

Reference: Own author (2023).

6.3.4 Drug-lipid interactions

In order to identify the main lipids that mediate the interactions with the platinum drugs, we analyzed the evolution of the number of drug-lipid contacts within a cutoff distance of 3.0 Å during the influx (Figure 6.9) and efflux (Figure D.9) processes through the c_memb.

By analyzing the influx processes (Figure 6.9), we observe that the interactions between drugs and polar heads (Figure 6.9A-D) are more recurrent around the ends of the trajectories (close to 0 Å and 70 Å in Figure D.2), whereas the drug--OL interactions (Figure 6.9F) are more frequent around the center of the trajectories (around 35 Å in Figure D.2). This behavior reflects the translocation mechanisms presented in Figure 6.6 and Figure D.7, where we saw the initial penetration of the metallodrugs in the polar region of the membrane, the permeation through the acyl tails, and the ultimate drug insertion in the second polar region before reaching the water phase.

Figure 6.9 - Moving average of the number of contacts drug--lipid established during the influx process (70 Å → 0 Å) of the Pt(II)-based drugs through the breast cancer cell membrane (c_memb) model. The symbols PC, PE, PS, PG, CHL, OL, cddp, cpx, and oxa stand for phosphocholine, phosphoethanolamine, phospho-L-serine, phospho-rac-(1-glycerol), cholesterol, oleoyl, cisplatin (cddp), carboplatin (cpx), and oxaliplatin (oxa), respectively.

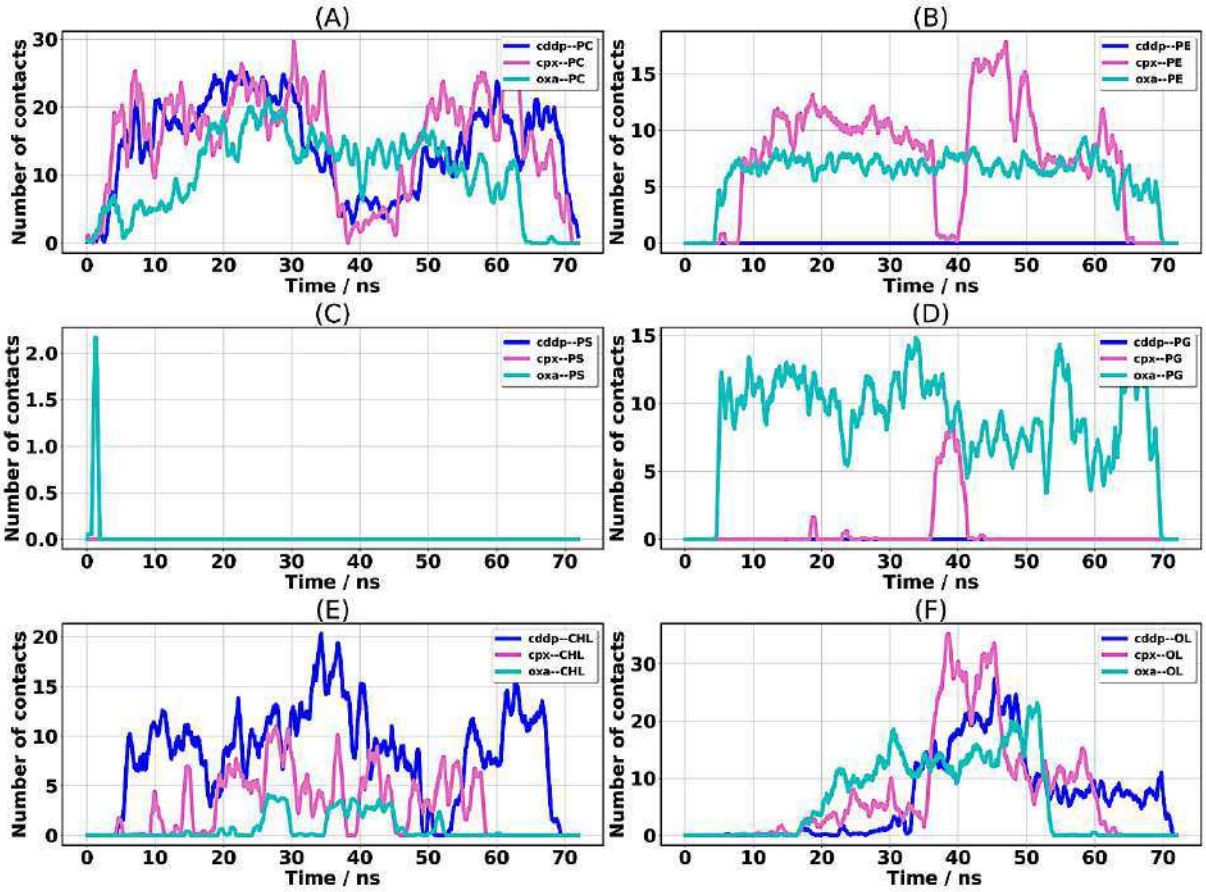

Reference: Own author (2023).

These results are more evidenced in the profiles of the drug--PC (Figure 6.9A) and drug--OL (Figure 6.9F) interactions. Specifically, Figure 6.9A shows that both cddp and cpx establish more interactions with the PC groups than the oxa. Data from Figure 6.10A indicate that while cpx formed 15 interactions/frame with the PC during the influx, cddp formed 14 interactions/frame and oxa formed 10 interactions/frame with the same polar head. This result emphasizes that despite the larger size of oxa, which could favor the interactions with the most expressed group (PC) in c_memb, there is a level of specificity of this platinum drug for other lipids. For instance, it is possible to notice preferential interactions of the oxa with the PE (Figure 6.9B) and mainly with the PG (Figure 6.9D).

Figure 6.10 - Average number of contacts per frame formed between Pt(II)-based drugs (cisplatin, carboplatin, and oxaliplatin) and the lipids of the breast cancer cell membrane (c_memb) during the translocation processes (72 ns): influx 70 Å → 0 Å (A), and efflux 0 Å → 70 Å (B).

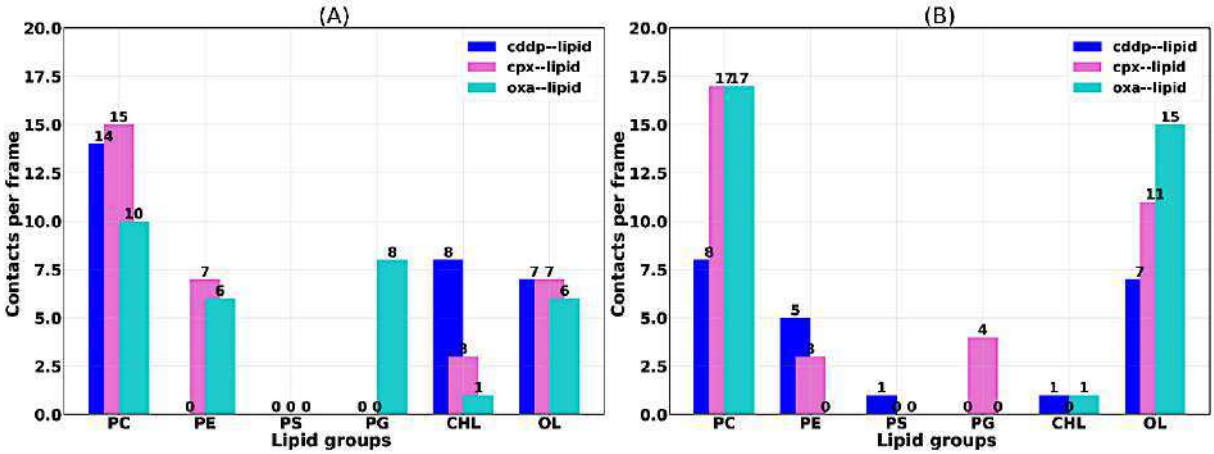

Reference: Own author (2023).

Interestingly, these figures reveal that the number of these contacts/frame is approximately constant along the trajectory, thereby pointing out the interaction of oxa with the PE and PG groups located at the two polar regions of the membrane. In particular, Figure 6.10A shows that oxa formed, on average, 8 contacts/frame with the PG units during the influx. In contrast, one of the lipid biomarkers of cancer cells (PS) did not mediate the influx processes of the platinum drugs (see Figure 6.9C), which may be related to its low concentration in the membrane (see Table 6.1).

Concerning the CHL, the cddp--CHL interactions are the most frequent among the drugs (8 per frame, Figure 6.10A) and they last longer (Figure 6.9E), which indicates a stable interaction during all influx process. Ultimately, the drug--OL contacts (Figure 6.9F) after 50 ns, which involve the stages of drug insertion in the polar region and the subsequent diffusion to the water phase (see Figure 6.5 and Figure D.6), reveal the membrane deformation and the adherence of the lipid tails around mainly cddp and cpx. Figure 6.9A shows that these acyl chains near the drugs refer to the DOPC lipids.

With regard to the efflux processes, the plots in Fig. D.9A display a decrease of the drug--PC contacts at 35 ns, which correspond to the stage where the metallodrugs reach the hydrophobic center of the membrane (see Figure 6.5). Consequently, the number of contacts drug--OL (Figure D.9F) is amplified in this region, especially for the case of oxa. Data from Figure 6.10B point out that the average number of contacts with the PC groups formed during

the efflux of cpx and oxa was about two times greater than the ones formed with cddp. In contrast to the influx process, the PE groups seem to mediate the efflux of cddp through the membrane (see Figure D.9B), forming, on average, 5 contacts/frame during this process (Figure 6.10B). As we noticed in the influx process, the PS group was not relevant for the efflux processes of the platinum drugs (Figure D.9C and Figure 6.10B). Moreover, the other anionic lipid (PG) did not mediate the efflux of both cddp and oxa through the c_memb (Figure D.9D and Figure 6.10B). The frequency of the cpx--PG contacts between 20 and 50 ns (Figure D.9D) indicates the favorable interaction between these molecules through the permeation stage along the lipid tails (Figure D.6). When it comes to the drug--CHL interactions, Figure 6.10B evidences that these contacts were not recurrent along the efflux, except for cddp after 50 ns when the drug reached the polar head region. Finally, we also noticed the effect of the membrane deformation in Figure D.9F after 50 ns, where the lipid tails reached the extracellular medium, especially for cpx due to its notable lipophilicity compared to cddp and oxa.

6.3.5 Free energy profiles

In this section, we discuss the possible spontaneous translocation processes of cddp, cpx, and oxa through the c_memb. To do this we based our analysis on the potential of mean force (PMF) plots presented in Figure 6.11A. Additionally, we also evaluate the free energy profiles related to the permeation events of the main species resulting from the hydrolysis of cddp (Figure 6.11B).

The decrease in free energy from 0 Å to 15 Å and from 70 Å to 50 Å along the reaction coordinate (see Figure 6.11A) points out the spontaneous character of the drug insertion (see Figure 6.5 and Figure D.6), thereby indicating favorable interactions between metallodrugs and polar heads of the membrane. This behavior is connected to the gradual increase of the number of interactions as the drugs approach the membrane. This leads to the stabilization of the system, in addition to the lipophilicity of these drugs that influence the drug insertion. Since cpx is the most lipophilic drug in this series (ORIYAMA, *et al*., 2020), it presents the highest energy well (~ -7.95 kcal mol^{-1}) followed by cddp (~ -8.63 kcal mol^{-1}) and oxa (~ -9.80 kcal mol^{-1}).

Figure 6.11 - Potentials of mean force (PMFs) referring to the influx and efflux processes of the platinum compounds through the breast cancer cell membrane (c_memb): PMFs referring to the translocation of cisplatin (cddp), carboplatin (cpx), and oxaliplatin (oxa) (A), and PMFs referring to the translocation of cddp, its mono-aqua derivative (cdcla), and its mono-hydroxo derivative (cdclo) (B). The reaction coordinate was defined as the axis perpendicular to the plane of the membrane considering a distance of 70 Å, where the position at 0 Å refers to the intracellular medium and the position at 70 Å refers to the extracellular medium. The black arrow indicates the coordinate for the drug influx (70 Å → 0 Å) whereas the red arrow indicates the coordinate for the drug efflux (0 Å → 70 Å).

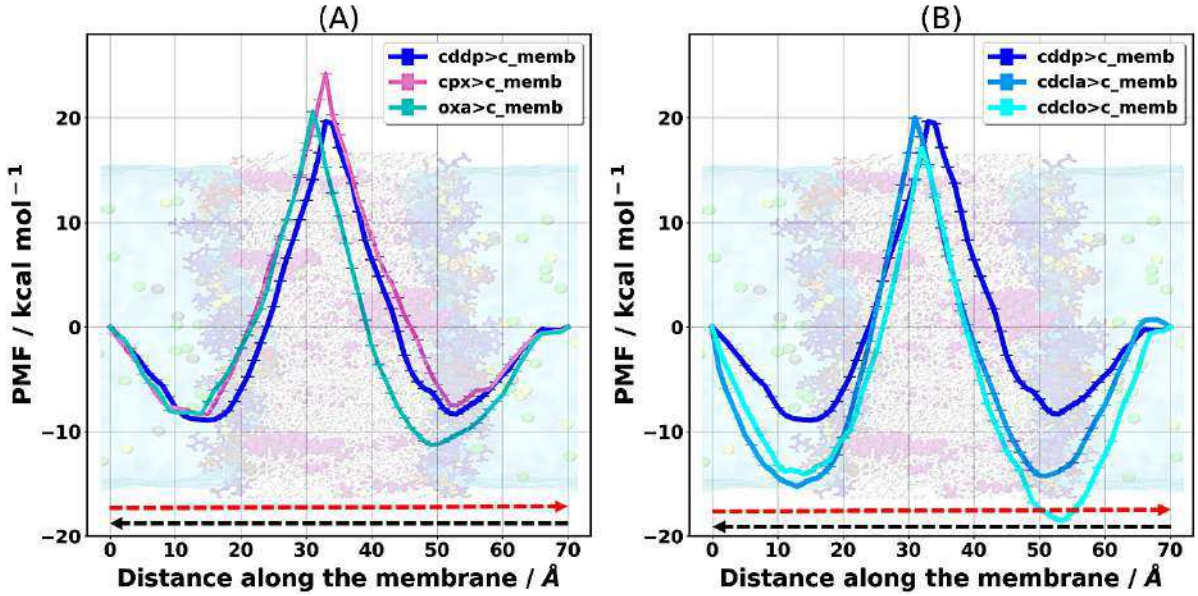

Reference: Own author (2023).

The spontaneous physisorption of cddp on the surface of a DOPC membrane was also reported by Ruano *et al.*, but with an energy drop of only 0.65 kcal mol^{-1} (RUANO, *et al.*, 2021). By using an asymmetric membrane model of a cancer cell, Rivel *et al.* also showed the favorable insertion of cddp in the polar region of this lipid bilayer (~ -5.0 kcal mol^{-1} depth) (RIVEL, *et al.*, 2019).

However, after the favorable interactions with the polar heads, the metallodrugs experience repulsive interactions if they continue the permeation process through the lipid tails, which is evidenced by the increase of the energy up to the drug reaches the center of the membrane (~35 Å). At this repulsive region, we have pronounced peaks in the PMFs (Figure 7.11A) that define the free energy barriers for the processes of influx ($\Delta G_{inf}^{\ddagger}$) and efflux ($\Delta G_{eff}^{\ddagger}$) of the drugs (see Table 6.5).

Table 6.5 - Free energy barriers for the efflux ($\Delta G^{\ddagger}_{eff}$) and influx ($\Delta G^{\ddagger}_{inf}$) processes of the three Pt(II)-based drugs (cddp, cpx, and oxa) and the cisplatin derivatives (cdcla and cdclo) through the breast cancer cell membrane (c_memb).

System	$\Delta G^{\ddagger}_{eff}$ / kcal mol^{-1} [a]	$\Delta G^{\ddagger}_{inf}$/ kcal mol^{-1} [b]
cddp>c_memb	28.6 ± 0.1	28.0 ± 0.1
cdcla>c_memb	35.2 ± 0.1	34.2 ± 0.1
cdclo>c_memb	31.2 ± 0.1	35.6 ± 0.1
cpx>c_memb	32.6 ± 0.08	31.7 ± 0.1
oxa>c_memb	28.9 ± 0.1	31.9 ± 0.1

[a]The values were derived from the potential of mean force (PMF) as the energy difference between the peak and the valleyat ~15 Å. [b]The values were derived from the PMF as the energy difference between the peak and the valley at ~52 Å. The notations cdcla and cdclo represent the *cis*-$[Pt(NH_3)_2(H_2O)Cl]^+$ and *cis*-$[Pt(NH_3)_2Cl(OH)]$.
Reference: Own author (2023).

In general, data from Table 6.5 reveal that the energetic barriers for the efflux processes of the platinum drugs are greater than the ones involving the influx processes. While the difference between the efflux and influx barriers for cddp is 0.6 kcal mol^{-1}, the same difference for cpx and oxa is 0.9 kcal mol^{-1} and -3.0 kcal mol^{-1}. Therefore, the expulsion of drugs from the intracellular medium is, on average, less spontaneous via non-facilitated (passive) diffusion than the drug uptake event, except for the oxa derivative.

Among the drugs, we notice that influx of cpx and oxa through the membrane required the highest energy (~32 kcal mol^{-1}) evidencing a difference with cddp of about 4 kcal mol^{-1}. These differences should be mainly due to the size of the molecules. The cpx and oxa molecules are much bigger than cddp one. The lipophilicity may also play a role on the diffusion through the lipid tails, as the partition coefficients (logP) differ significantly: cddp (logP = -2.19), cpx (logP = -0.46), and oxa (logP = -1.6) (ORIYAMA, *et al*., 2020).

By studying the uptake processes of cddp, cpx, and oxa through a normal membrane model, Rivel (RIVEL, *et al.*, 2019; RIVEL, 2020) obtained energy barriers of 16.7 kcal mol^{-1}, 26.8 kcal mol^{-1}, and 26.3 kcal mol^{-1}, respectively. Although these barriers cannot be directly compared to our results due to the differences in terms of systems, force fields, and simulation details, we can verify similar trends, such as the highest energy barriers for the bigger and lipophilic drugs (cpx and oxa). Most importantly, the barriers reported by us and Rivel (RIVEL, 2020) emphasize the relevance of realistic membrane prototypes for properly describe the PMFs referring to drug permeation. Lastly, the consistency of the PMFs is confirmed not only by the

negligible errors in the range of 0.4%, but also by the efficient sampling of the reaction coordinate with the overlap of the histograms of configuration (see Figure D.10-D11).

When it comes to cddp, the extracellular and intracellular media induce the hydrolysis of this drug to different extents with the consequent formation of charged species. At the extracellular medium, which is an acidic region (LEE & SHANTI, 2021) around the position at 70 Å in Figure 6.11B, the mathematical model reported by Yotsuyanagi and coworkers (YOTSUYANAGI, *et al*., 2002) predicts an equilibrium formed by 89% of cddp, 8% of cdclo, and 3% of cdcla (see Figure 7.1). The deeper potential wells for cdcla and cdclo in Fig. 11B demonstrates that the interactions of these species with the polar heads of the membrane are stronger than the ones involving the major species (cddp) in this region. For instance, the difference (influx) in terms of potential well depth between cdcla and cddp was -5.9 kcal mol^{-1}, whereas the same difference between cdclo and cddp was -10.2 kcal mol^{-1}. This behavior reveals a more polar character of these minor species compared to cddp, thereby suggesting a low tendency to permeate the membrane. In fact, Table 6.5 shows that the energy barriers for the uptake of cdcla and cdclo are increased by 6.3 kcal mol^{-1} and 7.6 kcal mol^{-1} in comparison to the cddp influx. The neutral form of cddp is therefore the most likely species to permeate the membrane from the extracellular medium of a breast cancer cell.

At last, in the alkaline intracellular medium with low Cl^- concentration (LEE & SHANTI, 2021), which is represented by the reservoir around the position at 0 Å in Figure 6.11B, cddp (44%) may coexist mainly with cdcla (24%) and cdclo (30%) according to the work of Yotsuyanagi and colleagues (YOTSUYANAGI, *et al*., 2002). Thus, after the influx process (~20 Å in Figure 6.11B), the cddp can form these derivatives, which establish, in turn, strong interactions with the polar region of the inner leaflet of the membrane as well as we noticed in the outer leaflet. Interestingly, the decrease of the energy barrier for the efflux ($\Delta G^{\ddagger}_{eff}$) of cdclo by 4.4 kcal mol^{-1} compared to its influx barrier ($\Delta G^{\ddagger}_{inf}$) suggests that the expulsion of this mono-hydroxo derivative from a breast cancer cell is more favorable than its cellular uptake. Nonetheless, the efflux of cddp is still the most likely process among the species in the intracellular medium

6.3.6 Diffusivity, resistivity, and permeability of the Pt(II) drugs

In order to calculate the permeability coefficients (*P*) of the platinum drugs, we used the PMF data ($\Delta G(z)$ in eq. 6.2) obtained in the previous section and computed the local diffusion

coefficients (*D(z)*) and the local resistance (*R(z)*) for the translocation of the molecules through the c_memb according to eq. 6.2-6.4. The *D(z)* profiles are presented in Figure 6.12, where it is possible to observe a decrease by about one order of magnitude referring to the diffusivity of the metallodrugs during their permeation across the membrane from the bulk solvent, as we can also see in Table 6.6.

This diffusivity drop of permeants in membranes is expected due to the high steric hindrance along the reaction coordinate, which is also dependent on both size and polarity of these molecules (AWOONOR-WILLIAMS & ROWLEY, 2016; VENABLE, *et al*., 2019). Regarding the platinum drugs (Figure 6.12A), data from Table 6.6 show that cddp has the highest diffusivity in water, whereas cpx has the highest diffusivity in the lipid tails region and oxa has the lowest *D(z)* in both water and lipids.

Since there is a tendency to larger molecules to present low diffusivities, (AWOONOR-WILLIAMS & ROWLEY, 2016), the highest molecular size of oxa and cpx may be the main factor for the lowest mobility in both water and membrane. The profiles in Figure 6.12A also display notable oscillations when the drugs cross the lipid-water interface, which may demonstrate the structural reorganization of these molecules after the transfer of media. The comparison of *D(z)* in aqueous solution with the experimental values (see Table 6.6) reinforces the accuracy of the data obtained in the present work, since they are in the same order of magnitude with an average difference of 22%. Finally, when it comes to cddp and its hydrolyzed species (cdcla and cdclo), data from Figure 6.12B and Table 6.6 indicate that the neutral form (cddp) has the highest diffusivity in both aqueous and lipid phases.

As expected, the *D(z)* of cdcla and cdclo is greater in water than in the lipid tails due to the unrestricted mobility in the physiological media. Besides, the strong interaction between cdclo and the polar heads of the membrane, which was evidenced by the potential wells in the PMF (see Figure 6.11B), may be connected to the decrease of 13% and 50% in its diffusivity (in aqueous solution) in comparison with cdcla and cddp, respectively. The more hydrophilic character of cdclo may have reduced the diffusion of this species at the hydrophobic center of the biomembrane.

Figure 6.12 - Local diffusion coefficient (D(z)) profiles of the Pt(II)-based drugs (cisplatin (cddp), carboplatin (cpx), and oxaliplatin (oxa)) and the hydrolyzed species of cddp (mono-aqua derivative (cdcla), and the mono-hydroxo derivative (cdclo)) referring to their translocation through the breast cancer cell membrane (c_memb): cddp>c_memb, cpx>c_memb, and oxa>c_memb (A), and cddp>c_memb, cdcla>c_memb, and cdclo>c_memb (B). The reaction coordinate was defined as the z axis perpendicular to the membrane plane considering the distance between 0 Å and 70 Å, where 0 Å represents the intracellular medium and 70 Å represents the extracellular medium.

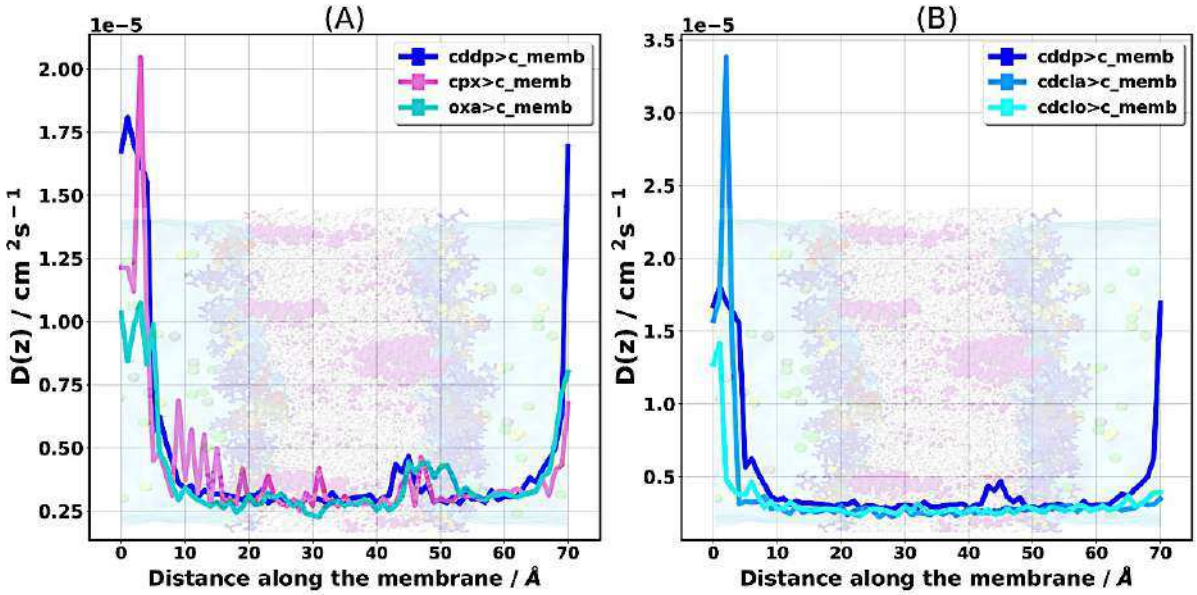

Reference: Own author (2023).

The *R(z)* profiles are presented in Figure D.12-D.13 while the the values of effective resistance (R_{eff}, see eq. 6.2) are organized in Table 6.7. These plots have in common a peak that is located at the center of the membrane (at ~35 Å) among the lipid tails, thereby indicating the most resistive region of the c_memb for the translocation of the platinum drugs. Based on eq. 6.2, the graphical representation of *R(z)* data (Figure D.12-D.13) reproduces the high energy barriers demonstrated in the PMFs (Figure 6.11), which are amplified due to the exponential relationship between R(z) and $\Delta G(z)$. In particular, the plot of *R(z)* referring to cddp is in agreement with the profiles reported in the literature (RIVEL, *et al.*, 2019; YESYLEVSKYY, *et al*., 2019). With regard to the R_{eff}, it is possible to notice that the cddp diffusion through the membrane is the least resistive process among the Pt(II)-based drugs, whereas the translocation of cpx presents the highest resistance.

Table 6.6 - Local diffusion coefficients (D(z)) of cisplatin (cddp), carboplatin (cpx), oxaliplatin (oxa), mono-aqua derivative (cdcla) of cddp, and mono-hydroxo derivative (cdclo) of cddp referring to their translocation through the breast cancer cell membrane (c_memb).

System	$D(z)$ ± std / cm s^{-1} [a]	$D(z)$ ± std / cm s^{-1} [b]
	lipid tails ($z = 35$Å)	water ($z = (0$Å $+ 70$Å$)/2$)
cddp	$(2.907\pm0.003)\cdot10^{-6}$	$(1.6838\pm0.0004)\cdot10^{-5}$
		$(2.3\cdot10^{-5})$ [c]
cdcla	$(2.635\pm0.004)\cdot10^{-6}$	$(9.602\pm0.003)\cdot10^{-6}$
cdclo	$(2.558\pm0.004)\cdot10^{-6}$	$(8.337\pm0.004)\cdot10^{-6}$
cpx	$(3.096\pm0.004)\cdot10^{-6}$	$(9.453\pm0.004)\cdot10^{-6}$
		$(7.8\cdot10^{-5})$ [d]
oxa	$(2.695\pm0.003)\cdot10^{-6}$	$(9.170\pm0.004)\cdot10^{-6}$
		$(8.2\cdot10^{-5})$ [e]

[a]Local diffusion coefficient at the center of the membrane, which refers to the position at z = 35 Å along the reaction coordinate. [b]Local diffusion coefficient at the aqueous phase, which refers to the position at z = 0 Å (intracellular medium) and z = 70 Å (extracellular medium) along the reaction coordinate. The term std denotes the standard deviation value. [c]Experimental value for cddp (see ref.: PANCZYK, *et al*., 2013)). [d]Experimental value for cpx (see ref.: PAMPEL, *et al*., 2002). [e]Estimate for oxa (see ref.: KOMEN, *et al*., 2020).
Reference: Own author (2023).

Specifically, the R_{eff} of cpx is about three orders of magnitude higher than the one of cddp and two orders of magnitude higher than the one of oxa (Table 6.7). This result is connected to the highest energy barrier (~32.2 kcal mol^{-1}) for the diffusion of cpx compared to the other drugs (see Table 6.5). Although the value of R_{eff} for cddp cannot be properly compared to our result (Table 6.7) and the result of Rivel and coworkers (RIVEL, *et al.*, 2019) due the differences related to the membrane model, force field and simulation details, the difference of one order of magnitude suggests that our c_memb prototype is more resistive to the permeation of cddp than the model reported by those authors. Finally, the reduced R_{eff} for cdclo, which is two orders of magnitude smaller than the ones for cdcla and cddp, may be related to the strong interaction of this species with the polar region of the membrane (see the potential wells in Figure 6.11) that contributes to the reduction of the *R(z)* values. Additionally, the reduced R_{eff} for cdclo in contrast to the one of cdcla may be explained by the lower energy barrier referring to the cdclo translocation in comparison to the one involving the hydrolyzed derivative of cddp (Table 6.5).

Table 6.7 - Values of the effective resistance (R_{eff}) and permeability coefficient (P) of the Pt(II)-based drugs (cddp, cpx, and oxa) and the hydrolyzed species of cddp (cdcla and cdclo) calculated from the simulations referring to their permeation through the breast cancer cell membrane (c_memb) model at 310 K and 1 bar.

System	R_{eff} / s cm^{-1}	P / cm s^{-1}
cddp>c_memb	$(4.1 \pm 0.3)\cdot10^{11}$	$(2.5 \pm 0.2)\cdot10^{-12}$
	$(6.3 \pm 0.2)\cdot10^{10}$ [a]	$(1.59 \pm 0.06)\cdot10^{-11}$ [a]
		$6.57\text{x}10^{-9}$ [b]
cdcla>c_memb	$(5.4 \pm 0.6)\cdot10^{11}$	$(1.8 \pm 0.2)\cdot10^{-12}$
cdclo>c_memb	$(3.9 \pm 0.4)\cdot10^{9}$	$(2.6 \pm 0.3)\cdot10^{-10}$
cpx>c_memb	$(4.0 \pm 0.5)\cdot10^{14}$	$(2.5 \pm 0.3)\cdot10^{-15}$
		$7.91\text{x}10^{-18}$ [c]
		$4.47\text{x}10^{-8}$ [b]
oxa>c_memb	$(1.6 \pm 0.2)\cdot10^{12}$	$(6.2 \pm 0.7)\cdot10^{-13}$
		$2.62\text{x}10^{-20}$ [c]
		$3.75\text{x}10^{-8}$ [b]

[a]Values for a cancer cell membrane model at 320 K, 1 atm using the NPT ensemble (see ref. 28). [b]Estimated values from a kinetic model for a spherical cell involving *in vitro* data (see ref.: RIVEL, *et al*., 2019). [c]Values for a normal cell membrane at 320 K, 1 atm using the NPT ensemble (see ref.: RIVEL, 2020).
Reference: Own author (2023).

At last, Table 6.7 shows that the cddp has the highest *P* with a difference by a factor of three orders of magnitude with cpx and one order of magnitude with oxa. Since the permeation rate is correlated with the free energy barriers for the drug translocation (Table 6.5) (LEE, *et al.*, 2016), so that high energy barriers of permeation reduce the *P* of molecules, the highest *P* for cddp indicates that its transmembrane transport is the fastest event among these metallodrugs. Conversely, the notable lipophilic character of cpx and its large size (logP=-0.46) (ORIYAMA, *et al*., 2020) may be the main factors responsible by its slowest permeability across the c_memb model, as evidenced by its high diffusion energy barrier (~32.2 kcal mol^{-1}, Table 6.5). In Table 6.7, we also present other estimates of *P* for the different platinum drugs, which cannot be directly compared to our results due to the differences related to models and simulation details. For instance, the permeability rate of cddp calculated in this work is about one order of magnitude smaller than the one reported by Rivel and coworkers (RIVEL, *et al.*,

2019; YESYLEVSKYY, *et al*., 2019). This difference is amplified if we compare our result (*P* of cddp) with the one referring to the kinetic model proposed by those authors. Overall, our result reproduces the low permeable character of cddp in cells (ZHANG, *et al*., 2020; YIN, *et al*., 2016).

Concerning the cpx and oxa drugs, data from Table 6.7 indicate that our membrane is more permeable to these anticancer molecules than the biomembrane models reported by Rivel and coworkers (RIVEL, *et al.*, 2019; YESYLEVSKYY, *et al*., 2019). While the values of *P* for cpx obtained in our work is three orders of magnitude higher than the one of these authors, the *P* value for oxa obtained herein is seven orders of magnitude higher than the one reported by the same authors.

With regard to the hydrolyzed species of cddp, it is possible to notice in Table 6.7 that the charged derivative (cdcla) would have the slowest permeation rate through the c_memb with a difference of 25.2% relative to cddp and 99.3% relative to cdclo. This unfavorable kinetics is connected to the high energy barrier (on average 35 kcal mol^{-1}) for the translocation process of this charged species (cdcla).

6.4 CONCLUSIONS

The platinum drugs (cddp, cpx, and oxa) are included in about half of the chemotherapies currently administered for the treatment of a serie of cancers, including the breast cancer. Despite their popularity and efficiency, the low specificity for cancer cells leads to serious side effects, which limit their prescription. Therefore, a deeper understanding of the cellular uptake of these drugs at a molecular level has been an important topic of study to optimize their chemotherapies. Herein, we investigate the translocation mechanisms (influx and efflux) of the Pt(II)-based drugs through a realistic membrane model of a breast cancer cell (c_memb), which considers the asymmetry referring to the ionic concentration between the intracellular and extracellular media, by means of biased MD simulations. Regarding the lipid-drug interactions, both influx and efflux processes were mainly mediated by neutral lipids (DOPC, DOPE and CHL), thereby indicating unfavorable interactions with the anionic species. The PMFs highlighted the spontaneity of the drug insertion in the region of polar heads of the membrane, which indicates a favorable uptake in cancer cells, especially for cddp and oxa. However, the permeation process through the lipid tails involved high energy barriers which were dependent of both size and lipophilic character of the drugs. The energy barrier for cpx was the highest (~32 kcal mol^{-1}) among the series studied. The PMFs also demonstrated strong

interactions between the hydrolyzed species of cddp (cdcla and cdclo) and the polar region of the c_memb in contrast to unfavorable interactions with the lipid tails, which reinforced their low tendency to a complete permeation, especially for the charged derivative, for which the barrier was ~35 kcal mol^{-1}. The diffusivity along the c_memb was also modulated by size and polarity of these drugs, so that the reduced size and lipophilicity of cddp facilitated its mobility in the aqueous and organic phases of the membrane.

Finally, the high energy barriers for the permeation of both cpx and oxa reduced their permeation rates across the c_memb, with differences relative to the *P* (cm s^{-1}) of cddp in the range of three and one orders of magnitude, respectively. The results presented herein provide a more realistic characterization referring to the cellular uptake of the platinum drugs in breast cancer cells, which may be relevant not only to understand the mechanisms of tumor resistance and toxicity, but also to the design of more efficient analogues. Future studies should evaluate the facilitate diffusion of these drugs by the application of electric fields in order to improve the permeability and, in turn, the efficiency of these chemotherapies.

In view of the high energy barriers, our studies open the way to another possible way for the chemotherapeutics uptake through the membrane via, for instance, a passive diffusion inside specific ionic channel. Indeed, the important modification of the energy path for hydrolyzed platinum drugs may influence strongly the interaction with these ionic channels, facilitating their diffusion through them. This will be studied in our future simulations.

REFERENCES

AHMAD, S. Kinetics aspects of platinum anticancer agents. **Polyhedron**, v. 138, p. 109-124, 2017.

ALMEIDA, E. R.; DOS SANTOS, H. F.; CAPRILES, P. V. S. Z. Carbon nanohorns as nanocontainers for cisplatin: insight into their interaction with the plasma membranes of normal and breast cancer cells. **Physical Chemistry Chemical Physics**, v. 23, p. 16376-16389, 2021.

ALMEIDA, E. R.; CAPRILES, P. V. S. Z.; DOS SANTOS, H. F. Unveiling the Releasing Processes of Pt(II)-Based Anticancer Drugs from Oxidized Carbon Nanohorn: An In Silico Study. **Journal of Physical Chemistry B**, v. 126, n. 23, 2022.

AMARA, S.; *et al*. Sodium channel γENaC mediates IL-17 synergized high salt induced inflammatory stress in breast cancer cells. Cellular Immunology, v. 302, p. 1-10, 2015.

ANTHONY, E. J.; *et al*. Metallodrugs are unique: opportunities and challenges of discovery

and development. **Chemical Science**, v. 11, p. 12888-12919, 2020.

ARNESANO, F.; LOSACCO, M.; NATILE, G. An Updated View of Cisplatin Transport. **European Journal of Inorganic Chemistry**, v. 2013, p. 2701-2711, 2013.

ARNOLD, M.; *et al*. Current and future burden of breast cancer: Global statistics for 2020 and 2040. **The Breast**, v. 66, p. 15-23, 2022.

AWOONOR-WILLIAMS, E. & ROWLEY, C. N. Molecular simulation of nonfacilitated membrane permeation. **Biochimica Biophysical Acta**, v. 1858, n. 7, p. 1672-1687, 2016.

BERENDSEN, H. J. C.; *et al*. Molecular dynamics with coupling to an external bath. **Journal of Chemical Physics**, v. 81, p. 3684-3690, 1984.

BERNADES, N. & FIALHO, A. M. Perturbing the Dynamics and Organization of Cell Membrane Components: A New Paradigm for Cancer-Targeted Therapies. **International Journal of Molecular Science**, v. 19, p. 1-19, 2018.

BOUBETA, F. M.; *et al*. Lessons learned about steered molecular dynamics simulations and free energy calculations. **Chemical Biology & Drug Design**, v. 93, p. 1-10, 2019.

BRENEMAN, C. M. & WIBERG, K. B. Determining atom-centered monopoles from molecular electrostatic potentials. The need for high sampling density in formamide conformational analysis. **Journal of Computational Chemistry**, v. 11, n. 3, 1990.

CANCÈS, E.; MENNUCCI, B.; TOMASI, B. M. J. A new integral equation formalism for the polarizable continuum model: theoretical background and applications to isotropic and anisotropic dielectrics. **Journal of Chemical Physics**, v.107, p. 3032-3041, 1997.

CÁRDENAS, G.; *et al*. Characterization of cisplatin/membrane interactions by QM/MM energy decomposition analysis. **Physical Chemistry Chemical Physics**., v. 23, p. 20533-20540, 2021.

CASE, D. A.; *et al.* AMBER 2019, University of California, San Francisco, 2019.

CASE, D. A.; *et al.* AMBER 2020, University of California, San Francisco, 2020.

CHOE, S. Molecular dynamics studies of interactions between Arg_9(nona-arginine) and a DOPC/DOPG(4:1) membrane. **AIP Advances**, v. 10, p. 1-12, 2020.

DICKSON, C. J.; *et al.* Lipid14: The Amber Lipid Force Field. **Journal of Chemical Theory and Computation**, v. 10, n. 2, p. 865-879, 2014.

EFRON, B. & TIBSHIRANI, R. J. **An introduction to the Bootstrap**, Chapman and Hall/CRC, New York, 1st edn, 1994.

EIL, R.; *et al*. Ionic immune suppression within the tumour microenvironment limits T cell effector function. **Nature**, v. 537, n. 7621, p. 539-543, 2016.

FENG, Y.; *et al*. Breast cancer development and progression: risk factors, cancer stem cells, signaling pathways, genomics, and molecular pathogenesis. **Genes & Diseases**, v. 5, n. 2, p. 77-106, 2018.

FRISCH, M. J.; *et al*. Gaussian 09, revisão D.01.; Gaussian, Inc.: Wallingford, CT, 2009.

GARUTTI, M.; *et al*. Platinum Salts in Patients with Breast Cancer: A Focus on Predictive Factors. **International Journal of Molecular Sciences**, v. 20, n. 14, p. 3390-3405, 2019.

GÖTZ, A. W.; *et al*. Routine Microsecond Molecular Dynamics Simulations with AMBER on GPUs. 1. Generalized Born. **Journal of Chemical Theory and Computation**, v. 8, n. 5, p. 1542-1555, 2012.

GROSSFIELD, A. WHAM: Weighted Histogram Analysis Method for Analyzing Umbrella Sampling Simulation Data, version 2.0.10.1. Available online: http://membrane.urmc.rochester.edu/wordpress/?page_id=126 (accessed on 04/06/2023).

HAY, P. J. & WADT, W. R. Ab initio effective core potentials for molecular calculations. Potentials for K to Au including the outermost core orbitals. **Journal of Chemical Physics**, v. 82, p. 299-310, 1985.

HEHRE, W. L.; DITCHFIELD, R.; POPLE, J. A. Self-Consistent Molecular Orbital Methods. XII. Further Extensions of Gaussian—Type Basis Sets for Use in Molecular Orbital Studies of Organic Molecules. **Journal of Chemical Physics**, v. 56, p. 2257-2261, 1972.

HUMMER, G. Position-dependent diffusion coefficients and free energies from Bayesian analysis of equilibrium and replica molecular dynamics simulations. **New Journal of Physics**, v, 7, p. 1-14, 2005.

JENSEN, F. **Introduction to Computational Chemistry**, John Wiley & Sons, 2nd edition, Chichester, UK, 2007

JO, S.; *et al*. CHARMM-GUI: A web-based graphical user interface for CHARMM. **Journal of Computational Chemistry**, v. 29, n. 11, p. 1859-1865, 2008.

JORGENSEN, W. L.; *et al*. Comparison of Simple Potential Functions for Simulating Liquid Water. **The Journal of Chemical Physics**, v. 79, p. 926-935, 1983.

JOUNG, I. S. & CHEATHAM III, T. E. Determination of Alkali and Halide Monovalent Ion Parameters for Use in Explicitly Solvated Biomolecular Simulations. Journal of Physical Chemistry B, v. 112, n. 30, p. 9020-9041, 2008.

KÄSTNER, J. Umbrella Sampling. **WIREs Computational Molecular Science**, v. 1, p.932-942, 2011.

KERR, A. J.; *et al*. Adjuvant and neoadjuvant breast cancer treatments: A systematic review of their effects on mortality. **Cancer Treatment Reviews**, v. 105, p. 102375-102387, 2022.

KHOURY, A.; *et al*. Recent advances in platinum-based chemotherapeutics that exhibit inhibitory and targeted mechanisms of action. **Journal of Inorganic Biochemistry**, v. 207, p. 111070-111088, 2020.

KOMEN, J.; *et al*. Controlled pharmacokinetic anti-cancer drug concentration profiles lead to growth inhibition of colorectal cancer cells in a microfluidic device. **Lab on a Chip**, v. 20, n. 17, p. 3167-3178, 2020.

KUMAR, S.; *et al.* The weighted histogram analysis method for free-energy calculations on biomolecules. I. The method. **Journal of Computational Chemistry**, v. 13, n. 8, p. 1011-1021, 1992.

KUMAR, S.; *et al.* Multidimensional free-energy calculations using the weighted histogram analysis method. **Journal of Computational Chemistry**, v. 16, n. 11, p. 1339-1350, 1995.

LEE, S. J.; SONG, Y.; BAKER, N. A. Double Bilayers and Transmembrane Gradients: A Molecular Dynamics Study of a Highly Charged Peptide. **Biophysical Journal**, v. 94, p. 3565-3576, 2008.

LEE, A. V.; OESTERREICH, S.; DAVIDSON, N. MCF-7 cells--changing the course of breast cancer research and care for 45 years. **Journal of National Cancer Institute**, v. 107, p. 1-4, 2015.

LEE, C. T.; *et al.* Simulation-Based Approaches for Determining Membrane Permeability of Small Compounds. **Journal of Chemical Information and Modeling**, v. 56, n. 4, p. 721-733, 2016.

LEE, J.; *et al*. CHARMM-GUI supports the Amber force fields. **The Journal of Chemical Physics,** v. 153, n. 3, p. 1-9, 2020.

LEE, S. & SHANTI, A. A. Effect of Exogenous pH on Cell Growth of Breast Cancer Cells. **International Journal of Molecular Sciences**, v. 22, p. 1-12, 2021.

LE GRAND, S.; GÖTZ, A. W.; WALKER, R. C. SPFP: Speed without compromise—A mixed precision model for GPU accelerated molecular dynamics simulations. **Computer Physics and Communications**, v. 184, p. 374-380, 2013.

LI, P. & MERZ JR, K. M. Taking into Account the Ion-Induced Dipole Interaction in the Nonbonded Model of Ions. **Journal of Chemical Theory and Computation**, v. 10, n. 1, p. 289-297, 2014.

LOPES, J. F.; *et al.* Theoretical study of the potential energy surface for the interaction of cisplatin and their aquated species with water. **Journal of Chemical Physical**, p. 128, n. 16, p. 16510-165117, 2008.

LUCAS, M. F. A.; *et al*. Neutral and Acidic Hydrolysis Reactions of the Third Generation Anticancer Drug Oxaliplatin. **The Journal of Physical Chemistry B**, v. 113, p. 831-838, 2009.

LUKASIEWICZ, S.; *et al*. A. Breast Cancer-Epidemiology, Risk Factors, Classification, Prognostic Markers, and Current Treatment Strategies-An Updated Review. **Cancers**, v. 13, n. 17, p. 1-30, 2021.

MAJED, B. D.; GOULD, I. R.; WALKER, R. C. A Parameterization of Cholesterol for Mixed Lipid Bilayer Simulation within the Amber Lipid14 Force Field. **Journal of Physical Chemistry B**, v. 119, n. 38, p. 12424-12435, 2015.

MARRINK, S. J. & BERENDSEN, H. J. C. Permeation Process of Small Molecules across Lipid Membranes Studied by Molecular Dynamics Simulations. **Journal of Physical Chemistry**, v. 100, n. 41, p. 16729-16738, 1996.

MARTÍNEZ, L.; *et al*. PACKMOL: a package for building initial configurations for molecular dynamics simulations. **Journal of Computational Chemistry**, v. 30, n. 12, p. 2157-2164, 2009.

MARTINHO, N.; *et al*. Cisplatin-Membrane Interactions and Their Influence on Platinum Complexes Activity and Toxicity. **Frontiers in physiology**, v. 9, p. 1-15, 2018.

MØLLER, C. & PLESSET, M. S. Note on an Approximation Treatment for Many-Electron Systems. **Physical Reviews**, v. 46, p. 618-622, 1934.

NIERZWICK, L.; *et al*. Interaction of cisplatin and two potential antitumoral platinum(ii) complexes with a model lipid membrane: a combined NMR and MD study. **Phys. Chem. Chem. Phys.**, v. 17, p. 1458-1468, 2015.

OBRESHKOVA, D.; IVANOVA, S.; YORDANOVA-LALEVA, P. Influence of chemical structure and mechanism of hydrolysis on pharmacological activity and toxicological profile of approved platinum drugs. **Pharmacia**, v. 69, p. 645-653, 2022.

ORIYAMA, T.; et al. Prediction of the permeability of antineoplastic agents through nitrile medical gloves by zone classification based on their physicochemical properties. **Journal of Pharmaceutical Health Care and Sciences**, v. 6, n. 23, p. 1-10, 2020.

PAMPEL, A.; MICHEL, D.; RESZKA, R. Pulsed field gradient MAS-NMR studies of the mobility of carboplatin in cubic liquid-crystalline phases. **Chemical Physics Letters**, 2002, v. 357 n. 1-2, p. 131-136, 2002.

PANCZYK, T.; *et al*. Molecular dynamics study of cisplatin release from carbon nanotubes capped by magnetic nanoparticles. **Journal of Physical Chemistry C**, v.117, n. 33, p. 17327-17336, 2013.

PAVELKA, M.; LUCAS, M. F. A.; RUSSO, N. On the hydrolysis mechanism of the second-generation anticancer drug carboplatin. **Chemistry: A European Journal**, v. 13, p. 10108-10116, 2007.

PEREIRA, M.; *et al*. Inhibitory effects of extracellular Mg^{2+} on intracellular Ca^{2+} dynamic changes and thapsigargin-induced apoptosis in human cancer MCF7 cells. **Molecular and Cellular Biochemistry**, v. 229, p. 163-171, 2002.

ROUX. B. The calculation of the potential of mean force using computer simulations. **Computer Physics Communications**, v. 91, n. 1-3, p. 275-282, 1995.

RIVEL, T.; RAMSEYER, C.; YESYLEVSKYY, S. The asymmetry of plasma membranes and their cholesterol content influence the uptake of cisplatin. **Scientific Reports**, v. 9, p. 1-14, 2019.

RIVEL, T. **Simulation numérique de l'interaction de sels de platine avec membranes lipidiques asymétriques**. 2020. Ph.D. thesis. Université Bourgogne Franche-Comté, Université de Franche-Comté, Besançon, 2020.

RYCKAERT, J. P.; CICCOTTI, G.; BERENDSEN, H. J. C. Numerical integration of the Cartesian equations of motion of a system with constraints: molecular dynamics of n-alkanes. **Journal of Computational Physics**, v. 23, n. 3, p. 327-341, 1977.

RUANO, L.; CÁRDENAS, G.; NOGUEIRA, J. J. The Permeation Mechanism of Cisplatin Through a Dioleoylphosphocholine Bilayer. **ChemPhyChem**. v. 22, p. 1251-1261, 2021.

RUSESKA, I. & ZIMMER, A. A. Internalization mechanisms of cell-penetrating peptides. **Beilstein Journal of Nanotechnology**, v. 11, p. 101-123, 2020.

SALOMON-FERRER, *et al*. Routine Microsecond Molecular Dynamics Simulations with AMBER on GPUs. 2. Explicit Solvent Particle Mesh Ewald. **Journal of Chemical Theory Computational**, v. 9, p. 3878-3888, 2013.

SAMSON, M. S. O. & BIGGIN, P. C. Molecular Simulations and Biomembranes: From Biophysics to Function. **RSC Biomolecular Sciences**, v. 20, 2010.

SANTANA, L. C. **Desenvolvimento de Parâmetros Intermoleculares para o Estudo de Carboplatina e Oxaliplatina em Solução Aquosa**. 2019. Master's dissertation. Universidade Federal de Itajubá, 2019.

SCHOCH, S.; *et al*. Comparative study of the mode of action of clinically approved platinum-based chemotherapeutics. **International Journal of Molecular Sciences**, v. 21, p. 6928-6949, 2020.

SOULE, H. D.; *et al*. A human cell line from a pleural effusion derived from a breast carcinoma. **Journal of National Cancer Institute**, v. 51, p. 1409-1416, 1973.

SZLASA, W.; *et al*. Lipid composition of the cancer cell membrane. **Journal of Bioenergetics and Biomembranes**, v. 52, p. 321-342, 2020.

TODOR, I. N.; LUKYANOVA, N. Y.; CHEKHUN, V. F. The lipid content of cisplatin- and doxorubicinresistant MCF-7 human breast cancer cells. **Experimental Oncology**, v. 34, n. 2, p. 97-100, 2012.

UBERUAGA, B. P.; ANGHEL, M.; VOTER, A. F. Synchronization of trajectories in canonical molecular-dynamics simulations: observation, explanation, and exploitation. **Journal of Chemical Physics**, v. 120, n. 14, p. 6363-6374, 2004.

VENABLE, R. M.; KRÄMER, A.; PASTOR, R. W. Molecular dynamics simulation of membrane permeability. **Chemical Reviews**, v. 119, p. 5954-5997, 2019.

WANG, J.; *et al*. Development and testing of a general amber force field. **Journal of Computational Chemistr**y, v. 25, n. 9, p. 1157-1174, 2004.

YESYLEVSKYY, S.; *et al*. Empirical force field for cisplatin based on quantum dynamics data: case study of new parameterization scheme for coordination compounds. **Journal of Molecular Modeling**, v. 21, p. 1-9, 2015.

YESYLEVSKYY, S. RIVEL, T.; RAMSEYER, C. Curvature increases permeability of the plasma membrane for ions, water and the anti-cancer drugs cisplatin and gemcitabine. **Scientific Reports**, v. 9, p. 1-8, 2019.

YIN, S.; *et al.* Nanosecond pulsed electric field (nsPEF) enhance cytotoxicity of cisplatin to hepatocellular cells by microdomain disruption on plasma membrane. **Experimental Cell Research**, v. 346 n. 2, p. 233-240, 2016.

YOTSUYANAGI, T.; *et al*. Computational consideration of cisplatin hydrolysis and acid dissociation in aqueous media: effect of total drug concentrations. **International Journal of Pharmaceutics**, v. 246, n. 1-2, p. 95-104, 2002.

ZHANG, L.; *et al*. Cisplatin under oriented external electric fields: A deeper insight into electrochemotherapy at the molecular level. **International Journal of Quantum Chemistry**, v. 121 n. 8, p. 1-9, 2020.

ZHANG, C.; *et al*. Platinum-based drugs for cancer therapy and anti-tumor strategies. **Theranostics**, v. 12, n. 5, p. 2115-2133, 2022.

ZHENG, S.; *et al*. VFFDT: a new software for preparing AMBER force field parameters for metal-containing molecular systems. **Journal of Chemical Information and Modeling**, v. 56, p. 811-818, 2016.

ZHOU, J.; *et al*. The Drug-Resistance Mechanisms of Five Platinum-Based Antitumor Agents. **Frontiers in Pharmacology**, v. 11, p. 1-17, 2020.

7 CHAPTER 7

Concluding remarks

7.1 GENERAL CONCLUSIONS

In this thesis, the key aspects of the interaction mechanism between CNHs, as nanovectors of the platinum drugs, and plasma membranes were elucidated by means of MD simulations in different approaches. The use of unbiased and biased simulations based on enhanced sampling methods provided the characterization of the dynamics and the free energy profile referring to the interaction of this class of carbon nanocarriers with cell membranes. In order to conduct the analyzes of this work, models of CNHs and their complexes with platinum drugs were developed by taking into account the main aspects resulting from the chemical modification processes applied to these carbon nanomaterials, such as the inclusion of polar functional groups and the nanowindows. These aspects were collected from the experimental studies involving synthesis, functionalization and characterization of CNHs. Moreover, this thesis involved the building of realistic prototypes of cell membranes referring to the human breast (considering cancer and normal cells). These models included both the distribution and concentration of lipids and ions experimentally reported for these cells. In view of the work developed in this thesis, the following conclusions could be drawn:

a) in chapter 3, the simulations of the complex 3cddp@CNHox in aqueous solution with models of a breast cancer cell membrane (C_memb) and a normal cell membrane (N_memb) revealed, at the molecular level, the mechanism of interaction of this nanovector with plasma membranes of the human breast. The mechanism was described in four stages: (i) approach, (ii) landing, (iii) insertion, and (iv) penetration. The unbiased simulations demonstrated the spontaneous character of all stages, which were confirmed by the free energy calculations with the MM/GBSA method. These calculations also demonstrated stronger interactions of the 3cddp@CNHox with the C_memb than with the N_membThese results suggest significant effect of the nanoformulation cddp@CNHox in cancer cells. Moreover, the relative decrease of the inclusion complex stability in the region near to the C_memb points out that the cddp release would be more favorable in the tumor microenvironment than in the one referring to a healthy cell. This result reveals that the CNH-based nanocarriers of cddp

are more susceptible to drug release in the breast tumor sites. Despite these promising results of the CNHox, the *in silico* experiments conducted here did not reproduce the drug release from the nanovector and the translocation process through the biomembranes. This behavior suggested the existence of energy barriers which are not characterized by unbiased simulations;

b) the trapping effect of platinum drugs inside CNHs observed in previous section was investigated in chapter 4 using steered molecular dynamics and the umbrella sampling method. The biased simulations confirmed the endergonic character of the drug release from CNHs, which involves free energy barriers for this escape in the order oxa > cpx ~ cddp, with the value for the oxa complex (21-26 kcal mol^{-1}) found to be about 36 and 30% larger than those for cpx and cddp, respectively. While the approximate residence time of the oxa drug inside the CNHox cavity was 5.45×10^8 s, the same measure for the cddp and cpx drugs was 5.3×10^5 and 1.60×10^3 s. In fact, these results evidence that CNHs are able to efficiently protect the drug load from undesirable interactions and side reactions in the physiological medium. This protection is the result of the high stability provided by the nanovectorization, mainly governed by van der Waals interactions. It is possible to speculate that these free energy barriers for drug release may be modified by variating the number of encapsulated drugs inside the CNHs (drug load concentration). Additionally, the chemistry microenvironment of cells may also influence these energy barriers. These *in silico* data also shed light on the application of automatizated therapies, including nanotheranostic based on the application of external stimuli that could provide a controlled released of drugs at the tumor sites;

c) biased molecular dynamics simulations were conducted in chapter 5 aiming to analyze the transmembrane transport of inclusion complexes formed by oxidized and functionalized CNH models loaded with cddp through a breast cancer cell membrane prototype. The simulations revealed four stages in the translocation mechanism: approach, insertion, permeation, and internalization. Despite the lowest structural disturbance to the membrane provided by the nanocarriers, the average free energy barrier of 55.2±3.7 kcal mol^{-1} for their translocation shows that this process is kinetically unfavorable by a passive process. In contrast, the free energy profiles revealed potential wells with an average minimum of -6.8 kcal mol^{-1} along the insertion stage in the polar heads of the membrane; thereby suggesting that the most likely cddp delivery

mechanism should involve the adsorption and retention of CNH on the surface of cancer cells. Thus, the loaded cisplatin should be slowly released and passively transported through the cell membrane. The favorable attachment of this nanocarrier on the surface of cancer cells is in line with *in vitro* analyzes that evidence through optical microscopy images the presence of clusters of CNHs with encapsulated cddp on this cellular region. In spite of the nonspontaneous character of the passive transport of CNHs, the active transport can be applied through the application of external stimuli such as light, ultrasound, heat, and electromagnetic fields, mainly due to the photothermal properties of this carbon nanomaterial;

d) in chapter 6, biased MD were applied to describe the molecular details referring to the translocation processes of the platinum drugs cddp, cpx, and oxa through a membrane prototype that takes into account the lipid composition and the asymmetric saline concentration between intracellular and extracellular media of the human breast cancer cells. The results showed that the permeation events were mainly mediated by neutral lipids (DOPC, DOPE and cholesterol) producing a low and temporary membrane deformation. The drug insertion in the region of polar heads was the most favorable stage of the translocation mechanism, especially for cddp and oxa with potential wells of -8.6 kcal mol^{-1} and -9.8 kcal mol^{-1}, respectively. However, the potentials of mean force revealed an unfavorable kinetics for the permeation of these drugs through lipid tails with energy barriers of 28.3 kcal mol^{-1} for cddp, 32.2 kcal mol^{-1} for cpx, and 30.4 kcal mol^{-1} for oxa. The notable energy barriers for cpx and oxa reflected on their permeability coefficients, which were three and one orders of magnitude superior than for cddp. Overall, the *in silico* experiments highlight the low permeability of the Pt(II)-based drugs through membranes in both influx and efflux processes, which is also in line with the experimental data that reveal that only 5-10% of the administered cddp load reaches the DNA of a cancer cell, thereby resulting in severe side effects and in the development of tumor resistance due to this drug evasion. The use of nanoparticle formulations, such as the encapsulation inside CNHs, is therefore a potential strategy to increase the accumulation of these metallodrugs in tumor sites.

The results reported in this thesis highlight the promising application of chemically modified CNHs as nanovectors of poorly permeable drugs, including the platinum drugs. In addition to show the thermodynamic stability of this nanoformulation, this work demonstrated

the favorable attachment of these system to cancer cell membranes. The potential usefulness of CNHs reported in this thesis also drives the need for further *in silico*, *in vitro*, and *in vivo* investigations in order to advance in the preclinical research of this carbon nanomaterial.

7.2 PROJETS, EVENTS, SCIENTIFIC PRODUCTION

The development of this thesis involved the use of computational resources of the research group *Núcleo de Estudos em Química Computacional* (NEQC-UFJF), and the resources of two supercomputer centers through the submission and approval of two projects derived from the subject of the present thesis. The first one involved the use of a national computing cluster:

2019-2022: Use of the national scientific computing cluster.

Project: *Modelagem da interação de nanomateriais de carbono carreando clusters de fármacos a base Pt(II) com membranas de células normais e tumorais: um estudo por dinâmica molecular. (NanoPtII).*

Computer time allocation: *Laboratório Nacional de Computação Científica (LNCC), Supercomputador Santos Dumont, Brasil.*

Subject: Modeling of inclusion complexes formed by carbon nanohorns as nanocarriers of anticancer Pt(II)-based drugs, plasma membranes of cancer and normal cells of the breast human, molecular dynamics simulations, steered molecular dynamics, and umbrella sampling method.

The second one involved the use of an international computing cluster during the doctoral stay through the *Programa de Doutorado-sanduíche no Exterior (PDSE)* at the *Université de Franche-Comté:*

2022-2023: Doctoral stay of 8 months financed by the Brazilian agency *Coordenação de Aperfeiçoamento de Pessoal de Nível Superior (CAPES)* at the *Université de Franche-Comté*, France.

Research group: *Laboratoire de Nanomédecine, Imagerie, Thérapeutique*. (Supervisor: Prof. Fabien Picaud).

Project: *Modélisation moléculaire de systèmes de libération contrôlée à base de nanostructures de carbone: Structure, fonction et application potentielle pour les complexes antitumoraux de Pt(II)*

Computer time allocation: *Institut du développement et des ressources en informatique scientifique (IDRIS) – Centre National de la Recherche Scientifique (CNRS). Mésocentre de Calcul de Franche-Comté.*

Subject: Structural, dynamic, and energetic characterization of the interaction and the permeation of carbon nanohorns as nanovectors of cisplatin molecules through cell membranes.

The development of this thesis also involved the participation in events:

Chemically modified carbon nanohorns as nanovectors of the cisplatin drug: a molecular dynamics study. E. R. Almeida, L. A. De Souza, W. B. De Almeida, H. F. Dos Santos. XX *Simpósio Brasileiro de Química Teórica,* 2019, *João Pessoa,* PB. Poster presentation.

Modeling the inclusion complexes of cisplatin and its aquated species with functionalized carbon nanohorns: a quantum chemical approach. E. R. Almeida, W. B. De Almeida, J. C. Belchior, L. A. De Souza, H. F. Dos Santos. *43ª Reunião Anual Virtual da Sociedade Brasileira de Química*, 2020, Poster presentation.

VIII *Simpósio de Estrutura Eletrônica e Dinâmica Molecular, 2020, realizado totalmente online com sede na Universidade de Brasília*. Listener participant.

Carbon nanohorn as nanocontainer for cisplatin: insights on the interaction with plasma membranes of normal and breast cancer cells. E. R. Almeida, H. F. Dos Santos, P. V. S. Z. Capriles. *XXI Simpósio Brasileiro de Química Teórica,* 2021, Poster presentation.

X *Escola de Modelagem Molecular em Sistemas Biológicos, 2021, online event. Short courses: Simulação de Enovelamento de Proteínas em Solvente Explícito, Métodos de Docking Receptor-Ligante e Virtual Screening,* and *Métodos de Aprendizagem de Máquina.*

II Workshop of Molecular Modelling in Drug Discovery and Design (WMMD3) in the Federal University of ABC in *Santo André*, SP, Brazil, 2022. Listener participant.

XXII *Simpósio Brasileiro de Química Teórica,* 2023, *Niterói,* RJ.: Short course: *Fundamentos de IA usando Deep Learning*. Modeling the cellular uptake of functionalized carbon nanohorns loaded with cisplatin through a breast cancer cell membrane. E. R. Almeida, P. V. S. Z. Capriles, H. F. Dos Santos, Fabien Picaud (poster under review).

At last, this thesis resulted in the publication of the following papers:

Almeida, E. R.; Dos Santos, H. F.; Capriles, P. V. S. Z. Carbon nanohorn as nanocontainer for cisplatin: insights on the interaction with plasma membranes of normal and breast cancer cells. **Physical Chemistry Chemical Physics**, v. 23, p. 16376-16389, 2021.

Almeida, E. R.; Capriles, P. V. S. Z.; Dos Santos, H. F. Unveiling the Releasing Processes of Pt(II)-Based Anticancer Drugs from Oxidized Carbon Nanohorn: An In Silico Study. **Journal of Physical Chemistry B**, v. 126, p. 4246-4260, 2022.

Almeida, E. R. & Dos Santos, H. Nanoconfinement effect on the hydrolysis of cisplatin. **Chemical Physics Letters**, v. 811, 140247. (cover)

Almeida, E. R.; Capriles, P. V. S. Z.; Dos Santos, H. F.; Picaud, F. Modeling the cellular uptake of functionalized carbon nanohorns loaded with cisplatin through a breast cancer cell membrane. **Molecular Pharmaceutics**, 2023. DOI: https://doi.org/10.1021/acs.molpharmaceut.3c00379 (cover).

Almeida, E. R.; Capriles, P. V. S. Z.; Dos Santos, H. F.; Picaud, F. Translocation processes of Pt(II)-based drugs through human breast cancer cell membrane: in silico experiments. **Journal of Chemical Information and Modeling,** 2023, DOI: https://doi.org/10.1021/acs.jcim.3c00943.

Collaborations also resulted in two papers that are related to the topic of this thesis:

De Souza, L. A.; Almeida, E. R.; Cunha e Silva, J. H.; Paschoal, D.; Belchior, J. C.; Dos Santos, H. F.; De Almeida, W. B. ^{1}H and ^{195}Pt NMR prediction for inclusion compounds formed by cisplatin and oxidized carbon nanostructures. **RSC Advance**s, v. 11, p. 599-611, 2021.

De Souza, L. A.; Almeida, E. R.; Belchior, J. C.; Dos Santos, H. F.; De Almeida, W. B. Cisplatin release from inclusion complex formed by oxidized carbon nanotube: a DFT study. **Chemical Physics Letters**, v. 774, p. 138619-138626, 2021.

7.3 PERSPECTIVES

Future studies should first investigate how the presence of cell membranes affects the free energy barrier for the drug release from the CNHf. In this case, different positions of the nanovector with respect to the lipid bilayer can be evaluated. The challenging aspect of this study will be the definition of the reaction coordinate to conduct the biased simulations. Besides, these *in silico* experiments will be also computationally expensive.

The use of MD simulations that considers the application of external electric fields is also an alternative of future study that models the so-called electrochemotherapy. This approach may be useful to study the drug release from CNHs and the transmembrane transports of drugs and CNHs, since it has been showing potential results with the nanopores.

Another perspective of study involves the development of larger CNH models with different functionalization schemes. The larger models can be built from the prototypes studied in this thesis, since they include the most likely opening angle of the cone reported in experimental studies. These new models will provide the encapsulation of larger cluster of platinum drugs and the analysis of their dynamics and thermodynamics. The effect of the drug saturation inside CNHs on the energy barrier to the drug release can be also a question to be investigated with these new nanocarriers.

At last, the modeling of CNH clusters, also known as dahlia-like structures, is also an interesting perspective of study. The equilibration of this system keeping the spherical symmetric will not be trivial during the simulations. However, this system may be relevant to understand the interaction of the CNH agglomerates with cell membranes.

APPENDIX A - SUPPLEMENTARY INFORMATION FOR CHAPTER 3

Carbon nanohorn as nanocontainer for cisplatin: insights on the interaction with plasma membranes of normal and breast cancer cells

Table A.1 - Number of lipids that compound the membrane models referring to N_memb and C_memb.

Components (lipids)	**Number of lipids**			
	N_memb[a]		**C_memb[b]**	
	outer monolayer	inner monolayer	outer monolayer	inner monolayer
DOPC	77	37	46	46
DOPE	4	16	18	18
DOPG	2	2	4	4
DOPS	0	26	8	8
CHL	16	16	22	22
Ions	**Number of ions[c]**			
Na^+	99		90	
Cl^-	69		66	

[a]Number of lipids based on the lipid composition of a normal breast tissue cell [47]. [b]Number of lipids based on the lipid composition of the MCF-7 cell line [46]. [c]Total number of ions included to neutralize and represent the molar concentration (0.15 M) of the Na^+ and Cl^- in the membrane models. DOPC: 1,2-dioleoyl-*sn*-glycero-3-phosphocholine. DOPE: 1,2-dioleoyl-*sn*-glycero-3-phosphoethanolamine. DOPG: 1,2-dioleoyl-*sn*-glycero-3-[phospho-rac-(1-glycerol)]. DOPS: 1,2-dioleoyl-*sn*-glycero-3-phospho-L-serine. CHL: cholesterol.
Reference: Own author (2021).

Figure A.1 - Structures and molecular formulas of the main lipids expressed in plasma membranes of normal and cancer cells referring to the human breast. DOPC: 1,2-dioleoyl-*sn*-glycero-3-phosphocholine. DOPE: 1,2-dioleoyl-*sn*-glycero-3-phosphoethanolamine. DOPG: 1,2-dioleoyl-*sn*-glycero-3-[phospho-rac-(1-glycerol)]. DOPS: 1,2-dioleoyl-*sn*-glycero-3-phospho-L-serine. CHL: cholesterol. The white, gray, red, golden, and blue colors in the licorice representations indicate the H, C, O, P, and N atoms.

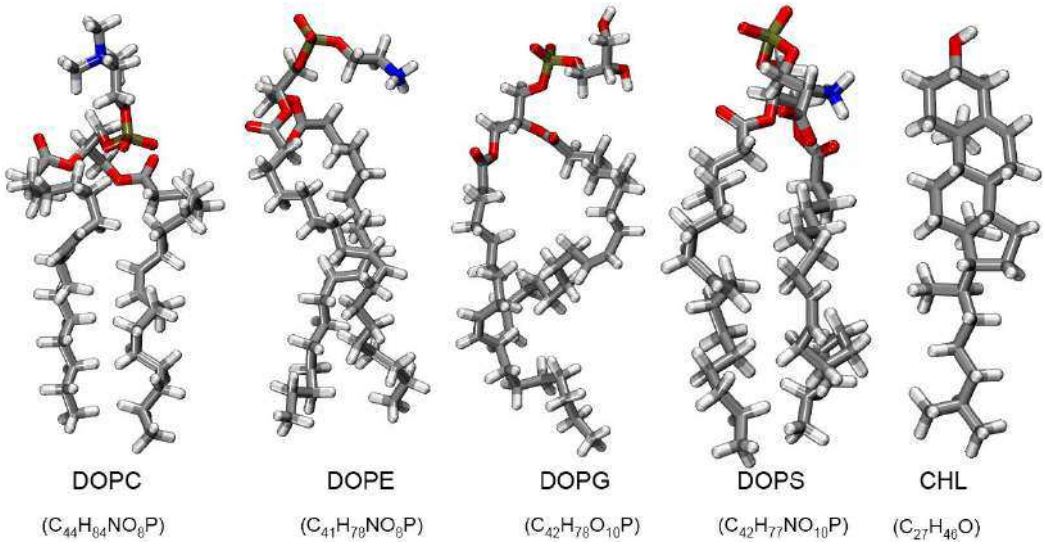

Reference: Own author (2021).

Figure A.2 - The temporal variation of the temperature (A), pressure (B), density (C) and volume (D) referring to the inclusion complex formed by three cddp molecules encapsulated into one CNHox (3cddp@CNHox) in aqueous solution with 0.15 M of NaCl during 200 ns simulation run. The green line represents the moving average calculated for sets of 350 frames.

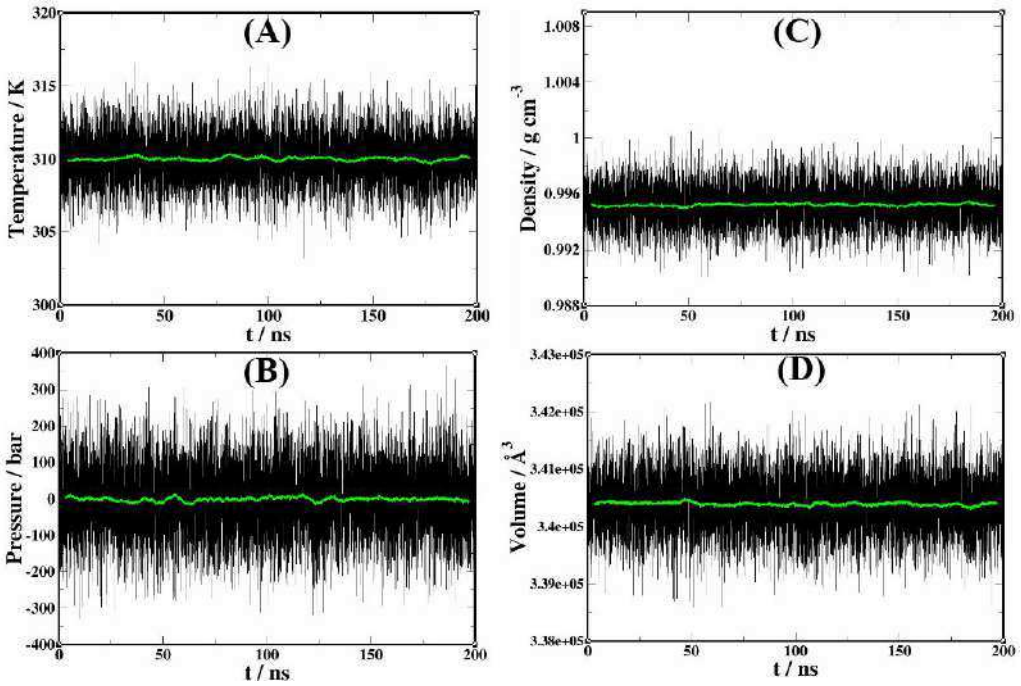

Reference: Own author (2021).

Figure A.3 - The temporal variation of the kinetic (E_{kin}), potential (E_{pot}), and total (E_{total}) energy of the inclusion complex formed by three cddp molecules encapsulated into one CNHox (3cddp@CNHox) in aqueous solution with 0.15 M of NaCl during 200 ns simulation run.

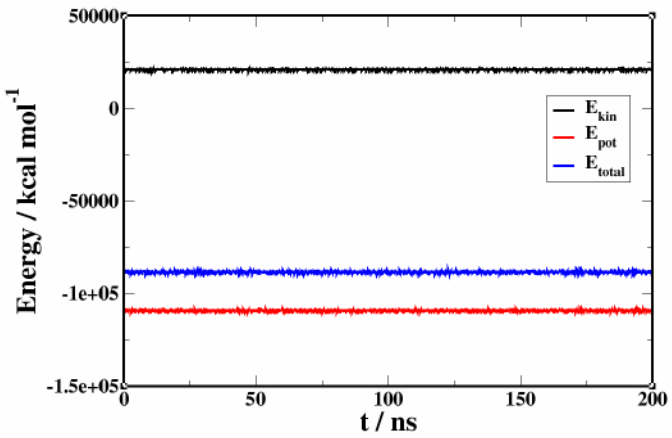

Reference: Own author (2021).

Figure A.4 - Temporal variation of the energetic components of the solute (3cddp@CNHox) during 200 ns simulation run. (A): energy required to the bond stretching (E_{bond}), angle bending (E_{angle}), and rotations about bonds referring to torsional angles ($E_{torsion}$). (B): electrostatic interaction energy (E_{elec}), electrostatic interaction energy between the end atoms involved in a dihedral angle ($E_{1\text{-}4\ elec}$), van der Waals interaction energy (E_{vdW}), van der Waals interaction energy between the end atoms involved in a dihedral angle ($E_{1\text{-}4\ vdW}$), and total potential energy (E_{tot}).

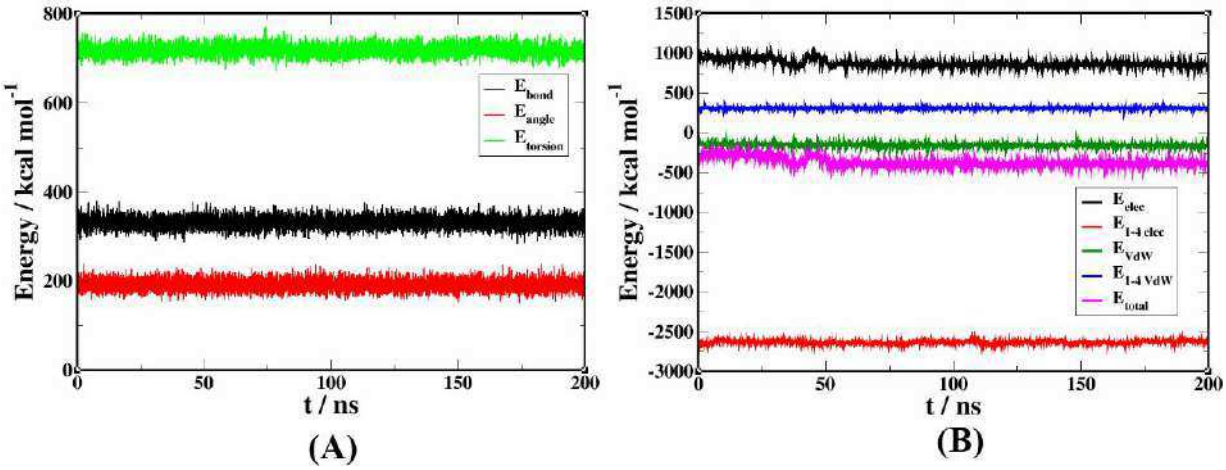

Reference: Own author (2021).

Table A.2 - Statistics of the energetic contributions to the total potential energy of the inclusion complex formed by three cddp molecules encapsulated into one CNHox (3cddp@CNHox) during 200 ns simulation. All values are in kcal mol^{-1}.

Components	**Average ± Std.**	**Max.**	**Min.**
E_{bond}	191.46±11.88	239.43	151.03
E_{angle}	331.12±12.69	380.85	285.05
$E_{torsion}$	717.83±12.20	771.83	670.46
E_{vdW1-4}	307.13±5.80	329.17	286.79
E_{vdW}	-156.18±11.86	-101.69	-190.76
$E_{elec1-4}$	-2635.02±18.33	-2564.59	-2694.60
E_{elec}	872.54±39.87	1006.18	787.64
E_{tot}	-371.12±48.23	-191.43	-459.44

The E_{bond}, E_{angle}, $E_{torsion}$, E_{vdW1-4}, E_{vdW}, $E_{elec1-4}$, E_{elec}, E_{tot}, Std., Max., and Min. terms refer to the energy required to the bond stretching, angle bending, rotations about bonds referring to torsional angles, van der Waals interaction energy between the end atoms involved in a dihedral angle, van der Waals interaction energy, electrostatic interaction energy between the end atoms involved in a dihedral angle, electrostatic interaction energy, total potential energy, standard deviation, maximum value, and minimum value, respectively.

Reference: Own author (2021).

Figure A.5 - The snapshots of the 200 ns MD trajectory referring to the inclusion complex formed by a cluster of three cddp molecules encapsulated into one CNHox (3cddp@CNHox). The silver, red, blue, white, and cyan colors indicate the CNH structure and the O, N, H, and Cl atoms of the cddp molecule.

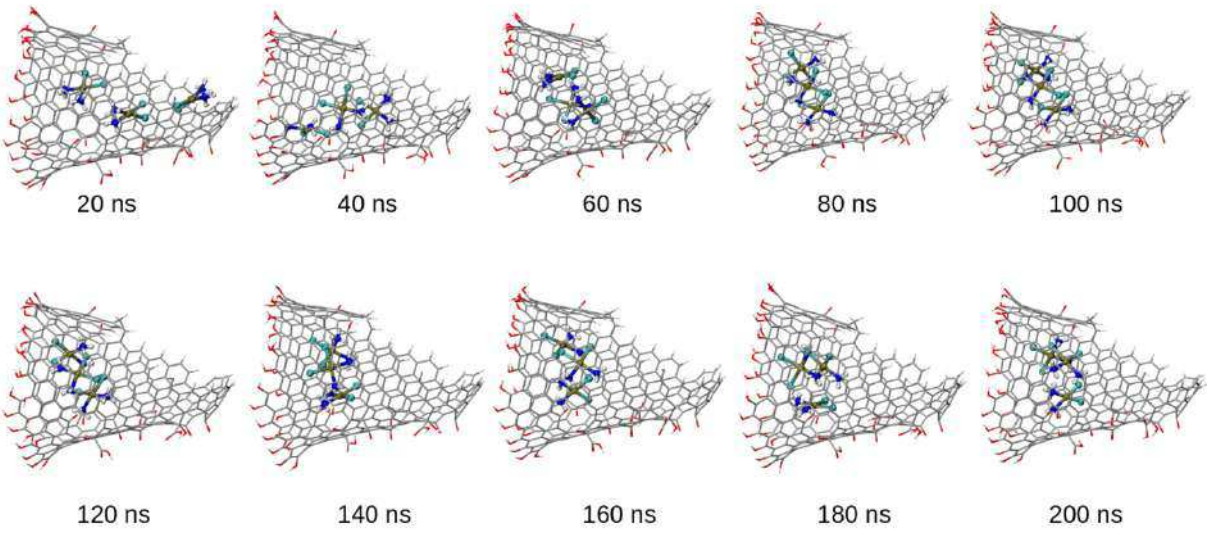

Reference: Own author (2021).

Figure A.6 - Spatial distribution of the cluster formed by three cddp molecules inside the CNHox cavity: (A) Side view and (B) front view. While the silver, red, and white colors represent the C, O, and H atoms of the CNHox structure, the blue, green, and golden spheres and clouds correspond to the temporal variation of the N, Cl, and Pt atoms. This distribution involves the superposition of 100 frames collected from the 200 ns simulation.

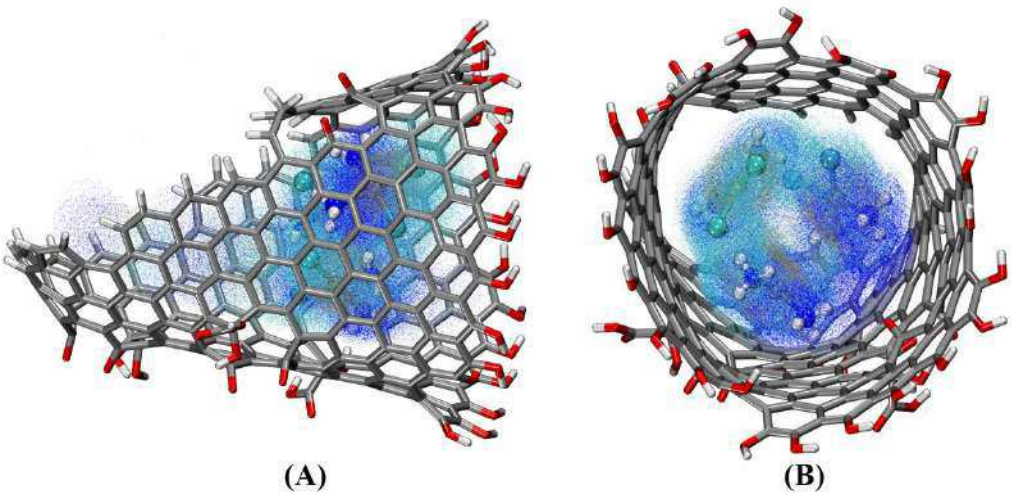

Reference: Own author (2021).

Figure A.7 - Radial distribution function (g(r) CM--O_w) defined between the CM of the CNHox model and the O atoms (O_w) of the water molecules (A) and the water molecules of the inner solvation shell (B).The red dashed line defines the region internal and external water molecules relative to the CNHox structure. The silver, red, white, blue, golden, and green colors represent the C, O, H, N, Pt, Cl atoms, respectively.

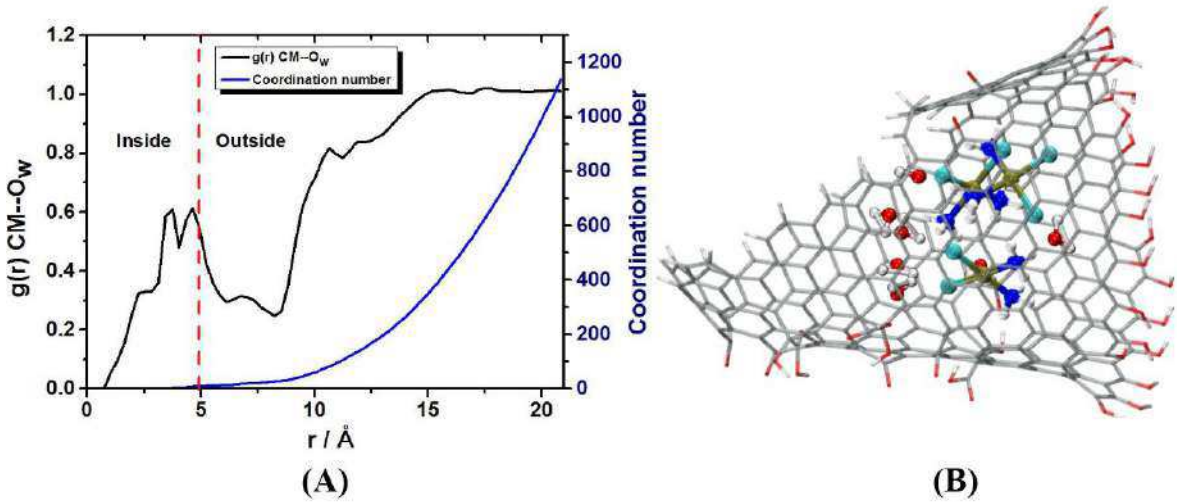

Reference: Own author (2021).

Figure A.8 - Radial distribution functions (RDF) involving the cddp cluster and the water molecules: g(r) Pt--O_w (A), g(r) Pt--H_w (B), g(r) NH--O_w (C), and g(r) Cl--H_w (D).

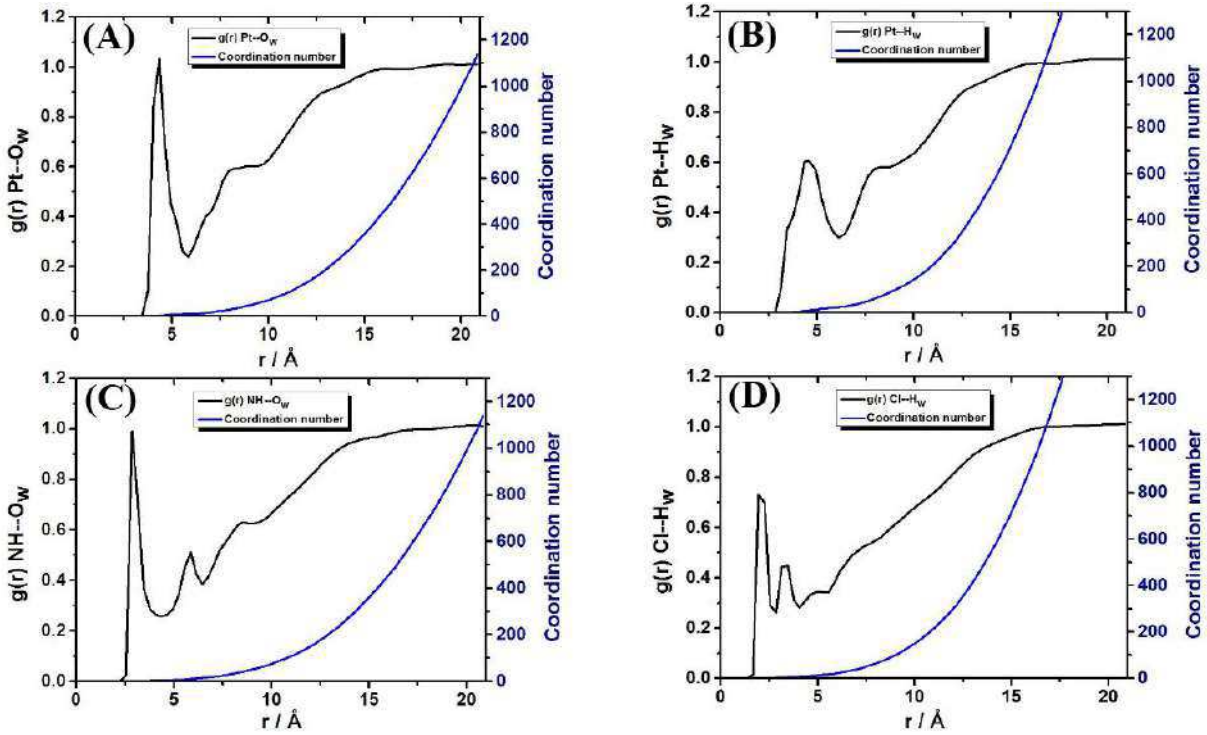

Reference: Own author (2021).

Figure A.9 - Snapshot of the 3cddp@CNHox complex collected from the 26 ns time of the 200 ns trajectory: (A) Side view and (B) front view from the oxidized end of the CNHox structure.

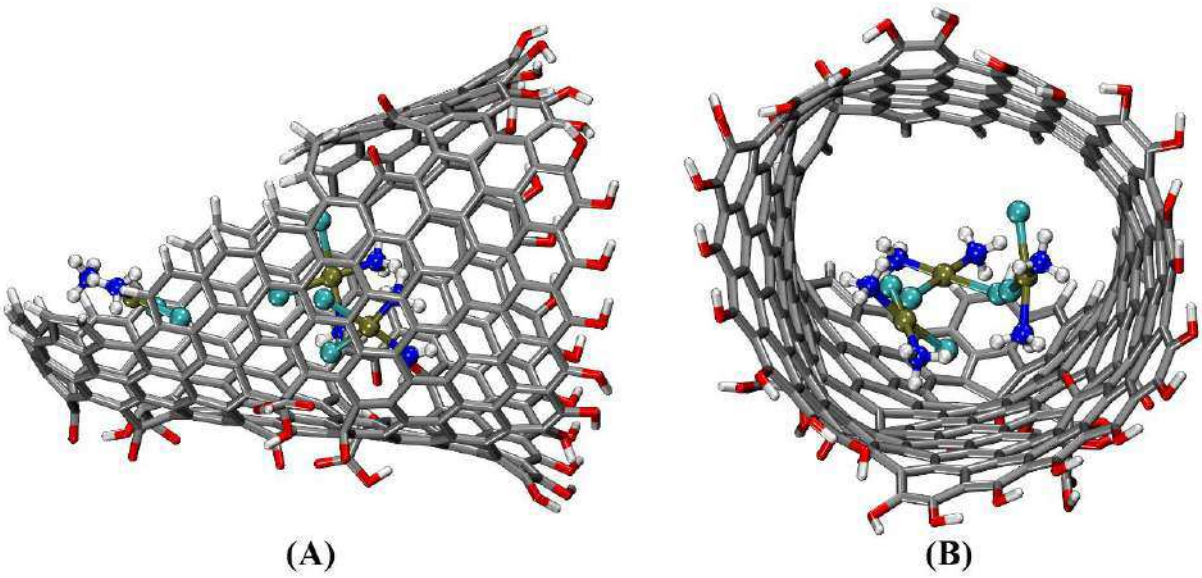

Reference: Own author (2021).

Figure A.10 - The temporal variation of the temperature (A), pressure (B), density (C) and volume (D) referring to the membrane model of a BC cell (C_memb model) in aqueous solution during 400 ns simulation run. The green line represents the moving average calculated for sets of 350 frames.

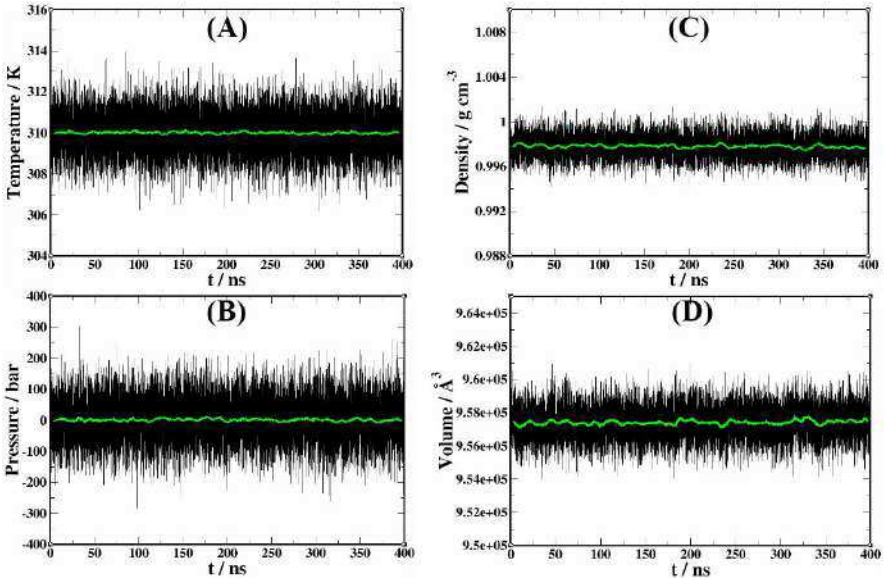

Reference: Own author (2021).

Figure A.11 - The temporal variation of the temperature (A), pressure (B), density (C) and volume (D) referring to the membrane model of a normal breast cell (N_memb model) in aqueous solution during 400 ns simulation run. The green line represents the moving average calculated for sets of 350 frames.

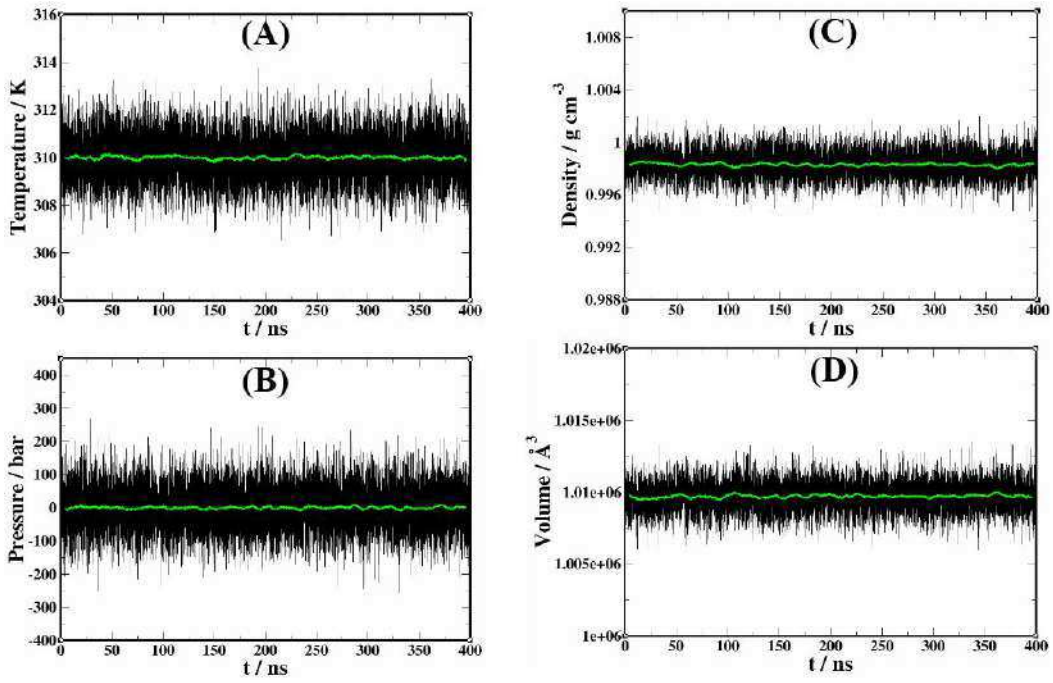

Reference: Own author (2021).

Figure A.12 - The temporal variation of the kinetic (E_{kin}), potential (E_{pot}), and total (E_{total}) energy of the membrane models referring to a breast cancer cell (C_memb model) and a normal breast cell (N_memb) in aqueous solution over the 400 ns simulation run.

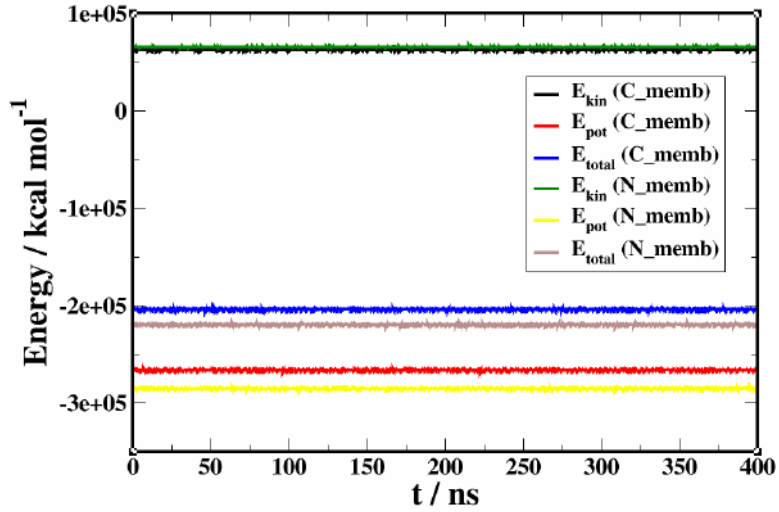

Reference: Own author (2021).

Figure A.13 - Temporal variation of the bonded energy terms referring to only the membrane models of a BC cell (C_memb) and a normal breast cell (N_memb) during 400 ns of simulation: energy required to the bond stretching (E_{bond}), energy required to the angle bending (E_{angle}), and energy required to the rotations about bonds referring to torsional angles ($E_{torsion}$).

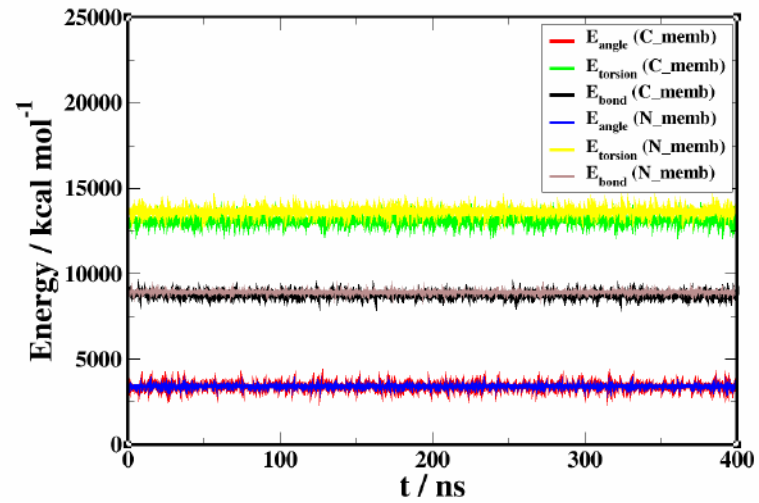

Reference: Own author (2021).

Figure A.14 - Temporal variation of the non-bonded energy terms referring to only the membrane model of a BC cell (C_memb) and a normal breast cell (N_memb) during 400 ns of simulation: electrostatic interaction energy (E_{elec}), electrostatic interaction energy between the end atoms involved in a dihedral angle ($E_{1\text{-}4\ elec}$), van der Waals interaction energy (E_{vdW}), van der Waals interaction energy between the end atoms involved in a dihedral angle ($E_{1\text{-}4\ vdW}$), and total potential energy (E_{tot}).

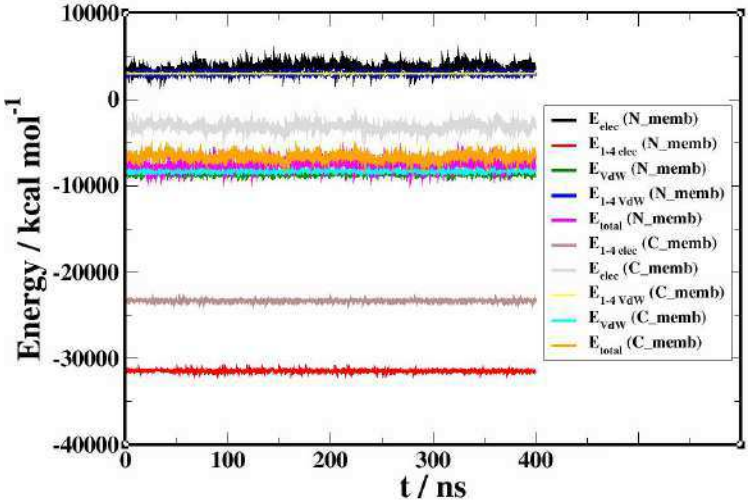

Reference: Own author (2021).

Table A.3 - Statistics of the energetic contributions to the total potential energy of the membrane models (only the solute) of a BC cell (C_memb) and a normal breast cell (N_memb) over 400 ns simulation. All values are in kcal mol^{-1}.

Components	N_memb[a]			C_memb[b]		
	Average ± Std.	**Max.**	**Min.**	**Average ± Std.**	**Max.**	**Min.**
E_{bond}	3403.40±48.14	3579.91	3221.03	3288.42±47.77	3502.08	3097.47
E_{angle}	13631.30±89.90	14004.00	13304.70	13125.30±87.09	13507.40	12805.60
$E_{torsion}$	8919.19±46.32	9093.02	8752.87	8774.08±46.58	8965.50	8593.05
E_{vdW1-4}	2971.16±22.76	3073.62	2879.97	2956.93±22.45	3049.50	2875.18
E_{vdW}	-8698.08±62.70	-8455.61	-8935.51	-8339.59±61.52	-8099.17	-8596.65
$E_{elec1-4}$	-31449.40±50.99	-	-	-23340.40±48.18	-	-
		31246.10	31641.60		23152.30	23524.20
E_{elec}	3625.08±397.58	4999.17	2270.42	-3175.52±343.94	-1842.30	-4540.90
E_{tot}	-7597.37±403.55	-6104.03	-9029.89	-6710.73±367.02	-5327.72	-8119.96

[a]Simulation box dimensions: 118x87x169 Å. [b]Simulation box dimensions: 103x86x175 Å The E_{bond}, E_{angle}, $E_{torsion}$, E_{vdW1-4}, E_{vdW}, $E_{elec1-4}$, E_{elec}, E_{tot}, Std., Max., and Min. terms refer to the energy required to the bond stretching, energy required to the angle bending, energy required to the rotations about bonds referring to torsional angles, van der Waals interaction energy between the end atoms involved in a dihedral angle, van der Waals interaction energy, electrostatic interaction energy between the end atoms involved in a dihedral angle, electrostatic interaction energy, total potential energy, standard deviation, maximum value, and minimum value, respectively.
Reference: Own author (2021).

Figure A.15 - Temporal variation of the area per lipid (A_L) calculated from the membrane models referring to a normal breast cell (N_memb) and a BC cell (C_memb) over the last 100 ns of the 400 ns simulation: N_memb (A) and C_memb (B).

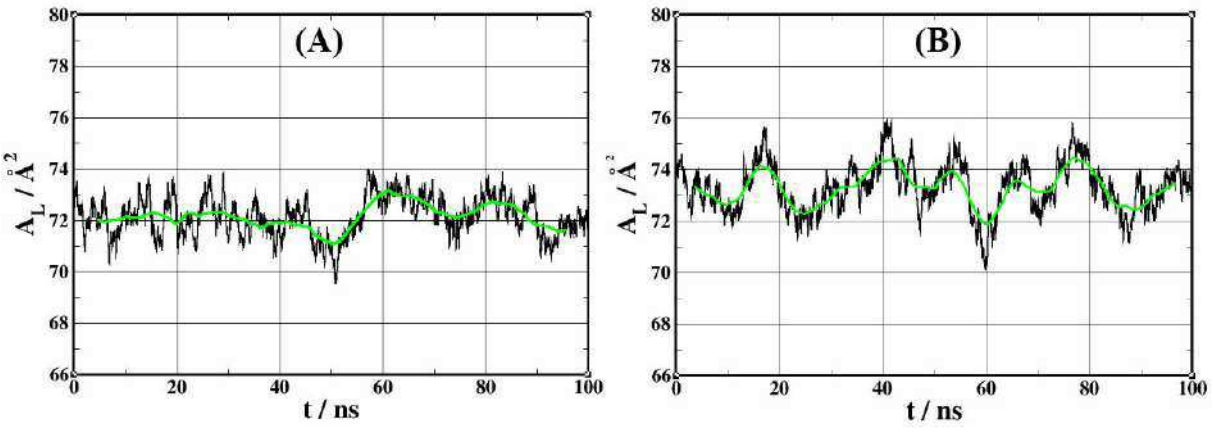

Reference: Own author (2021).

Figure A.16 - The temporal variation of the temperature (A), pressure (B), density (C) and volume (D) referring to the 3cddp@CNHox>C_memb system in aqueous solution during the first 100 ns of the 800 ns trajectory. The green line represents the moving average calculated for sets of 350 frames.

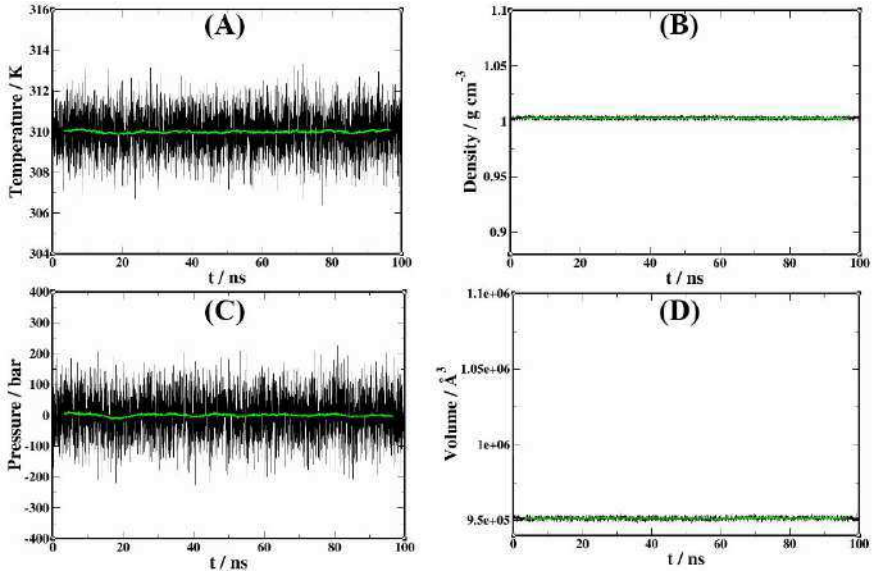

Reference: Own author (2021).

Figure A.17 - The temporal variation of the temperature (A), pressure (B), density (C) and volume (D) referring to the 3cddp@CNHox>N_memb system in aqueous solution during the first 100 ns of the 800 ns trajectory. The green line represents the moving average calculated for sets of 350 frames.

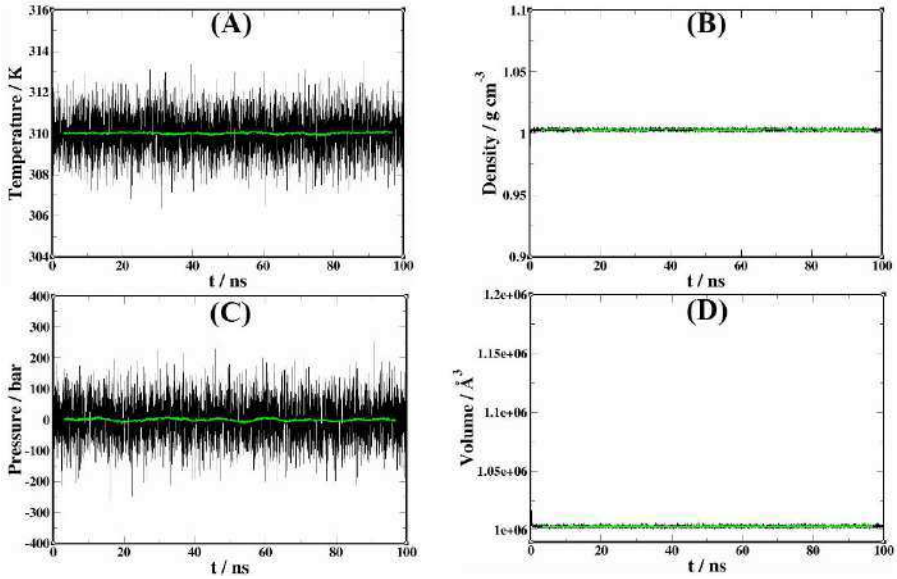

Reference: Own author (2021).

Figure A.18 - The temporal variation of the kinetic (E_{kin}), potential (E_{pot}), and total (E_{total}) energy of the 3cddp@CNHox>C_memb and 3cddp@CNHox>N_memb systems in aqueous solution the first 100 ns of the 800 ns simulation.

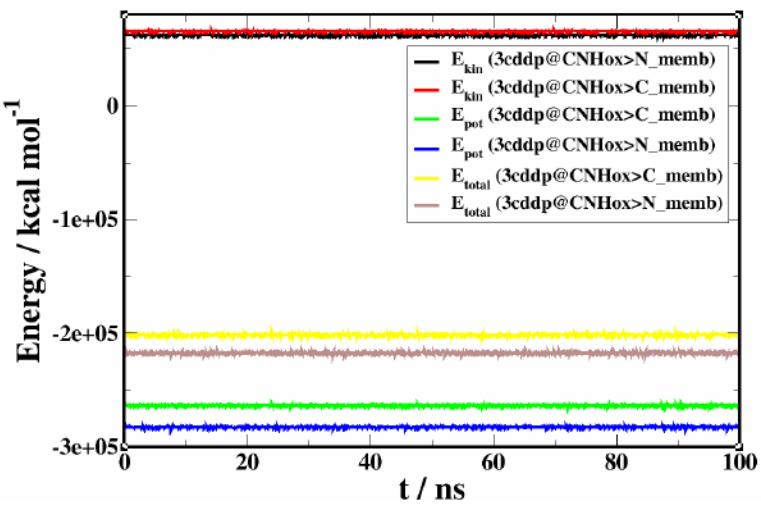

Reference: Own author (2021).

Figure A.19 - Snapshots of the 800 ns simulation referring to the system 3cddp@CNHox>C_memb, which corresponds to the interaction between the inclusion complex formed by a cluster of three cddp molecules encapsulated into one CNHox structure (3cddp@CNHox) and a plasma membrane model of a BC cell (C_memb). In the membrane structure, the blue, red, yellow, green, magenta, and white colors correspond to the DOPC, DOPE, DOPS, DOPG, CHL, and OL species. In the inclusion complex, while the black color indicated the CNH structure, the blue, white, cyan, and golden colors indicate the N, H, Cl, and Pt atoms of the cddp molecule.

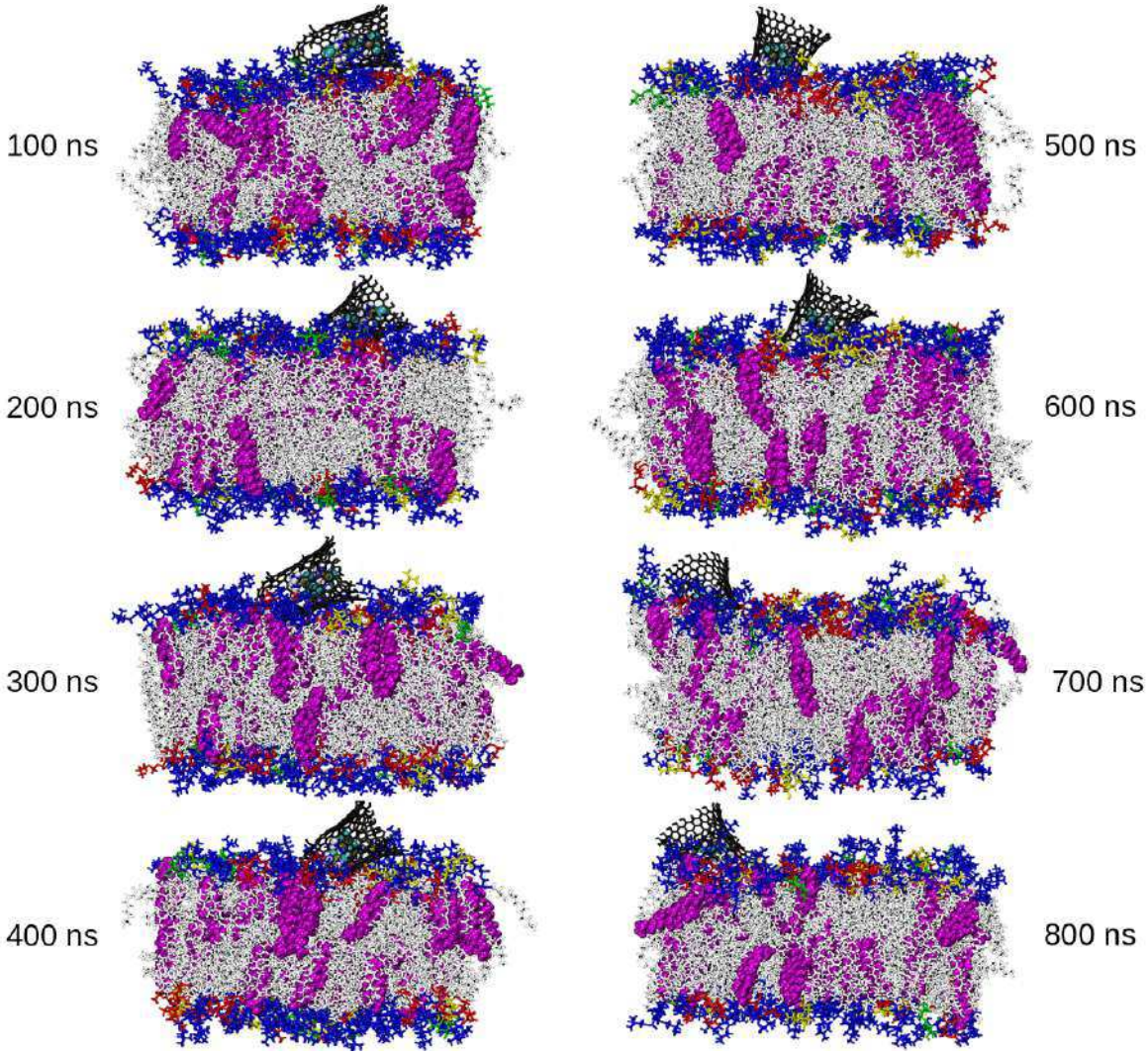

Reference: Own author (2021).

Figure A.20 - Snapshots of the 800 ns simulation referring to the system 3cddp@CNHox>N_memb, which corresponds to the interaction between the inclusion complex formed by a cluster of three cddp molecules encapsulated into one CNHox) structure (3cddp@CNHox), and a plasma membrane model of a normal breast cell (N_memb). In the membrane structure, the blue, red, yellow, green, magenta, and white colors correspond to the DOPC, DOPE, DOPS, DOPG, CHL, and OL species. In the inclusion complex, while the black color indicated the CNH structure, the blue, white, cyan, and ochre colors indicate the N, H, Cl, and Pt atoms of the cddp molecule.

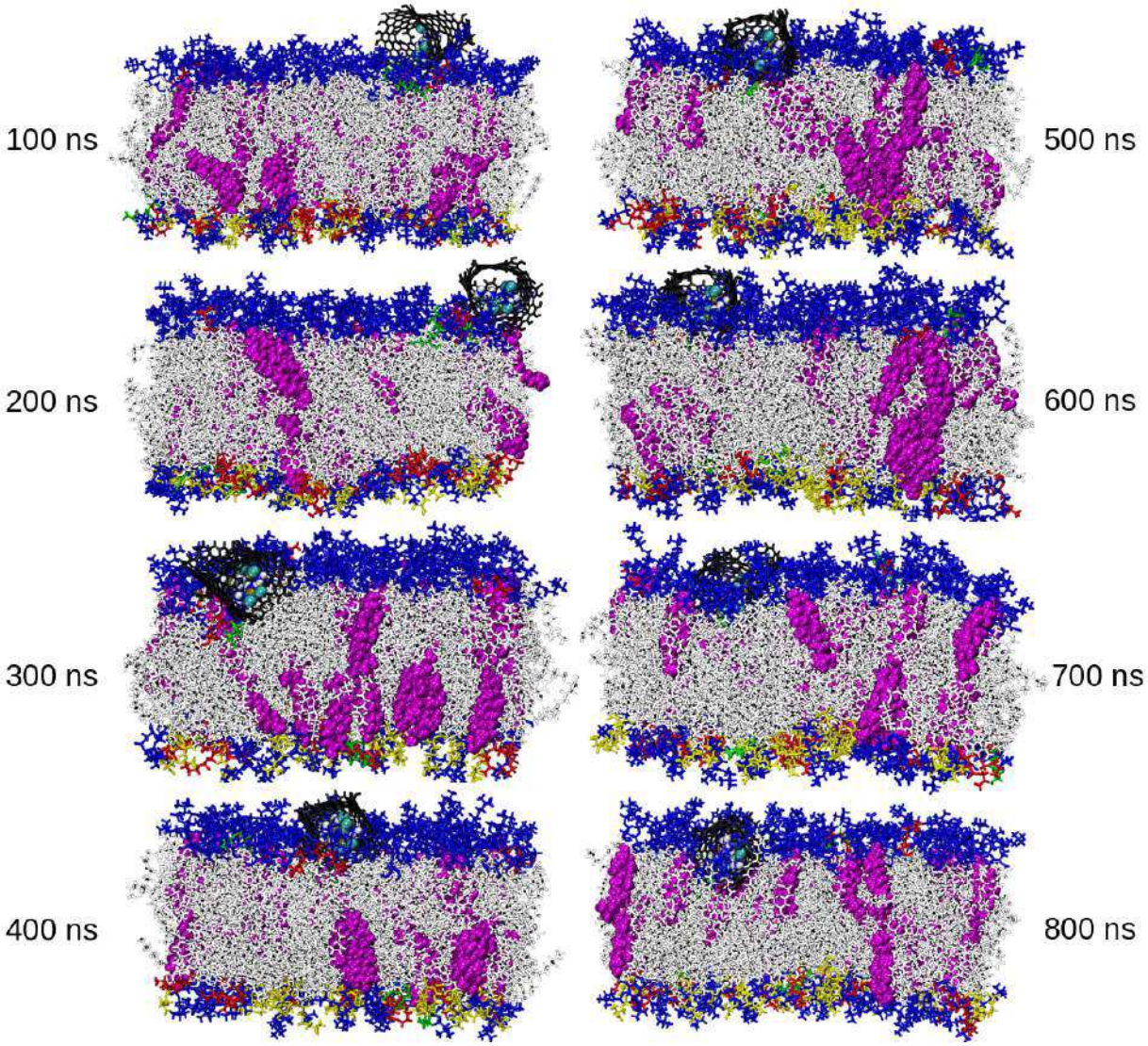

Reference: Own author (2021).

Figure A.21 - Insertion of the PC headgroup of the 1,2-dioleoyl-*sn*-glycero-3-phosphocholine (DOPC) lipid located in both C_memb (A) and N_memb (B) models into the cavity of the CNHox) by the time of 260 ns and 280 ns, respectively.

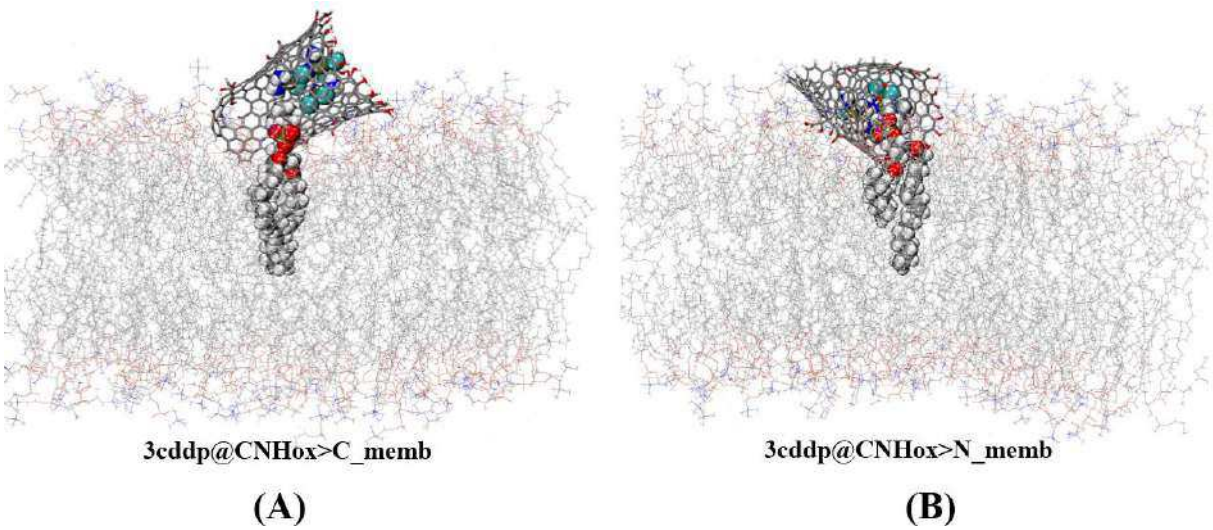

Reference: Own author (2021).

APPENDIX B - SUPPLEMENTARY INFORMATION FOR CHAPTER 4

Unveiling the Releasing Processes of Pt(II)-Based Anticancer Drugs from Oxidized Carbon Nanohorn: An In Silico Study

Figure B.1 - Temporal variation of the properties referring to the equilibration stage of the cddp@CNHox complex (replica 1): temperature (A), volume (B), kinetic energy (C), density (D), potential energy (E), and total energy (F). The red line represents the moving average calculate for sets of 10 frames.

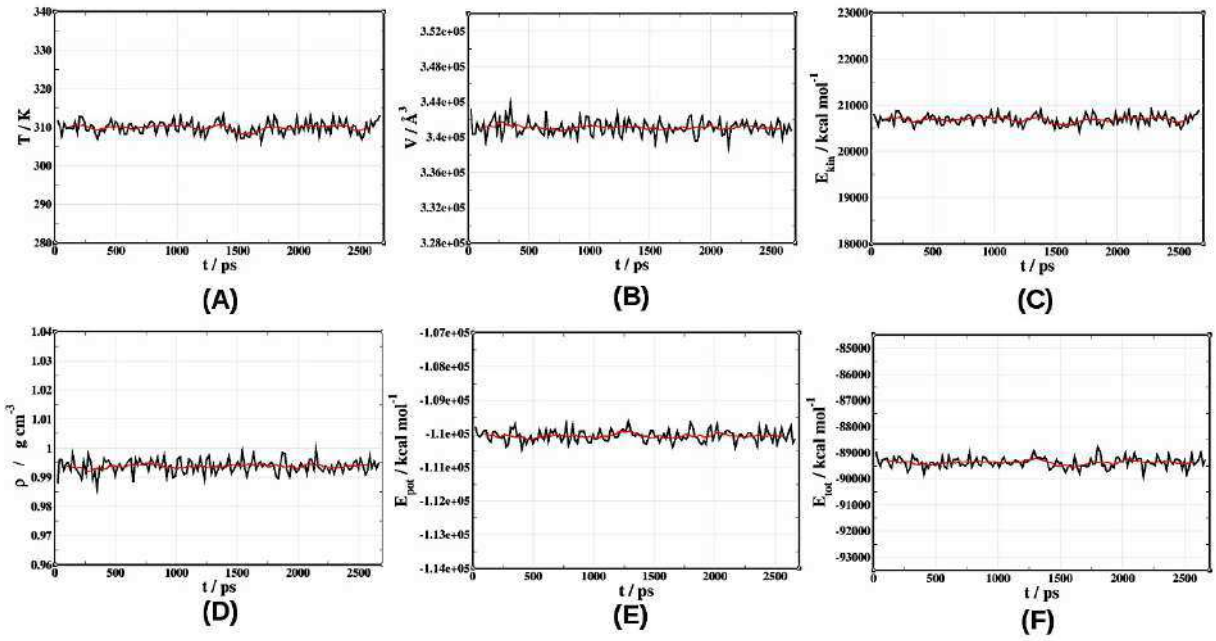

Reference: Own author (2022).

Table B.1 - Statistics of the thermodynamic properties calculated from the equilibration stage (2.7 ns) of the inclusion and adsorption complexes. Each average value was calculated by taking into account the simulation triplicates.

Complex	T / K	ρ / g cm^{-3}	V / Å^3	E_{pot} / kcal mol^{-1}	E_{kin} / kcal mol^{-1}	E_{tot} / kcal mol^{-1}
	<A>±Std.	<A>±Std.	<A>±Std.	<A>±Std.	<A>±Std.	<A>±Std.
cddp@CNHox	310.05±1.64	0.99±0.00	341168.33±867.39	-110053.33±168.27	20696.07±109.76	-89357.10±198.91
cpx@CNHox	309.92±1.74	0.99±0.00	341120.67±913.67	-109757.00±171.47	20683.70±115.92	-89073.33±213.94
oxa@CNHox	309.85±1.73	0.99±0.00	341309.33±912.66	-109833.67±169.74	20693.27±115.81	-89140.63±212.74
cddp>CNHox	310.08±1.67	0.99±0.00	333893.00±898.78	-107827.67±167.52	20257.90±108.91	-87569.73±205.26
cpx>CNHox	309.90±1.63	0.99±0.00	351031.33±962.66	-113011.67±160.88	21291.87±111.77	-91719.53±191.40
oxa>CNHox	310.07±1.64	0.99±0.00	345850.67±944.43	-109904.33±160.50	20724.43±109.74	-89180.10±196.55

*The T, ρ, V, E_{pot}, E_{cin}, ,E_{tot}, <A>, and Std. terms correspond to the temperature, density, volume, potential energy, kinetic energy, total energy, average value, and standard deviation, respectively.
Reference: Own author (2022).

Figure B.2 - Temporal variation of the root mean square deviation (RMSD) related to the equilibration run (2.7 ns) of the cddp@CNHox complex (replica 1).

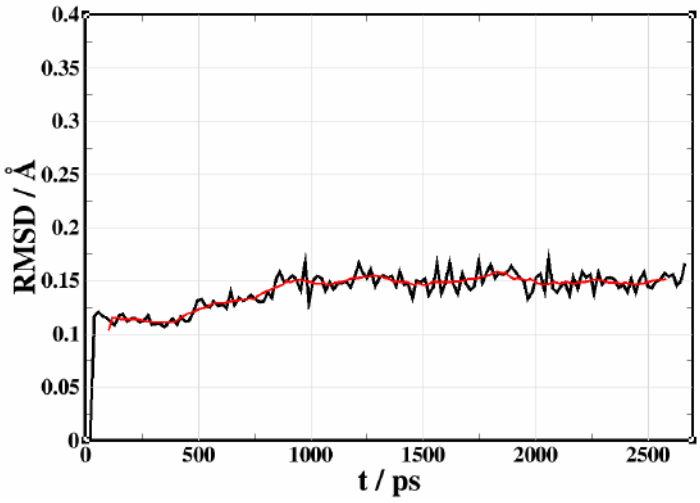

Reference: Own author (2022).

Figure B.3 - Final snapshots of the 200 ns production trajectory (replica 1) referring to the inclusion and adsorption complexes studied in this work: cddp@CNHox (A), cpx@CNHox (B), oxa@CNHox (C), cddp>CNHox (D), cpx>CNHox (E), and oxa>CNHox (F).

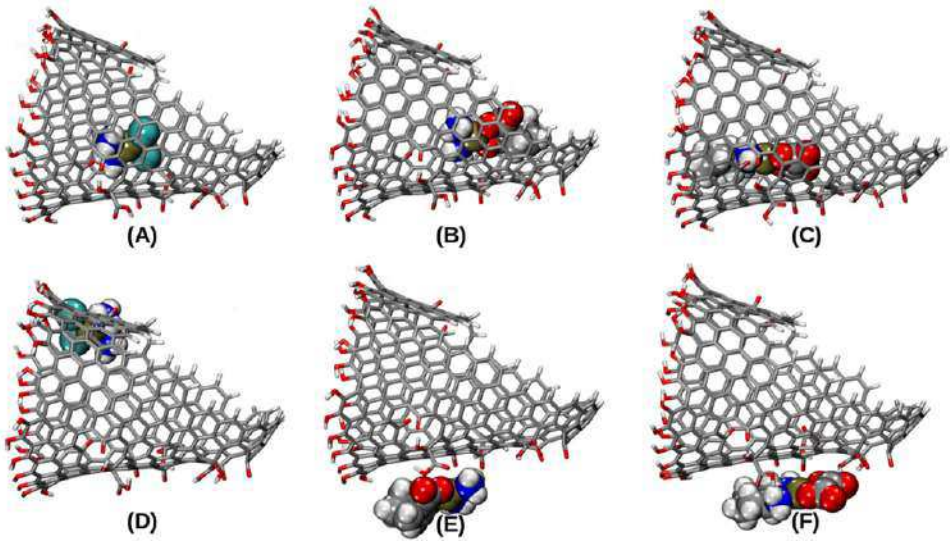

Reference: Own author (2022).

Figure B.4 - Final snapshots of the 200 ns production trajectory (replica 2) referring to the inclusion and adsorption complexes studied in this work: cddp@CNHox (A), cpx@CNHox (B), oxa@CNHox (C), cddp>CNHox (D), cpx>CNHox (E), and oxa>CNHox (F).

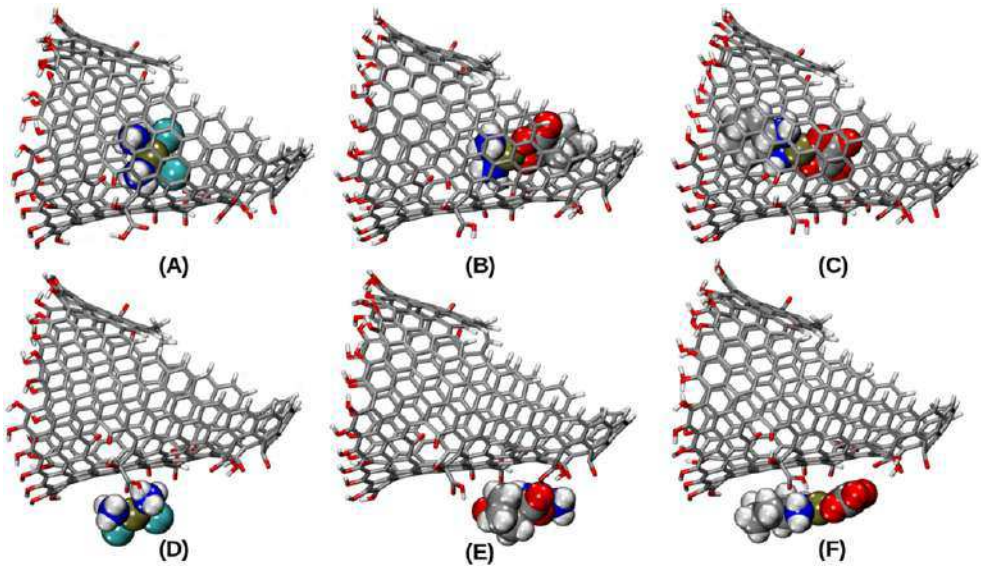

Reference: Own author (2022).

Figure B.5 - Final snapshots of the 200 ns production trajectory (replica 3) referring to the inclusion and adsorption complexes studied in this work: cddp@CNHox (A), cpx@CNHox (B), oxa@CNHox (C), cddp>CNHox (D), cpx>CNHox (E), and oxa>CNHox (F).

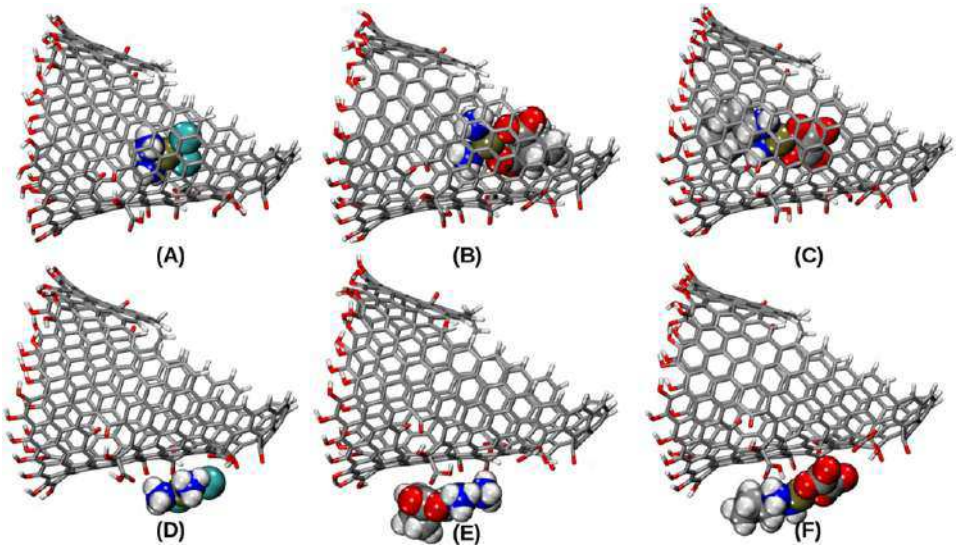

Reference: Own author (2022).

Figure B.6 - Spatial distribution of the Pt(II)-based drugs in the inclusion and adsorption complexes during the 200 ns production run (replica 2). The green, blue, red, silver, and golden colors indicate the mobility of the Cl, N, O, C, and Pt atoms of these metallodrugs.

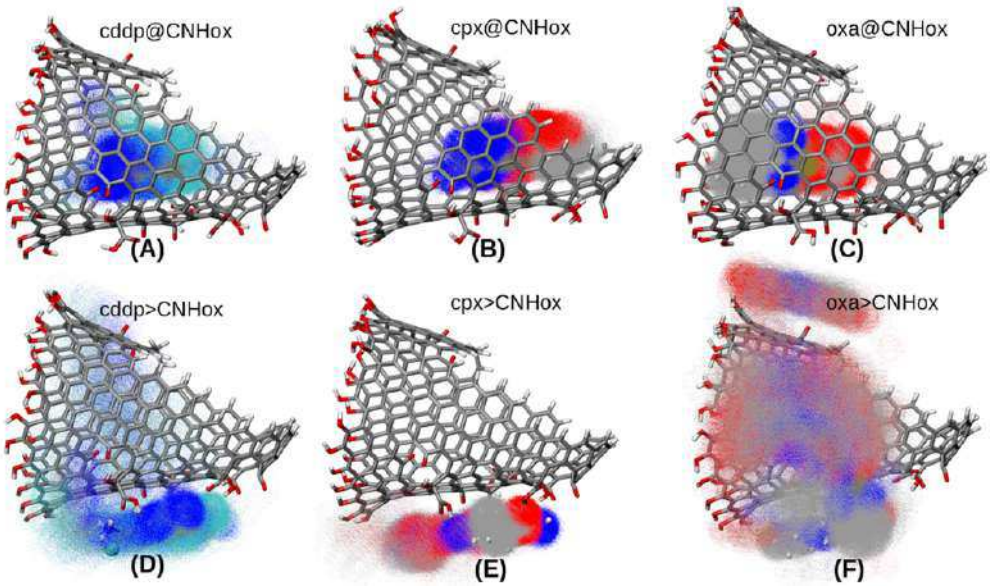

Reference: Own author (2022).

Figure B.7 - Spatial distribution of the Pt(II)-based drugs in the inclusion and adsorption complexes during the 200 ns production run (replica 3). The green, blue, red, silver, and golden colors indicate the mobility of the Cl, N, O, C, and Pt atoms of these metallodrugs.

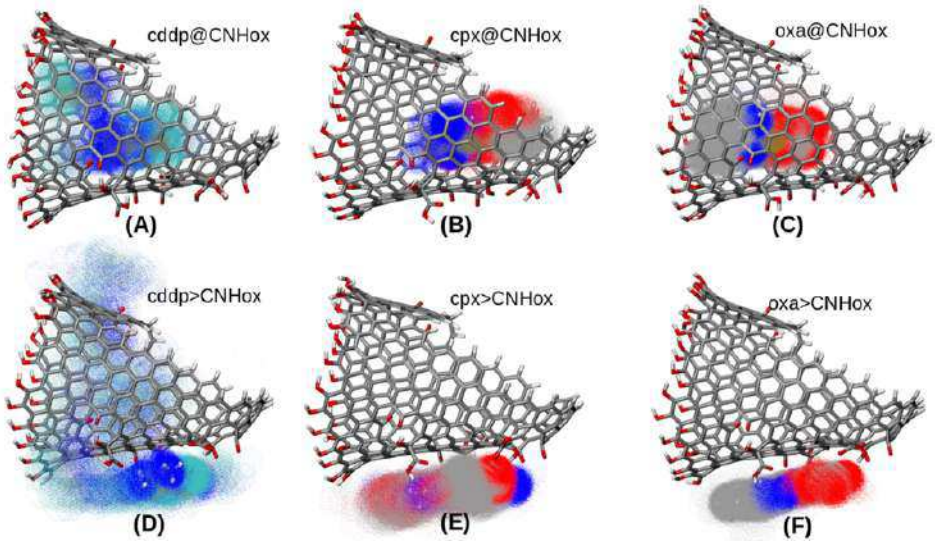

Reference: Own author (2022).

Figure B.8 - Radial distribution functions g(r) CM--O_w defined between the center of mass of the CNHox prototype and the oxygen atom (O_w) of the solvent molecules (water) referring to the 200 ns trajectories of the complexes: inclusion complexes (A) and adsorption complexes (B).

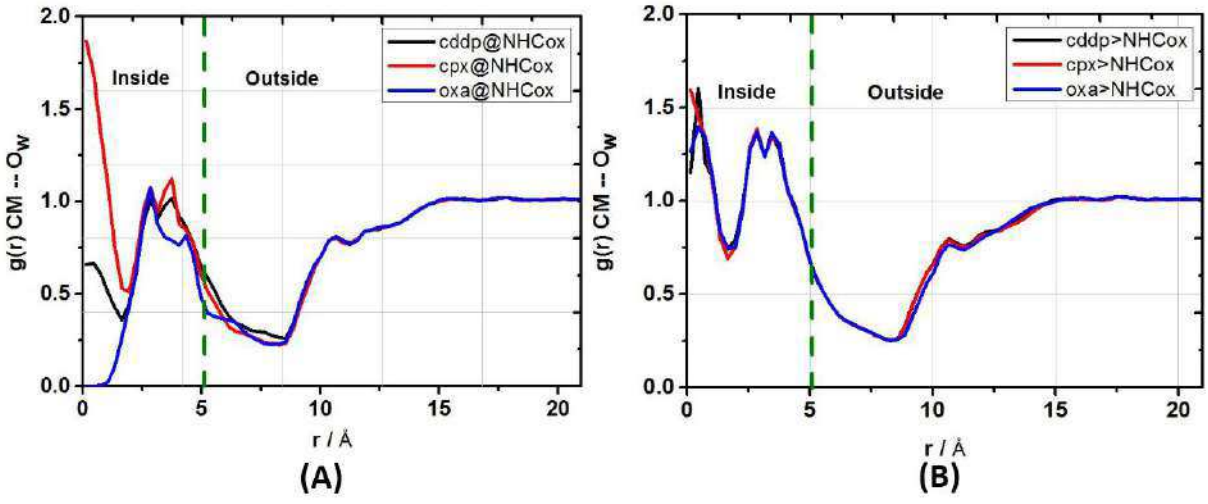

Reference: Own author (2022).

Figure B.9 - Temporal variation of the pair energies during the 200 ns simulations (production runs) referring to the inclusion complexes: replica 2 (A) and replica 3 (C) and the adsorption complexes: replica 2 (B) and replica 3 (D).

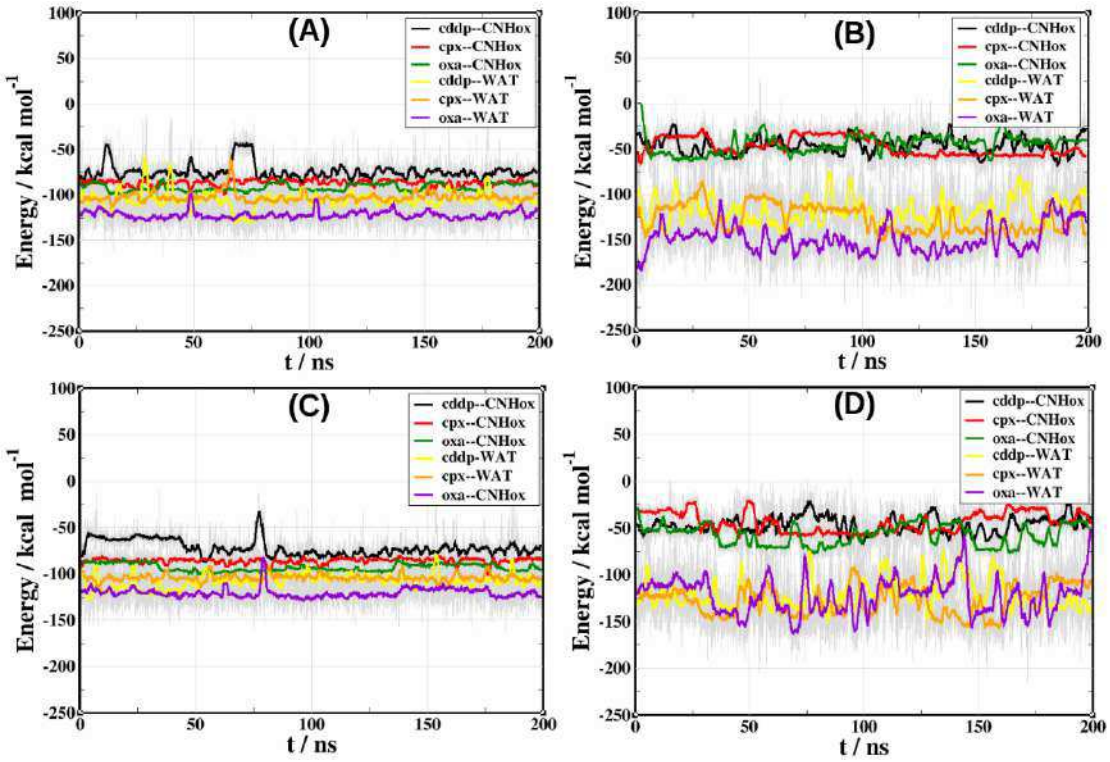

Reference: Own author (2022).

Figure B.10 - Radial distribution functions g(r) Pt--O_w defined between the Pt atom of the anticancer drug and the oxygen atom (O_w) of the solvent molecules (water) referring to the 200 ns trajectories of the complexes: inclusion complexes (A) and adsorption complexes (B).

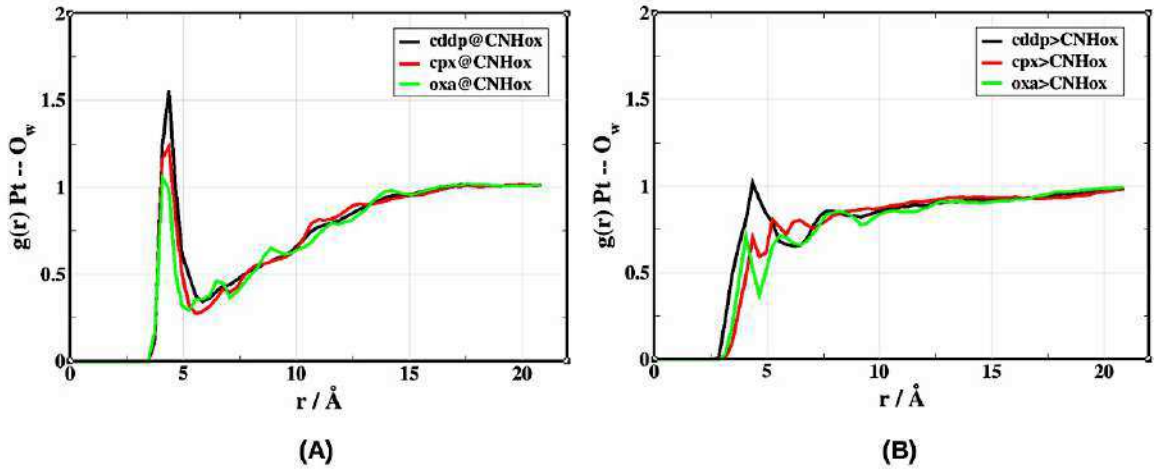

Reference: Own author (2022).

Figure B.11 - The main frames of the cddp1@CNHox complex indicating the cddp release (Mode 1) from the CNH during the 32 ns of SMD.

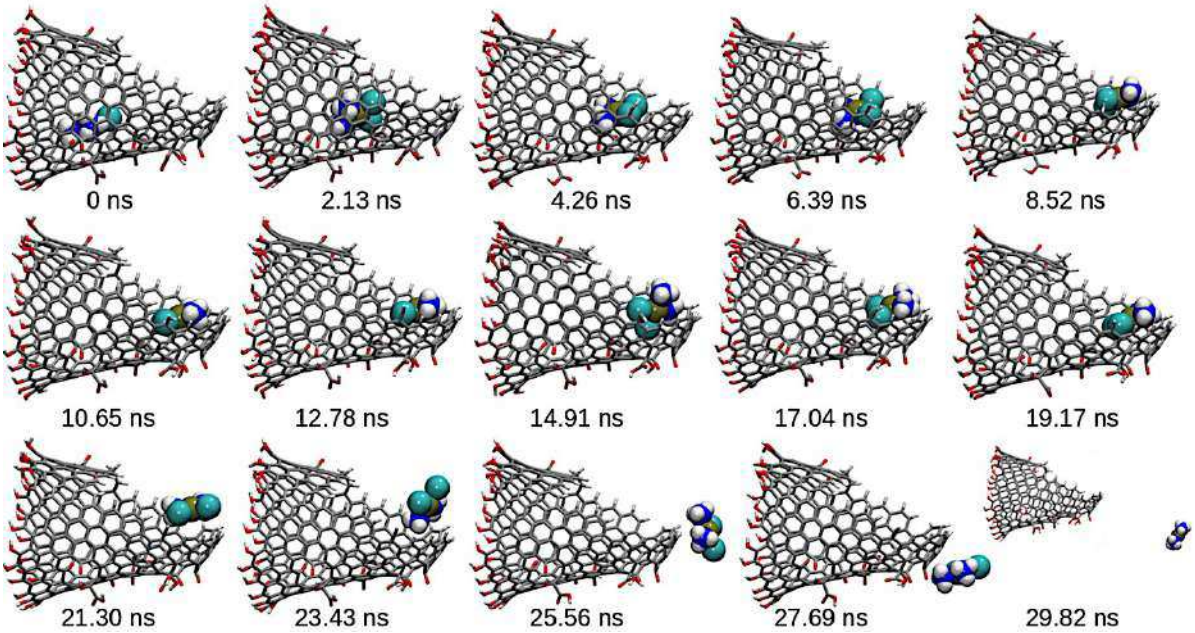

Reference: Own author (2022).

Figure B.12 - The main frames of the cpx1@CNHox complex indicating the cpx release (Mode 1) from the CNH during the 32 ns of SMD.

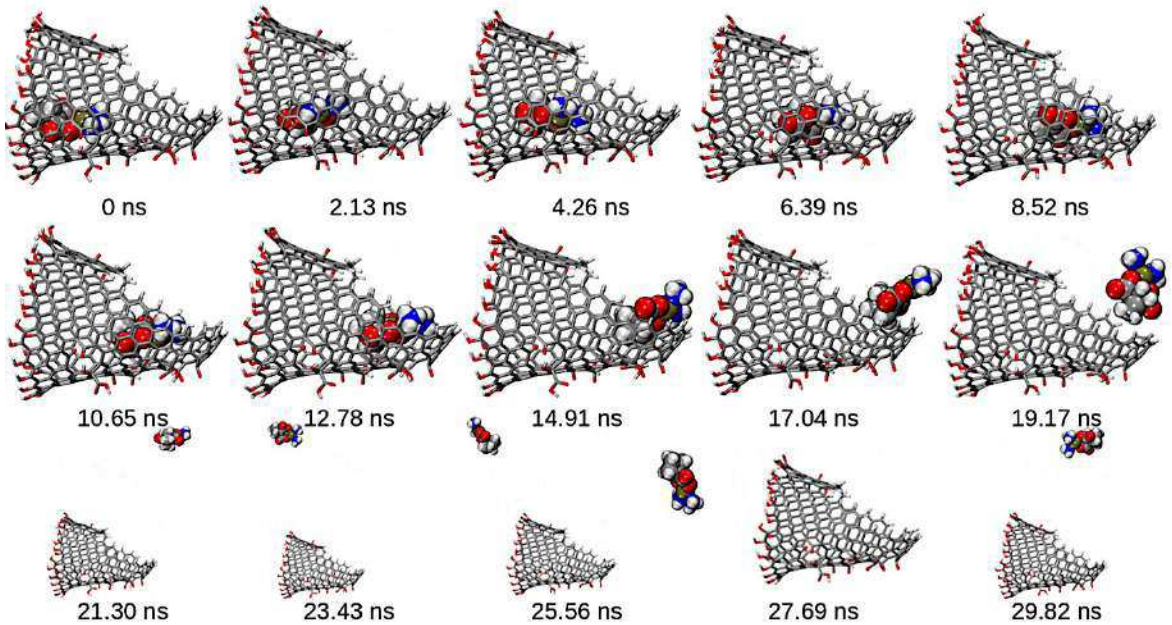

Reference: Own author (2022).

Figure B.13 - The main frames of the oxa1@CNHox complex indicating the oxa release (Mode 1) from the CNH during the 32 ns of SMD.

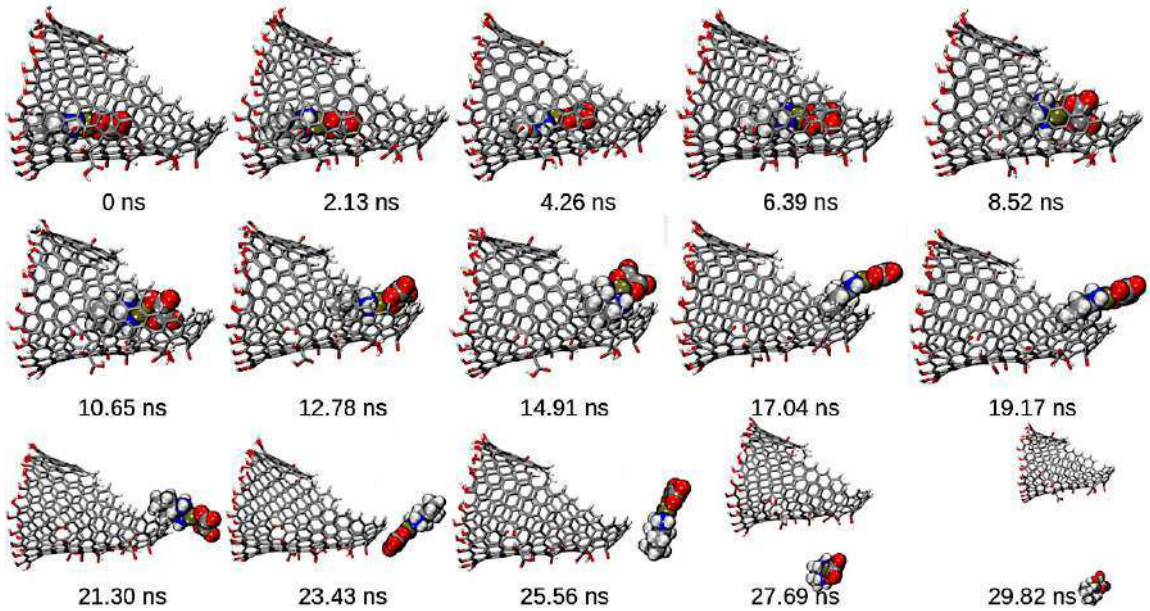

Reference: Own author (2022).

Figure B.14 - The main frames of the cddp2@CNHox complex indicating the cddp release (Mode 2) from the CNH during the 32 ns of SMD.

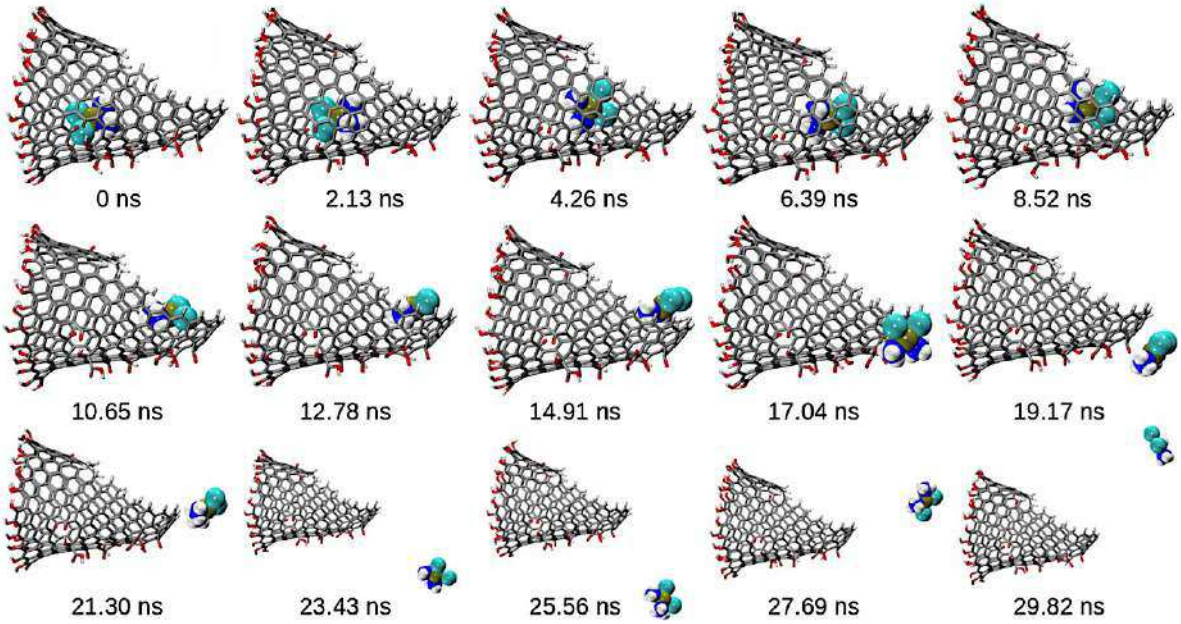

Reference: Own author (2022).

Figure B.15 - The main frames of the cpx2@CNHox complex indicating the cpx release (Mode 2) from the CNH during the 32 ns of SMD.

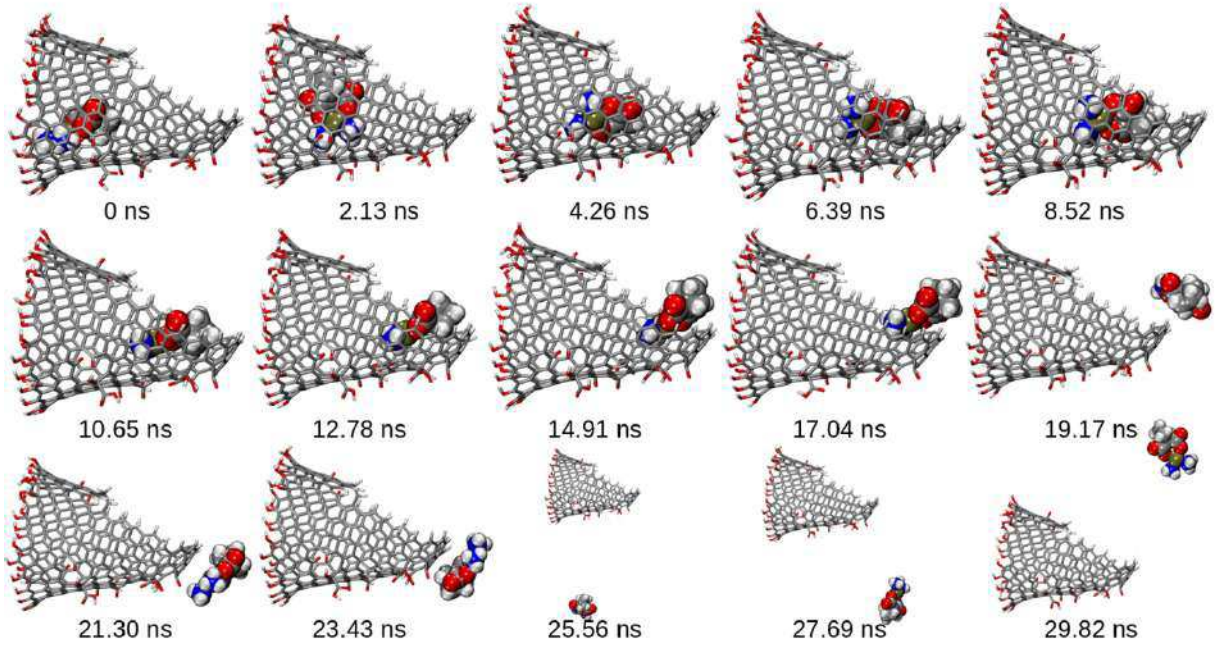

Reference: Own author (2022).

Figure B.16 - The main frames of the oxa2@CNHox complex indicating the oxa release (Mode 2) from the CNH during the 32 ns of SMD.

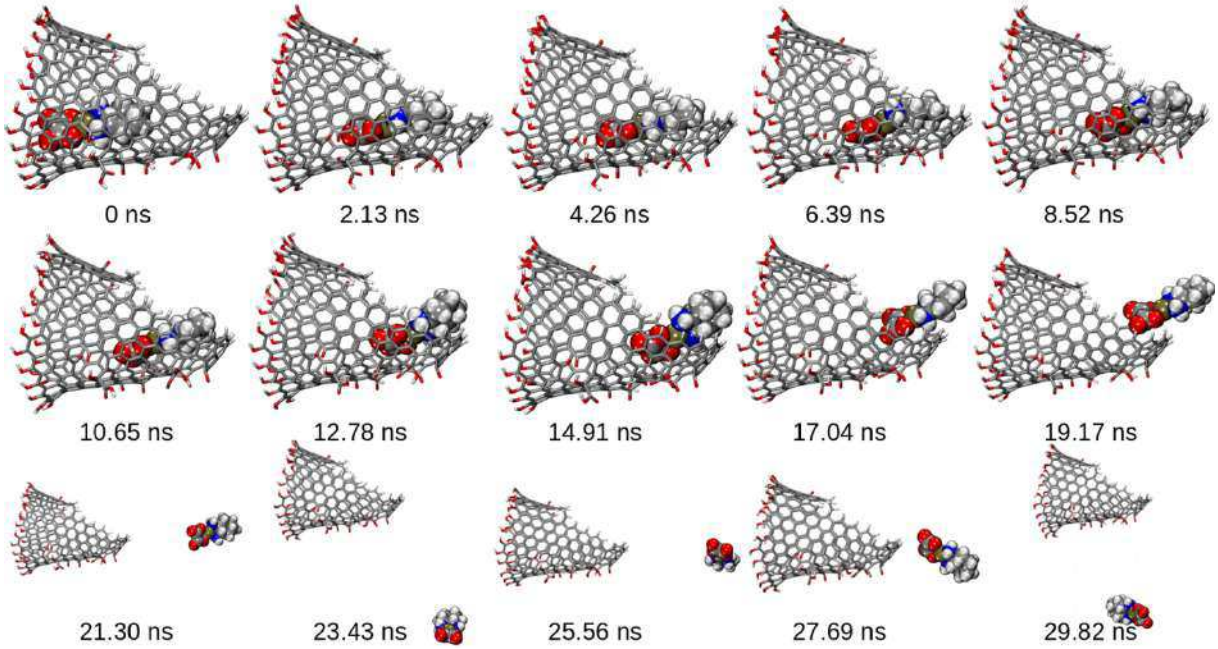

Reference: Own author (2022).

Figure B.17 - Histograms of the probability distribution referring to the 30 windows sampled through the reaction coordinate of the US simulations for the inclusion complexes: cddp1@CNHox (A), cpx1@CNHox (B), oxa1@CNHox (C), cddp2@CNHox (D), cpx2@CNHox (E), and oxa2@CNHox (F).

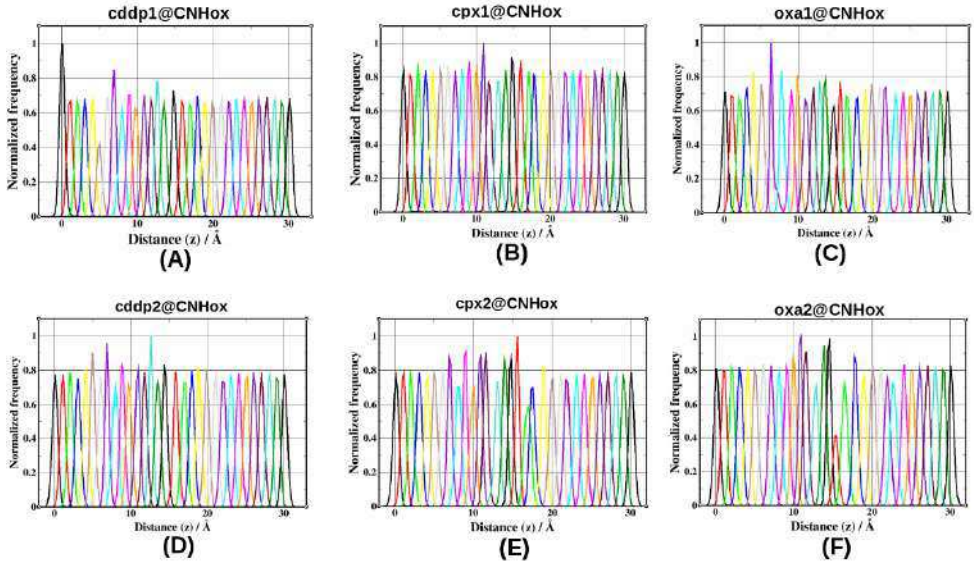

Reference: Own author (2022).

Figure B.18 - Variation of the van der Waals (ΔE_{vdw}) and the electrostatic (ΔE_{elec}) contributions to the binding free energy ($\Delta_b G$) referring to the windows of the US simulations which described the drug release process from the CNHox for the inclusion complexes: cddp1@CNHox and cddp2@CNHox (A), cpx1@CNHox and cpx2@CNHox (B), and oxa1@CNHox and oxa2@CNHox (C). All values were calculated using the MM/GBSA method.

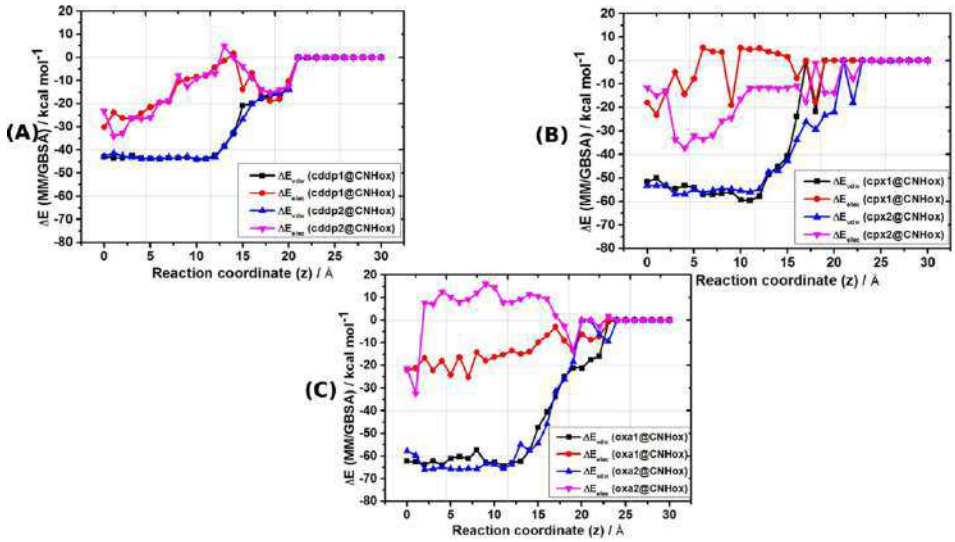

Reference: Own author (2022).

APPENDIX C - SUPPLEMENTARY INFORMATION FOR CHAPTER 5

Modeling the cellular uptake of functionalized carbon nanohorns loaded with cisplatin through a breast cancer cell membrane

Figure C.1 - The 115 Å reaction coordinate defined for the steered molecular dynamics (SMD) simulations referring to the translocation processes of the inclusion complexes (3cddp@CNHox, 3cddp@CNHf-cov, and 3cddp@CNHf-ncov) through the C_memb. While the blue arrow indicates the reaction coordinate starting from 50 Å to -65 Å, the red arrow refers to the same reaction coordinate starting from -50 Å to 65 Å.

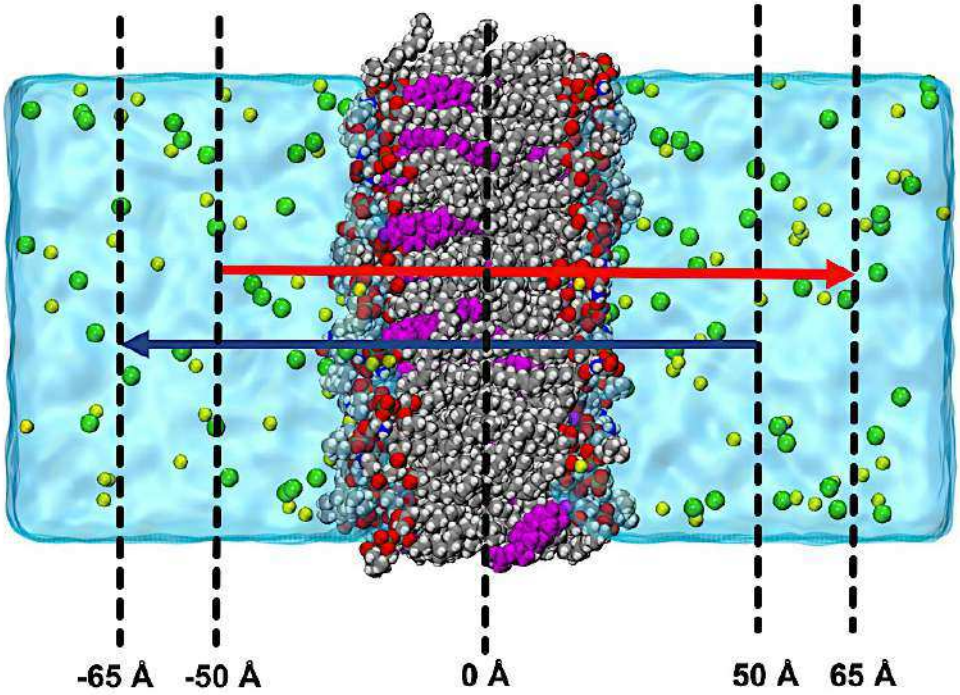

Reference: Own author (2023).

Figure C.2 - Temporal variation (moving average) of the root mean square deviation (RMSD) calculated with respect to the first frame of the 300 ns simulations referring to the CNH models and the inclusion complexes: CNHox and 3cddp@CNHox (A), CNHf-cov and 3cddp@CNHf-cov (B), and CNHf-ncov and 3cddp@CNHf-ncov. The moving averages were calculated for sets of 300 frames. The total number of 7,500 frames corresponds to the total simulation time of 300 ns. The plots consider the three simulation replicas.

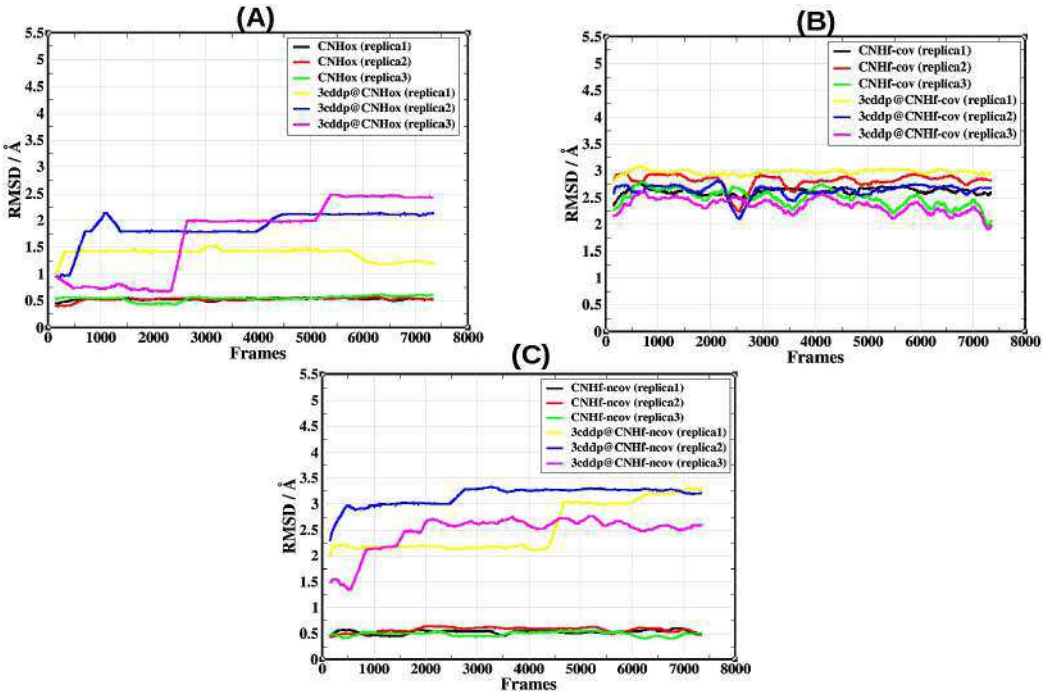

Reference: Own author (2023).

Table C.1 - Statistics of the root mean square deviation (RMSD) referring to the molecular dynamics simulations of the carbon nanohorn (CNH) models and their inclusion complexes with cisplatin (cddp) molecules.

System	Equilibration stage		Production stage	
	RMSD ± std / Å[a]		RMSD ± std / Å	
	CNH	Inclusion complex	CNH	Inclusion complex
3cddp@CNHox	0.47±0.07 [b]	1.58±0.40 [b]	0.42±0.06 [e]	0.49±0.13 [e]
3cddp@CNHf-cov	2.60±0.30 [c]	2.65±0.24 [c]	1.40±0.40 [f]	1.44±0.33 [f]
3cddp@CNHf-ncov	0.47±0.08 [d]	2.54±0.33 [d]	0.44±0.08 [g]	0.90±0.27 [g]

[a]The values were calculated with respect to the first frame of the 300 ns runs referring to either the CNH models or the inclusion complexes. Each value is an average of the simulation triplicates. The standard deviation (std) is also presented. [b]The equilibration time for the CNHox was 25 ns while the equilibration time for the 3cddp@CNHox was 240 ns. [c]The equilibration time for the CNHf-cov was 40 ns while the equilibration time for the 3cddp@CNHf-cov was 120 ns. [d]The equilibration time for the CNHf-ncov was 25 ns while the equilibration time for the 3cddp@CNHfn-cov was 190 ns. [e]The production dynamics times of the CNHox and the 3cddp@CNHox were 275 ns and 60 ns, respectively. [f]The production dynamics times of the CNHf-cov and the 3cddp@CNHf-cov were 275 ns and 120 ns, respectively. [g]The production dynamics times of the CNHf-ncov and the 3cddp@CNHf-ncov were 275 ns and 110 ns, respectively.
Reference: Own author (2023).

Figure C.3 - Temporal evolution of the temperature (A), density (B), volume (C), pressure (D), kinetic and potential energy (E), and total energy (F) referring to the molecular dynamics simulation (300 ns) of the 3cddp@CNHox system (replica 1). The red line represents the running averages calculated for sets of 300 frames.

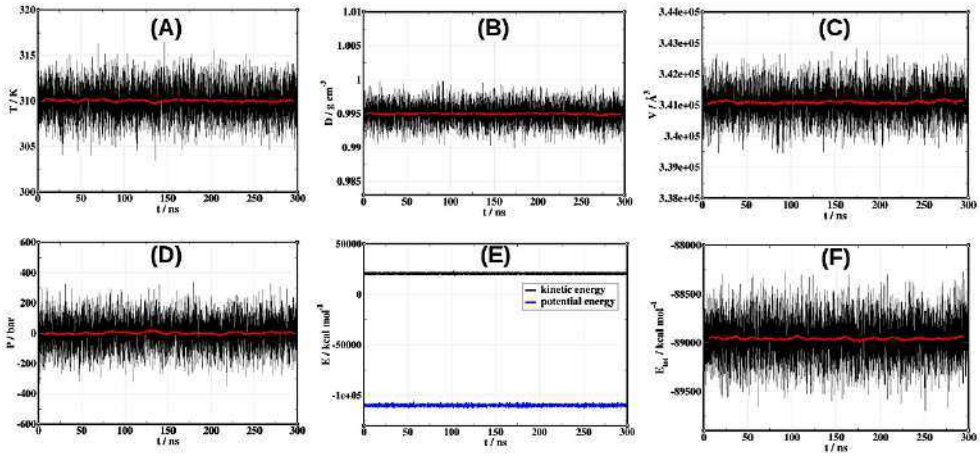

Reference: Own author (2023).

Table C.2 - Statistics of the evolution of the main thermodynamic properties referring to the molecular dynamics simulations of the inclusion complexes studied in this work during their equilibration stage.

Complex	T / K	D / g cm^{-3}	V / Å^3	E_{pot} / kcal mol^{-1}	E_{kin} / kcal mol^{-1}	E_{tot} / kcal mol^{-1}
	<A>±Std.	<A>±Std.	<A>±Std.	<A>±Std.	<A>±Std.	<A>±Std.
3cddp@CNHox	310.0±2.0	1.00±0.00	341600.00±500.00	-109460.00±160.00	20680.00±100.00	-88950.00±200.00
3cddp@CNHf-cov	310.0±2.0	0.99±0.00	380040.00±510.00	-121660.00±170.00	23040.00±120.00	-98620.00±210.00
3cddp@CNHf-ncov	310.0±2.0	0.99±0.00	402440.00±530.00	-129040.00±180.00	24400.00±120.00	-104630.00±150.00

*The T, D, V, E_{pot}, E_{kin}, ,E_{tot}, <A>, and Std. terms correspond to the temperature, density, volume, potential energy, kinetic energy, total energy, average value, and standard deviation value, respectively. Each temporal average was calculated by considering the simulation triplicates.

Reference: Own author (2023).

Figure C.4 - Temporal variation of the distance between the centers of mass of both membrane (C_memb) and carbon nanohorn (CNH) models that compose the inclusion complexes studied in this work: 3cddp@CNHox (A), 3cddp@CNHf-cov (B), and 3cddp@CNHf-ncov (C). While the blue line corresponds to the steered molecular dynamics (SMD) simulation from 50 Å to -65 Å along the reaction coordinate, the red line refers to the same simulation from -50 Å to 65 Å along the reaction coordinate.

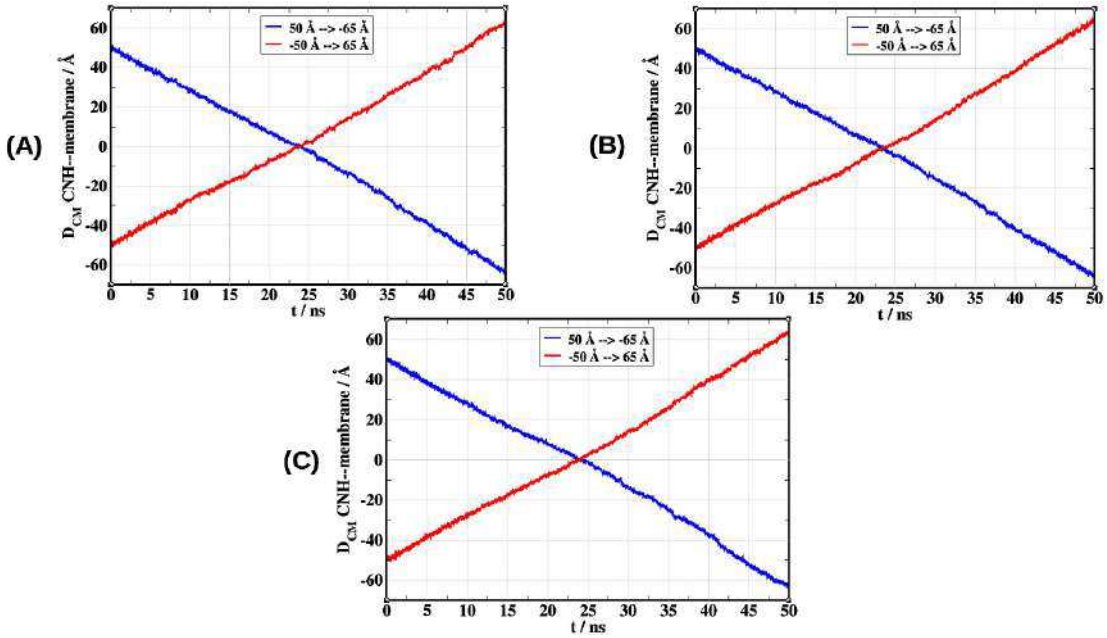

Reference: Own author (2023).

Figure C.5 - Permeation of inclusion complexes. Main frames of the steered molecular dynamics (SMD) simulations referring to the permeation processes (reaction coordinate: -50 Å → 65 Å) of the inclusion complexes through a cancer cell membrane (C_memb): 3cddp@CNHox>C_memb (A), 3cddp@CNHf-cov>C_memb (B), and 3cddp@CNHf-ncov>C_memb (C). The violet, red, orange, and tan in the membrane indicate the PC, PE, PS, and PGR polar heads of lipids, while the magenta and silver represent the CHL and OL species. For the nanostructures, the silver, red, blue, white, green, and ochre color correspond to the C, O, N, H, Cl, and Pt atoms. Water molecules are omitted for clarity. Dashed lines delimit the sates of the mechanism.

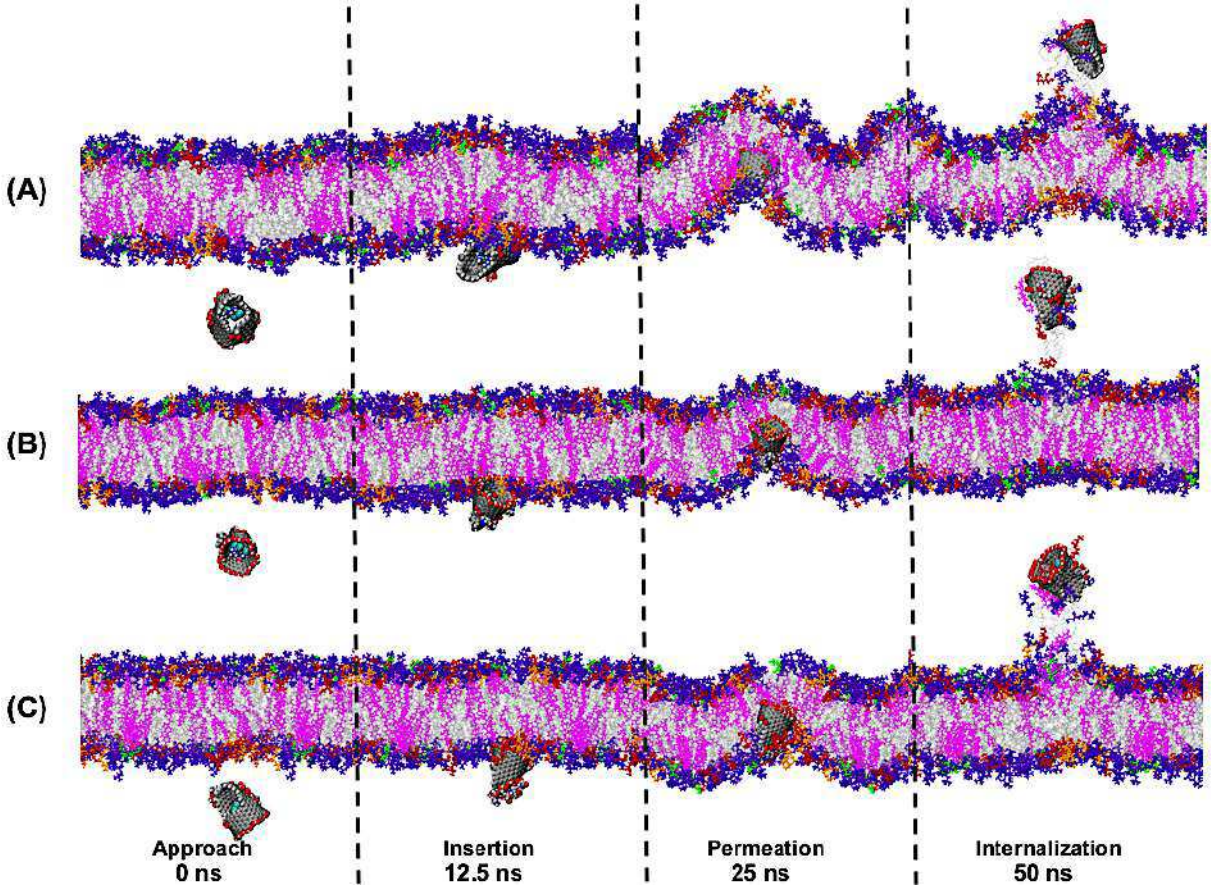

Reference: Own author (2023).

Figure C.6 - Numbering scheme of the C atoms located at the oleoyl chains of the lipid 1,2-dioleoyl-*sn*-glycero-3-phosphocholine (DOPC) considered in the calculation of the deuterium order parameter (SCD). The same lipid tails are present in the other lipids of the C_memb: 1,2-dioleoyl-*sn*-glycero-3-phosphoethanolamine (DOPE), 1,2-dioleoyl-*sn*-glycero-3-[phospho-rac-(1-glycerol)] (DOPGR), and 1,2-dioleoyl-*sn*-glycero-3-phospho-L-serine (DOPS). The silver, white, blue, red, and ochre represent the C, H, N, O, and S atoms.

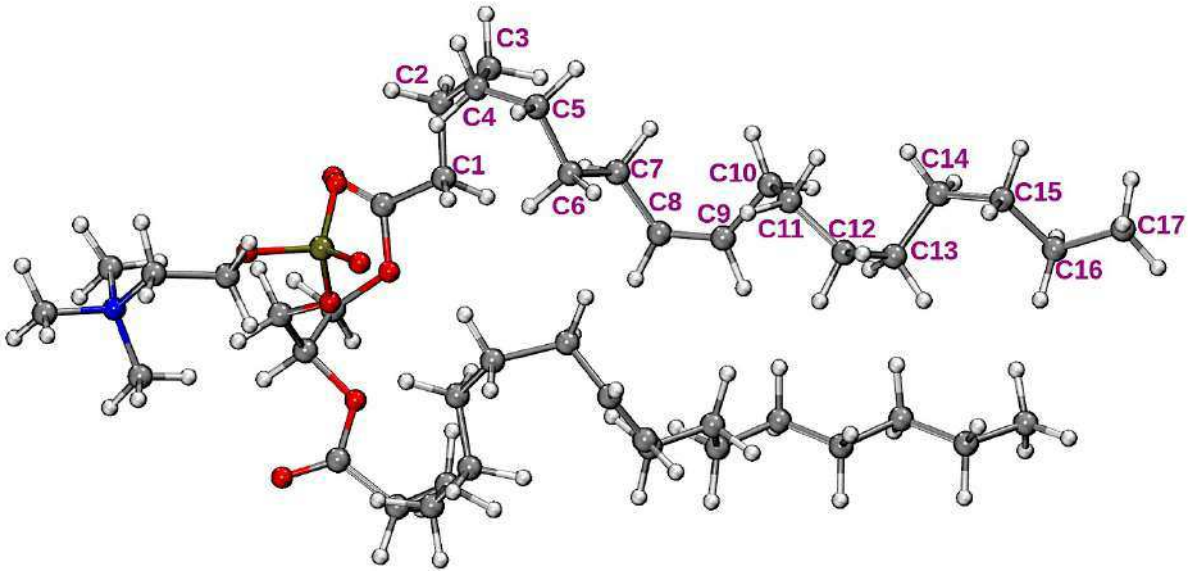

Reference: Own author (2023).

Figure C.7 - Numbering scheme of the atoms referring to the oxidized carbon nanohorn (CNHox) model. Side view (A) and front view from the open end. (B)

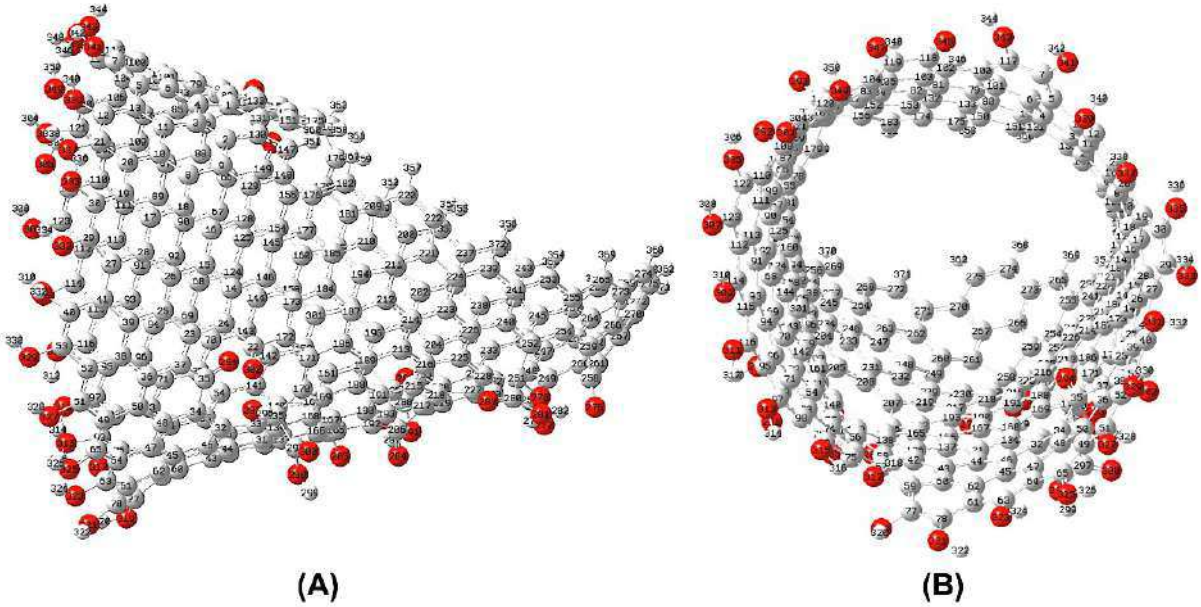

Reference: Own author (2023).

Figure C.8 - Numbering scheme of the atoms referring to the covalently functionalized carbon nanohorn (CNHf-cov) model. Side view (A) and front view from the open end. (B)

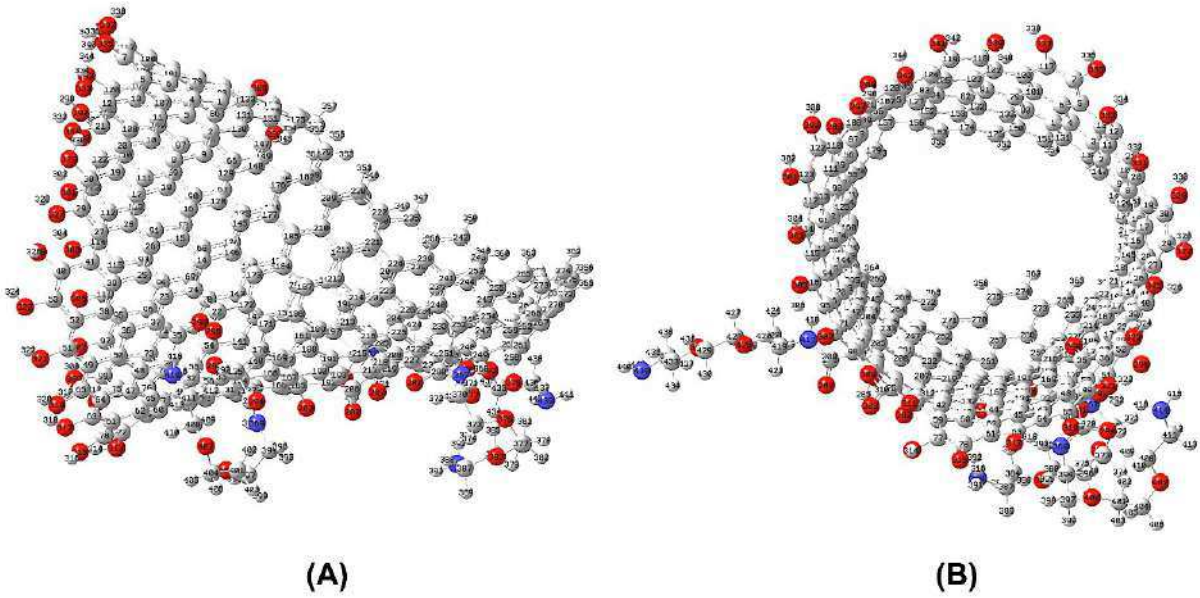

Reference: Own author (2023).

Figure C.9 - Numbering scheme of the atoms referring to the noncovalently functionalized carbon nanohorn (CNHf-ncov) model. Side view (A) and front view from the open end. (B)

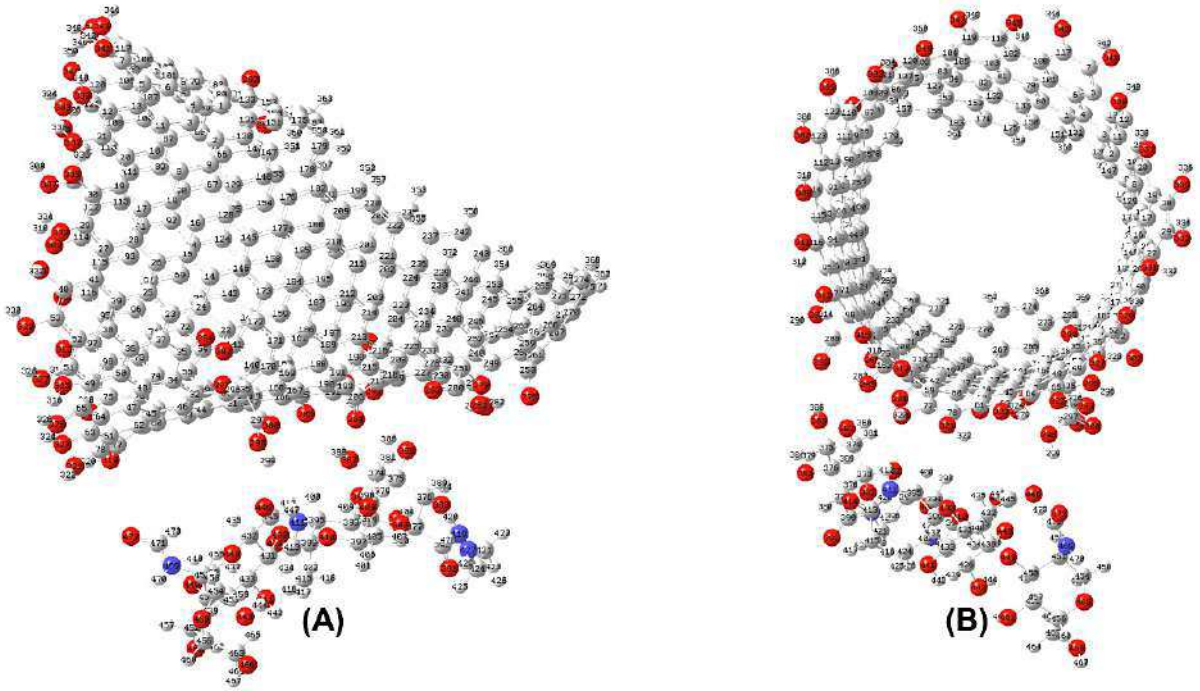

Reference: Own author (2023).

Figure C.10 - Temporal variation of the spatial distribution referring to both three cddp molecules encapsulated in the CNHf-ncov model that presents a modified chain of hyaluronic acid (HA-NH_2) adsorbed on its surface. The distributions represent the overlap of 750 frames selected from the production runs in triplicate. Green, blue, ochre, silver, and red colors in the distributions refer to the mobility of the Cl, N, Pt, C, and O atoms during the simulations.

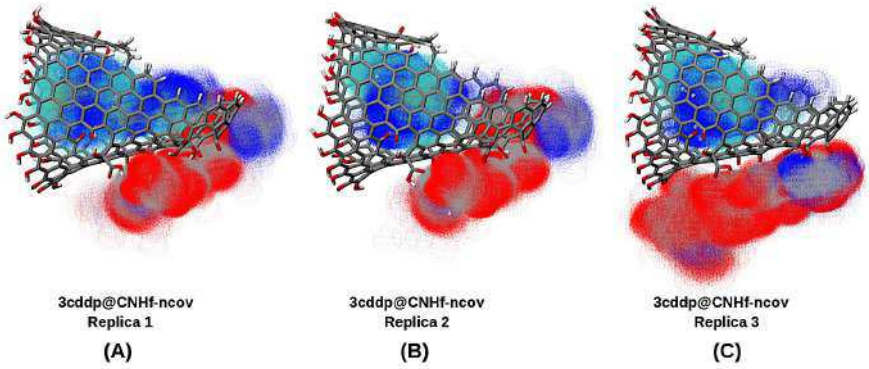

Reference: Own author (2023).

Figure C.11 - The potential wells shown in the potential of mean forces (PMF) referring to the transmembrane transport of the inclusion complexes 3cddp@CNHox, 3cddp@CNHf-cov, and 3cddp@CNHf-ncov through the C_memb considering the two directions along the reaction coordinate (50 Å → -65 Å and -50 Å → 65 Å): 3cddp@CNHox>C_memb (A), 3cddp@CNHf-cov>C_memb (B), and 3cddp@CNHf-ncov>C_memb (C). While the blue arrow refers to translocation from 50 Å to -65 Å along the reaction coordinate, the red arrow represents the translocation from -50 Å to 65 Å along the same axis. The black arrow indicates the energy of the potential well.

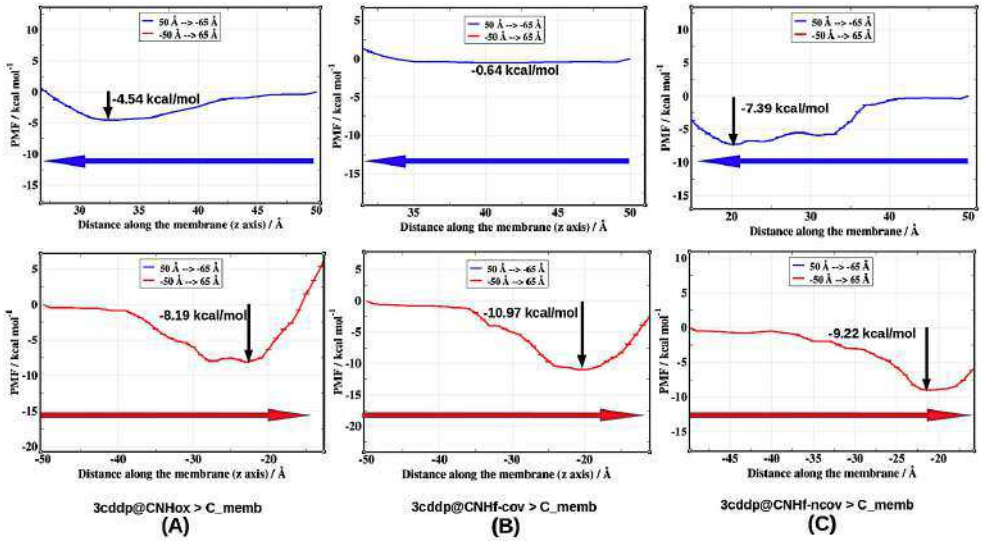

Reference: Own author (2023).

Figure C.12 - Histograms of the probability distributions referring to the 115 windows sampled with the US method along the reaction coordinate for the transmembrane permeation processes of the three inclusion complexes through the C_memb model: 3cddp@CNHox>C_memb (A), 3cddp@CNHf-cov>C_memb (B), and 3cddp@CNHf-ncov>C_memb (C).

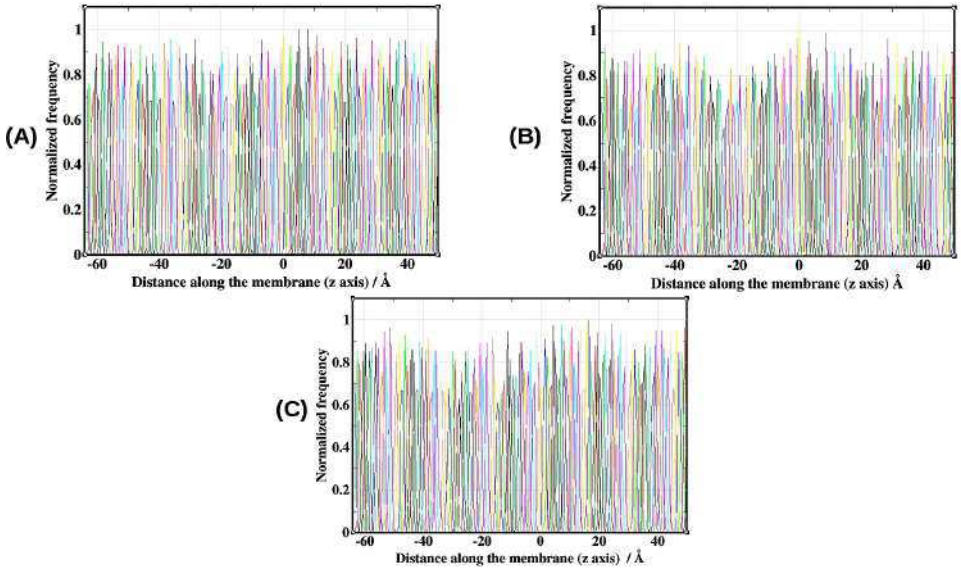

Reference: Own author (2023).

Figure C.13 - Final frames of the 300 ns molecular dynamics simulations (replica 1) of the inclusion complexes formed by three cisplatin (cddp) molecules encapsulated into an oxidized carbon nanohorn (CNHox), a carbon nanohorn with a covalent functionalization (CNHf-cov), and a carbon nanohorn with a noncovalent functionalization (CNHf-ncov): 3cddp@CNHox (A), 3cddp@CNHf-cov (B), and 3cddp@CNHf-ncov (C).

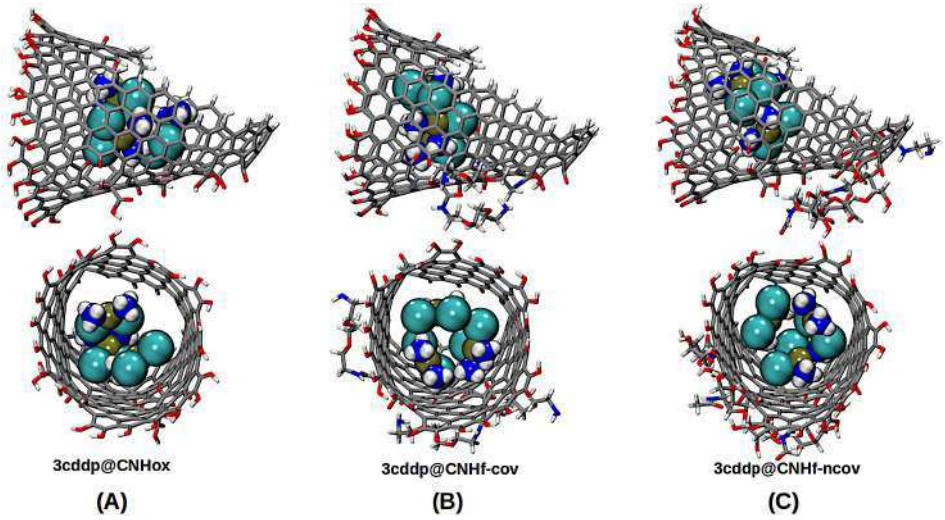

Reference: Own author (2023).

Figure C.14 - Final frames of the 300 ns molecular dynamics simulations (replica 2) of the inclusion complexes formed by three cisplatin (cddp) molecules encapsulated into an oxidized carbon nanohorn (CNHox), a carbon nanohorn with a covalent functionalization (CNHf-cov), and a carbon nanohorn with a noncovalent functionalization (CNHf-ncov): 3cddp@CNHox (A), 3cddp@CNHf-cov (B), and 3cddp@CNHf-ncov (C).

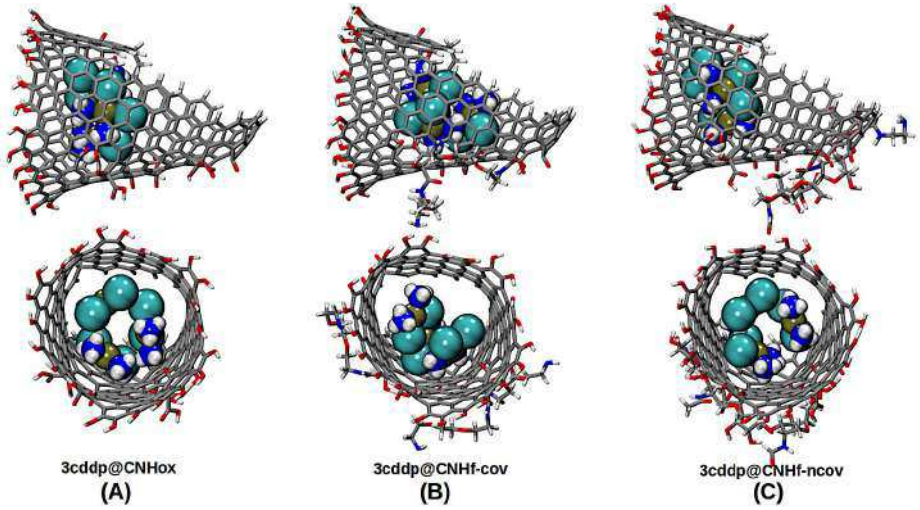

Reference: Own author (2023).

Figure C.15 - Final frames of the 300 ns molecular dynamics simulations (replica 3) of the inclusion complexes formed by three cisplatin (cddp) molecules encapsulated into an oxidized carbon nanohorn (CNHox), a carbon nanohorn with a covalent functionalization (CNHf-cov), and a carbon nanohorn with a noncovalent functionalization (CNHf-ncov): 3cddp@CNHox (A), 3cddp@CNHf-cov (B), and 3cddp@CNHf-ncov (C).

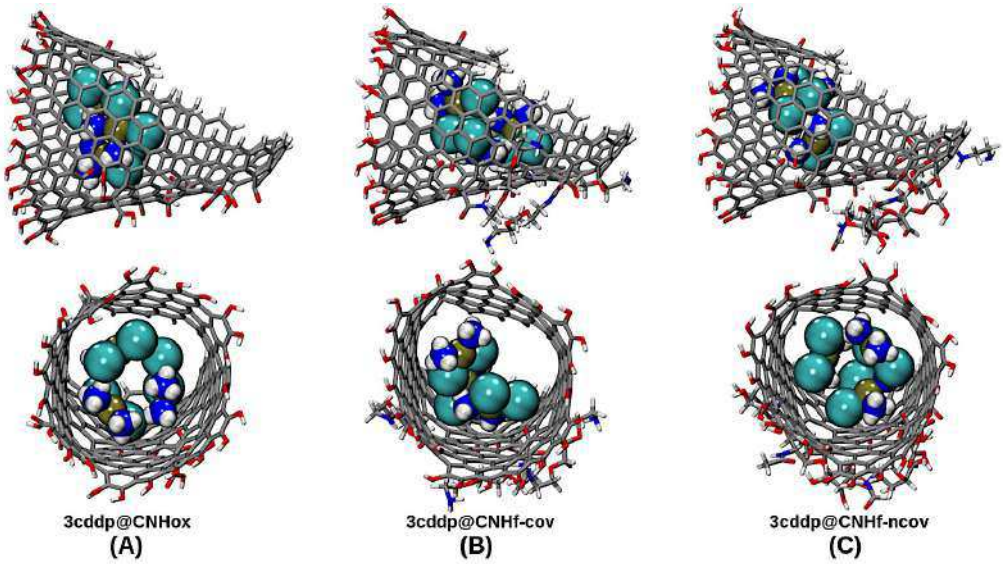

Reference: Own author (2023).

Table C.3 - Statistics of the root mean square deviation (RMSD) referring to the molecular dynamics simulations of the cisplatin (cddp) cluster in two situations: encapsulated in CNH models forming the free inclusion complexes in aqueous solution, and encapsulated in the same CNHs models during their translocation through a breast cancer cell membrane (C_memb) prototype.

System	Equilibration stage[a]	Production stage[a]	Pulling stage (C_memb)[b]
	RMSD ± std / Å[c]	RMSD ± std / Å	RMSD ± std / Å
	3cddp[d]	3cddp	3cddp
3cddp@CNHox	1.63±0.43	0.48±0.22	0.39±0.11
3cddp@CNHf-cov	1.21±0.19	0.75±0.25	0.93±0.13
3cddp@CNHf-ncov	2.05±0.69	1.07±0.60	0.67±0.15

[a]These stages correspond to the simulation of the free inclusion complexes in aqueous soluction discussed in section 3.1. The values were obtained by the differences (CNH and inclusion complex) in Table S1. [b]This stage corresponds to the simulations referring to the translocation (50 ns) of the inclusion complexes through the C_memb model. [c]The RMSD values were calculated using a reference the first frame of each trajectory (stage). The term std refers to the standard deviation value of the RMSD. [d]The cisplatin cluster is formed by three units of this drug.
Reference: Own author (2023).

Figure C.16 - Temporal variation of the spatial distribution referring to the three cisplatin (cddp) molecules encapsulated in the oxidized carbon nanohorn (CNHox) model, the covalently functionalized carbon nanohorn (CNHf-cov) model, and the noncovalently functionalized carbon nanohorn (CNHf-ncov) model. The distributions represent the overlap of 750 frames selected from the production runs (replica 1). Green, blue, and ochre colors in the distributions refer to the mobility of the Cl, N, and Pt atoms during the simulations.

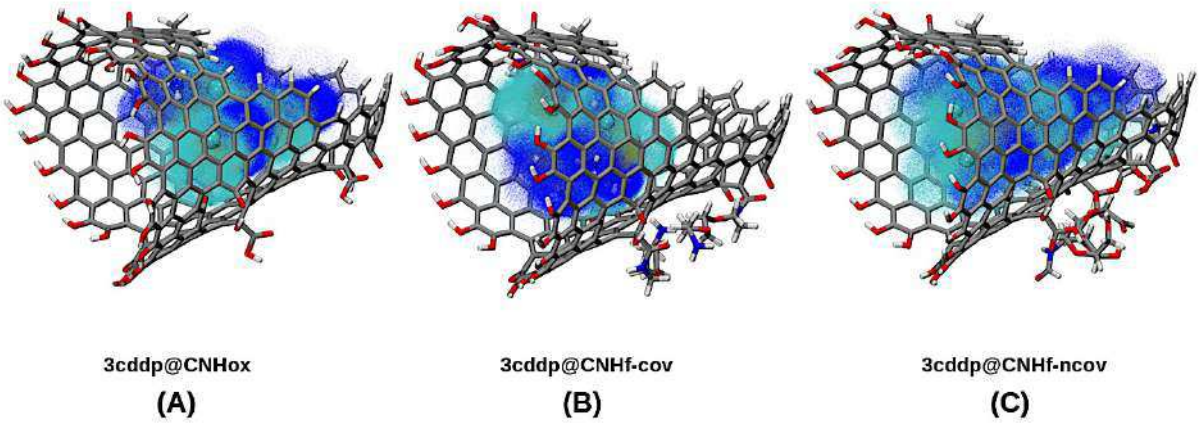

Reference: Own author (2023).

Figure C.17 - Temporal variation of the spatial distribution referring to the three cisplatin (cddp) molecules encapsulated in the oxidized carbon nanohorn (CNHox) model, the covalently functionalized carbon nanohorn (CNHf-cov) model, and the non-covalently functionalized carbon nanohorn (CNHf-ncov) model. The distributions represent the overlap of 750 frames selected from the production runs (replica 2). Green, blue, and ochre colors in the distributions refer to the mobility of the Cl, N, and Pt atoms during the simulations.

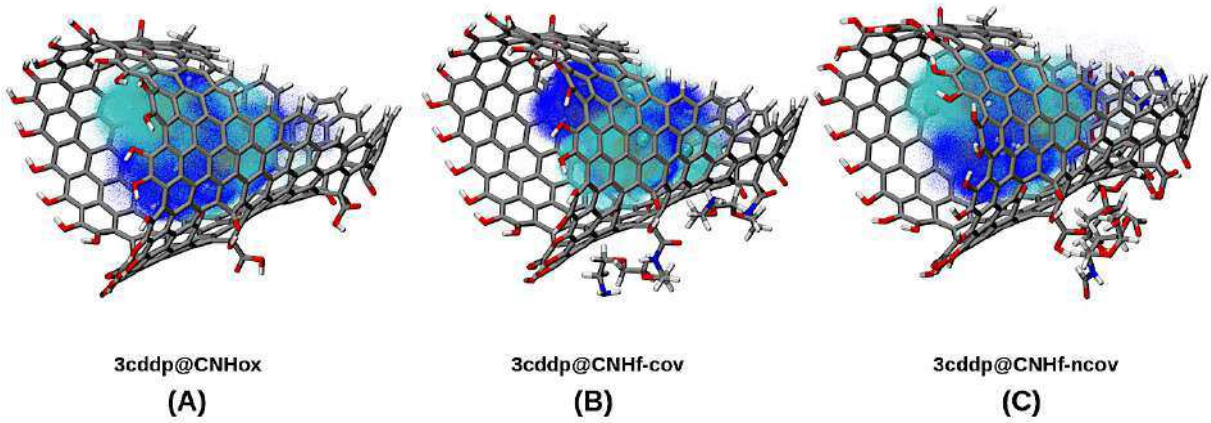

Reference: Own author (2023).

Figure C.18 - Temporal variation of the spatial distribution referring to the three cisplatin (cddp) molecules encapsulated in the oxidized carbon nanohorn (CNHox) model, the covalently functionalized carbon nanohorn (CNHf-cov) model, and the non-covalently functionalized carbon nanohorn (CNHf-ncov) model. The distributions represent the overlap of 750 frames selected from the production runs (replica 3). Green, blue, and ochre colors in the distributions refer to the mobility of the Cl, N, and Pt atoms during the simulations.

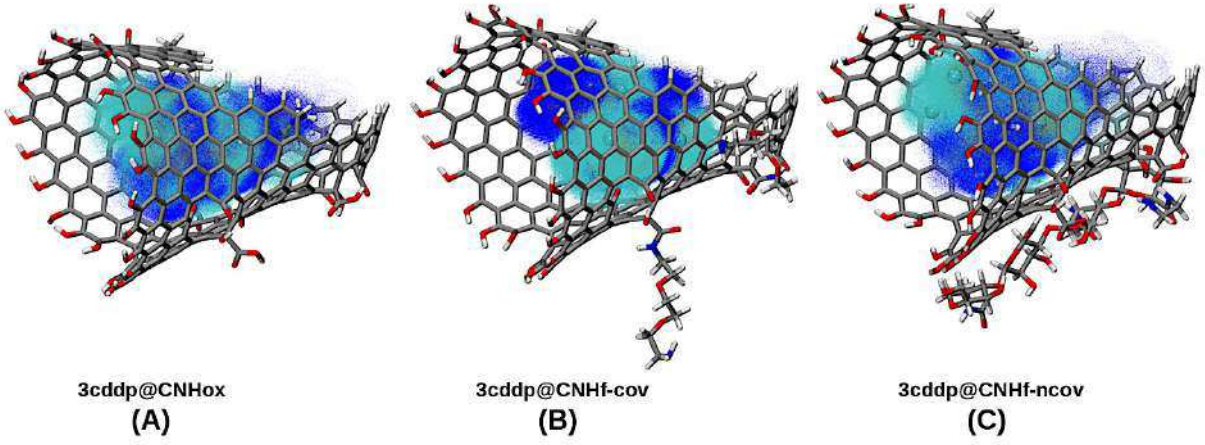

Reference: Own author (2023).

Figure C.19 - Spatial distribution of the inclusion complexes over their transmembrane transport (-50 Å → 65 Å) through the breast cancer cell membrane (C_memb) as function of time during the steered molecular dynamics. The image illustrates the overlapping of only 13 frames for clarity: 3cddp@CNHox>C_memb (A), 3cddp@CNHf-cov (B), and 3cddp@CNHf-ncov (C).

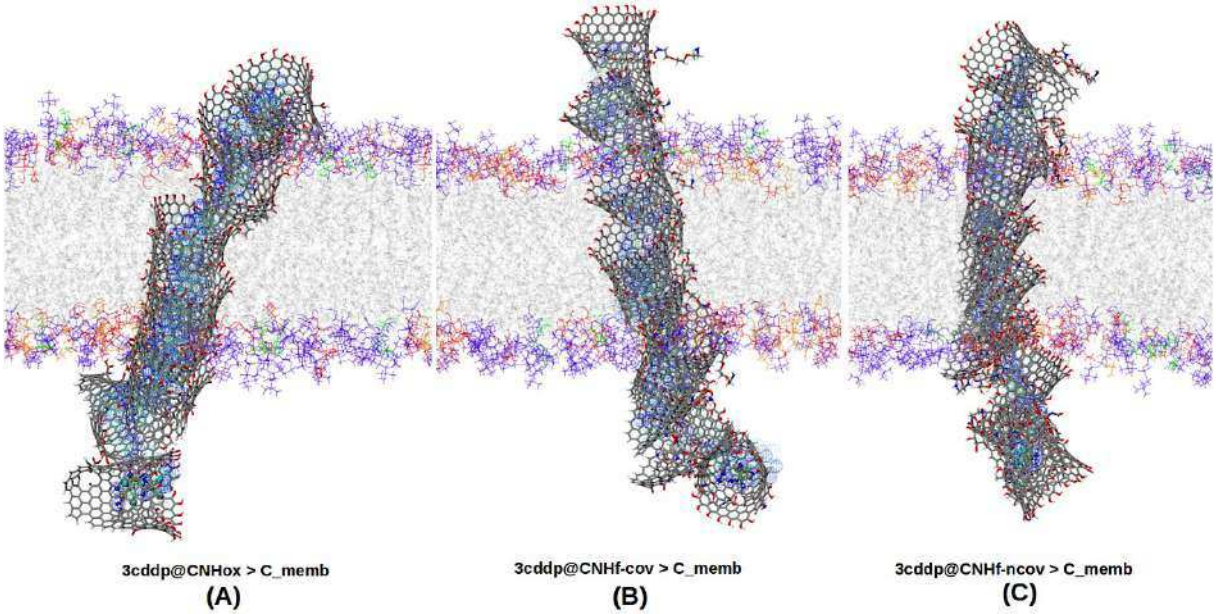

Reference: Own author (2023).

APPENDIX D - SUPPLEMENTARY INFORMATION FOR CHAPTER 6

Translocation processes of Pt(II)-based drugs through human breast cancer cell membrane: in silico experiments

Figure D.1 - Structures of the lipids that compose the membrane model of a breast cancer cell (c_memb): 1,2-dioleoyl-*sn*-glycero-3-phosphocholine (DOPC), 1,2-dioleoyl-*sn*-glycero-3-phosphoethanolamine (DOPE), 1,2-dioleoyl-*sn*-glycero-3-phospho-L-serine (DOPS), 1,2-dioleoyl-*sn*-glycero-3-[phospho-rac-(1-glycerol)] (DOPG), and cholesterol (CHL). The silver, white, red, blue, and ochre spheres represent the C, H, O, N, and S atoms.

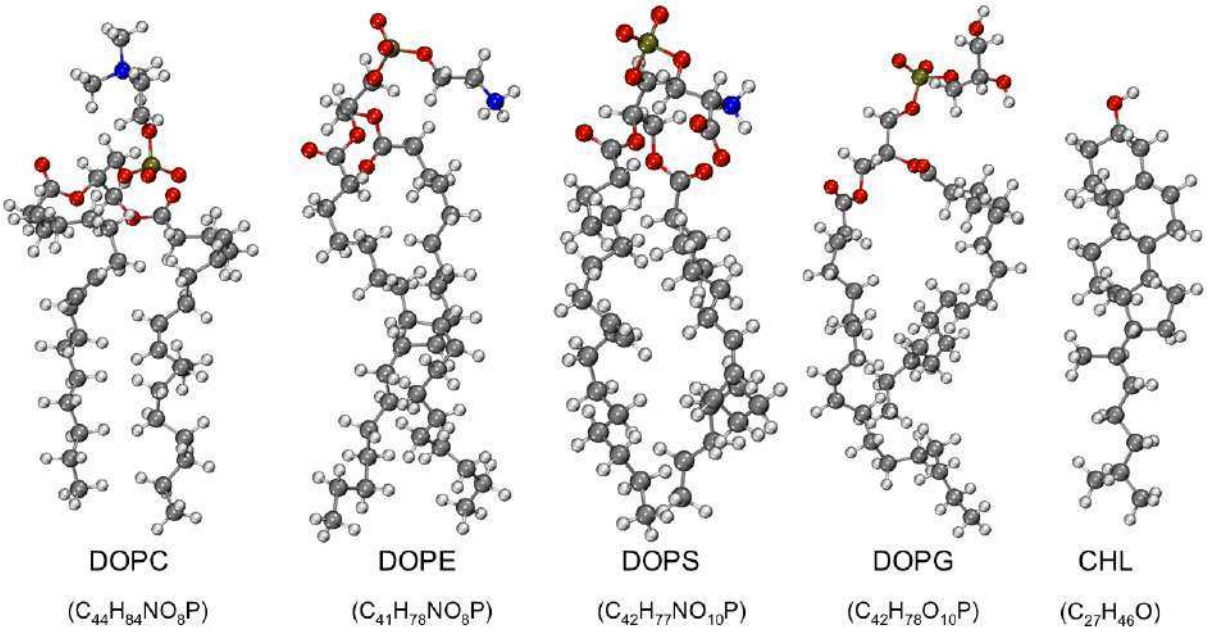

Reference: Own author (2023).

Figure D.2 - Reaction coordinate for the steered molecular dynamics simulations referring to the translocation processes (influx and efflux) of the Pt(II)-based drugs (cisplatin, carboplatin, and oxaliplatin) through the breast cancer cell membrane (c_memb) model. The black arrow indicates the coordinate for the drug influx (70 Å → 0 Å) whereas the red arrow indicates the coordinate for the drug efflux (0 Å → 70 Å).

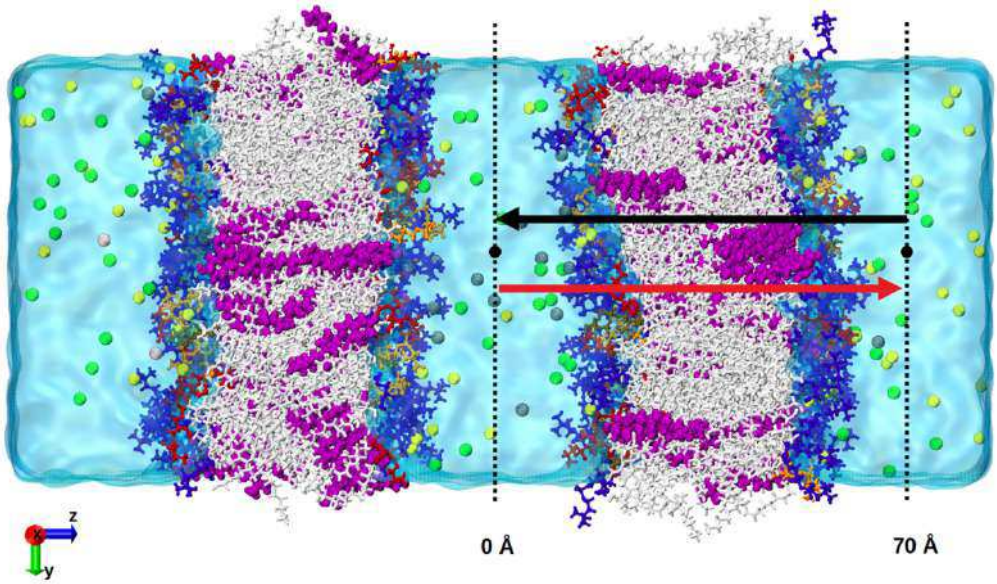

Reference: Own author (2023).

Figure D.3 - Temporal variation of the simulation properties for c_memb during the last 100 ns of the 470 ns run (c_memb model): temperature (A), pressure (B), volume (C), and density (D).

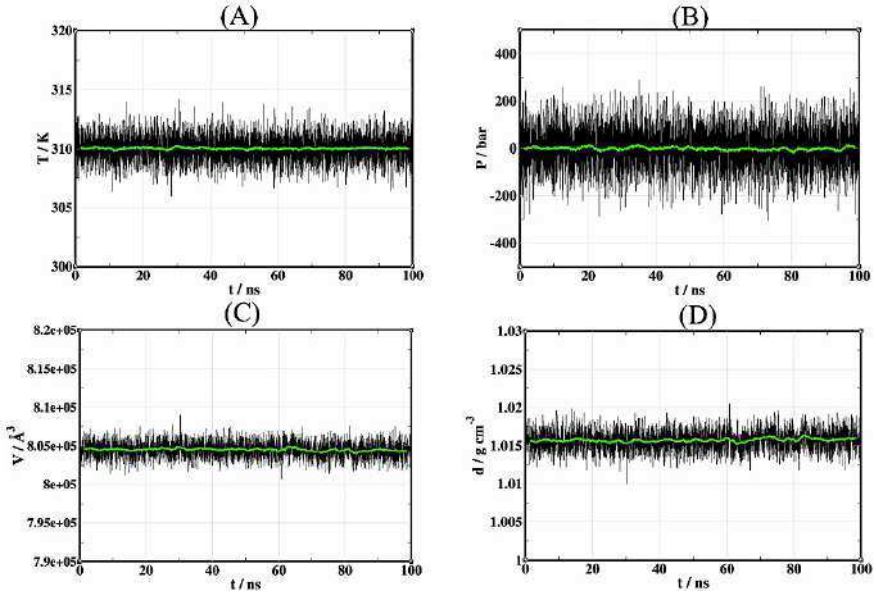

Reference: Own author (2023).

Figure D.4 - Evolution of the energies of the entire system (c_memb) during the last 100 ns of the 470 ns run: kinetic energy (A), potential energy (B), and total energy (C).

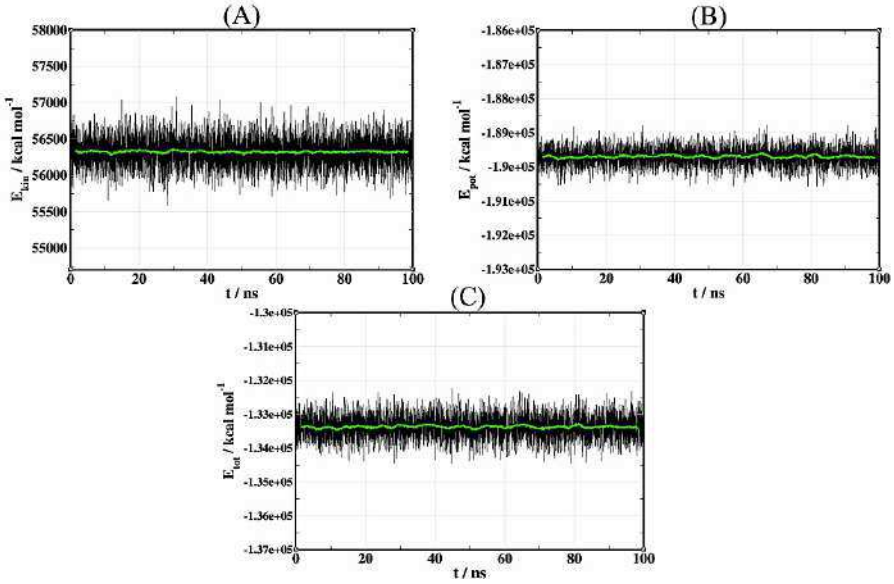

Reference: Own author (2023).

Table D.1 - Statistics of the energetic components referring to the total potential energy of the breast cancer cell membrane (c_memb) model during the last 100 ns of the 470 ns equilibration run.

Energetic components	**Energies / kcal mol^{-1}**		
	<E> ± std.	**Max.**	**Min.**
E_{bond}	5501.53±4.56	5512.68	5489.16
E_{angle}	21972.40±7.45	21991.90	21952.30
E_{dihed}	14695.00±10.75	14721.70	14670.80
E_{vdw1-4}	4937.70±2.44	4944.46	4932.64
E_{vdw}	-14629.20±30.70	-14552.40	-14703.90
$E_{elec1-4}$	-38017.10±14.89	-37970.10	-38056.60
E_{elec}	-8172.93±172.77	-7615.01	-8563.30
E_{tot}	-13712.60±183.00	-13159.70	-14128.20

The terms E_{bond}, E_{angle}, E_{dihed}, E_{vdw1-4}, E_{vdw}, $E_{elec1-4}$, E_{elec}, E_{tot}, <E>, std, Max., and Min refer to the energy related to the bond stretching, energy related to the angle bending, energy related to the rotations involving the dihedral angle, the van der Waals energy involving the end atoms in the dihedral angles, the total van der Waals energy, electrostatic interaction energy involving the end atoms in the dihedral angles, total electrostatic interaction energy, total potential energy, average energy, standard deviation, maximum value, and minimum value, respectively.

Reference: Own author (2023).

Figure D.5 - Evolution of the structural properties of the breast cancer cell membrane (c_memb) model considering the last 100 ns of the 470 ns run (equilibration stage): area per lipid (A) and volume per lipid (B). The green line represents the moving average for sets of 200 frames.

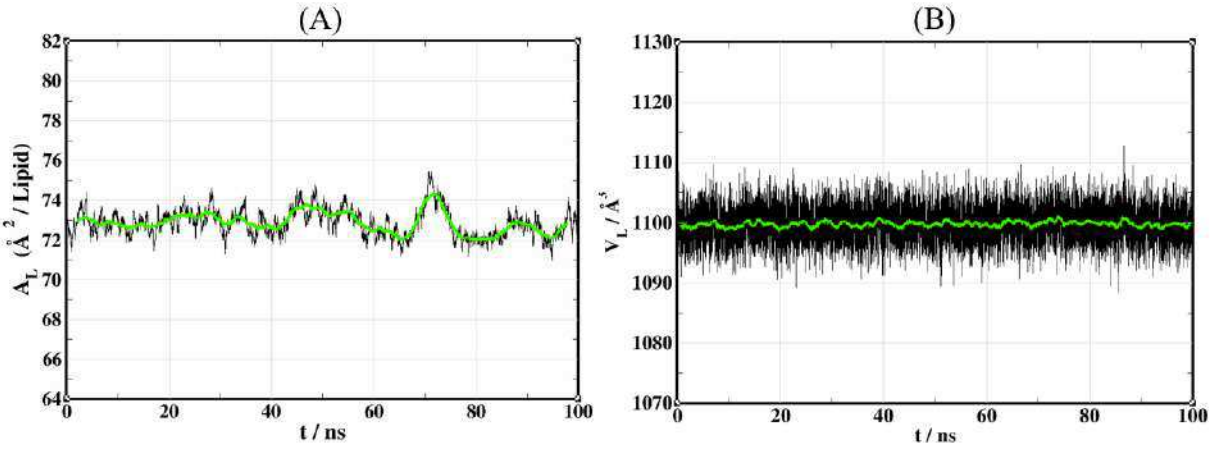

Reference: Own author (2023).

Figure D.6 - Temporal variation of the position of the Pt(II)-based drugs during their permeation (efflux, 0 Å → 70 Å) through the breast cancer cell membrane (c_memb): cddp>c_memb (A), cpx>c_memb (B), and oxa>c_mem (C). The frames of the drugs, which were collected from the steered molecular dynamics simulations of 72 ns, are superimposed keeping the membrane fixed.

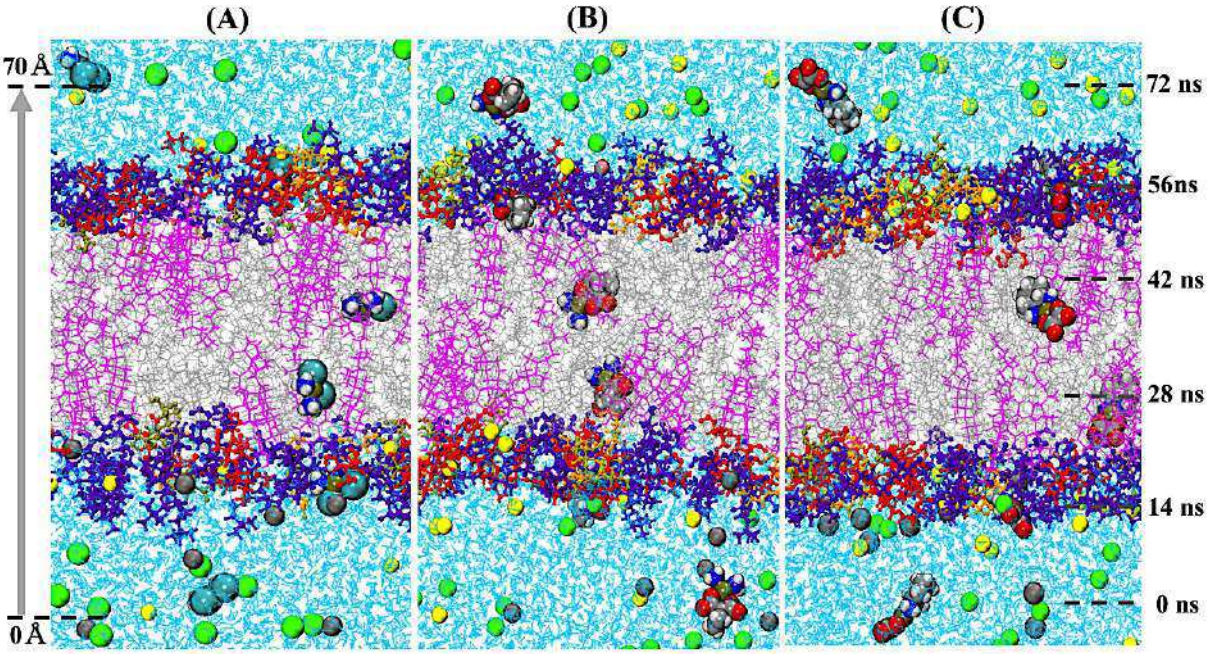

Reference: Own author (2023).

Figure D.7 - Efflux mechanism (0 Å → 70 Å) of the Pt(II)-based drugs through the breast cancer cell membrane (c_memb) model using steered molecular dynamics simulations: cddp>c_memb (A), cpx>c_memb (B), and oxa>c_mem (C).

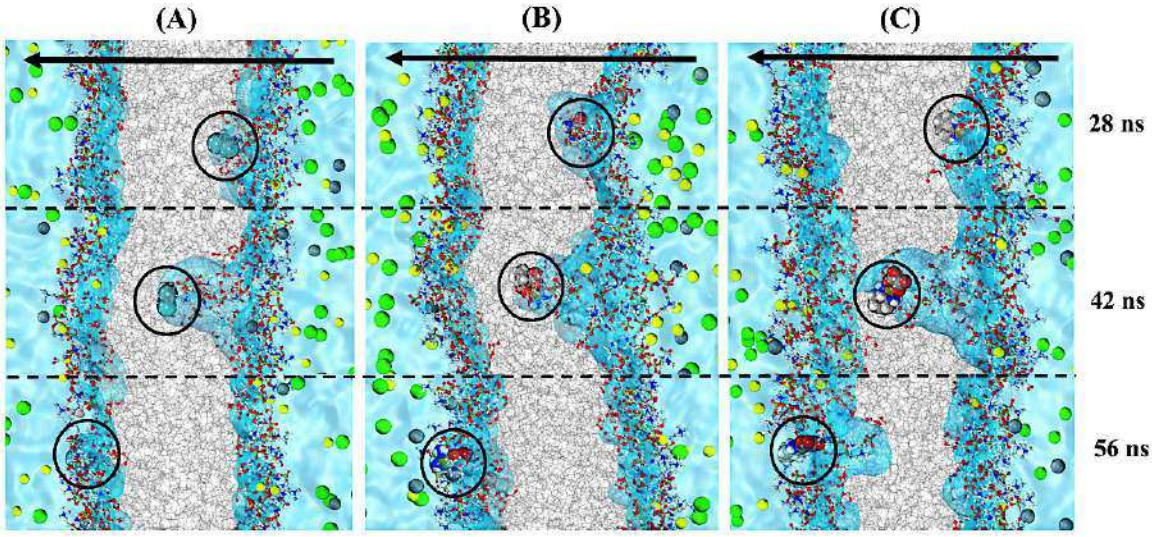

Reference: Own author (2023).

Figure D.8 - Profiles of the average density of water molecules (number of water molecules / Å3) along the breast cancer cell membrane (c_memb) model during the permeation processes of the Pt(II)-based drugs: influx of cddp (A), influx of cpx (B), influx of oxa (C), efflux of cddp (D), efflux of cpx (E), and efflux of oxa (F). The profiles were computed from the 72 ns steered molecular dynamics (SMD) simulations. The black dashed lines indicate the directions of the influx (A, B, and C) and efflux (D, E, and F) processes of the drugs.

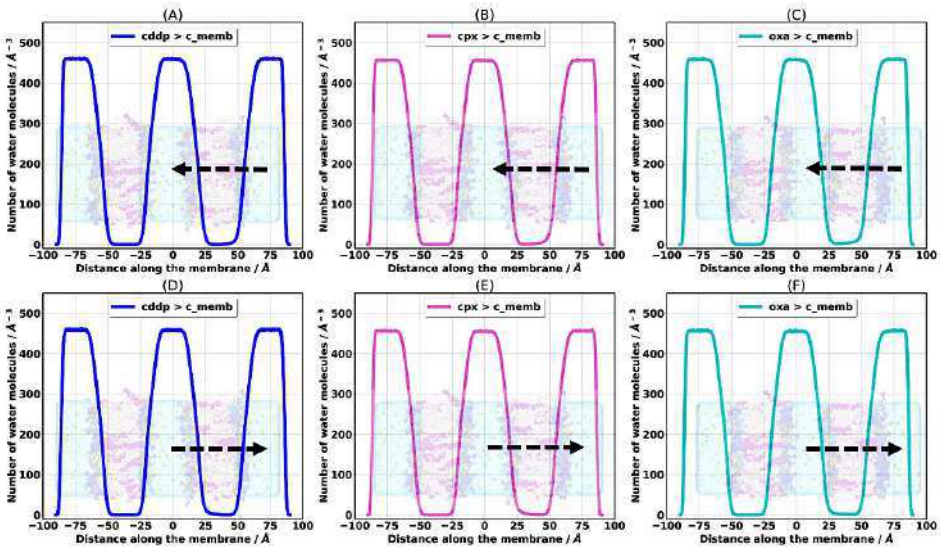

Reference: Own author (2023).

Figure D.9 - Moving average of the the number of contacts drug--lipid established during the efflux process (0 Å → 70 Å) of the Pt(II)-based drugs through the breast cancer cell membrane (c_memb) model. The symbols PC, PE, PS, PG, CHL, OL, cddp, cpx, and oxa stand for phosphocholine, phosphoethanolamine, phospho-L-serine, phospho-rac-(1-glycerol), cholesterol, oleoyl, cisplatin, carboplatin, and oxaliplatin, respectively.

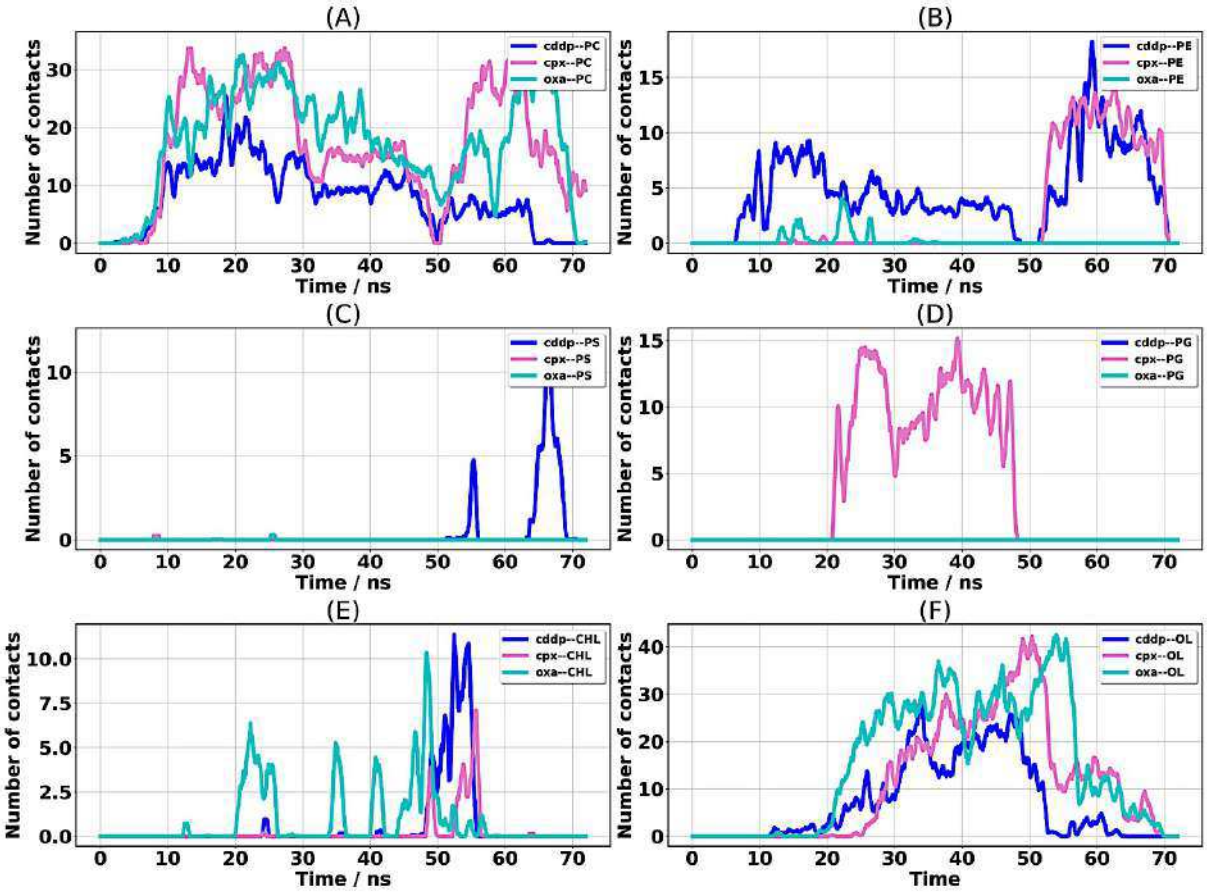

Reference: Own author (2023).

Figure D.10 - Histograms of the probability distribution referring to the 70 windows sampled with the umbrella sampling method along the reaction coordinate that defined the efflux (0 Å → 70 Å) of the Pt(II)-based drugs through the breast cancer cell membrane (c_memb) model: cddp>c_memb (A), cpx>c_memb (B), and oxa>c_memb (C).

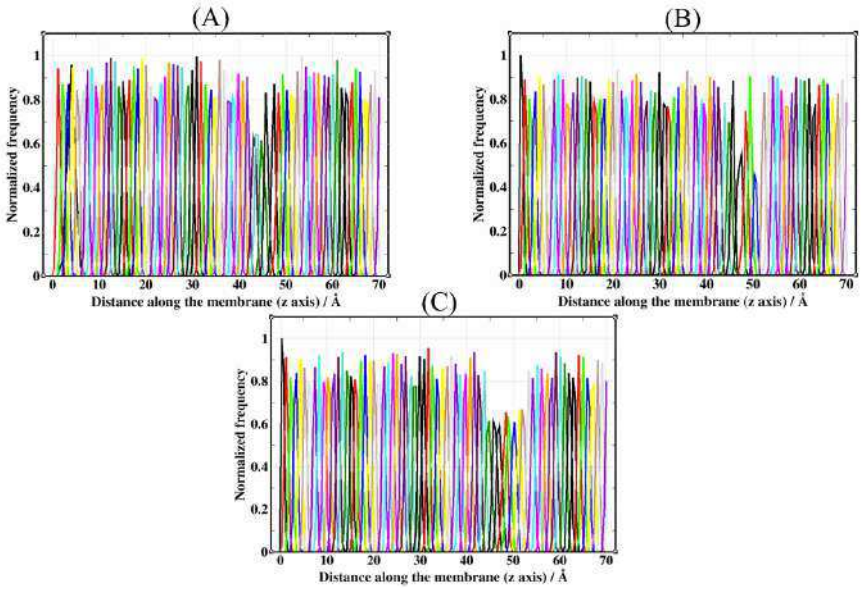

Reference: Own author (2023).

Figure D.11 - Histograms of the probability distribution referring to the 70 windows sampled with the umbrella sampling method along the reaction coordinate that defined the influx (70 Å → 0 Å) of the Pt(II)-based drugs through the breast cancer cell membrane (c_memb) model: cddp>c_memb (A), cpx>c_memb (B), and oxa>c_memb (C).

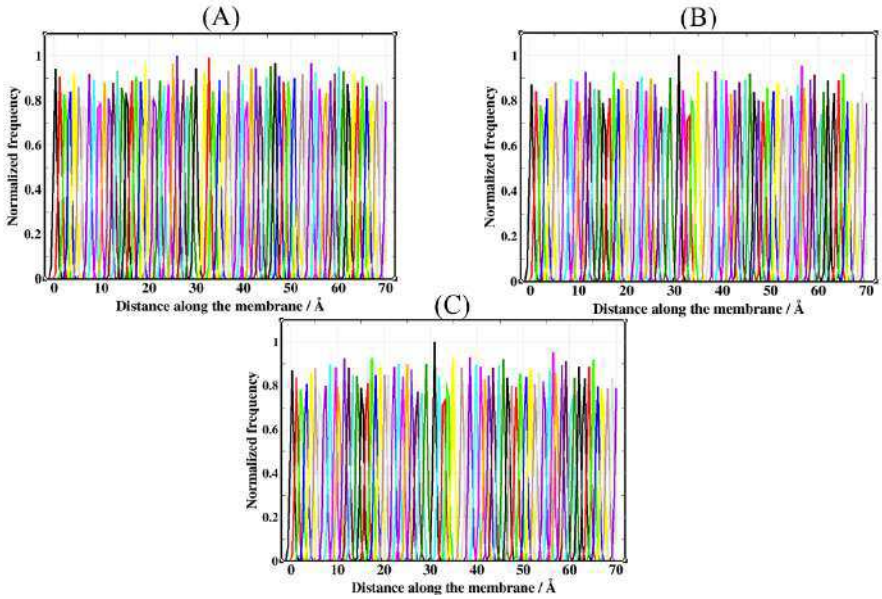

Reference: Own author (2023).

Figure D.12 - Local resistance (R(z)) profiles of the Pt(II)-based drugs (cisplatin (cddp), carboplatin (cpx), and oxaliplatin (oxa)) referring to their translocation through the breast cancer cell membrane (c_memb). The reaction coordinate was defined as the z axis perpendicular to the membrane plane considering the distance between 0 Å and 70 Å, where 0 Å represents the intracellular medium and 70 Å represents the extracellular medium: cddp>c_memb (A), cpx>c_memb (B), and oxa>c_memb (C).

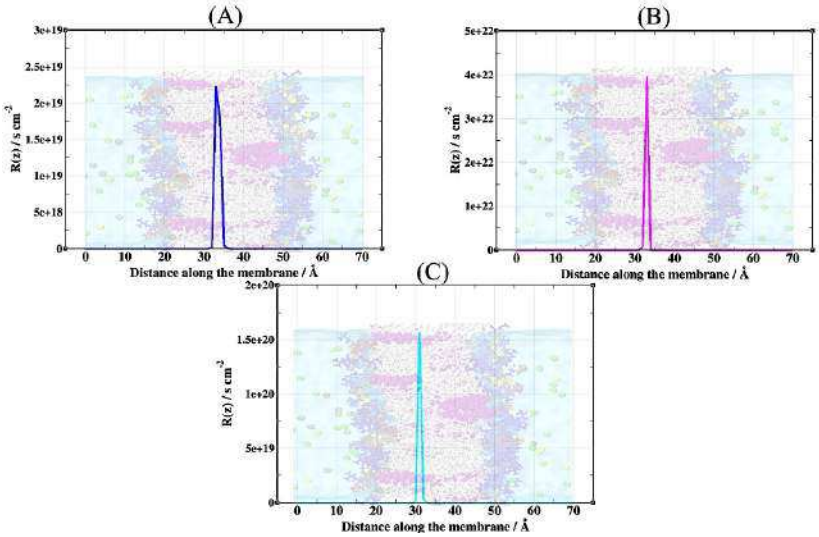

Reference: Own author (2023).

Figure D.13 - Local resistance (R(z)) profiles of cisplatin (cddp) and its hydrolyzed species (mono-aqua derivative (cdcla), and the mono-hydroxo derivative (cdclo)) referring to their translocation through the breast cancer cell membrane (c_memb). The reaction coordinate was defined as the z axis perpendicular to the membrane plane considering the distance between 0 Å and 70 Å, where 0 Å represents the intracellular medium and 70 Å represents the extracellular medium: cddp>c_memb (A), cdcla>c_memb (B), and cdclo>c_memb (C).

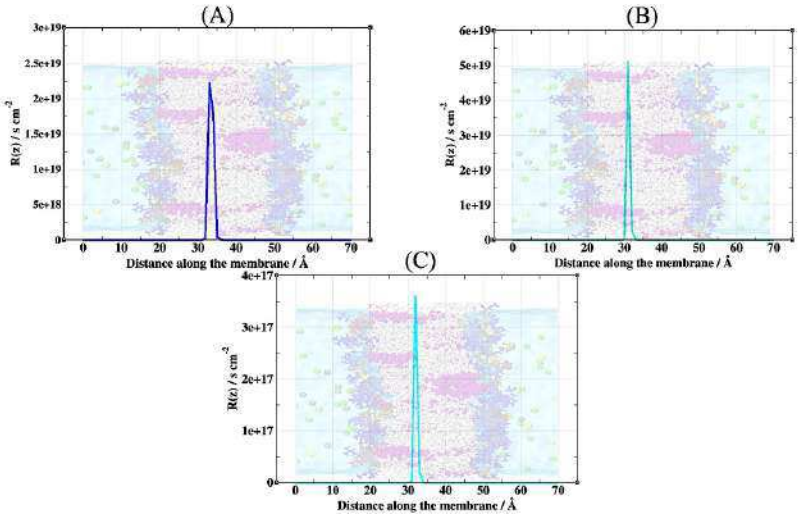

Reference: Own author (2023).